

TECHNISCHE UNIVERSITÄT MÜNCHEN

Fakultät für Informatik
I-16 / Computer Aided Medical Procedures

Tomographic Reconstruction Methods for Optical and Intra-operative Functional Imaging

Tobias Roman Lasser

Vollständiger Abdruck der von der Fakultät für Informatik der Technischen Universität München zur Erlangung des akademischen Grades eines

Doktors der Naturwissenschaften (Dr. rer. nat.)

genehmigten Dissertation.

Vorsitzender: Univ.-Prof. Dr. Daniel Cremers

Prüfer der Dissertation:

1. Univ.-Prof. Dr. Nassir Navab
2. apl. Prof. Dr. Sibylle Ziegler

Die Dissertation wurde am 2. November 2010 bei der Technischen Universität München eingereicht und durch die Fakultät für Informatik am 23. Mai 2011 angenommen.

“Life — the way it really is — is a battle not between good and bad, but between bad and worse.”

Joseph Brodsky

Abstract

Tomographic imaging has revolutionized the medical domain over the last 50 years. Imaging modalities like CT, PET or SPECT have enabled non-invasive diagnosis, patient-specific modeling as well as more accurate treatment, and are increasingly establishing themselves also for interventional use.

The theoretical basis for tomographic imaging has been developing over the last century as well, with series expansion methods quickly being adopted as the method of choice for many modalities due to their flexibility. This work explores series expansion based methods for two novel, emerging imaging modalities.

Diffuse Optical Tomography together with new fluorescent tracers enables visualization of molecular processes in vivo using non-ionizing radiation. In this work an implementation for full-projection free-space Fluorescence Molecular Tomography based on series expansion methods was developed along with a thorough analysis of the system design for the new acquisition geometries. The system was evaluated on phantoms as well as on mice, both ex vivo and in vivo.

While functional imaging is standard-of-care for many pathologies today, interventional use has been hampered by imaging system requirements incompatible with operating room realities. Over the course of this work, a new imaging modality called Freehand SPECT has been developed to overcome this incompatibility. By using tracked functional detectors and series expansion methods adapted to sparse ad-hoc acquisition geometries, Freehand SPECT enables localized intra-operative SPECT imaging. Experiments and evaluations were performed on phantoms as well as on patients both pre- and intra-operatively, and validated the feasibility of this new approach to imaging.

Zusammenfassung

Tomographische Bildgebungsverfahren haben in den letzten 50 Jahren die Medizin revolutioniert. Modalitäten wie zum Beispiel CT, PET oder SPECT ermöglichen nicht-invasive Diagnosen, patientenspezifische Modelle sowie präzisere Therapien und etablieren sich zunehmend auch im interventionellen Bereich.

Die theoretische Basis tomographischer Verfahren wurde über das letzte Jahrhundert hinweg entwickelt, wobei sich algebraische Methoden dank ihrer Flexibilität in vielen Modalitäten etabliert haben. Diese Arbeit behandelt algebraische Methoden für zwei neuartige Bildgebungsverfahren.

Diffuse Optical Tomography ist ein Verfahren, welches zusammen mit neuen fluoreszierenden Markern die Visualisierung von molekularen Prozessen in vivo mittels nicht-ionisierender Strahlung ermöglicht. In dieser Arbeit wurde eine Implementation von full-projection free-space Fluorescence Molecular Tomography basierend auf algebraischen Methoden entwickelt, zusammen mit einer gründlichen Analyse des System-Designs für die neuen Aufnahme-Geometrien. Das System wurde anhand von Phantomen und sowohl ex-vivo als auch in-vivo Mausmodellen evaluiert.

Während funktionale Bildgebung der aktuelle Standard für viele Pathologien ist, hat sich der interventionelle Einsatz als schwierig herausgestellt, aufgrund der Anforderung der Bildgebungs-Systeme, die inkompatibel mit den Realitäten im Operationssaal sind. Im Laufe dieser Arbeit wurde eine neue Bildgebungs-Modalität genannt Freehand SPECT entwickelt, um diese Inkompatibilität zu beseitigen. Mittels getrackter funktionaler Detektoren und algebraischer Methoden adaptiert auf nicht dichte, ad-hoc Aufnahme-Geometrien, ermöglicht Freehand SPECT lokalisiertes, intra-operatives SPECT. Experimente und Evaluationen wurden sowohl an Phantomen als auch an Patienten pre- und intra-operativ durchgeführt, und die Realisierbarkeit dieses neuen Bildgebungsverfahrens validiert.

Acknowledgements

The last few years were quite a journey for me, sometimes it was smooth sailing, sometimes it was rocky and a very few times it was a plunge into the abyss. But it was always interesting and exciting, dull moments were non-existent. I would like to take this chance here to thank and acknowledge the people who have enabled me to function properly along with supporting me and collaborating with me to produce the work you are now holding in your hands. I would also like to apologize for my frequent bad and grumpy moods to those who had to endure them!

I would like to thank my family for providing me the chance to pursue my chosen career path and supporting me in my choices, always present with advice and help whenever necessary. I want to especially thank Susi for her unflagging support and her constant belief in my success, regardless of outcomes. I also want to thank Lili, Paula, Paul and Felix for making it a joy to get up every morning.

My main collaborator in the last four years was Thomas Wendler. Thank you for everything, it has been a pleasure to work together with you (and I hope we will continue to do so). Thomas' sheer limitless energy is awe inspiring, although it sometimes was frustrating as well when I was not able to follow due to being a mere human. Thank you for understanding my strengths and weaknesses, and thank you for letting me come along for the ride in the whirlwind you created here in Munich.

I also want to thank my two supervisors, Nassir Navab and Sibylle Ziegler. Thank you Nassir, for making me part of your chair, for trusting me in my work and for providing the best PhD environment I can imagine. Thank you Sibylle, for your trust and all your invaluable advice, which was available whenever needed.

I want to thank all the people at the CAMP chair for providing an experience second to none. In particular I want to thank Alexandru Dului for our joyful discussions and joint works. I also want to thank Dzhoshkun Shakir and Alexander Hartl for their cooperation and suffering through my various antics. I want to thank José Gardiazabal for his friendship and ready willingness to help with anything.

I would also like to especially thank Vasilis Ntziachristos, for taking me into his lab for a year, helping me survive in Boston as well as providing me an absolutely amazing entry into the field of tomographic imaging. Special thanks go to Joshua Dunham, a ready friend and always extremely helpful! I want to thank Diane Moschella for helping me through all the painful formalities. And last but not least I want to thank the guys at LBMI for making it an experience worth remembering, Antonio Molins, Nikolaos Deliolanis, Stephen Windsor, Antoine Soubret, Damon Hyde, Claudio Vinegoni and Magda Pilatou.

Contents

| | |
|---|------------|
| Abstract | v |
| Zusammenfassung | vii |
| Acknowledgements | ix |
| | |
| 1 Introduction | 1 |
| 1.1 Looking Inside | 1 |
| 1.2 Formulating the Tomographic Problem | 3 |
| 1.3 Imaging Modalities | 5 |
| 1.3.1 X-ray Computed Tomography | 7 |
| 1.3.2 Single Photon Emission Computed Tomography | 10 |
| 1.3.3 Positron Emission Tomography | 12 |
| 1.3.4 Optical Tomography | 14 |
| 1.4 Thesis Outline | 15 |
| | |
| 2 Analytic Reconstruction Methods | 17 |
| 2.1 The Radon Transform | 17 |
| 2.2 Fourier Reconstruction | 19 |
| 2.3 Filtered Backprojection | 21 |
| 2.4 Summary | 23 |
| | |
| 3 Series Expansion Methods | 27 |
| 3.1 General Series Expansion Principle | 27 |
| 3.2 SVD-based Solvers | 31 |
| 3.2.1 Truncated SVD | 33 |
| 3.2.2 Tikhonov Regularization | 34 |
| 3.3 Constraint-based Solvers | 35 |
| 3.3.1 Algebraic Reconstruction Technique and Variants | 35 |
| 3.3.2 Landweber Methods | 37 |
| 3.4 Statistics-based Solvers | 40 |
| 3.5 Summary | 43 |
| | |
| 4 Application: Optical Tomography | 45 |
| 4.1 Imaging Fluorescence | 45 |

| | | |
|----------|---|-----------|
| 4.1.1 | Modeling Light Propagation | 47 |
| 4.2 | Tomographic Reconstruction of Full-Projection FMT | 51 |
| 4.2.1 | Methods | 52 |
| 4.2.1.1 | Experimental setup | 52 |
| 4.2.1.2 | Surface Reconstruction | 54 |
| 4.2.1.3 | Fluorescence Reconstruction | 56 |
| 4.2.1.4 | Experimental Procedures | 57 |
| 4.2.1.5 | Phantoms | 57 |
| 4.2.1.6 | Characterization of animal motion | 58 |
| 4.2.2 | Results | 59 |
| 4.2.2.1 | Accuracy of Surface Reconstruction | 59 |
| 4.2.2.2 | Free-space fluorescence tomography | 60 |
| 4.2.2.3 | In-vivo Accuracy — a Study of Breathing | 60 |
| 4.2.3 | Discussion | 62 |
| 4.3 | Acquisition Optimization via Singular Value Analysis | 64 |
| 4.3.1 | Methods | 66 |
| 4.3.1.1 | Forward model generation | 66 |
| 4.3.1.2 | Singular-value decomposition and noise threshold | 67 |
| 4.3.1.3 | Singular values above threshold | 67 |
| 4.3.1.4 | Experimental setup | 68 |
| | Parallel-plate rotational geometry. | 68 |
| | Cylindrical rotational geometry. | 69 |
| 4.3.1.5 | Experimental measurements | 71 |
| 4.3.2 | Results | 72 |
| 4.3.2.1 | Singular-value analysis, slab geometry | 72 |
| 4.3.2.2 | Experimental reconstructions, slab geometry | 75 |
| 4.3.2.3 | Singular-value analysis, cylindrical geometry | 75 |
| 4.3.2.4 | Experimental reconstructions, cylindrical geometry | 78 |
| 4.3.3 | Discussion | 78 |
| 4.4 | Ex-vivo and In-vivo Studies | 80 |
| 4.4.1 | Methods | 80 |
| 4.4.2 | Experiments and Results | 82 |
| 4.4.2.1 | Ex-vivo | 82 |
| 4.4.2.2 | In-vivo | 85 |
| 4.4.3 | Discussion | 86 |
| 4.5 | Recent Developments | 86 |
| 5 | Application: Freehand SPECT | 89 |
| 5.1 | Freehand SPECT — A New Approach to Intra-operative 3D Nuclear Imaging | 89 |
| 5.2 | Materials and Methods | 91 |
| 5.2.1 | Hardware Setup | 91 |
| 5.2.2 | Reconstruction Pipeline | 92 |
| 5.2.3 | Acquisition Guidance | 95 |
| 5.3 | Phantom Studies | 99 |
| 5.3.1 | Phantom Design | 99 |
| 5.3.2 | Scanning Scheme | 100 |
| 5.3.3 | Acquisition and Reconstruction | 100 |

| | | |
|----------|--|------------|
| 5.3.4 | Evaluation | 103 |
| 5.3.5 | Results | 104 |
| 5.3.6 | Discussion | 109 |
| 5.4 | Pre-operative Patient Studies in Sentinel Lymph Node Mapping | 110 |
| 5.4.1 | Methods | 112 |
| 5.4.2 | Results | 118 |
| 5.4.3 | Discussion | 121 |
| 5.5 | First Intra-operative Patient Studies | 124 |
| 5.6 | NanuLib: the Engine of Freehand SPECT | 126 |
| 5.6.1 | Design and Implementation: first version | 126 |
| 5.6.2 | Advancing the Design: second version | 128 |
| 5.7 | Conclusion and Outlook | 129 |
| 6 | Conclusion | 133 |
| A | List of Publications | 135 |
| A.1 | Journal Publications | 135 |
| A.1.1 | Submitted Journal Publications | 135 |
| A.2 | Conference publications, full papers | 136 |
| A.3 | Conference publications, short papers | 136 |
| A.4 | Conference contributions, abstracts | 137 |
| | Bibliography | 141 |

Chapter 1

Introduction

1.1 Looking Inside

Looking inside a patient or an object is often helpful or even required for many tasks. The diagnosis of many diseases for example requires knowledge of what is happening inside the patient. In a more industrial context, looking inside is also very useful, for example to check the structural integrity of a manufactured product part, or to investigate the internal structure of a raw crystal. However, it is also often not desirable to actually open up the patient or the object to look inside, as it might cause unnecessary harm or damage, or in extreme cases it might even lead to death of the patient or destruction of the object. Therefore many methods have been developed over time to look inside non-invasively. Some methods are indirect, trying to infer interior properties by outside observations. An example from medicine is electrocardiography (ECG, developed for medical use by Willem Einthoven (1860–1927) between 1894 and 1908 [1], for which he was awarded the Nobel prize in Medicine 1924 [2]) to determine the heart rhythm and detect cardiovascular disorders. For industry, example indirect methods are the Rockwell hardness test to determine the tensile strength of metals like steel (original invention by Hugh M. Rockwell (1890–1957) and Stanley P. Rockwell (1886–1940) in 1919 [3], later standardized by ISO 6508-1 in 2005), or goniometry in crystallography to determine the atomic structure in crystals, as introduced by Arnould Carangeot in 1782 [4].

In 1895 Wilhelm Conrad Röntgen (1845–1923) discovered X-rays [5], for which he received the first Nobel prize in Physics 1901 [6]. Looking inside in a direct, non-invasive manner with X-rays quickly established itself as the prime method in multiple fields. Material tests and quality control for industrial manufacturing, but also geology, archeology, astronomy and crystallography are just some examples where X-ray imaging quickly established itself.



Figure 1.1: X-ray image of the hand of Anna Bertha Röntgen, one of the first X-ray images taken in 1895.

The field of medical imaging can trace its roots to the first X-ray picture of the hand of Röntgen's wife Anna Bertha in 1895, see Figure 1.1. X-rays are now routinely used in medical diagnostics, from imaging bone structure, visualizing disease processes in soft tissue to detecting tumors. Since X-rays are ionizing radiation, there are also adverse effects to X-ray exposure, necessitating protective measures and limitation of the radiation dose to patients. On the other hand, this property also enables X-rays to be used for treatment in radiotherapy, in order to destroy unwanted tissue like cancer cells.

However, planar X-ray images can only show a sum of the information gathered as the X-rays transverse the patient. While this is enough for many purposes and is used commonly for example to diagnose pneumonia in patients, the lack of any depth information is often detrimental and can be misleading, potentially resulting in a wrong diagnosis. To overcome this defect, Alessandro Vallebona (1899–1987) in 1930 proposed a method using projective geometry to image a single slice of a patient body by moving a connected X-ray tube and film synchronously in opposite directions. He called this method *Stratigraphy* [7], it produces images which are sharp in the target slice and blurred otherwise. This technique is still used today for example in Orthopantomography to create panoramic dental X-ray images.

In 1971, Sir Godfried Hounsfield (1919–2004) developed the first Computed Tomography scanner [8], based on theoretical work of Allan M. Cormack (1924–1998) published in 1963 and 1964 [9, 10]. Both received the Nobel Prize in Medicine 1979 [11] for the development of *computer assisted tomography*, in short CT. The invention of CT and the subsequent storm of developments enabled the visualization of near-perfect slices of the full body and later on even whole 3D volumes. This has found ample application in medical diagnosis

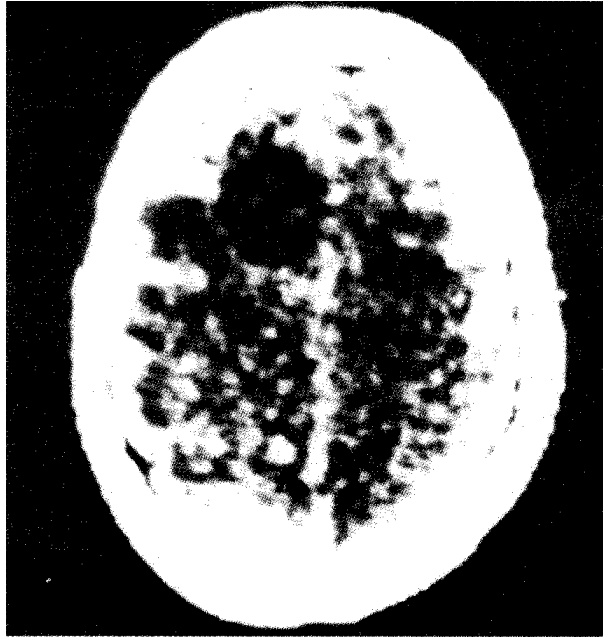


Figure 1.2: First clinical CT slice of a woman with a suspected brain lesion, taken in 1972 by the group of Sir Godfried Hounsfield. *Image Copyright: The Nobel Foundation.*

(see for example the first clinical CT slice in Figure 1.2), with ten thousands of CT scanners installed in hospitals all over the world [12], as well as in other science fields. More recent developments like C-arms with cone-beam reconstruction even allow intra-operative tomographic imaging.

1.2 Formulating the Tomographic Problem

Tomographic imaging generally acquires a series of observations of some physical effect (like the passage of X-rays through an object or patient) and tries to compute some physical property at each location inside the object or patient (like the X-ray attenuation coefficient) from these observations. This process is typically called an **Inverse Problem**.

Mathematically this can be formulated for example as

$$\underbrace{g(x)}_{\text{effect}} = \int \underbrace{k(x, y)}_{\text{cause}} \underbrace{f(y)}_{\text{cause}} dy,$$

where g denotes the observation of the effects and k and f are a parametrization of the causes. In the case of X-ray CT, $g(x)$ would be the measurements of the X-ray detectors, $k(x, y)$ models the process of X-rays passing through the object or patient and $f(y)$ denotes the to-be-determined attenuation coefficients inside the object or patients.

Conversely, the determination of effects from a complete description of their causes is called **Forward Problem**. In the case of X-ray CT, if we had a map of attenuation coefficients $f(y)$ as well as a model $k(x, y)$ of X-rays passing through the objects or patient, the forward problem allows to compute (simulated) measurements $g(x)$ of the X-ray detectors.

The formulation of the inverse problem and the subsequent (usually approximate) solution to it is the heart of every tomographic imaging modality. X-ray CT is just one of many examples of imaging modalities employed for medical use, some of the other common imaging modalities for medical purposes are outlined in section 1.3.

In 1902, Jaques Hadamard (1865–1963) introduced the notions of *well-posed* and *ill-posed* mathematical problems [13].

Definition 1.1 (Hadamard). *A mathematical problem is **well-posed** if all of the following criteria are true:*

1. *A solution exists.*
2. *The solution is unique.*
3. *The solution depends continuously on the data (in some topology).*

*A mathematical problem is called **ill-posed** if one (or more) of these criteria are not met.*

Unfortunately, most of the tomographic inverse problems fall into the ill-posed category. The main cause for this is the discrete sampling of the observations along with typically incomplete observations to keep imaging time in an acceptable range, as well as noise and other errors in the detection and reconstruction process. Thus most (if not all) practical tomographic imaging modalities have no unique solution, or their solution has some non-continuous dependencies on the data. In quite a few cases a solution does not even exist, and only an approximation to something resembling a solution can be computed.

Nevertheless, tomographic imaging has been a huge success so far both in medical and industrial applications, as even those imperfect approximate “solutions” allow to visualize an unprecedented wealth of information about what is inside of patients or objects, without the detrimental side-effects of the established invasive or destructive investigation methods.

While the tomographic inverse problems pose considerable difficulty in dealing with them, they are also an exciting field of research with many interesting and unsolved questions.

1.3 Imaging Modalities

Most imaging modalities use a specific part of the electromagnetic spectrum (see Figure 1.3) to image the object of interest or patient. The most popular example is X-ray Computed Tomography (CT) [8], which sends in X-rays from a dedicated source through the object and detects the modified X-rays at the detector. Other modalities may use one particular part of the spectrum first to excite a certain reaction in the object, and then a different part of the spectrum to detect that reaction, which is what happens for example in near-infrared fluorescence imaging [14]. Some imaging modalities do not use the electromagnetic spectrum, but use for example sound waves like in Ultrasound [15]. There are also hybrid imaging modalities, the most prominent example being Magnetic Resonance Imaging (MRI) [16] where modulated radio waves excite hydrogen nuclei so that their magnetic moments can be detected. Another recent example is photo-acoustic imaging [17], where absorption of electromagnetic energy (for example near-infrared laser light) induces acoustic pressure waves, which in turn are detected by ultrasound transducers.

All the previously mentioned imaging modalities can be classified as **transmission** modalities, where some signal is sent in and another signal is detected coming out. **Emission** modalities however skip the sending in of some signal and only detect the signal coming out, see Figure 1.4 for an illustration. The two most prominent examples for this are Positron Emission Tomography (PET) [18] and Single Photon Emission Computed Tomography (SPECT) [19], which both detect gamma rays (of different energies) coming out from the object or patient. These gamma rays are created by the radioactive decay of some radioactive material inside the object or patient, for example β^+ radiation which in turn produces high-energy gamma rays through annihilation in the case of PET. Typically the object or patient does not contain radioactive material naturally, so in most cases that material has to be administered or implanted in some fashion before the imaging process.

These materials are usually called **tracers** or **probes**, or more generally **imaging agents**. While most of the transmission modalities image the structure of the patient or object, the usage of imaging agents is not only limited to emission modalities. Imaging these tracers allows visualization of physiological activities or molecular processes, which is why this process is called **functional imaging** as opposed to **structural or anatomical imaging**. The beginning of this tracer principle can be attributed to George de Hevesy (1885–1966), for which he received the Nobel prize in Chemistry in 1943 [20]. Functional imaging opens up new horizons of what can be imaged, examples ranging from visualizing blood flow, identifying specific kinds of tumors to imaging disease progression. Various imaging agents exist for almost every imaging modality, a brief summary can be found for example in [21] in the context of small animal imaging. Typically, functional imaging is combined with

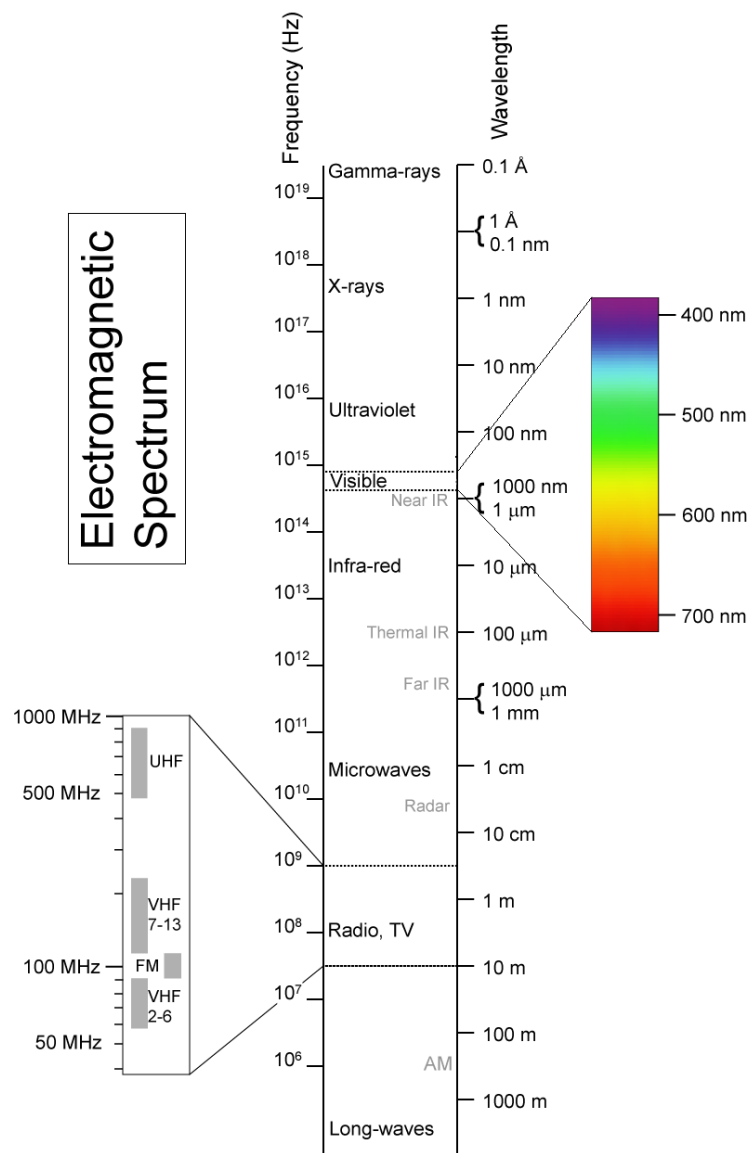


Figure 1.3: The electromagnetic spectrum. (Image source: <http://en.wikipedia.org/wiki/File:Electromagnetic-Spectrum.png>. Author: User Materialscientist. License: CC-by-sa/2.5.)

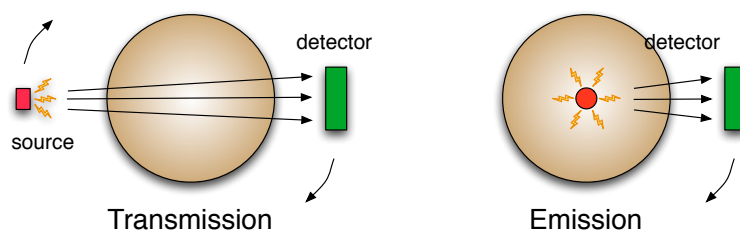


Figure 1.4: Illustration of transmission and emission imaging modalities.

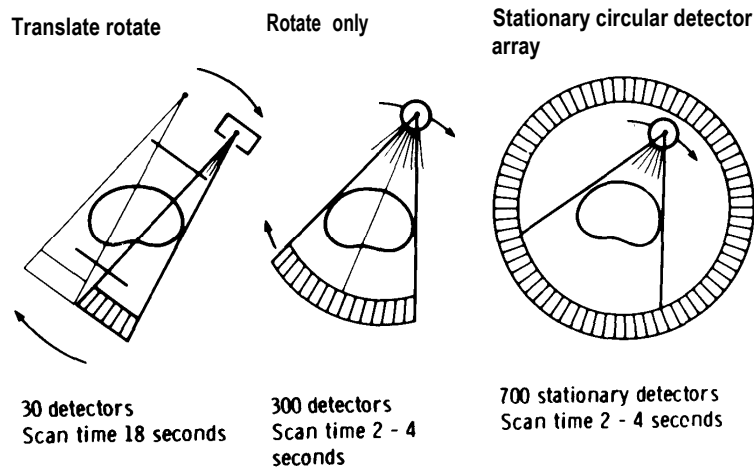


Figure 1.5: Illustration of early slice-scanning geometries by Sir Godfried Hounsfield, 1979. *Image Copyright: The Nobel Foundation.*

some form of anatomical imaging where possible, to allow co-localization of the functional information within the anatomical context.

In the following subsections there are brief outlines of three of the clinically well-established imaging modalities for patients as well as one emerging modality that so far is mostly limited to animal models.

1.3.1 X-ray Computed Tomography

X-ray computed tomography uses X-rays to image three-dimensional absorption contrast inside a patient or object in a transmission geometry. The first system was developed in 1971 by Sir Godfried Hounsfield [8], able to visualize slices of a 3D volume using a parallel scanning geometry with translation and rotation as illustrated in Figure 1.5. The fan-beam geometry to reduce scanning times is also illustrated in Figure 1.5, and since then has been expanded into the cone-beam geometry by using two-dimensional detectors, necessitating fully 3D reconstruction methods as opposed to slice-based methods. Modern full body CT devices typically employ a cone-beam geometry with detectors arranged in an imaging gantry, and do spiral or helical scans for full body imaging with scanning times in the range of seconds, with sub-millimeter accuracies (for example down to 0.24mm on a current Siemens SOMATOM Sensation device).

Other developments include correcting for motion (like breathing or heartbeat) by using gating techniques, or the use of contrast agents to visualize vessels in angiography. Some of the new scanners include dual energy sources to image a second contrast simultaneously, for example allowing acquisition of non-contrast images of a patient undergoing angiography at the same time. Due to the imaging gantry and the patient bed, almost all the medical CT

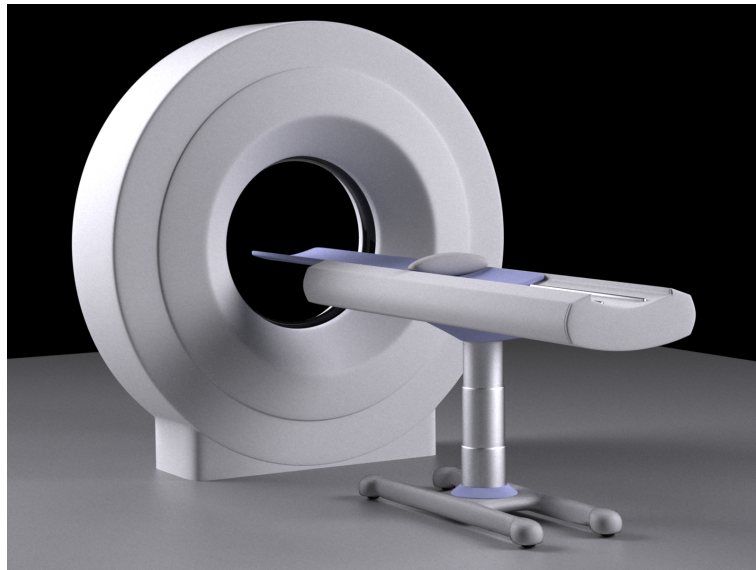


Figure 1.6: Schematic drawing of a modern CT scanner. *Image courtesy Alexandru Dului.*



Figure 1.7: Photograph of a C-arm system used intra-operatively. *Image courtesy of Leijing Wang.*

scanners have a relatively large footprint (see the schematic drawing in Figure 1.6) which along with the cooling, stability and shielding requirements necessitate the installation in separate rooms specifically designed for those scanners. For interventional use, there exist smaller C-arm systems (see Figure 1.7), which typically consist of a (semi-)robotic arm in a C-shape with an X-ray source and a detector plate mounted opposite each other. This allows X-ray snapshots of the patient (when acquired in video rate this is also called fluoroscopy), and with movement of the C-arm (typically in a 120° to 210° arc) it also allows tomographic reconstruction.

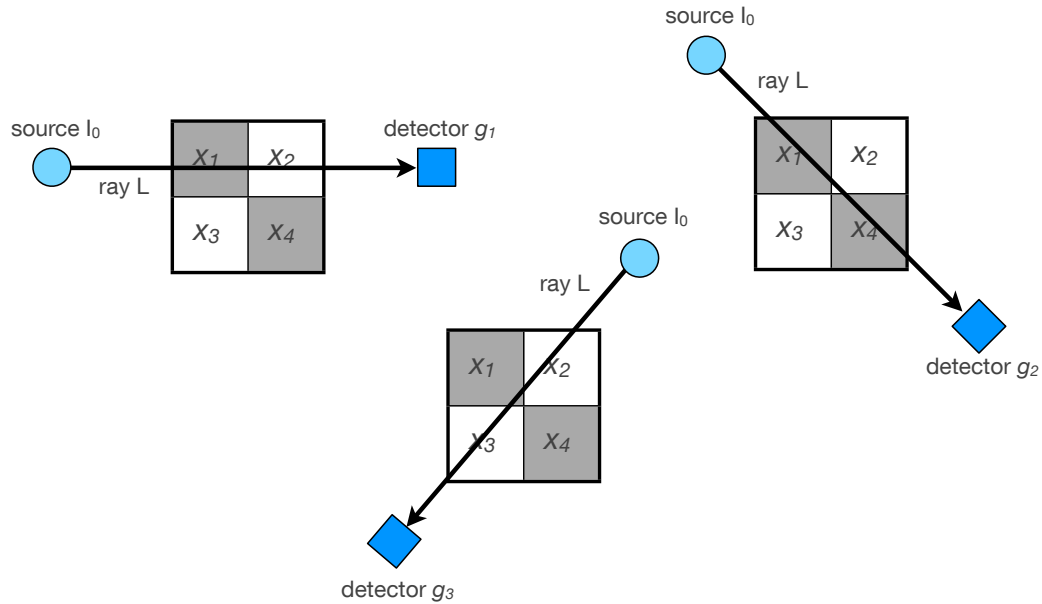


Figure 1.8: Illustration of a very simplistic two-dimensional CT setup.

To illustrate image reconstruction in CT, Figure 1.8 demonstrates a very simplistic two-dimensional CT setup. Let V denote the volume of interest discretized into four voxels, $V = \{x_1, x_2, x_3, x_4\}$. The function $f : V \rightarrow \mathbb{R}$ denotes the attenuation coefficient in each voxel, which is to be determined by CT. Given the three measurements $g = \{g_1, g_2, g_3\}$ and source strength I_0 , the task is then to compute f , an inverse problem.

More generally, a two-dimensional CT setup can be described using the following simple forward model: Let $V \subset \mathbb{R}^2$ again denote the volume of interest, $f : V \rightarrow \mathbb{R}$ the unknown attenuation coefficient. With I_0 the source intensity and L denoting the ray of measurement as illustrated in Figure 1.8, then the detector g is measuring

$$g = I_0 e^{-\int_L f(x) dx},$$

or

$$\ln \frac{I_0}{g} = \int_L f(x) dx.$$

The right hand side of this equation is also known as the **2D Radon Transform**. Several analytic methods exist how to directly invert this integral transform, some of them are outlined in chapter 2. This simple model is enough to produce pleasing CT reconstructions. However, while it does consider the attenuation process, several other physical effects in the detection process are ignored, like for example photon statistics, beam hardening or partial volume effect (see [22] for more details). While these effects can be integrated into the forward model, solving the corresponding inverse problem quickly becomes impractical to impossible. Instead, one approach is to avoid analytically solving the inverse problem

and instead discretize immediately, which leads to the series expansion methods outlined in chapter 3, using for example ART for inversion (see section 3.3.1).

Extensions to 3D setups with more complicated source–detector geometries, while employing very similar concepts, are in most cases not straightforward to approach analytically. For the sake of brevity this work does not consider 3D analytical methods, the interested reader is referred to standard literature instead [22–24]. However, using the series expansion methods introduced in chapter 3 the extension to the 3D case utilizing arbitrary source–detector geometries is straightforward.

1.3.2 Single Photon Emission Computed Tomography

Single Photon Emission Computed Tomography (or in short: SPECT) is a functional emission imaging modality, requiring the use of radioactive tracers emitting gamma rays. One of the common radioactive tracers for SPECT is based on the radioactive isotope Technetium–99m (or ^{99m}Tc) attached to some radio–ligand, which defines what function can be imaged. ^{99m}Tc has a half–life of 6.01 hours and emits gamma rays mainly at an energy of 140.51keV . One of the first SPECT devices can be attributed to David E. Kuhl and Roy Q. Edwards in 1963 [19]. As with CT, the system hardware has developed fast and is still developing. Most systems today include also a CT scanner (see Figure 1.9), to allow attenuation correction as well as anatomical co–localization. Since the emission signal has to be relatively weak to ensure the health of the patients, scanning times are in the 20 to 60 minutes region to collect enough data. SPECT is also a lot less accurate than CT, the typical resolutions of modern systems range from 4.4mm to 11mm . Due to the long acquisition times, breathing and other patient motions are a big issue, combatted with gating and motion compensation techniques.

To illustrate image reconstruction in SPECT, Figure 1.10 demonstrates a very simplistic two–dimensional SPECT setup. Let V denote the volume of interest discretized into four voxels, $V = \{x_1, x_2, x_3, x_4\}$. The function $f : V \rightarrow \mathbb{R}$ denotes the distribution of radioactivity in each voxel, which is to be determined by SPECT. Given the three measurements $g = \{g_1, g_2, g_3\}$ the inverse problem is then to compute f .

More generally, a two–dimensional SPECT setup can be described using the following simple forward model: Let $V \subset \mathbb{R}^2$ again denote the volume of interest, $f : V \rightarrow \mathbb{R}$ the unknown activity distribution and $\mu : V \rightarrow \mathbb{R}$ the attenuation coefficient (as for example reconstructed by CT). Let L denote the ray of measurement and $L(x)$ the section of L between $x \in V$ and the detector, then

$$g = \int_L f(x) e^{-\int_{L(x)} \mu(y) dy} dx.$$

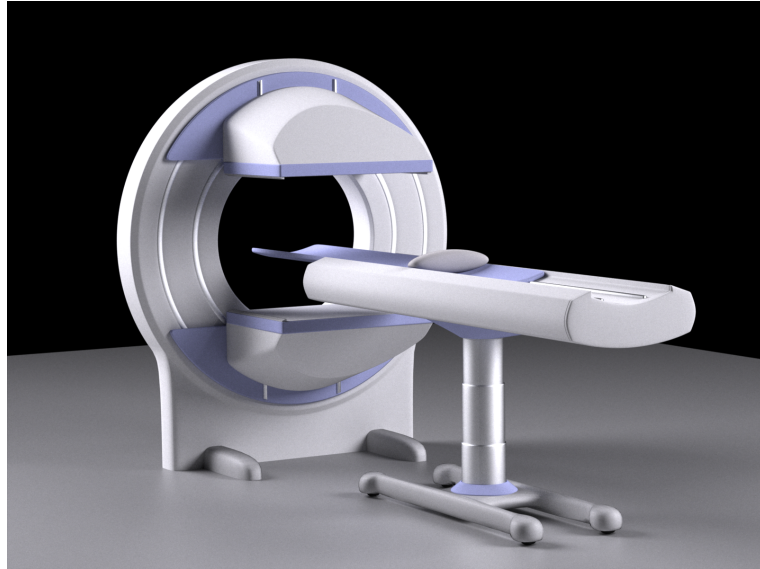


Figure 1.9: Schematic drawing of a modern SPECT scanner. *Image courtesy Alexandru Dului.*

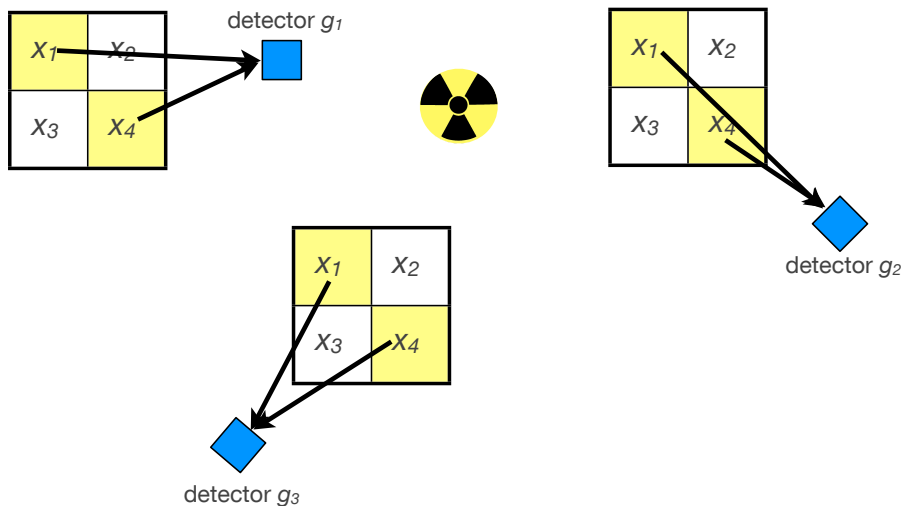


Figure 1.10: Illustration of a very simplistic two-dimensional SPECT setup. Yellow pixels are radioactive, no collimator is displayed for simplicity.

The right hand side of the equation is also known as the **2D attenuated Ray Transform**. Like for CT, this transform is not considering all the physical effects actually occurring in the detection process, like photon statistics, scattering and partial volume effect (see [25] for more details). Early SPECT systems assumed $\mu = 0$, thus reducing the forward problem to the Radon transform, treatable with CT reconstruction methods. However, attenuation is non-negligible in patients, and modern hybrid SPECT/CT scanners can supply an estimation of μ in form of a CT reconstruction. Analytical methods to directly invert the attenuated Ray Transform were discovered relatively recently in 2001 [26, 27]. Nevertheless, series expansion methods are the method of choice for most modern scanners due to their

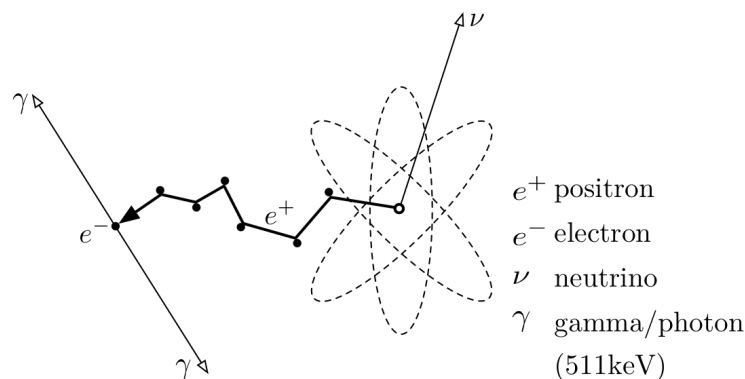


Figure 1.11: Illustration of electron–positron annihilation. The emitted positron “annihilates” with a nearby electron and emits two gamma rays in opposite directions at an energy of 511keV each. *Image courtesy Jens Langner.*

flexibility of modeling physical effects, often using Maximum Likelihood Expectation Maximization (MLEM) or Ordered Subsets Expectation Maximization (OSEM) for inversion, see section 3.4 for details.

1.3.3 Positron Emission Tomography

Positron Emission Tomography (in short: PET) is another functional emission imaging modality. Here, the employed radioactive tracers are labelled with a positron emitter. The most popular one is fluorodeoxyglucose (or ^{18}F -FDG) with a half-life of 110 minutes; it is a glucose analog and tends to aggregate in any body area actively using glucose (for example growing tumors). These emitted positrons however are not directly detectable unless they originate from directly below the surface with the detector being close to the surface, as positrons annihilate with nearby electrons. The typical travel distance before annihilation occurs in tissue is less than 1mm . As illustrated in Figure 1.11, during annihilation two gamma rays are emitted in opposite directions at an energy of 511keV . PET devices are detecting these two “coincident” gamma rays, so the source is known to be localized along the so-called line of response (LOR).

One of the first PET scanners was developed by Michel M. Ter-Pogossian (1925–1996) and Michael E. Phelps (born 1939) in 1975 [18]. Like in SPECT, modern PET devices also include a CT scanner (see Figure 1.12) for attenuation correction and anatomical co-localization. Scanning times are in the 30 minute range and the typical resolution of modern PET scanners is 4.2mm to 7mm . Due to the long acquisition times, compensating for breathing and other patient motions is very important, one more recent approach is to reconstruct both the motion and the activity simultaneously [28].



Figure 1.12: Photograph of a modern PET/CT device, a Siemens Biograph 64.

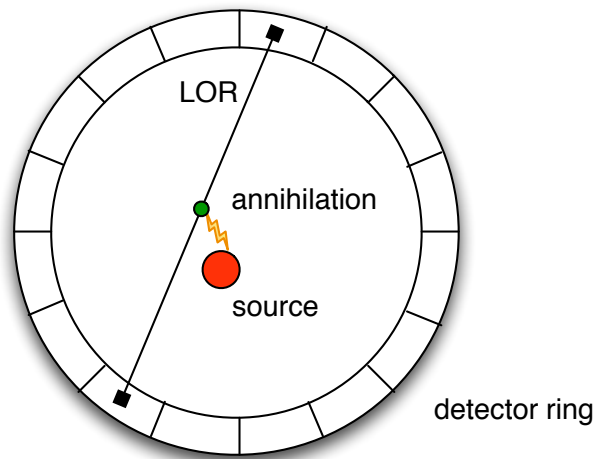


Figure 1.13: Illustration of a two-dimensional PET setup.

A simple two-dimensional PET setup is demonstrated in Figure 1.13. Let $V \subset \mathbb{R}^2$ denote the volume of interest, $f : V \rightarrow \mathbb{R}$ the unknown radioactivity distribution and $\mu : V \rightarrow \mathbb{R}$ the attenuation coefficient. Let L denote the line of response and $L_-(x)$, $L_+(x)$ the half-lines of L with endpoint $x \in V$, then

$$g = \int_L f(x) e^{-\int_{L_-} \mu(y) dy - \int_{L_+} \mu(y) dy} dx.$$

This can be simplified to

$$g = e^{-\int_L \mu(y) dy} \int_L f(x) dx,$$

which is the 2D Radon transform multiplied with an attenuation term. Again, this transform is ignoring many of the physical effects occurring, like photon statistics, scattering or false

coincidences (see [25] for more details). In practice, very early PET systems assumed $\mu = 0$ in order to use reconstruction methods like for CT. Nowadays most PET systems perform attenuation correction and employ series expansion methods to model all the physical effects, in many cases utilizing MLEM or OSEM for inversion (see section 3.4).

1.3.4 Optical Tomography

Employing the visible spectrum to observe objects is natural for human beings as it corresponds to what our eyes see. The visible spectrum however does not penetrate solid objects very well, making it difficult to visualize anything beyond the surface. This is mainly due to high absorption and high scattering of visible light. Moving to the near-infrared as well as investigating objects of smaller size and depth (like mice or human extremities) however enables visualizing the interior using optical techniques.

Diffuse Optical Tomography is such a technique for macroscopic imaging, mainly employed for small animals, but also for human extremities like the breast. Illumination is typically provided by a laser, and imaging is often performed using sensitive, high-resolution cameras. As in other imaging modalities, the use of imaging agents allows to visualize functions like molecular processes. In the case of optical imaging, these agents typically are fluorescent. Fluorescent molecules, when excited by light at the appropriate wavelength emit fluorescent light at another particular wavelength.

This principle is used in the modality called Fluorescence Molecular Tomography (in short: FMT). Mainly used for small animal imaging, a laser emitting at the excitation wavelength of the employed fluorochrome is scanned across the animal, and the corresponding fluorescence emissions are captured using a camera with appropriate filters. While tomography can already be performed without rotating the animal (or the source-detector setup) thanks to the diffusivity of photon propagation through tissue, better depth resolution is possible with full-projection system like those employed for the CT, SPECT or PET modalities presented earlier. An example full-projection setup is displayed in Figure 1.14 and presented in more detail in chapter 4.

Combining FMT with anatomical imaging modalities like CT is advantageous, both for anatomical co-localization and for improving the FMT reconstruction performance, as for example demonstrated in the FMT-XCT system introduced in [29]. Depending on the setup and the fluorochrome employed, scanning times range from 5 to 30 minutes, the achievable resolution is below 1mm .

The forward model for FMT is unfortunately quite complicated. The commonly used model is the radiative transfer equation (RTE), which is introduced and discussed in greater detail



Figure 1.14: Photograph of a FMT system built in 2005 at CMIR, Boston, USA.

in section 4.1.1. Using the notation of section 4.1.1, the RTE reads as follows:

$$\frac{n}{c} \frac{\partial I(r, \hat{s})}{\partial t} + \hat{s} \cdot \nabla I(r, \hat{s}) + \mu_t I(r, \hat{s}) = \frac{\mu_t}{4\pi} \int_{4\pi} p(\hat{s}, \hat{s}') I(r, \hat{s}') d\Omega' + \varepsilon(r, \hat{s}). \quad (1.1)$$

Except for special cases, there is no analytic solution to this equation. The inverse problem for FMT and related optical tomographic modalities is thus usually tackled via series expansion methods, as described in chapter 3.

1.4 Thesis Outline

In this thesis we present mathematical methods for tomographic image reconstruction, along with two applications of these methods to two novel, emerging imaging modalities: full-projection free-space Fluorescence Molecular Tomography and Freehand SPECT. Tomographic reconstruction methods can be classified into two types, chapter 2 presents the first type called analytical methods (or transform methods) for two-dimensional CT-like setups, while chapter 3 presents the second type, series expansion methods (or algebraic methods) for general tomography setups. Series expansion methods have quickly been adopted as the method of choice for many modalities due to their flexibility. It is thus no surprise that the two applications presented in chapters 4 and 5 are based on series expansion methods. Chapter 4 presents the full-projection free-space FMT imaging modality for use in small animal imaging, describing the system setup and methods as well as validation experiments of the system design using phantoms and mice. In chapter 5 the intra-operative Freehand SPECT modality is presented, from the system setup and methods to validation experiments on phantoms and patients. The last chapter 6 contains a short conclusion.

Chapter 2

Analytic Reconstruction Methods

Tomographic reconstruction methods can be classified into two types, analytical and series expansion methods. Analytical methods (also called transform methods) attempt to model the inverse problem and solve it analytically, only discretizing at the very end to implement the reconstruction method. Series expansion methods (also called algebraic methods, see chapter 3 for more details) discretize the problem right away and try to solve it that way.

In this chapter we present some of the analytical reconstruction methods for modalities based on the 2D Radon transform using parallel scanning geometry. 3D reconstructions can be achieved by stacking several 2D slices. Extensions to different transforms and different source–detector geometries are possible as well as fully 3D reconstructions, but matters quickly get complicated and for the sake of brevity this is not considered in this work, instead we refer to [22–24].

While this section attempts to be mathematically precise in its formulations, we do not provide the most general conditions on the involved functions and parameters (for example we generally settle on a vague “ f sufficiently nice”) and neither do we provide proofs. Again the interested reader is referred to standard literature [23, 30] and references therein.

2.1 The Radon Transform

Johann Radon (1887–1956) introduced an integral transform mapping a function into integrals over the hyperplanes in \mathbb{R}^n in 1917, which was named after him.

Definition 2.1 (Radon transform, n –dimensional version). *Let $f : \mathbb{R}^n \rightarrow \mathbb{R}$ be sufficiently nice, then the mapping $\mathcal{R}f : (f : \mathbb{R}^n \rightarrow \mathbb{R}) \rightarrow (\mathcal{R}f : S^{n-1} \times \mathbb{R} \rightarrow \mathbb{R})$ defined by*

$$\mathcal{R}f(u, t) := \int_{u^\perp} f(tu + y) dy$$

is called the **Radon Transform** for $u \in S^{n-1} \subset \mathbb{R}^n$, $t \in \mathbb{R}$ and $u^\perp := \{y \in \mathbb{R}^n : \langle y, u \rangle = 0\}$.

We will also use the short-hand notation: $f_u : \mathbb{R} \rightarrow \mathbb{R}$, $f_u(t) := \mathcal{R}f(u, t)$.

Mapping a function into integrals over straight lines has a different name:

Definition 2.2 (Ray transform, n -dimensional version). *Let $f : \mathbb{R}^n \rightarrow \mathbb{R}$ be sufficiently nice and define $T^n := \{(u, x) : u \in S^{n-1}, x \in u^\perp\}$, then the mapping $\mathcal{P}f : (f : \mathbb{R}^n \rightarrow \mathbb{R}) \rightarrow (\mathcal{P}f : T^n \rightarrow \mathbb{R})$ defined by*

$$\mathcal{P}f(u, x) := \int_{\mathbb{R}} f(x + tu) dt$$

is called the **Ray Transform** for $(u, x) \in T^n$.

For the case $n = 2$ the Radon transform and the Ray transform are identical save for notational differences.

An inversion formula for $\mathcal{R}f$ was first shown by Radon in 1917 [31] (English translation [32]), stated here for the two-dimensional case:

Theorem 2.3 (Radon inversion formula, $n = 2$). *Let $f : \mathbb{R}^2 \rightarrow \mathbb{R}$ be sufficiently nice, then*

$$f(x) = -\frac{1}{4\pi^2} \int_{S^1} \int_{\mathbb{R}} \frac{f'_u(\langle x, u \rangle + t)}{t} dt du.$$

The integral in t is in the Cauchy principal value sense.

Unfortunately this inversion formula is not very useful for practical reconstruction. The operations are complex to implement, and all line integrals are needed to calculate $f(x)$, even for lines far away from x , which conflicts with practical scanning schemes. More practical inversion formulas are presented in the following sections.

The 2D parallel scanning geometry we are employing here can be discretized using $2q + 1$ detectors equidistantly spaced at $t_l = \frac{1}{q}l$, $l = -q, \dots, q$, rotated by p projection angles u_1, \dots, u_p uniformly distributed over the half-circle, see Figure 2.1 for an illustration. That means $\mathcal{R}f$ is sampled at $\mathcal{R}f(u_j, t_l)$. Other scanning geometries are not considered in this chapter.

Acquiring images using this 2D parallel scanning geometry, that is, computing or measuring the 2D Radon transform, is often called taking **sinograms**. As illustrated in Figure 2.2, the Radon transform of a simple point looks like a sine wave, hence the name sinogram. For demonstration purposes the so-called ‘‘Shepp–Logan phantom’’ will be used in this chapter (see Figure 2.3a), it is named after L.A. Shepp and B.F. Logan, who introduced

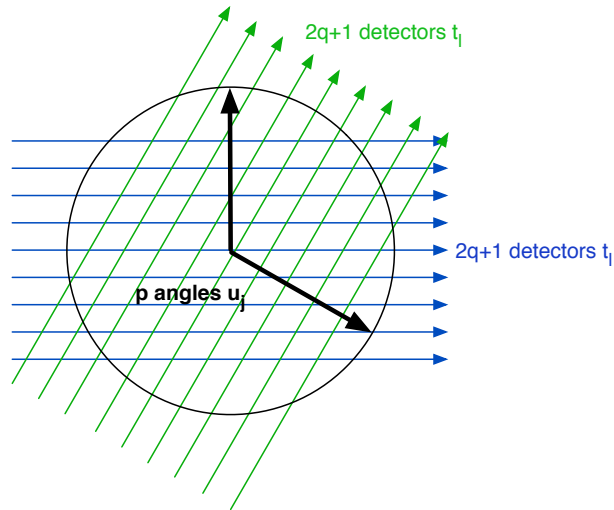


Figure 2.1: Illustration of 2D parallel scanning geometry employed in this chapter.



Figure 2.2: *Left*: image with three points, *right*: sinogram of those three points created using a parallel scanning geometry.

this simplified head phantom in 1974 [33]. The Radon transform of this phantom calculated for the angles 0° to 180° in 1° steps, its sinogram, is shown in Figure 2.3b. All the images shown here were generated using Matlab.

2.2 Fourier Reconstruction

The Fourier reconstruction method is taking advantage of the following relationship between the Radon transform and the Fourier transform, also called the Fourier Slice Theorem or the Central Slice Theorem [23, 34]:

Theorem 2.4 (Central Slice Theorem, n -dimensional version). *Let $f : \mathbb{R}^n \rightarrow \mathbb{R}$ be sufficiently nice. Then for $u \in S^{n-1}$ and $t \in \mathbb{R}$*

$$\mathcal{F}_1(\mathcal{R}f(u, \cdot))(t) = (2\pi)^{\frac{n-1}{2}} (\mathcal{F}_n f)(tu),$$

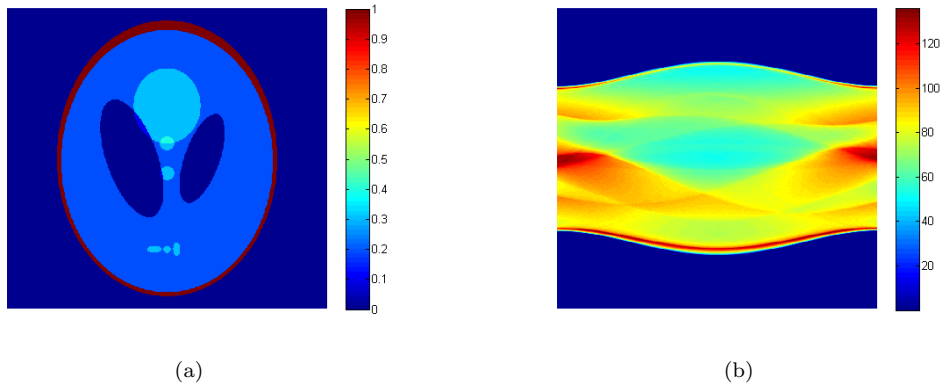


Figure 2.3: (a) Shepp–Logan simplified head phantom, (b) sinogram of Shepp–Logan phantom created using parallel scanning geometry.

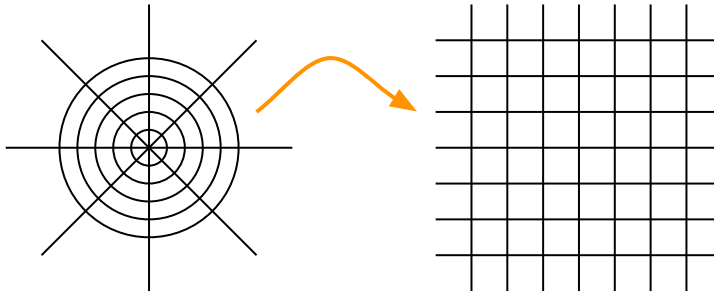


Figure 2.4: Coordinate system change in step 2 of the Fourier reconstruction algorithm.

where \mathcal{F}_n denotes the n -dimensional Fourier transform.

Calculating Fourier transforms on a computer is very efficient thanks to the Fast Fourier Transform algorithm (FFT), thus a practical inversion algorithm called **Fourier Reconstruction** employs the Central Slice Theorem. Here is the algorithm for the case $n = 2$:

Algorithm 1 Fourier Reconstruction

$$f = \mathcal{F}_2^{-1} \left(\frac{1}{\sqrt{2\pi}} \mathcal{F}_1(\mathcal{R}f(u, t)) \right).$$

1. Compute 1D DFT of $\mathcal{R}f(u_j, t_l)$,

$$\hat{f}_{jl} \approx \mathcal{F}_1(\mathcal{R}f(u_j, t_l)).$$

2. Find nearest $k \in \mathbb{Z}^2$ for $\pi l u_j \in \mathbb{R}^2$ (see Figure 2.4).
3. Compute 2D IDFT of \hat{f}_k ,

$$f_m \approx f\left(\frac{1}{q}m\right).$$

The complexity of this algorithm is $O(q^2 \log q)$.

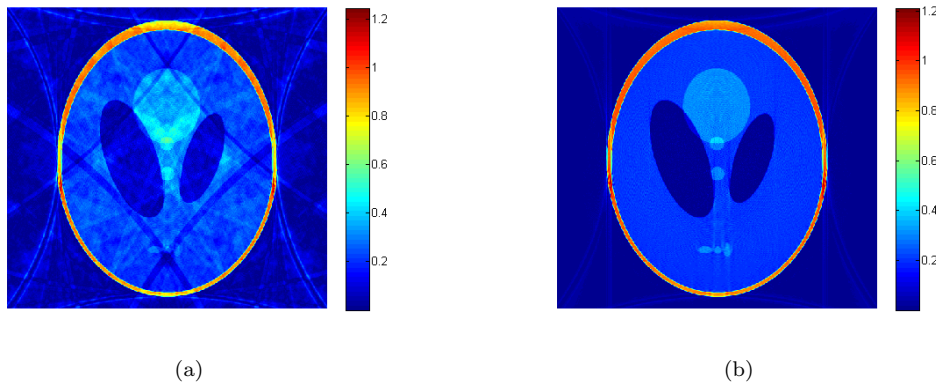


Figure 2.5: Sample reconstructions of the Shepp–Logan phantom using the Fourier reconstruction method, (a) using nearest–neighbor and (b) cubic spline interpolation.

The deciding reconstruction quality factor here is the coordinate system change in step 2 of the algorithm. The naive approach of nearest–neighbor interpolation works, Figure 2.5a shows an example reconstruction of the Shepp–Logan sinogram from Figure 2.3b using Matlab. A reconstruction using cubic spline interpolation is shown in Figure 2.5b. There are several more sophisticated methods available to increase the reconstruction quality, these include oversampling, filtering and smoothing, or implementing a one–dimensional FFT that directly evaluates onto the cartesian grid, see for example [34–38].

2.3 Filtered Backprojection

A backprojection operator \mathcal{R}^* can be defined for sufficiently nice $g : S^{n-1} \times \mathbb{R} \rightarrow \mathbb{R}$ and $x \in \mathbb{R}^n$,

$$\mathcal{R}^*g(x) = \int_{S^{n-1}} g(u, \langle x, u \rangle) du.$$

If $g = \mathcal{R}f$, then $(\mathcal{R}^*g)(x)$ is the average of all hyperplane integrals of f through x . It can be shown [23] that \mathcal{R}^* is the adjoint operator of \mathcal{R} , that is for f, g sufficiently nice

$$\int_{S^{n-1}} \int_{\mathbb{R}} (g\mathcal{R}f)(u, t) dt du = \int_{\mathbb{R}^n} (\mathcal{R}^*g)f(x) dx.$$

The following theorem is the basis for the Filtered Backprojection (FBP) reconstruction method [23, 30]:

Theorem 2.5. *Let $f : \mathbb{R}^n \rightarrow \mathbb{R}$, $g : S^{n-1} \times \mathbb{R} \rightarrow \mathbb{R}$ be sufficiently nice, then*

$$(\mathcal{R}^*g) * f = \mathcal{R}^*(g * \mathcal{R}f).$$

The idea of FBP is now to find a function g such that $\mathcal{R}^*g \approx \delta$ is an approximate identity, then $((\mathcal{R}^*g) * f)(x) \approx (\delta * f)(x) = f(x)$. As convolution is also called filtering in certain fields, g is typically called a filter, which explains the name of the filtered backprojection algorithm. The FBP algorithm can then be stated as:

Algorithm 2 Filtered Backprojection

1. Choose filter g such that $\mathcal{R}^*g \approx \delta$.
2. Apply filter g to $\mathcal{R}f(u_j, t_l)$, i.e. compute

$$v_{jl} = (g * \mathcal{R}f(u_j, t_l))(u_j, t_l).$$

3. Calculate discrete backprojection of the v_{jl} ,

$$f(x) \approx (\mathcal{R}_{\text{disc}}^*(v_{jl}))(x).$$

The complexity of FBP is $O(q^3)$.

Besides a proper implementation of the discrete backprojection operator, the choice of the filter g is the crucial parameter for reconstructed image quality. Step 2 of the FBP algorithm (computing $g * \mathcal{R}f$) is typically performed in the Fourier domain, as $\widehat{g * \mathcal{R}f} = \sqrt{(2\pi)^n} \widehat{g} \cdot \widehat{\mathcal{R}f}$. Thus it is convenient to specify the filter g in the Fourier domain as \widehat{g} . One family of filters typically employed for FBP [24] is

$$\widehat{g}_b(\sigma) = \frac{1}{2} (2\pi)^{\frac{1}{2}-n} |\sigma|^{n-1} \widehat{\Phi}\left(\frac{\sigma}{b}\right),$$

where b is the cut-off frequency and $\widehat{\Phi}$ is the filter factor that has to be chosen.

One of the more popular choices is the so-called *Ram-Lak* filter developed by G.N. Ramachandran and A.V. Lakshminarayanan in 1971 [39], it is an ideal low-pass,

$$\widehat{\Phi}(\sigma) = \begin{cases} 1 & \sigma \in [0, 1] \\ 0 & \text{else.} \end{cases}$$

This filter is also called *Ramp* filter, due to the shape shown for example in Figure 2.6. Another filter, also shown in Figure 2.6, was suggested by L.A. Shepp and B.F. Logan in 1974 [33],

$$\widehat{\Phi}(\sigma) = \begin{cases} \text{sinc}\left(\frac{\sigma\pi}{2}\right) & \sigma \in [0, 1] \\ 0 & \text{else,} \end{cases}$$

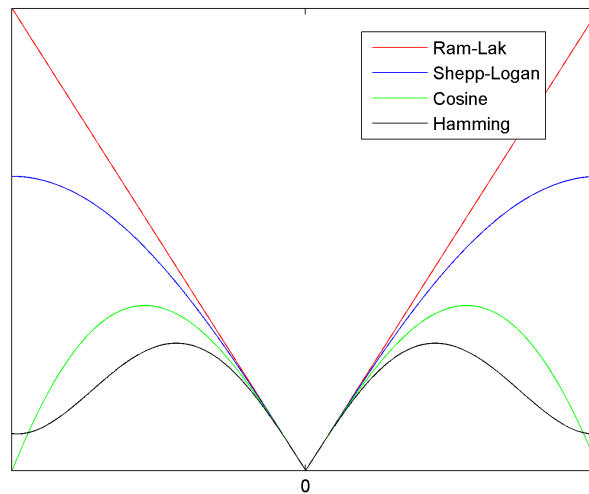


Figure 2.6: Potential filters for use in FBP, Ram–Lak (red), Shepp–Logan (blue), Cosine (green) and Hamming (black), plotted in the Fourier domain.

where $\text{sinc}(x) := \frac{\sin(x)}{x}$ for $x \neq 0$ and $\text{sinc}(0) = 1$. There are many more variants, Figure 2.6 is showing two more, the *Cosine* filter mentioned for example in [24]

$$\widehat{\Phi}(\sigma) = \begin{cases} \cos\left(\frac{\sigma\pi}{2}\right) & \sigma \in [0, 1] \\ 0 & \text{else,} \end{cases}$$

and the Hamming filter mentioned for example in [40]

$$\widehat{\Phi}(\sigma) = \begin{cases} 0.54 + 0.46 \cos(\sigma\pi) & \sigma \in [0, 1] \\ 0 & \text{else.} \end{cases}$$

Example reconstructions of the Shepp–Logan phantom from Figure 2.3a using FBP are shown in Figure 2.7, first the unacceptable result without any filter and then using the ramp, cosine and Hamming filter.

2.4 Summary

In this chapter we presented the Radon transform as well as two methods on how to invert the Radon transform with practical and efficient algorithms: Fourier reconstruction and Filtered Backprojection. Algorithms were specified for the two–dimensional parallel scanning geometry along with example reconstructions of the Shepp–Logan phantom using these algorithms, see Figure 2.8.

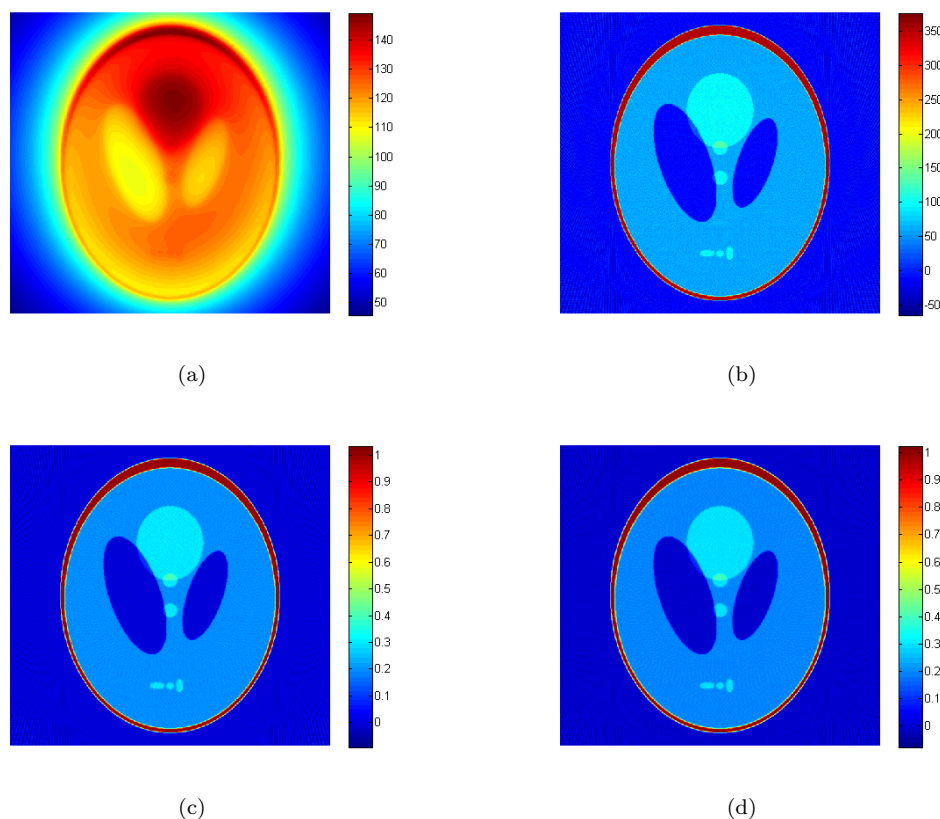


Figure 2.7: Sample reconstructions of the Shepp–Logan phantom using the Filtered back-projection method (a) without any filter, (b) with the ramp filter, (c) the cosine filter and (d) the Hamming filter.

While the Fourier Reconstruction algorithm is slightly more efficient computationally, the Filtered Backprojection method is more popular. The main reason for that is not reconstructed image quality, as it is comparable if the parameters of the algorithms are chosen carefully. However, the method can be easily understood by anyone with an engineering background as the employed concepts are familiar, which is one of the main reasons for the popularity of the FBP method.

Extensions of both methods to more complex scanning geometries can be performed for example by resampling the acquired data into a parallel scanning geometry (this is typically called “rebinning”). Better results however can be achieved by adapting the methods for the particular scanning geometry which can range in difficulty from straightforward to complicated, see for example [24].

Extending the reconstructions of the 2D slices to three dimensions can be achieved by processing several slices and stacking them together into a 3D volume. However, performing a fully 3D reconstruction is often more desirable, or in case of for example the cone–beam scanning geometry, necessary. While the concepts remain the same, the actual extensions

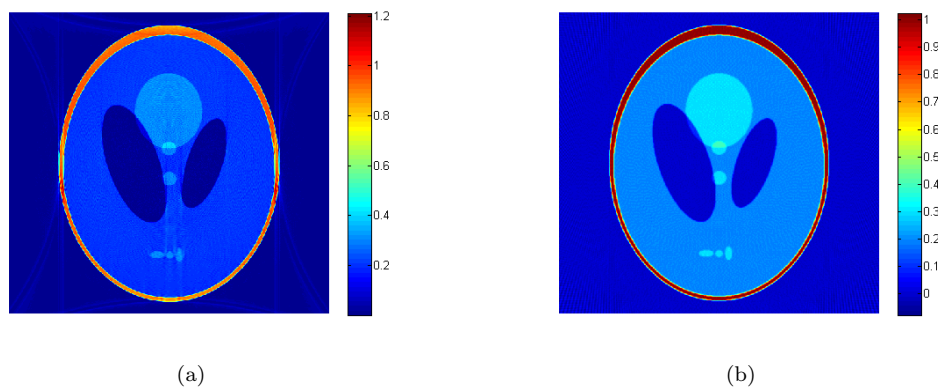


Figure 2.8: Comparison of sample reconstructions of the Shepp–Logan phantom using (a) Fourier reconstruction and cubic spline interpolation and (b) Filtered Backprojection with the Hamming filter.

for $n = 3$ are often not straightforward. The popular Feldkamp method for cone–beam scanning geometries [41] for example is a 3D extension of the FBP method presented in this chapter.

Chapter 3

Series Expansion Methods

In this chapter we present some of the series expansion methods for tomographic reconstruction. As opposed to the analytic methods from chapter 2 which attempt to solve the inverse problem analytically and discretize only at the end for computations, here the problem is discretized straight away, yielding a linear system that has to be solved to obtain the reconstruction.

This chapter presents the general series expansion principle and several standard approaches to compute a solution of the resulting linear system. As in chapter 2, an exhaustive treatment of all available series expansion methods is not possible within the scope of this work, the interested reader is referred to for example [22, 30] as starting points to the literature.

3.1 General Series Expansion Principle

In tomographic reconstruction we are typically interested in recovering a function $f : V \rightarrow \mathbb{R}$, mapping a volume of interest $V \subset \mathbb{R}^n$ to some real-valued property like the attenuation factor in CT (vector-valued properties are not considered in this work).

The series expansion approach is to discretize f immediately. Let $\{b_i\}_{i \in I}$ denote a finite set of basis functions $b_i : V \rightarrow \mathbb{R}$ chosen such that there exists a linear combination \hat{f} of the basis functions b_i which is a suitable approximation of f in some metric,

$$\hat{f} = \sum_{i \in I} x_i b_i \quad \text{with } \{x_i\}_{i \in I} \subset \mathbb{R}. \quad (3.1)$$

Then the coefficient vector $x = \{x_i\}_{i \in I}$ is the discretized version of the quantity to be reconstructed, f . If the basis functions are linearly independent, then the mapping of \hat{f} to x is bijective.

A common example of discretization is a $k \times k$ -pixel grid overlaid over a two-dimensional rectangular image, or a $k \times k \times k$ -voxel grid overlaid over a three-dimensional rectangular volume. Then in the two-dimensional case $I = \{1, \dots, k^2\}$ and the basis functions are

$$b_i(c_1, c_2) = \begin{cases} 1 & \text{if } (c_1, c_2) \text{ is inside the } i\text{-th pixel} \\ 0 & \text{else,} \end{cases} \quad (3.2)$$

while $I = \{1, \dots, k^3\}$ for the three-dimensional case and

$$b_i(c_1, c_2, c_3) = \begin{cases} 1 & \text{if } (c_1, c_2, c_3) \text{ is inside the } i\text{-th voxel} \\ 0 & \text{else.} \end{cases} \quad (3.3)$$

Let $y = \{y_j\}_{j \in J} \subset \mathbb{R}$ denote the finite set of physical measurements performed in the tomographic imaging modality, and let $\mathcal{M}_j : (f : \mathbb{R}^n \rightarrow \mathbb{R}) \rightarrow \mathbb{R}$ be the physical model of the measurement process (also called forward model) such that $\mathcal{M}_j f = y_j$. The major assumption in the series expansion method is now the validity of

$$\mathcal{M}_j f \approx \mathcal{M}_j \hat{f} = \sum_{i \in I} x_i \mathcal{M}_j b_i. \quad (3.4)$$

This is automatically true if \mathcal{M}_j is a continuous linear functional.

In the example of chapter 2, the case of two-dimensional CT with parallel scanning geometry, we have $\mathcal{M}_j f = \mathcal{R}f(u_{k_j}, t_{l_j})$ and $y = \{\mathcal{R}f(u_{k_j}, t_{l_j})\}$.

Finally, denoting $a_{ji} = \mathcal{M}_j b_i$ and $A = (a_{ji}) \in \mathbb{R}^{|J| \times |I|}$, the series expansion approach results in a linear system

$$Ax = y. \quad (3.5)$$

A is usually called the **system matrix**. The final step is now to determine a solution (or an approximate solution) x^* via some solving procedure, resulting in a reconstruction of f ,

$$f^* = \sum_{i \in I} x_i^* b_i.$$

In summary, the series expansion method can be written as algorithm 3.

Algorithm 3 Series Expansion Method

1. Discretize using a set of basis functions $\{b_i\}$.
 2. Compute the system matrix $A = (a_{ji})$ using the forward model $a_{ji} = \mathcal{M}_j b_i$.
 3. Solve $Ax = y$.
-

Typically, most of the “intelligence” of this method is in the forward model, which depends on the imaging modality and the actual device setup. Any modality can be modeled here (as long as equation (3.4) holds), which explains the flexibility of the series expansion method.

Choosing the basis functions appropriately can help in increasing the reconstruction quality as well. While the most common choice of basis functions are the regular, rectangular grid basis functions defined in equations (3.2) and (3.3), another popular choice are the generalized Kaiser–Bessel window functions, also called spherically–symmetric volume elements or in short blobs [22, 42–44]. Blobs have a bell-shaped profile, falling off smoothly in radial direction with continuous derivatives, leading to a smoother reconstruction, useful for imaging modalities with noisy data. However, in practice several parameters of the blobs have to be fixed, and choosing them optimally for the problem at hand to enable image fidelity is not a trivial process [45, 46]. Furthermore there is a significant computational overhead.

The choice of the solution method for the linear system $Ax = y$ also factors into reconstruction quality. Some of the commonly used methods are outlined in the following sections of this chapter. Due to different origins and properties, some methods might be better suited than others for a specific imaging modality, like MLEM (see section 3.4) for emission tomography modalities.

To note here is that the system $Ax = y$ does not necessarily have a solution. Measurement errors, noise, insufficient data or deficiencies in the forward model \mathcal{M} may lead to the system having no unique solution or no solution at all. Thus step 3 of the series expansion method is also formulated using an error vector $e \in \mathbb{R}^{|J|}$ [22]

$$Ax + e = y. \tag{3.6}$$

e is however typically unknown, so the problem of computing a solution to (3.6) becomes an optimization process to compute an estimate of the “solution” depending on chosen criteria. The most common example here is finding the least squares solution,

$$\min_x \|y - Ax\|_2.$$

Extensions include adding additional terms to the optimization criterion like for example the total variation or other prior knowledge, or adding constraints like for example forcing the reconstruction to be non–negative. Another possibility is to model x and e as samples of a random variable and then use a Bayesian approach with priors or a maximum likelihood approach. A brief overview over possible optimization criteria can be found in [22].

The computational complexity of the series expansion methods is typically higher than for analytic methods. Using the simple line–based 0, 1 approach as a forward model for CT as

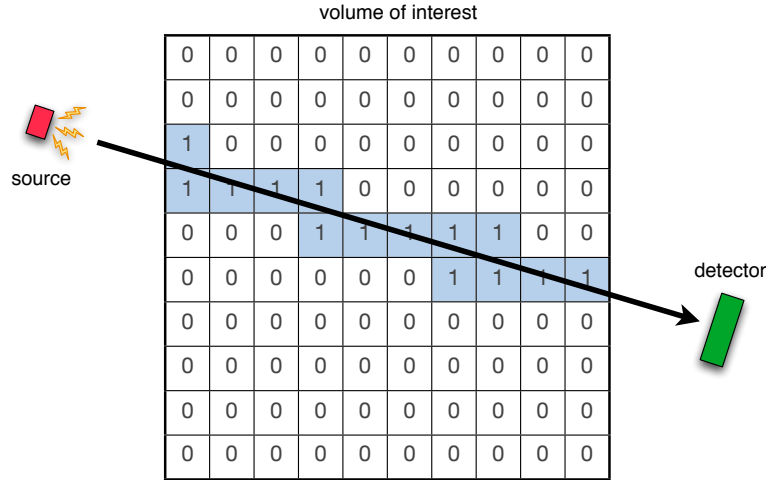


Figure 3.1: Illustration of a simple forward model for a 2D CT setup with one line integral passing from source through the volume of interest to the detector. Any pixel that is hit by the line is assigned a 1, all others a 0. Linearized into a row vector these values form one row of the system matrix A .

outlined in the following example along with the ART inversion method (see section 3.3.1 below) yields a complexity of $O(q^3)$ using the notations from chapter 2. This is comparable to the FBP reconstruction method. However, the strength of the series expansion methods lies in the flexibility and accuracy of the forward model, and it is not uncommon to have a forward model with a computational complexity an order of magnitude higher than the inversion process (an example is optical tomography, see chapter 4).

To illustrate the series expansion approach, a simple two-dimensional parallel scanning geometry CT setup serves as an example, see Figure 3.1. More complicated examples can be found in the two following chapters 4 and 5 detailing the Fluorescence Molecular Tomography and Freehand SPECT imaging modalities.

Figure 3.1 displays a volume of interest $V \subset \mathbb{R}^2$ discretized into 10×10 pixels using the basis functions $b_i(c_1, c_2)$ from (3.2), with a source projecting X-rays along a line to the detector. The reading of the detector corresponds to y_j for some j . According to how the X-rays are passing through V , the pixels are marked with 0 (no intersection of pixel and line) or 1 (intersection of pixel and line). These zeros and ones correspond to $\mathcal{M}_j b_i = a_{ji}$, and together form the j -th row of the system matrix A ,

$$\underbrace{\begin{pmatrix} \cdot & \cdots & \cdot \\ a_{j1} & \cdots & a_{j100} \\ \cdot & \cdots & \cdot \end{pmatrix}}_A \underbrace{\begin{pmatrix} x_1 \\ \vdots \\ x_{100} \end{pmatrix}}_x = \underbrace{\begin{pmatrix} \vdots \\ y_j \\ \vdots \end{pmatrix}}_y.$$

Repeating this process for all measurements $j \in J$ yields the system equation $Ax = y$.

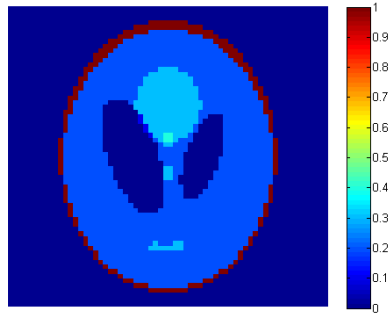


Figure 3.2: Shepp–Logan phantom used for example reconstructions throughout this chapter, the resolution is lower than in chapter 2 due to computational limitations.

As an example, this simple forward model was used to generate the system matrix A for the Shepp–Logan phantom from chapter 2 using Matlab, albeit at a lower resolution due to computational limitations. The phantom was discretized into 64×64 pixels, see Figure 3.2, the system matrix A was created using 4096 simulated measurements y in a parallel scanning geometry.

3.2 SVD–based Solvers

Let $A \in \mathbb{R}^{m \times n}$ with $m \geq n$ (for $m < n$ use A^t instead of A). The Singular Value Decomposition (SVD) of A is defined as

$$A = U\Sigma V^t = \sum_{i=1}^n u_i \sigma_i v_i^t,$$

where $U = (u_1, \dots, u_n) \in \mathbb{R}^{m \times n}$ and $V = (v_1, \dots, v_n) \in \mathbb{R}^{n \times n}$ are orthogonal matrices, $U^t U = V^t V = I_n$ (I_n is the $n \times n$ identity matrix). $\Sigma = \text{diag}(\sigma_1, \dots, \sigma_n)$ is a diagonal matrix with non–negative elements sorted in non–increasing order, $\sigma_1 \geq \sigma_2 \geq \dots \sigma_n \geq 0$. The SVD exists for any matrix A .

If A is invertible, then $\sigma_i > 0$ for all $i = 1, \dots, n$ and we can use SVD to calculate $A^{-1} = V\Sigma^{-1}U^t$ with $\Sigma^{-1} = \text{diag}(\sigma_1^{-1}, \dots, \sigma_n^{-1})$. Thus the solution to our series expansion reconstruction problem $Ax = y$ would read as

$$x^* = \sum_{i=1}^n \frac{u_i^t y}{\sigma_i} v_i. \quad (3.7)$$

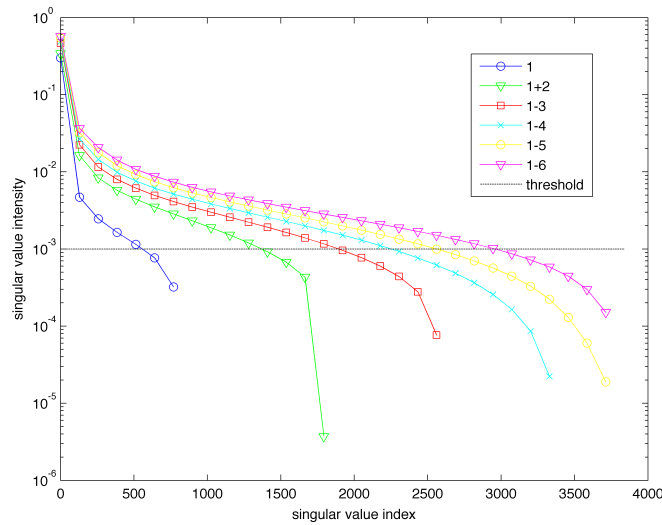


Figure 3.3: Example singular value spectra of the system matrix A of several Freehand SPECT acquisitions, see chapter 5.

If A is not invertible, that is $\text{rank}(A) < n$, then leaving out the terms with $\sigma_i = 0$ in (3.7) leads to

$$x^* = \sum_{i=1}^{\text{rank}(A)} \frac{u_i^t y}{\sigma_i} v_i, \quad (3.8)$$

which is the least squares solution of $\min_x \|Ax - y\|_2$ with minimum 2-norm [47]. Incidentally, $A^+ = \sum_{i=1}^{\text{rank}(A)} v_i \sigma_i^{-1} u_i^t$ is called the pseudoinverse or Moore–Penrose inverse [48]. Using A^+ , the condition number of A according to the 2-norm is defined as

$$\text{cond}(A) = \|A\|_2 \|A^+\|_2 = \frac{\sigma_1}{\sigma_{\text{rank}(A)}}.$$

However, the system matrices A from series expansion methods are typically not rank-deficient. Instead, the singular values σ_i decay gradually to zero with no particular gap in the spectrum. Figure 3.3 shows an example of the singular value spectrum of A in case of several different Freehand SPECT acquisitions (see chapter 5). Thus, A is also highly ill-conditioned [47].

While the SVD allows computing a solution x^* to $Ax = y$ as outlined above, this solution is in most cases not pleasing, both in mathematical terms (for example a too high norm $\|x\|$) and in terms of visual quality, see Figure 3.4a. A common remedy is including additional terms or constraints to select a more desirable solution, this is called regularization. Two regularization approaches are outlined in the following sections, for a more complete overview see [47].

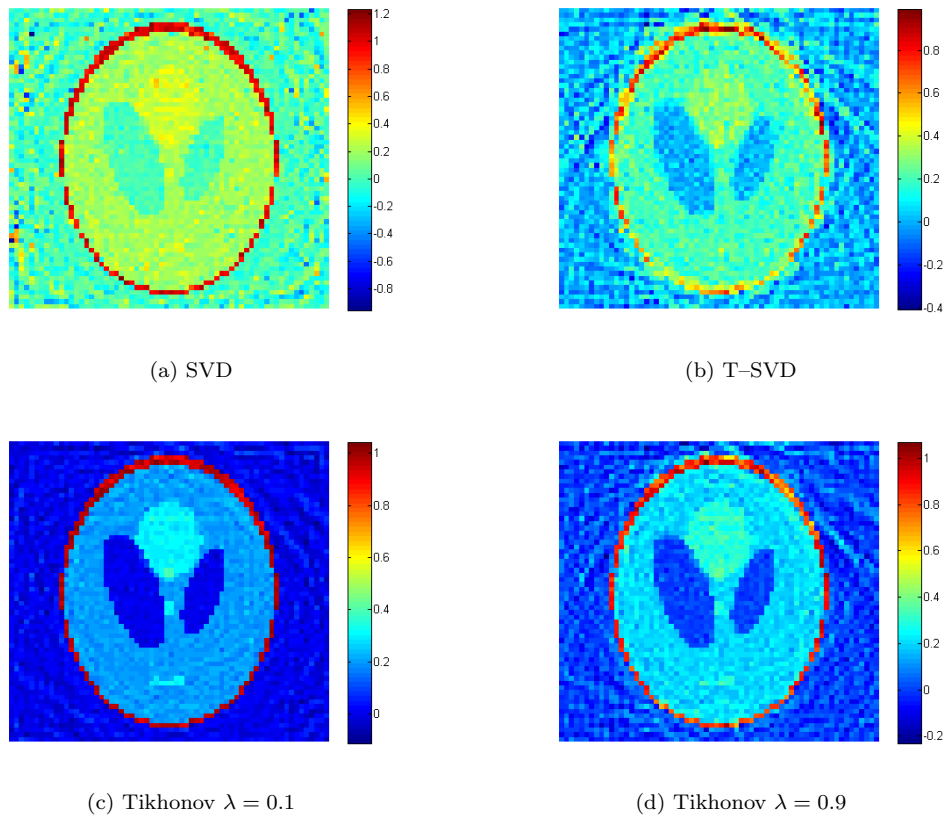


Figure 3.4: SVD-based reconstructions of the Shepp–Logan phantom from Figure 3.2, using (a) plain SVD inversion, (b) truncated SVD with $k = \frac{m}{2}$, (c) and (d) Tikhonov regularization with $\lambda = 0.1$ and $\lambda = 0.9$.

In practice, even regularized SVD-based solvers are not in common use. As the system matrices A of series expansion methods tend to be huge sparse matrices, the SVD calculation is very costly in terms of memory requirements and computation time, furthermore it can take no advantage of the sparsity of A .

3.2.1 Truncated SVD

The truncated SVD solution to $Ax = y$ is

$$x_k^* = \sum_{i=1}^k \frac{u_i^t y}{\sigma_i} v_i, \quad (3.9)$$

using the notation of the previous section and $k \in \mathbb{N}$ [49, 50]. This is essentially identical to (3.8), except that k is now a parameter instead of the fixed $\text{rank}(A)$. x_k^* is in fact the minimum 2-norm solution to the least squares problem $\min_x \|A_k x - y\|_2$, where $A_k = \sum_{i=1}^k u_i \sigma_i v_i^t$ is the matrix created from A by setting the small singular values $\sigma_{k+1}, \dots, \sigma_n$

to zero. An example reconstruction of the phantom from Figure 3.2 using $k = \frac{m}{2}$ is shown in Figure 3.4b.

One way to select the parameter k according to a given tolerance ε is to use the numerical ε -rank, which can be defined as the smallest integer k such that $\sigma_{k+1}^2 + \dots + \sigma_n^2 \leq \varepsilon^2$ [51].

3.2.2 Tikhonov Regularization

Tikhonov regularization [52, 53] for our series expansion problem $Ax = y$ takes the form

$$\min_x (\|Ax - y\|_2^2 + \lambda^2 \|Lx\|_2^2) \quad (3.10)$$

for some parameter $\lambda > 0$ and $L \in \mathbb{R}^{n \times n}$. L controls the additional desired properties of the solution x^* , while λ regulates the relative weight of the regularization compared to the minimization of the residual norm. For this section we choose the simplest case of $L = I_n$. Other choices include diagonal weighting matrices or derivative operators and require calculation of the generalized SVD (GSVD) of the pair (A, L) , see [47] for more details.

For $L = I_n$ the regularized Tikhonov solution is

$$x^* = \sum_{i=1}^n f_i \frac{u_i^t y}{\sigma_i} v_i, \quad (3.11)$$

where the

$$f_i = \frac{\sigma_i^2}{\sigma_i^2 + \lambda^2}$$

are called filter factors.

This is similar to the truncated SVD, except that here the filter factors are not a hard cut-off, but diminishes the contribution of the smaller σ_i depending on the value of λ . In fact, the truncated SVD solution can be written as (3.10), but with filter factors

$$f_i = \begin{cases} 1 & i \leq k \\ 0 & i > k, \end{cases}$$

and is close to the Tikhonov solution for certain λ [54].

The parameter λ can be chosen heuristically, but there are also methods like Generalized cross-validation [55, 56] or L -curve analysis [57, 58], which plots $\log \|Ax_\lambda - y\|_2$ versus $\log \|Lx_\lambda\|_2$ for different λ values, resulting in an L -shaped curve which allows selecting an

optimal λ . For a more detailed overview the reader is referred to [47]. Example reconstructions of the phantom from Figure 3.2 can be found in Figures 3.4c and 3.4d for $\lambda = 0.1$ and $\lambda = 0.9$.

3.3 Constraint-based Solvers

The linear system $Ax = y$ employed in series expansion methods can be viewed as a special case of the convex feasibility problem (CFP). Given closed convex subsets $C_i \subset \mathbb{R}^n$, $i = 1, \dots, M$, the CFP is to find a point $x^* \in \bigcap_{i=1}^M C_i$. This definition can also be extended to general Hilbert spaces instead of \mathbb{R}^n . Each row $a_{j1}x_1 + \dots + a_{jn}x_n = y_j$ of the linear system $Ax = y$ defines a hyperplane in \mathbb{R}^n , which is a closed convex subset of \mathbb{R}^n , and the solution x^* is the intersection of all these hyperplanes.

This section presents an overview of several methods to approach the convex feasibility problem, which we loosely sub-summed under the general heading of “constraint-based” solvers. References to the literature are given as a starting point for more detailed studies of the various methods. General overviews can be found for example in [59–62].

3.3.1 Algebraic Reconstruction Technique and Variants

The Algebraic Reconstruction Technique (ART) is one of the most popular solvers used in series expansion methods. Based on the Kaczmarz method [63] first published in 1937 by S. Kaczmarz, the method was termed Algebraic Reconstruction Technique in the context of tomographic reconstruction by R. Gordon, R. Bender and G.T. Herman in 1970 [64].

Consider the linear system $Ax = y$ with $A \in \mathbb{R}^{m \times n}$, let a_j denote the j -th row of A . The system is interpreted as a set of hyperplanes H_j for $j = 1, \dots, m$,

$$H_j = \{x \in \mathbb{R}^n : \langle a_j, x \rangle = y_j\}.$$

The Algebraic Reconstruction Technique is an iterative algorithm which successively projects the starting vector x^0 orthogonally onto the next hyperplane H_j , iterating over all rows of the matrix A repeatedly. With P_{H_j} denoting the orthogonal projection operator onto H_j the k -th iterative step of ART is

$$x^{k+1} = P_{H_{j(k)}}(x^k) \tag{3.12}$$

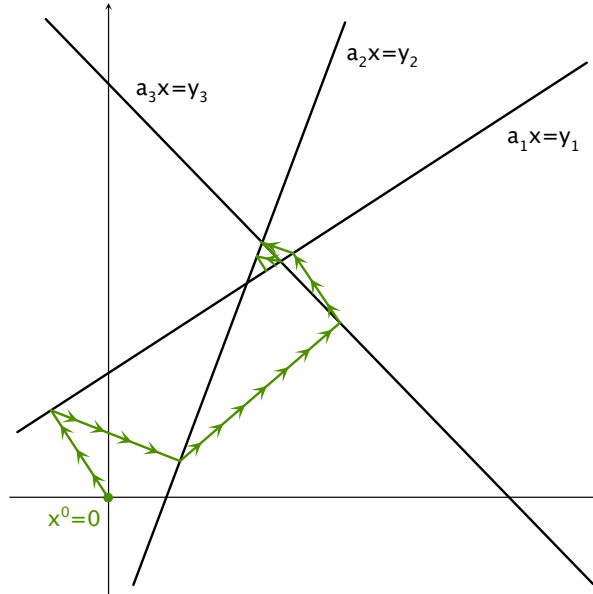


Figure 3.5: Illustration of ART for a linear system $(a_1^t, a_2^t, a_3^t)^t x = (y_1, y_2, y_3)^t$ with start vector $x^0 = 0$.

with $j(k) = (k \bmod m) + 1$. Each iteration step is updating the solution using one row of A , this is why this method is also called a row-action method [65]. The iteration process is illustrated for a simple example in Figure 3.5.

In more practical terms the k -th iterative step of ART is

$$x^{k+1} = x^k + \frac{y_{j(k)} - \langle a_{j(k)}, x^k \rangle}{\|a_{j(k)}\|_2^2} a_{j(k)} \quad (3.13)$$

with $j(k) = (k \bmod m) + 1$.

If the system $Ax = y$ has solutions (this is also called consistent), ART converges to the solution closest to x^0 (see for example [61] for a proof). When there are no solutions, ART does not converge. However, for $t \in \{1, \dots, m\}$ the subsequence $(x^{lm+t})_{l \in \mathbb{N}}$ converges to a vector z^t , and the set $\{z^t : t = 1, \dots, m\}$ is called limit cycle [66].

There are various modifications to the algebraic reconstruction technique. A popular one is the introduction of a relaxation factors $\lambda_k \in (0, 2)$ into the iteration step,

$$x^{k+1} = x^k + \lambda_k \frac{y_{j(k)} - \langle a_{j(k)}, x^k \rangle}{\|a_{j(k)}\|_2^2} a_{j(k)}. \quad (3.14)$$

This amounts to cutting short the hyperplane projection in case of $\lambda_k < 1$, or elongating it in case of $\lambda_k > 1$. The original ART uses $\lambda_k = 1$ for all k . Especially small relaxation parameters have turned out beneficial in practice (see for example [22]), the intuition is that a small λ_k can minimize the influence of a noisy or erroneous hyperplane in exchange for

sacrificing convergence speed. The convergence of the relaxed ART was proven in [67] for consistent systems, in the case of inconsistent systems the existence of a limit cycle was shown in [68] if the relaxation factors are periodic. It was shown in [69] that with $\lambda_k \rightarrow 0$ the limits of the cyclic subsequences converge to a weighted least squares solution of $Ax = y$ with minimum norm, confirming the intuition.

Another modification to ART is the choice of $j(k)$. Regular ART is just iterating through A from the first row to the last row repeatedly. If however the projections in each iterative step could be chosen somehow optimally, the convergence speed could be increased. A scheme choosing the next projection to be as “orthogonal as possible” was explored in [70] and [71]. The most common scheme is to choose projections randomly, which has proven beneficial in many practical cases (see for example [22, 72]). A certain random projection access order scheme was shown to have exponential convergence rate in [73] for certain cases, however that is not true in general [74].

A third common modification is to restrict the solution to a closed convex set $C \subset \mathbb{R}^n$ in each iterative step, like for example enforcing non-negativity on the estimates x^k [22, 61].

There exist various other variants of like blocked versions of ART [61, 75] or regularized ART [68, 76]. A short review with further references to the literature is available in [77]. ART can also be seen as a special case of the general Projection onto Convex Sets method (POCS) used in signal and image processing [78].

Example reconstructions of the phantom from Figure 3.2 using ART with different parameters can be found in Figure 3.6. As opposed to the row-action method ART, the following section presents an overview of iterative methods using a simultaneous update step.

3.3.2 Landweber Methods

Let $A = (a_{ji}) \in \mathbb{R}^{m \times n}$ and let $C \subset \mathbb{R}^n$ and $Q \subset \mathbb{R}^m$ be closed convex sets. The problem of finding $c \in C$ with $Ac \in Q$ is called the split feasibility problem (SFP) [79], a special case of the convex feasibility problem. The **CQ algorithm** is a method to solve the SFP [80], it has the k -th iterative step

$$x^{k+1} = P_C(x^k - \gamma A^t(I_m - P_Q)Ax^k), \quad (3.15)$$

where P_C, P_Q are the projection operators onto C and Q and $\gamma \in \left(0, \frac{2}{\rho(A^t A)}\right)$ with $\rho(A^t A)$ denoting the spectral radius of $A^t A$, which equals the largest eigenvalue.

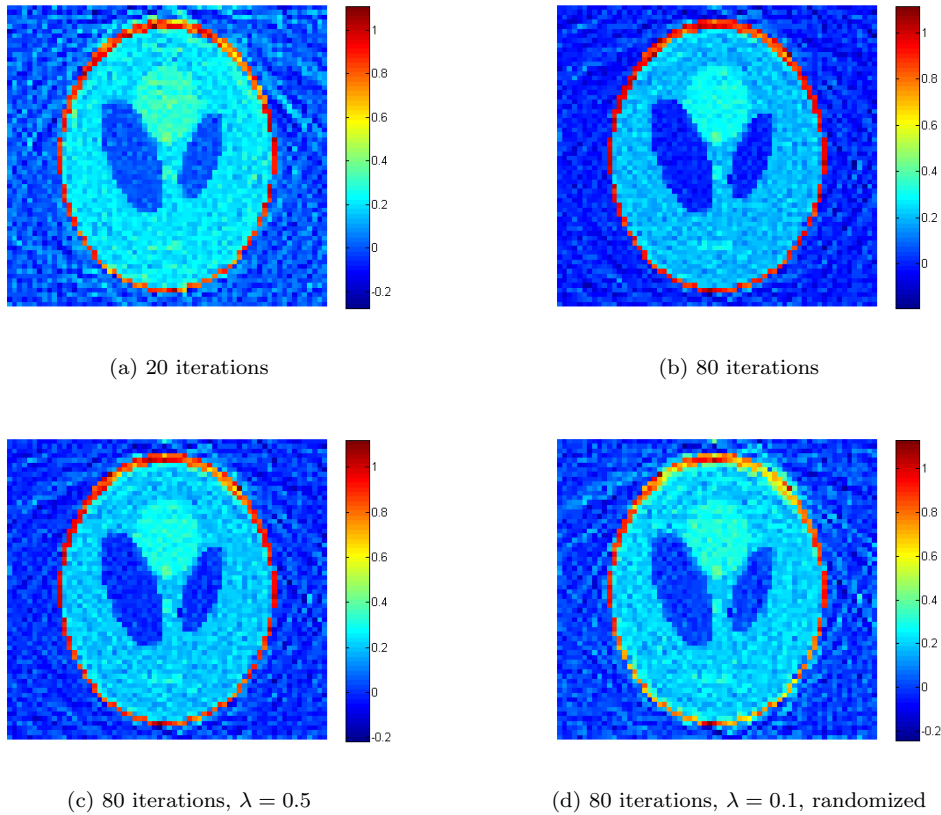


Figure 3.6: ART reconstructions of the Shepp–Logan phantom from Figure 3.2, using (a) 20 iterations, (b) 80 iterations, (c) 80 iterations and $\lambda = 0.5$ and (d) 80 iterations with $\lambda = 0.1$ and randomized projection access order.

If a solution of the SFP exists, the CQ algorithm converges to it for any starting vector $x^0 \in \mathbb{R}^n$ [61]. If there is no solution, the CQ algorithm converges to a minimizer of

$$\min_{x \in C} \frac{1}{2} \|P_Q Ax - Ax\|_2^2.$$

The convergence of the CQ algorithm is a consequence of the Krasnoselskii/Mann theorem [81] using fixed point iteration of an averaged operator, see also [62] for more details on the proof.

In the following we present a few special cases of the CQ algorithm, which conveniently have assured convergence as noted above.

The first example is the **Landweber algorithm** introduced by L. Landweber in 1951 [82]. Set $C = \mathbb{R}^n$ and $Q = \{y\}$, then the SFP is equivalent to solving the linear system $Ax = y$. The Landweber iteration is

$$x^{k+1} = x^k + \gamma A^t(y - Ax^k), \quad (3.16)$$

with again $\gamma \in \left(0, \frac{2}{\rho(A^t A)}\right)$ and arbitrary $x^0 \in \mathbb{R}^n$. A strategy to choose γ is outlined for example in [61].

If we choose $C \subsetneq \mathbb{R}^n$ closed and convex, the CQ algorithm specialization is called the **Projected Landweber algorithm** and calculates a solution of $Ax = y$ requiring $x \in C$. A typical example would be $C = (\mathbb{R}_0^+)^n := \{x \in \mathbb{R}^n : x_i \geq 0 \forall i = 1, \dots, n\}$ to restrict the solution to non-negative images, which is usually desired in most imaging modalities. The projected Landweber iteration is

$$x^{k+1} = P_C(x^k + \gamma A^t(y - Ax^k)), \quad (3.17)$$

with again $\gamma \in \left(0, \frac{2}{\rho(A^t A)}\right)$ and arbitrary $x^0 \in \mathbb{R}^n$.

The **Simultaneous Algebraic Reconstruction Technique (SART)** introduced in [83] is a variant of the Landweber algorithm with $\gamma = 1$ as demonstrated for example in [80]. Here $Ax = y$ is solved for the case of $A \in (\mathbb{R}_0^+)^{m \times n}$ using the k -th iteration step

$$x_i^{k+1} = x_i^k + \frac{1}{\sum_{j=1}^m a_{ji}} \sum_{j=1}^m \frac{a_{ji}}{\sum_{i'=1}^n a_{ji'}} (y_j - (Ax^k)_j) \quad (3.18)$$

for $i = 1, \dots, n$ and arbitrary $x^0 \in \mathbb{R}^n$.

Another variant of the Landweber algorithm with $\gamma = \frac{1}{m}$ is **Cimmino's algorithm** introduced by G. Cimmino in 1938 [84], here the k -th iteration step is

$$x^{k+1} = x^k + \frac{1}{m} A^t(y - Ax^k) \quad (3.19)$$

for any $x^0 \in \mathbb{R}^n$. The idea of this method is to project the current solution estimate x^k onto all the hyperplanes of $Ax = y$ and taking the arithmetic mean. Unfortunately convergence is typically very slow. This method is also referred to as Simultaneous Iterative Reconstruction Technique (SIRT) and has several other variants, see [85, 86].

A method called **component averaging (CAV)** to accelerate the convergence of Cimmino's algorithm while keeping its convergence properties was suggested by Y. Censor et al. in 2001 [87]. The general idea is to introduce a diagonal weighting matrix in the iteration step. Let $\|x\|_G^2 := \langle x, Gx \rangle$ for a symmetric positive definite matrix $G \in \mathbb{R}^{n \times n}$, let s_i denote the number of nonzero elements a_{ji} in the i -th column of A and set $S := \text{diag}(s_1, \dots, s_n)$. Assuming that $s_i \neq 0$ for all $i = 1, \dots, n$ we can define $D_S := \text{diag}\left(\frac{1}{\|a^1\|_S^2}, \dots, \frac{1}{\|a^m\|_S^2}\right)$. The k -th CAV iteration step is then

$$x^{k+1} = x^k + \lambda_k A^t D_S (y - Ax^k) \quad (3.20)$$

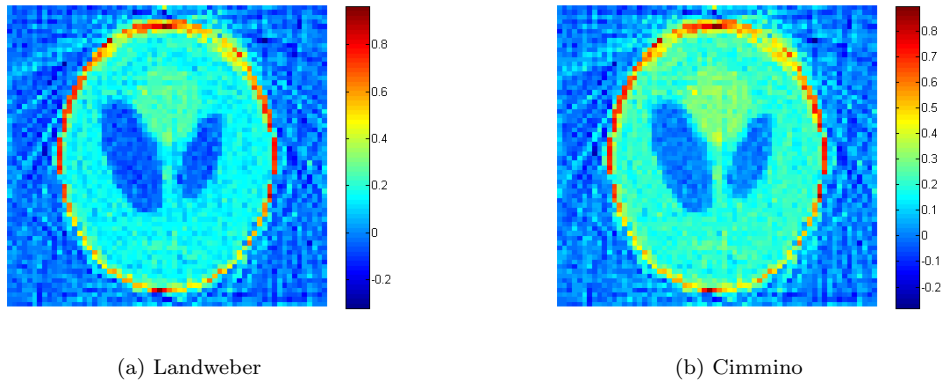


Figure 3.7: Reconstructions of the Shepp–Logan phantom from Figure 3.2 using (a) the Landweber method with 80 iterations and $\gamma = 0.0004$, (b) Cimmino’s method with 80 iterations.

with $\lambda_k > 0$ denoting relaxation factors and $x^0 \in \mathbb{R}^n$. A block–iterative variant of CAV called BiCAV with even quicker convergence was introduced shortly afterwards in [88]. Both methods parallelize well.

Example reconstructions of the phantom from Figure 3.2 using the Landweber method and Cimmino’s method can be found in Figure 3.7. There exist many more methods and variants of iterative reconstruction methods that can be loosely classified as constraint–based solvers, however the interested reader is referred to the literature, a good starting point is [61].

3.4 Statistics–based Solvers

Statistics–based solvers treat the series expansion problem $Ax = y$ (or $Ax + e = y$ with an error term) with statistical methods. Assuming x (or x and e) is a sample of a random variable, a Bayesian framework can be used to obtain a reconstruction, for example employed a Maximum A Posteriori (MAP) estimator. The necessary prior information can be supplied for example by Gibbs priors or Markov Random Field (MRF) image models, see [89]. A more thorough introduction of the Bayesian methods for image reconstruction can be found in [22].

This section however is focusing on the so–called **Maximum Likelihood Expectation Maximization** (in short **MLEM** or **EMML**) method as introduced by L.A. Shepp and Y. Vardi in 1982 [90]. This method assumes each voxel to be an emitter according to a Poisson distribution, which is one of the widely accepted models for radioactive decay, explaining the popularity of this method in emission tomography.

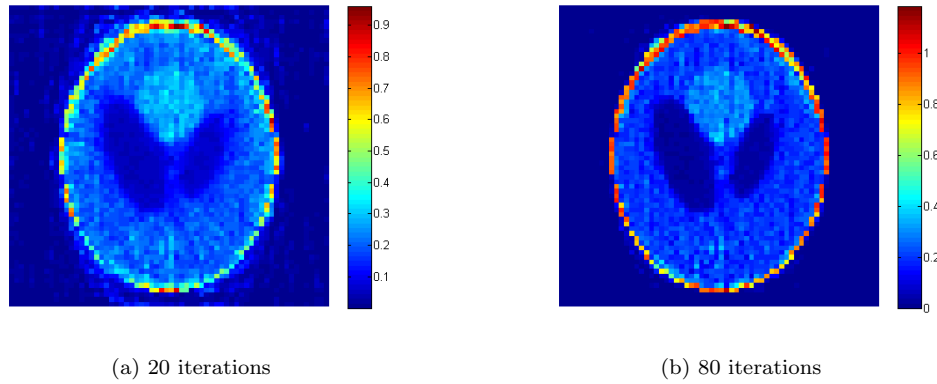


Figure 3.8: MLEM reconstructions of the Shepp–Logan phantom from Figure 3.2 using (a) 20 iterations and (b) 80 iterations.

Using the series expansion notations as introduced earlier in this chapter, the voxels b_i are assumed to be independent Poisson–distributed random variables ϕ_i with expectation $x_i = \mathbb{E}(\phi_i)$, representing the unknown activity in voxel b_i . The measurements y_j represent the realization of random variables γ_j denoting the counts detected in the detector j . Finally, the matrix elements of $A = (a_{ji})$ denote the probability that an event in b_i is detected in detector j . Then

$$\mathbb{E}(\gamma) = Ax.$$

The likelihood function of x is then

$$L(x) = \prod_{j=1}^m \frac{Ax_j^{y_j}}{y_j!} e^{-(Ax)_j},$$

and x can be determined using the expectation maximization (EM) method [91], yielding the MLEM algorithm with the k -th iterative step

$$x_i^{k+1} = \frac{x_i^k}{\sum_{j=1}^m a_{ji}} \sum_{j=1}^m \frac{y_j}{(Ax^k)_j} a_{ji} \quad \forall i = 1, \dots, n. \quad (3.21)$$

Here it is required that $x^0 > 0$ element–wise, and that $A \geq 0$ element–wise as well as $\sum_{j=1}^m a_{ji} > 0$ for all $i = 1, \dots, n$. This algorithm was derived in [90], convergence was proven in [92]. Example reconstructions of the phantom from Figure 3.2 are shown in Figure 3.8.

It was found that the statistically motivated MLEM method can be brought into the setting of the projection onto convex sets (POCS) methods mentioned in the previous section. For this the distance measure used in the projections needed to be generalized from metrics to so–called Bregman distances [93, 94]. Iterative algorithms can then be created just as with the POCS method [75]. A particular example of a Bregman distance is the Shannon

entropy-based Kullback–Leibler distance [95], which for $x, z \in \mathbb{R}^m$ is defined as

$$KL(x, z) = \sum_{j=1}^m x_j \log \left(\frac{x_j}{z_j} \right) + z_j - x_j.$$

The projection onto convex sets iteration using the distance $KL(y, Ax)$ and the weighted arithmetic mean of these projections is identical to MLEM as shown in [96].

Using the distance $KL(Ax, y)$ instead yields the **Simultaneous Multiplicative ART (SMART)** method [97],

$$x_i^{k+1} = x_i^k \exp \left(\frac{1}{\sum_{j=1}^m a_{ji}} \sum_{j=1}^m a_{ji} \log \frac{y_j}{(Ax^k)_j} \right) \quad (3.22)$$

with $x^0 > 0$ element-wise again. Like MLEM, SMART can also be derived via likelihood maximization [61].

The convergence rate of the MLEM method is not particularly fast, as a remedy a block-iterative variant was developed [98, 99]. This variant is called **Ordered Subsets Expectation Maximization (OSEM)**. Let $B = \{1, \dots, m\}$ and define a partition $\{B_t\}$ of T non-empty subsets B_t such that

$$B = \bigcup_{t=1}^T B_t.$$

The iterative step of OSEM sums up only over the subsets B_t and reads as

$$x_i^{k+1} = \frac{x_i^k}{\sum_{j \in B_{[k]}} a_{ji}} \sum_{j \in B_{[k]}} \frac{y_j}{(Ax^k)_j} a_{ji}, \quad (3.23)$$

where $[k] := (k \bmod T) + 1$ and the iteration from $k = lT$ to $k = (l+1)T$ is called one ordered subset cycle. Careful arrangement of the subset order can speed up the convergence rate just like with ART and the projection access order. Convergence has been proven only for consistent systems $Ax = y$ in a special case with the subset balance property [99]. OSEM does not converge in the inconsistent case, but like ART exhibits limit cycles [100]. To eliminate those limit cycles a modification of OSEM was introduced in [100] using strong under-relaxation, it is called Row-Action Maximization Likelihood Algorithm (RAMLA). A similar modification is the rescaled block-iterative version of MLEM, introduced as RBI-EMML in [101, 102].

The OSEM algorithm has been implemented in several modern commercial emission tomography systems [77] due to similar reconstruction quality compared to MLEM while being a lot more computationally efficient.

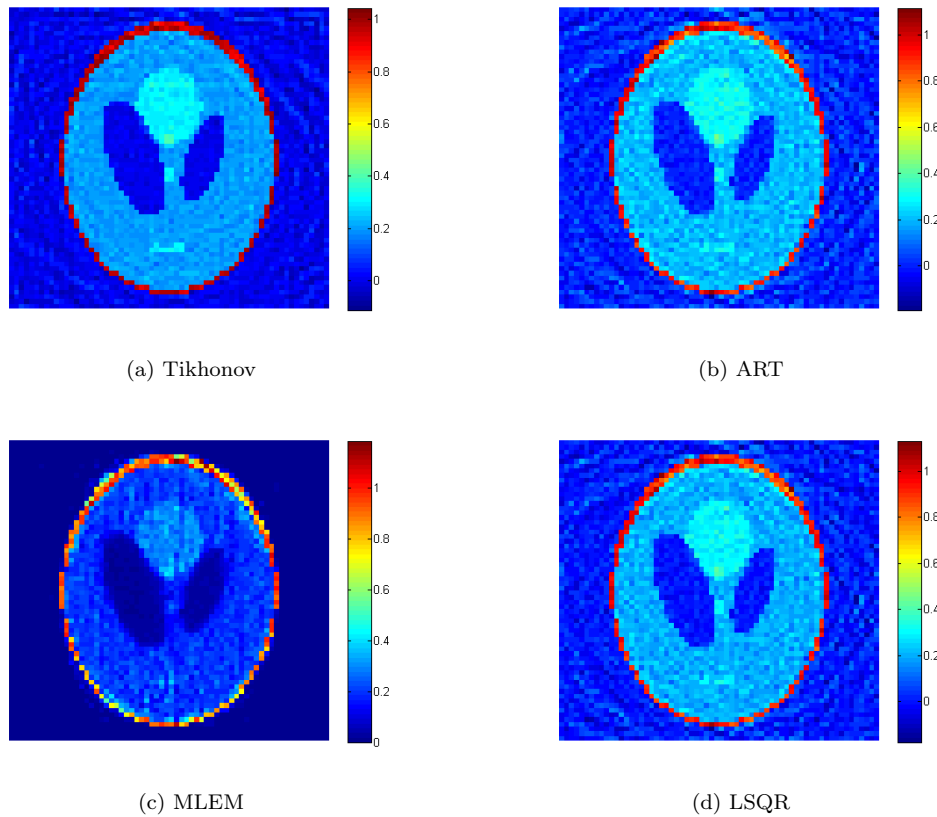


Figure 3.9: Example reconstructions of the Shepp–Logan phantom from Figure 3.2 using (a) Tikhonov regularization with $\lambda = 0.1$, (b) ART with $\lambda = 1$, (c) MLEM and (d) LSQR. The iterative methods all employed 80 iterations.

3.5 Summary

In this chapter we presented the series expansion method for tomographic reconstruction, from choosing suitable basis functions for discretization to calculating the system matrix according to the forward model and solving the resulting linear system $Ax = y$. Furthermore we presented an overview of different solving methods, ranging from SVD–based methods to the popular Algebraic Reconstruction Technique (ART), but also presenting Landweber–based methods as well as statistics–based methods like the MLEM algorithm, which is very popular in emission tomography.

Typical numerical solvers like the conjugate gradient (CG) method were omitted as they are rarely used as solvers for the series expansion approach, even though the mathematical aspects are very well understood. For a review of CG and related methods see [60]. However, the so–called LSQR algorithm introduced in [103] can also be classified as a CG–type method, and it has recently found application in the field of optical tomography, see for example [29, 104] or section 4.5.

Figure 3.9 compares example reconstructions of the Shepp–Logan phantom from Figure 3.2 using Tikhonov regularization, ART, MLEM to one using LSQR. Examples of series expansion methods in actual imaging modalities will be presented in chapters 4 (Fluorescence Molecular Tomography employing ART) and 5 (Freehand SPECT employing both ART and MLEM).

Chapter 4

Application: Optical Tomography

One of the many potential applications of the series expansion methods from chapter 3 is presented in this chapter — optical tomography. There are many different variants of doing optical tomography, with key differences on the detection side using for example interferometry, microscopes or cameras, as well as on how to deal with the high scattering of light in tissue, for example by acquiring time-resolved or frequency domain data. In this chapter one such method is presented: Fluorescence Molecular Tomography (or in short: FMT), based on imaging fluorescence using the diffusion approximation and continuous-wave sources. The work in this chapter was supervised by Prof. Vasilis Ntziachristos.

4.1 Imaging Fluorescence

Imaging fluorescence in living tissue can provide valuable information about tissue oxygenation, pH and glucose. Bio-molecules have been developed that are able to target molecular markers specific to cancer cells or certain processes like apoptosis (programmed cell death), and by conjugating fluorochromes to these molecules, biochemical processes at the molecular and cellular level can be imaged by fluorescent imaging techniques in living subjects (in-vivo molecular imaging). Besides these so-called “targeted probes”, there is another type of probes called “activatable” probes. These are not excitable in their normal state, however as soon as they attach to their target, structural changes within these molecules enable them to fluoresce. Utilizing these markers, specific biochemical processes at cellular and sub-cellular levels are detectable via fluorescence imaging that could not be imaged by conventional imaging techniques [105–107].

The main interest is in fluorescent dyes that emit in the near-infrared window (NIR), that is at wavelengths above $600nm$. Figure 4.1 shows that the main absorber in tissue —

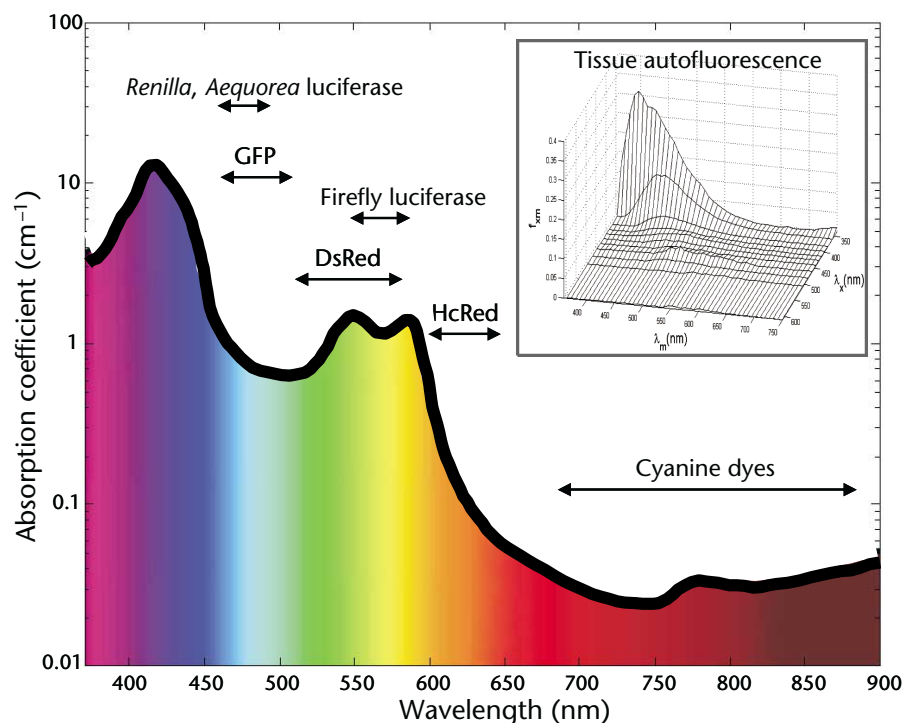


Figure 4.1: Absorption coefficients of light in typical tissue plotted against wavelength. Also shown: emission spectra of several fluorochromes and tissue autofluorescence spectra at different excitation wavelengths. Reprinted by permission from Macmillan Publishers Ltd: *Nature Medicine* [14], copyright 2003.

hemoglobin — allows for imaging in the NIR window, starting from 600nm up to 900nm , as water has increased absorption above 900nm . Within this spectral window light can propagate through tissue for distances on the order of multiple centimeters, e.g. through large human organs [108]. Two excellent reviews of imaging fluorescence can be found in [14, 109].

The most simple technique of imaging fluorescence is fluorescence reflectance imaging, used for example extensively in histology. Here a light source provides the excitation light, and the fluorescent light emitted is detected by a camera or microscope with appropriate filters placed on the same side of the object, see Figure 4.2. The detected signal is a superposition of fluorescent light emitted at different depths in the object, with the lower depths contributing less and less to the signal due to scattering and attenuation of the photons.

Tomographic techniques can overcome this limitation and enable three-dimensional quantitative visualization of the fluorescence bio-distribution. In the presented implementation, FMT collects photons at the emission wavelength of fluorochromes distributed in tissues at multiple projections in a transmission geometry, and combines these measurements tomographically with photons collected at the excitation wavelength to obtain fluorescence images of deep tissues. To achieve this, FMT typically employs a mathematical model of

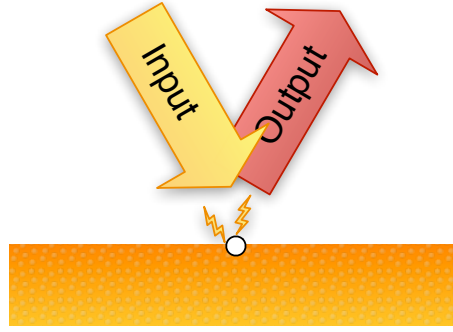


Figure 4.2: Schematic of Fluorescence Reflectance Imaging: a fluorescent molecule is excited by source light and emits fluorescence at emission wavelength, which is captured by a camera.

photon propagation in diffusive media and constructs a forward model which is then solved for the unknown fluorochrome bio-distribution.

Due to the limitations of light penetration depth in tissue even in the near-infrared part of the spectrum, FMT is mostly used to image small animals like mice [110, 111]. The ability to image several engineered fluorochromes with specificity to various molecular processes in-vivo has so far been applied to resolving tumor-related protease activity, responses to chemotherapy, inflammation and angiogenesis [112–115] and is expected to find increasing further application to pre-clinical research and drug discovery. However, systems for imaging human extremities have also been demonstrated, for example imaging the breast or the brain [116]. One key issue here, besides limited depth penetration of photons in tissue, is also the scarcity of fluorescent tracers approved for use in humans.

4.1.1 Modeling Light Propagation

In order to enable tomography of the captured projection images of fluorescence, a model for light propagation in tissue is required.

One common approach to model light propagation in scattering and absorbing media is the Radiative Transport Equation (RTE, for a more detailed explanation and a derivation see for example [117, 118])

$$\frac{n}{c} \frac{\partial I(r, \hat{s})}{\partial t} + \hat{s} \cdot \nabla I(r, \hat{s}) + \mu_t I(r, \hat{s}) = \frac{\mu_t}{4\pi} \int_{4\pi} p(\hat{s}, \hat{s}') I(r, \hat{s}') d\Omega' + \varepsilon(r, \hat{s}). \quad (4.1)$$

Here $I(r, \hat{s})$ denotes the specific intensity, which represents the average power flux at point r in the direction \hat{s} (power per unit area and unit solid angle), n is the refractive index of the medium, c the speed of light in vacuum and $\mu_t = \mu_s + \mu_a$ are the transport coefficient, the scattering and absorption coefficients respectively (depending on the wavelength λ). Finally $p(\hat{s}, \hat{s}')$ denotes the scattering phase function (the probability of scattering in the direction

\hat{s} from the direction \hat{s}') and $\varepsilon(r, \hat{s})$ denotes the radiant source function, the power that is radiated by the medium at point r per unit volume and per unit solid angle in the direction of \hat{s} . Assuming a small element of space at position r with a small solid angle in direction of \hat{s} , the left-hand-side terms describe the photons entering the element, the flux of photons in direction of \hat{s} and the scattering and absorption inside the element. On the right-hand side the first term accounts for photons at position r being scattered from all directions \hat{s}' into the direction \hat{s} and the last term describes the photon source.

There are no results available on how to apply Radon-like methods as in chapter 2 for tomographic reconstruction based on the Radiative Transfer Equation 4.1, however the series expansion framework in chapter 3 is perfectly suited to this problem. To derive a model to calculate the system matrix, a solution of equation 4.1 has to be derived. Unfortunately analytical solutions are only available in special cases, whereas numerical solutions are usually very computationally intensive. Thus several approximations have been considered, such as expanding the specific intensity into spherical harmonics truncated to first order, or assuming media which has much higher scattering coefficients than absorption coefficients (as usually occurred in living tissue) and assuming isotropic light sources (for more details see [119]). This yields the Diffusion Equation

$$\frac{1}{c} \frac{\partial U(r)}{\partial t} - D_\lambda \Delta U(r) + \mu_a U(r) = E(r) + \nabla D_\lambda \cdot \nabla U(r), \quad (4.2)$$

where $U(r) = \int_{4\pi} I(r, \hat{s}) d\Omega$ denotes the average intensity at point r (photon fluence), $D_\lambda = \frac{1}{3\mu'_s}$ is called the diffusion coefficient for wavelength λ with $\mu'_s = \mu_s(1 - g)$ the reduced scattering coefficient and g the anisotropy factor, and finally $E(r)$ denotes the source power at point r . These approximations typically hold in the context of actual implementations of FMT devices, it is for example required that the system size is much bigger than the transport mean free path $l_{tr} = \frac{1}{\mu'_s}$, and in turn that l_{tr} is much bigger than the employed photon wavelength. In particular, the diffusion approximation breaks down when encountering non-diffusive regions, which is why first-generation FMT systems employed matching fluids and why non-contact systems without matching fluids require a modified forward model (see section 4.2).

Two further assumptions can be made to further simplify the diffusion equation in case the FMT system operates in continuous-wave mode (CW), that is the laser beam is not modulated (thus eliminating the time dependence), and by assuming that the medium is homogeneous, which implies that D_λ is constant. This yields

$$-D_\lambda \Delta U(r) + \mu_a U(r) = E(r). \quad (4.3)$$

To solve this equation for objects of limited size, certain boundary conditions have to be

introduced for U , where light is leaving the object at its boundaries into non-diffusive medium, disturbing the process of diffusion, see [119–121] and section 4.2. For now we will assume the simplest case of performing FMT with matching fluids, where we can assume an infinite homogeneous medium using no boundary conditions.

Assuming an infinite homogeneous medium and setting $E(r) = \delta(r - r')$ (a Dirac pulse at position r') the diffusion equation (4.3) is solved by the Green's function G_λ for wavelength λ ,

$$U^\lambda(r) = G_\lambda(r - r') = \frac{e^{-k_\lambda|r-r'|}}{4\pi D_\lambda|r-r'|},$$

where $k_\lambda = \sqrt{-\mu_a/D_\lambda}$ describes the photon wave propagation (see [122]). Applying this for $E(r) = \Theta_s(r_s)\delta(r - r_s)$, that is a point source at location r_s with strength $\Theta_s(r_s)$ (for example a laser source), we receive

$$U_0^\lambda(r_s, r) = \Theta_s(r_s)G_\lambda(r - r_s)$$

as a solution to equation (4.3), describing the photon wave induced at point r by the source at point r_s .

Let λ_1 denote the excitation wavelength of the fluorochrome considered (for example 673nm in the device presented in section 4.2). If $\Theta_d(r_d)$ accounts for detection gain and losses at detector position r_d and QE^{λ_1} is the detector quantum efficiency at wavelength λ_1 , then the incident photon field induced by source r_s detected at position r_d is

$$U_{\text{inc}}(r_s, r_d) = QE^{\lambda_1} \cdot \Theta_d(r_d) \cdot U_0^{\lambda_1}(r_s, r_d). \quad (4.4)$$

Let λ_2 denote the emission wavelength of the fluorochrome (in this case 692nm). When considering a fluorescent molecule at position r as a light source, its emission can be characterized by (see [123])

$$E_{\text{fluor}}(r) = n(r) \cdot U^{\lambda_1}(r),$$

where

$$n(r) = \gamma c(r)$$

is the product of the fluorochrome concentration $c(r)$ at position r at the quantum yield of the fluorochrome γ . $n(r)$ is actually the quantity we will reconstruct as a result of FMT. Thus the fluorescence field induced at point r by a source at position r_s is

$$\begin{aligned} U_{\text{fluor}}(r_s, r) &= \int_V G_{\lambda_2}(r - r') \cdot n(r') \cdot U_0^{\lambda_1}(r_s, r') dr' \\ &= \int_V G_{\lambda_2}(r - r') \cdot \Theta_s(r_s)G_{\lambda_1}(r' - r_s) \cdot n(r') dr', \end{aligned}$$

where V denotes the volume under consideration. Let finally denote Θ_f the attenuation of the filter used to collect the fluorescent field and QE^{λ_2} the quantum efficiency of the detector at wavelength λ_2 , the fluorescent field induced by source r_s at detector r_d is

$$U_{\text{fluo}}(r_s, r_d) = \int_V \Theta_f \Theta_s(r_s) \Theta_d(r_d) QE^{\lambda_2} \cdot G_{\lambda_2}(r_d - r') G_{\lambda_1}(r' - r_s) \cdot n(r') dr'. \quad (4.5)$$

This model of the fluorescent field is of the same form as the first-order perturbative model for a scattering medium with inhomogeneous absorption (see [124]), the so-called ‘‘first-order Born approximation’’.

In order to reconstruct the fluorochrome distribution n the factors $\Theta_s(r_s)$, $\Theta_d(r_d)$ have to be known for each source–detector pair r_s, r_d . To alleviate this situation the ‘‘normalized Born’’ ratio U^{nB} was introduced in [123],

$$\begin{aligned} U^{\text{nB}}(r_s, r_d) &= \frac{1}{\Theta_f} \cdot \frac{QE^{\lambda_1}}{QE^{\lambda_2}} \cdot \frac{U_{\text{fluo}}(r_s, r_d)}{U_{\text{inc}}(r_s, r_d)} \\ &= \frac{1}{\Theta_f} \cdot \frac{QE^{\lambda_1}}{QE^{\lambda_2}} \cdot \int_V \frac{G_{\lambda_2}(r_d - r') G_{\lambda_1}(r' - r_s)}{G_{\lambda_1}(r_d - r_s)} n(r') dr'. \end{aligned} \quad (4.6)$$

The terms Θ_f and $\frac{QE^{\lambda_1}}{QE^{\lambda_2}}$ can be determined experimentally for a given setup, and usually we have $\frac{QE^{\lambda_1}}{QE^{\lambda_2}} \approx 1$ due to the proximity of λ_1 and λ_2 .

Discretizing the volume V into N voxels r_1, \dots, r_N allows reformulation of equation (4.6) into a linear equation for the source–detector pair r_{s_i}, r_{d_i} ($i = 1, \dots, M$)

$$U^{\text{nB}}(r_{s_i}, r_{d_i}) = \begin{pmatrix} W_{i1} & \cdots & W_{iN} \end{pmatrix} \begin{pmatrix} n(r_1) \\ \vdots \\ n(r_N) \end{pmatrix},$$

where

$$W_{ij} = \frac{1}{\Theta_f} \cdot \frac{QE^{\lambda_1}}{QE^{\lambda_2}} \cdot \frac{G_{\lambda_2}(r_{d_i} - r_j) G_{\lambda_1}(r_j - r_{s_i})}{G_{\lambda_1}(r_{d_i} - r_{s_i})}.$$

The resulting linear system for all M source–detector pairs is thus the standard series expansion formulation

$$\begin{pmatrix} U^{\text{nB}}(r_{s_1}, r_{d_1}) \\ \vdots \\ U^{\text{nB}}(r_{s_M}, r_{d_M}) \end{pmatrix} = \begin{pmatrix} W_{11} & \cdots & W_{1N} \\ \vdots & \ddots & \vdots \\ W_{M1} & \cdots & W_{MN} \end{pmatrix} \begin{pmatrix} n(r_1) \\ \vdots \\ n(r_N) \end{pmatrix},$$

or in short

$$m = Wn, \quad (4.7)$$

with m being the measurements, W the system matrix and n the fluorochrome distribution.



Figure 4.3: First generation FMT setup developed at CMIR utilizing fibers to deliver and collect photons. Reprinted by permission from Macmillan Publishers Ltd: *Nature Medicine* [14], copyright 2003.

4.2 Tomographic Reconstruction of Full-Projection FMT

Several tomographic systems developed so far for the near-infrared have typically utilized fibers to deliver and collect photons from the animal periphery (see Figure 4.3) or are implemented using charged coupled device (CCD) cameras in the slab geometry, occasionally using matching fluids to simplify theoretical assumptions [123, 125–127].

Central to improving FMT imaging performance over fiber-based systems or slab-geometry based systems is the collection and utilization of data sets that offer high information content and symmetrical sampling of the volume imaged. This can be achieved by allowing complete-angle (360°) projection illumination and detection with high spatial sampling of photons propagating through diffuse media. Such an approach is expected to yield the new generation of performance for optical tomography systems. Key features of this development are the implementation of non-contact illumination, for example by using beam scanning techniques for light delivery on the tissue surface and direct non-contact imaging with CCD cameras, which allows for high spatial sampling of photon fields propagating through tissues. Similarly, the development of free-space geometries, i.e. implementations that do not utilize immersion of the animal in matching fluids, are essential for obtaining appropriate experimental simplicity and avoid unnecessary diffusion through scattering matching media.

To facilitate these developments it is important to retrieve the three-dimensional surface and a common coordinate system for the illumination system, the detection system and the animal. Methodologies developed in the past for non-contact and free-space imaging assuming limited projection angle ($\sim 90^\circ$) geometries [121, 128] utilized photogrammetry for obtaining surfaces over $\sim 150^\circ$ view angles. Limited-projection systems however compromise the resolution along the depth axis and do not offer symmetric volume coverage.

In this section, we instead report on the integration of a silhouette-based 3D surface reconstruction method into a 360° free-space system. The geometry of the system falls under the general design of evolving systems where the mouse is rotated over 360° in front of a CCD camera while intersecting a laser scanning beam (or the optical system around the mouse) [129, 130]. We examine the accuracy of the surface extraction method considered for the small animal imaging case and demonstrate how this surface extraction method can be utilized in an FMT inversion scheme. With this ability to capture three-dimensional animal surfaces we further characterize the statistics of the movement of anesthetized mice and investigate the effect of this movement in FMT reconstructions.

The results of this section have also been published in [131].

4.2.1 Methods

4.2.1.1 Experimental setup

To implement 360°-projection FMT, a free-space system was developed as shown in Figures 4.4 and 4.5. This system is used to acquire the three-dimensional (3D) surface of the object imaged as well as FMT raw measurements in the same geometry and under identical placement conditions. The central part of the system is the rotational stage that is used for mouse placement and rotation over 360° angles. The rotational stage is a custom made device where two mounting stages at the top and the bottom of a rigid frame are identically rotated taking motion from a central shaft mounted on a stepper motor (model PR50PP, attached to an ESP300 Universal Motion Controller, both from Newport Corp., Irvine CA) with a 0.01° resolution and a maximum speed of 20°/s. The dual rotational system allows for securing the top and bottom parts of the mouse body using appropriate cylinders and cups to support its weight. This way motion is minimized compared to a freely pendant mouse while the use of connecting rods that could obstruct the field of view is avoided.

Photon detection is based on a VersArray 16bit CCD camera (Princeton Instruments Inc., NJ 08619, Trenton, USA; 1024 × 1024 pixels) cooled to -70° C for reduced dark noise, and a Nikkor 50mm f/1.2D lens (Nikon Corp. Imaging Company, Tokyo, Japan). For FMT acquisitions a filter wheel was employed containing two band-pass filters to separate the excitation channel (Andover Corp. filter 671ES10-50, NH 03079, Salem, USA) from the emission channel (Chroma Technology Corp. filter HQ710/50, VT 05101, Rockingham, USA).

Two sources of illumination were used. For FMT, a continuous wave (CW) diode laser emitting at 665nm with up to 200mW output power (B & W TEK Inc., Newark, USA) is coupled via an optical fiber and a two-way optical switch to a laser scanhead (Nutfield

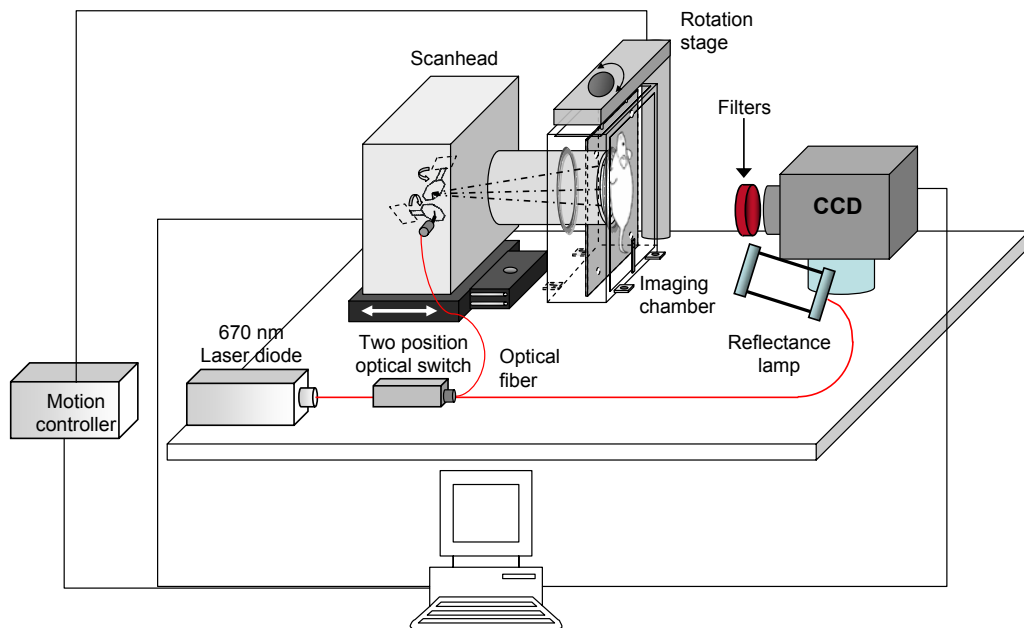


Figure 4.4: Schematic of experimental setup for 3D surface reconstruction and FMT.

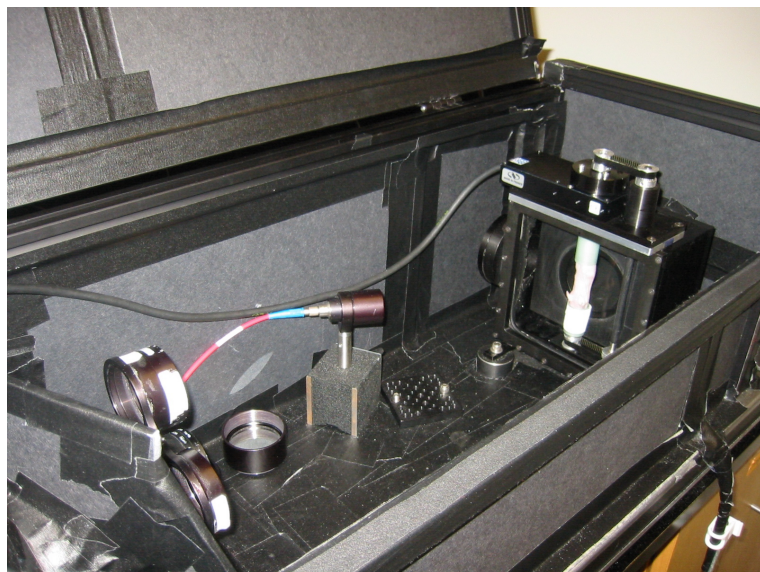


Figure 4.5: Photograph of the experimental setup for 3D surface reconstruction and FMT.

Technology Inc., Windham, NH) using a tele-centric lens for focusing the laser beam on the object imaged over a depth of field of $\sim 4mm$ ($300\mu m$ spot size, $50\mu m$ positional accuracy or better). To acquire the surface silhouettes a photo-luminescent acrylic plate (GloTech International, GTA3BG, Auckland, New Zealand) was employed and could be placed between the object imaged and the scan-head as an alternative photon source, while the laser light was off. This plate was used to provide homogeneous back-illumination.

The timing and data acquisition process for both 3D surface reconstruction and FMT data collection was controlled by a custom made software developed in Microsoft Visual C, running on a 2GHz Pentium4 PC with 256MB RAM.

4.2.1.2 Surface Reconstruction

A variant of the volume carving method [132] was employed to reconstruct the three-dimensional (3D) surface of an object A from its silhouettes. Consider a set of viewing angles R from which we observe the silhouettes of A . In short, for each viewing angle $r \in R$ the silhouette s_r is back-projected using the known camera geometry yielding a viewing cone vh_r of half-lines starting from r and intersecting the silhouette s_r . Each viewing cone vh_r contains the object A and the intersection of all the cones vh_r , $VH_R(A) = \bigcap_{r \in R} vh_r$ (see Figure 4.6) yields a reconstruction of the surface of A , the Visual Hull [133]. It has been shown that $VH_R(A)$ is the closest approximation to A that can be obtained using the silhouettes s_r , $r \in R$, and that $VH_R(A)$ contains A and is contained in the convex hull of A , $A \subseteq VH_R(A) \subseteq \text{conv}(A)$, see [134] for proof.

It is obvious that for convex objects A a near perfect approximation of A can be achieved using the Visual Hull $VH_R(A)$, provided the viewpoints R are chosen appropriately. However, it is less obvious how concavities in A affect $VH_R(A)$; concave areas of A can be reconstructed in case they provide silhouette-active surfaces, but a deep dent in one of the surfaces of a cube for example will have silhouette-inactive surfaces that cannot be reconstructed. For an in-depth study of the limitations of silhouette based object reconstruction with the Visual Hull see [134, 135]. This feature is not generally restrictive in small animal imaging of the head and torso (see also Figure 4.10), but could yield some inaccuracy when imaging the lower abdomen due to the concavities formed at the pelvis by the lower limbs. In this case photogrammetry methods, as described in [128], may be necessary.

Images of the back-illuminated object were acquired from multiple viewing angles R (typically using 72 angles with a 5° step) using the experimental setup of Figure 4.4. These images s_r , $r \in R$ were converted into binary images b_r based on a segmentation algorithm employing adaptive thresholding. The threshold is determined for each image captured by

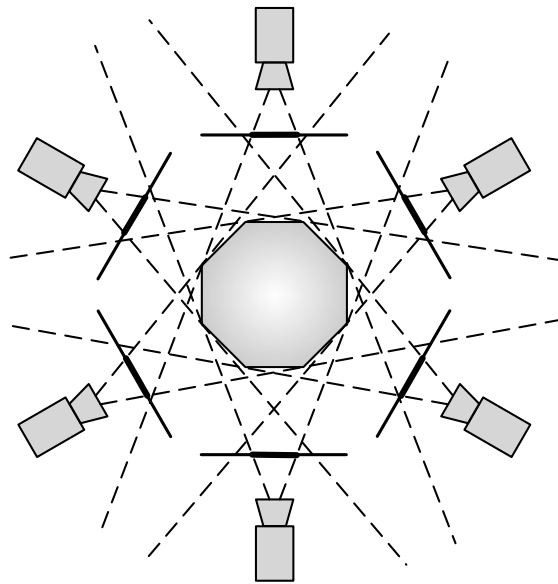


Figure 4.6: 2D schematic of intersecting viewing cones (generated by back-projecting the silhouettes) to generate the Visual Hull.

averaging the intensity of pixels with high gradient values [136] and applied to each of the images respectively.

The Visual Hull $VH_R(A)$ was computed employing a recursive volume carving algorithm, which removes (carves away) unoccupied regions of the volume containing the object A . The initial three-dimensional bounding box B is supposed to contain A . For each viewing angle $r \in R$ the box B is back-projected onto the segmented silhouette b_r using an orthographic camera model, yielding the 2D image $bp(B, r)$. Depending on the intersection $bp(B, r) \cap b_r$ the volume B is 1) marked as empty, 2) marked as opaque or 3) B is subdivided into 8 subvoxels, on each of which the algorithm is applied again recursively. If $bp(B, r) \subset b_r$ for all $r \in R$ the voxel B is marked opaque, if $bp(B, r) \cap b_r = \emptyset$ the voxel B is marked empty and in all other cases the recursive subdivision takes place. The algorithm terminates either when no more voxels have to be subdivided, that is when all voxels in any level of subdivision have been marked as empty or opaque, or it terminates when the desired resolution has been reached (here typically 8 levels corresponding to $256 \times 256 \times 256$ voxels). The initial bounding box B and all its subdivisions are represented as a data-structure *octree* (a tree where each internal node has 8 child nodes).

For implementation purposes this algorithm was transformed into an iterative variant to enable computational efficiency.

As a final step the 3D octree model is meshed to a regular grid ($256 \times 256 \times 256$ voxels) and the triangulated surface is computed via a Marching Cubes type algorithm [137].

Algorithm 4 compute_vh(B)**Require:** B — bounding box to be investigated.**Ensure:** $octree(B)$ marked as empty or opaque.

```

for all  $r \in R$  do
   $bp(B, r) =$  backproject  $B$  onto  $b_r$ 
  calculate intersections  $bp(B, r) \cap b_r$ 
end for
if  $bp(B, r) \subset b_r$  for all  $r \in R$  then
   $octree(B) =$  opaque;
  return
end if
if  $bp(B, r) \cap b_r = \emptyset$  for all  $r \in R$  then
   $octree(B) =$  empty;
  return
end if
if maximum_level( $octree$ ) reached (i.e. desired resolution) then
   $octree(B) =$  opaque;
  return
end if
 $B_1, \dots, B_8 =$  subdivide( $B$ )
for  $i = 1$  to 8 do
  compute_vh( $B_i$ )
end for
return

```

4.2.1.3 Fluorescence Reconstruction

For tomographic reconstructions of the fluorescence distribution the normalized Born approximation was employed (see section 4.1.1 and [123]), which utilizes a synthetic measurement generated as the ratio of the measured fluorescence intensity $U_{\text{fluo}}(r_s, r_d)$ to the corresponding measured intensity $U_0(r_s, r_d)$ at the excitation wavelength for each source position at r_s and detector position at r_d ,

$$U^{\text{nB}}(r_s, r_d) = \frac{U_{\text{fluo}}(r_s, r_d)}{U_0(r_s, r_d)}.$$

As in [123] we generated a forward model to predict photon propagation in a diffuse medium, however to accommodate for the non-contact sources and detectors we included free space photon propagation in our model using the first order Kirchhoff approximation to implement arbitrary boundaries (as reconstructed from the silhouettes), see [120, 121, 128], as well as [138] for a detailed derivation of the appropriate weight functions. The resulting weight matrix is then inverted with a randomized ART algorithm (see section 3.3.1 and [72]).

Alternatively to the diffusion equation based solutions employed herein, solutions to the radiative transfer equation can be utilized, which is theoretically more accurate at or near

boundaries. However, due to the computational burden associated with the use of more accurate propagation models, but also because of the proven efficacy of the diffusion approximation for in-vivo imaging [112], we limited ourselves to diffusion based imaging in this work, even though imaging using the radiative transfer equation in planar geometry systems has been reported in [139].

4.2.1.4 Experimental Procedures

For surface reconstruction, the photo-luminescent plate was inserted into the chamber so that the object or the animal imaged was placed between the photo-luminescent plate and the CCD camera. 72 silhouettes (1024×1024 pixel images) of the subject were acquired, rotating 5° in each step. Each camera pixel in this setup corresponds to a $0.011\text{cm} \times 0.011\text{cm}$ square on the imaging plane. For surface reconstructions, an eight-level octree was used (corresponding to $256 \times 256 \times 256$ voxels). The initial bounding box covered a volume of 2.2cm width \times 2.3cm depth \times 5.1cm height.

FMT data acquisition was performed using 30 rotations (12° each step) and an evenly spaced 7×3 source pattern over a 1.47cm vertical and 0.29cm horizontal field-of-view. To register the source positions of the sources in space, this pattern scan was repeated on a mock diffusive layer placed in the chamber after mouse measurements were completed. The center of the photon distribution pattern collected was then used to determine the exact location of each source in the horizontal and vertical axes, while the third dimension of the intersection of the laser beam with the imaged surface is calculated based on the known geometry of the device along the axis that is perpendicular to the CCD detection plane and the reconstructed surface metrics (see section 4.2.1.2 and [140]).

All diffuse photons propagating through tissue or mock diffuse plate were acquired at the emission and excitation wavelengths using 2×2 CCD chip hardware binning. For fluorescence reconstructions, the forward problem assumed a regular 18×18 detector grid spanning 2.5cm vertically and 1.8cm horizontally and a regular $18 \times 18 \times 18$ mesh grid spanning 2.6cm vertically \times 2.2cm horizontally \times 2.3cm depth. All voxels that were found outside the surface were included in the inversion but were assigned zero values. For inversion, 50 iterations of a randomized ART inversion algorithm was utilized, as previously reported in [72]. The inversion time in all reconstructions was kept within 5min .

4.2.1.5 Phantoms

Two phantoms were employed to examine the accuracy of the surface reconstruction.

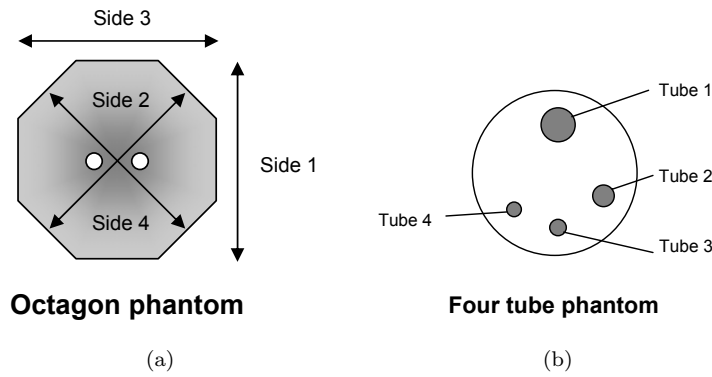


Figure 4.7: Cross-sectional view of the two phantom shapes as used in the accuracy experiments.

The first phantom was a solid, three-dimensional octagonal shape made of black Delrin, as seen in the schematic of Figure 4.7a. The second phantom consisted of four cylindrical tubes of different diameters, as reported in Table 4.1, the tubes were attached on the top and the bottom on two circular holders made out of black Delrin, as shown in Figure 4.7b. The two small tubes were capillary tubes with slightly different diameters, the two other tubes were made out of plastic, and all tubes were painted black. Both phantoms had a height of 5.33cm .

In order to test the ability to implement three-dimensional surface information into a non-contact FMT scheme, we employed a third phantom shaped similarly to that of Figure 4.7a, but made out of polyester resin mixed with TiO_2 spheres and India ink at concentrations that simulate the optical parameters of tissue, i.e. absorption coefficient of $\mu_a = 0.58\text{cm}^{-1}$ and reduced scattering coefficient of $\mu'_s = 10\text{cm}^{-1}$. This phantom block contained two hollow cylinders (by drilling) as indicated by the two white circles in Figure 4.7a with 0.19cm diameter and 2.8cm length. The cylinders were filled with the fluorescent dye Cy5.5 at a concentration of 250nM .

4.2.1.6 Characterization of animal motion

To characterize animal motion and its effects on FMT performance, we acquired 64 images of the silhouette of an anesthetized nude mouse at each of 0° , 45° and 90° viewing angles over a period of 2min . at CCD camera exposure time (integration time) of 10ms . With these settings different instances of the breathing and cardiac cycles were randomly captured for statistical analysis. The acquired silhouettes were segmented into fore- and background using the adaptive thresholding method outlined in section 4.2.1.2.

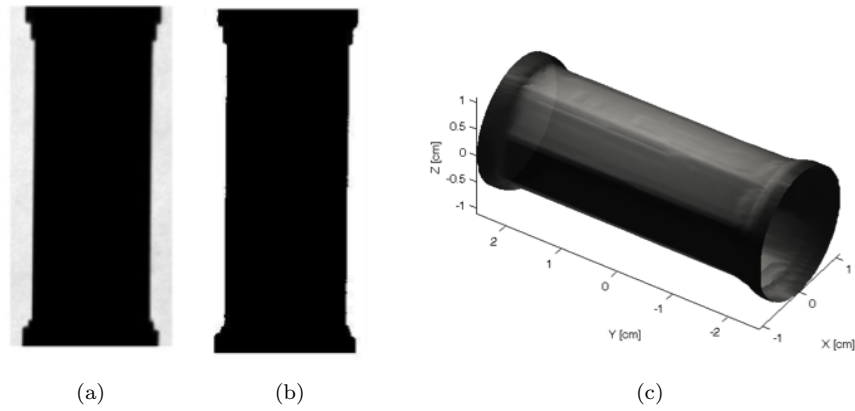


Figure 4.8: (a) Raw image of octagon silhouette (b) Segmented binary silhouette (c) Surface rendering of the reconstruction.

| Phantom | Actual diameter | Diameter measured | Error |
|------------------|-----------------|-------------------|---------|
| Tubes (tube 1) | 0.336cm | 0.331cm | 0.005cm |
| Tubes (tube 2) | 0.210cm | 0.209cm | 0.001cm |
| Tubes (tube 3) | 0.168cm | 0.160cm | 0.008cm |
| Tubes (tube 4) | 0.142cm | 0.139cm | 0.003cm |
| Octagon (side 1) | 1.774cm | 1.771cm | 0.003cm |
| Octagon (side 2) | 1.762cm | 1.765cm | 0.003cm |
| Octagon (side 3) | 1.772cm | 1.779cm | 0.007cm |
| Octagon (side 4) | 1.766cm | 1.762cm | 0.004cm |

Table 4.1: Expected and reconstructed diameters of the two studied phantoms.

4.2.2 Results

4.2.2.1 Accuracy of Surface Reconstruction

Figure 4.8 shows the silhouettes captured from the octagonal phantom at 0° angle as well as the reconstructed surface. Figure 4.8a shows a raw image captured by the experimental setup, Figure 4.8b depicts the result of the segmentation of the raw image into a binary fore- and background image, and Figure 4.8c shows a rendered image of the 3D surface as reconstructed from the binary silhouettes.

Similar reconstructions were obtained with the four-cylinder phantom (results not shown for brevity). To evaluate the accuracy of the method a vertically centered slice of the reconstructed surface was extracted and measured against the known manufactured dimensions of the phantoms, the results are summarized in Table 4.1.

The performance described in Table 4.1 was obtained using reconstruction parameters that were optimized for accuracy and computational efficiency, as derived by repeating surface reconstructions using a significantly wider selection of the viewing angles and the octree

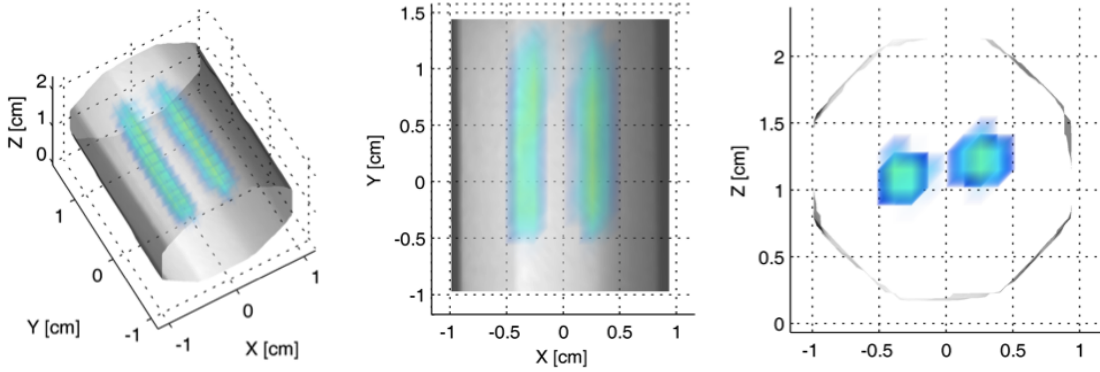


Figure 4.9: 3D reconstruction of two tubes of fluorescent dye in the resin octagon phantom.

level employed. We found that using less than 72 viewing angles (5° steps) degraded the reconstruction accuracy ($> 2\%$ error at 60 viewing angles), whereas increasing the number of angles beyond 72 yielded asymptotically changing surface with error of $< 1\%$. Similarly using an octree with less levels for reconstruction (e.g. seven levels corresponding to $128 \times 128 \times 128$ voxels) resulted in noticeably lower accuracy of the surface ($\sim 5\%$ error), while increasing the octree depth beyond eight levels (corresponding to $256 \times 256 \times 256$ voxels) effected no change at all — since the voxel size in this setting was smaller than the equivalent size of the object imaged corresponding to a single CCD pixel.

4.2.2.2 Free-space fluorescence tomography

Figure 4.9 shows the results of surface reconstruction of the resin octagon and the overlaid fluorescence reconstruction of fluorescent dye distribution, rendered from different viewing angles. The registration of surface and tomographic data is straightforward since the surface and the diffuse data are acquired under the same geometrical frame. The simultaneous rendering generally enables more accurate orientation because some high resolution anatomical information is viewed together with the fluorescence tomography data.

The fluorescent tubes were accurately reconstructed along a length of 1.7cm . The cross-sectional positional accuracy of the reconstructed tubes in this case is within the voxel dimension utilized.

4.2.2.3 In-vivo Accuracy — a Study of Breathing

Figure 4.10 shows representative images acquired from the mouse at the 0° , 45° and 90° viewing angles and the corresponding reconstructed surface rendered three-dimensionally.

Silhouettes were used as raw data for animal motion characterization. We measured the mean horizontal thickness of the segmented animal silhouette in pixels (one camera pixel

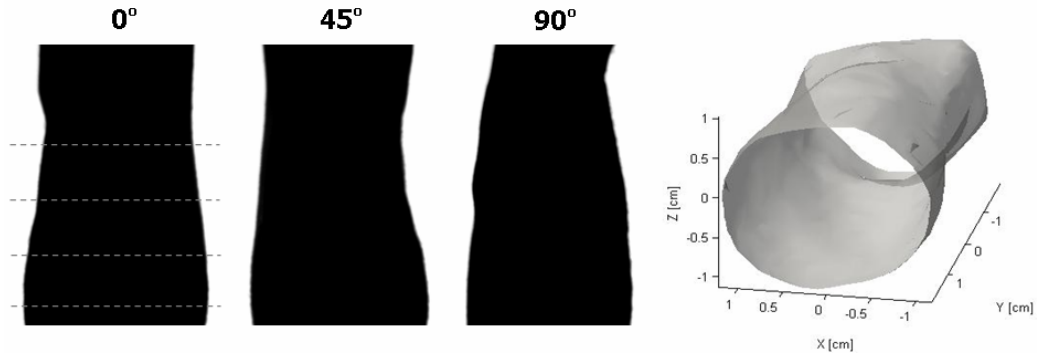


Figure 4.10: Instances of mouse silhouettes acquired in-vivo at 0° , 45° , 90° and a corresponding rendering of a reconstructed surface. The dashed lines in the left most picture indicate the positions where the measurements of Table 4.2 were acquired from.

Table 4.2: Standard deviations and maximum deviation from mean of horizontal thickness at different heights of the animal silhouette (in pixels; 1 pixel = $110\mu m^2$).

| σ (max. dev.) | 0° view | 45° view | 90° view |
|----------------------|-----------------|-----------------|-----------------|
| Lower abdomen | 0.93px (5.33px) | 0.61px (1.58px) | 0.62px (1.03px) |
| Upper abdomen | 0.63px (3.72px) | 0.80px (1.80px) | 0.76px (2.11px) |
| Lower thorax | 0.77px (4.72px) | 0.57px (2.08px) | 0.70px (1.66px) |
| Upper thorax | 0.91px (5.33px) | 0.76px (2.75px) | 0.84px (2.34px) |

corresponds to $0.011cm^2$) at different heights for each time series and the corresponding standard and maximum deviations due to breathing are displayed in Table 4.2 for three viewing angles. Generally the values recorded depend on the state of anesthesia. Correspondingly, the values in Table 4.2 reflect measurements from an animal towards the end of anesthesia where some more motion was observed; at the peak of anesthesia even smaller deviations were recorded. Generally, standard deviations of less than $100\mu m$ were observed at all different locations measured.

To study the effects of breathing on the FMT performance, we reconstructed the data set from section 4.2.2.2, first using the originally reconstructed 3D surface, see Figure 4.11a, and afterwards using an artificially modified 3D surface, shrunk by $0.011cm$ (corresponding to the length of one camera pixel) as seen in Figure 4.11b and expanded by $0.011cm$ in Figure 4.11c. To observe finer changes, a smaller volume ($2.2cm \times 2.3cm \times 0.5cm$) along the y -axis was reconstructed, compared to the one used in Figure 4.9, so that a finer mesh could be practically implemented at $30 \times 30 \times 7$ voxels. In this case, one row of three sources (spanning $0.29cm$ horizontally) and a detector grid of 7×30 detectors over $0.5cm$ vertically and $1.8cm$ horizontally was employed.

The effects of surface deformation on the image performance appear to be within the resolution limits of FMT. For the reduced diameter surface the reconstructed tubes appear slightly larger by one voxel, i.e. $\sim 0.07cm^2$. Correspondingly, the inflated surface also reconstructs

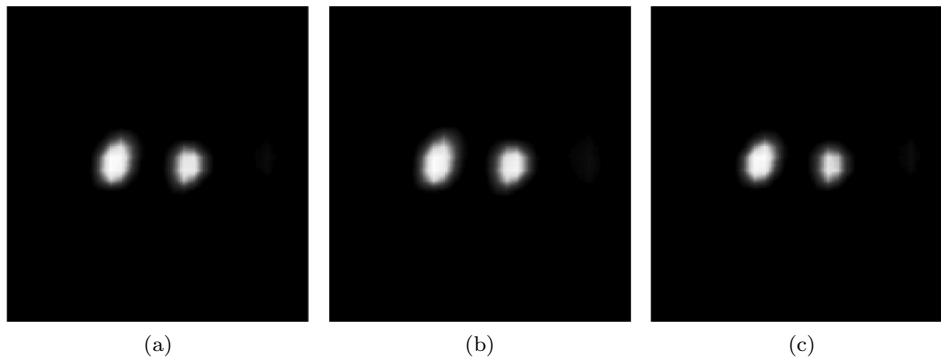


Figure 4.11: Slice reconstruction of two tubes of fluorescent dye in the resin octagon phantom (a) using surface as reconstructed (b) using surface artificially deflated by 0.011cm (c) using surface artificially inflated by 0.011cm .

tube diameters that are slightly smaller by again about 0.07cm^2 . The induced deformation does not appear to change however the shape or the position of the objects reconstructed with the geometrical metrics assumed herein.

4.2.3 Discussion

In this section we presented a method for reconstructing 3D surfaces from silhouettes to facilitate free-space FMT. We studied the accuracy of the surface reconstruction technique employed for the small animal dimensions, characterized the respiratory movement of a small animal placed in the experimental setup developed, and demonstrated the effect of this movement on image reconstruction.

The surface reconstruction accuracy of the herein described method was found to be within the limits of the camera resolution (i.e. $110\mu\text{m}$). Using such a surface description it was possible to reconstruct two fluorescent tubes inside a solid phantom with tissue-like properties using the non-contact illumination and detection scheme as well as free-space theory [138]. A limitation of surface reconstruction from silhouettes over previously employed photogrammetry methods [128] is that certain concave surfaces cannot be captured. As outlined in section 4.2.1.2, concavities with silhouette-inactive surfaces are not visible using silhouettes and as such cannot be reconstructed. Generally, mouse bodies do not offer significant concave surfaces but in the pelvis and possibly some skin-folds. As such, the methodology presented herein is appropriate for imaging in the torso and animal head, especially after care is taken to appropriately extend the limbs away from the field-of-view as seen in Figure 4.9.

With respect to utilizing these techniques for in-vivo small animal experiments, we characterized the motion of nude mice and demonstrated the effects of the corresponding surface

movement on 3D fluorescence reconstructions. Mouse motion, due to breathing, cardiac function and other physiological processes yielded changes with $\sim 100\mu\text{m}$ standard deviation, whereas no absolute deviation from the mean that was larger than $600\mu\text{m}$ was observed. The upper thorax consistently yielded the highest motion in all views compared to the movement observed for other parts of the animal. These deviation metrics did not significantly affect image reconstruction performance yielding spatial errors that were within the resolution accuracy of the reconstruction method [126] ($\sim 0.07\text{cm}$) when reconstructing two fluorescent tubes in a diffusive mouse-like medium, although the effects were larger than the actual standard deviation observed. Correspondingly the quantification errors in this case were $< 7\%$. While only 10ms averaging time per measurement was employed to yield the observations of Table 4.2 and Figure 4.11, practical FMT measurements are typically acquired over longer integration times ($0.1\text{--}1\text{s}$). Such integration times far exceed the cardiac and breathing cycle of a mouse and correspond to standard deviations of animal motion that are significantly smaller than in Table 4.2 due to further averaging effects. Therefore, in-vivo experiments are generally less sensitive to high-frequency motion since the surfaces mean can be acquired with greater certainty, and are expected to offer reduced effects on FMT image reconstructions compared to the findings in this study. Therefore, the results in this study represent a worst case scenario within the approximations of diffusion theory.

While technologically more complex methods like X-ray CT or 3D laser scanning for surface reconstruction will offer higher accuracy than the proposed method, they cannot be integrated into an FMT imaging device as seamlessly. The necessary calibration and registration steps to match the surface reconstruction and FMT coordinate systems impose additional computational overhead and may introduce registration errors. Conversely, the silhouette-based volume carving method employed herein is inherently registered with the tomographic data captured under identical viewing conditions. We note however that the particular vertical geometry implemented herein was guided by experimental simplicity and does not propose a preferred imaging geometry. Based on these developments, we anticipate that future FMT devices will accommodate horizontal placement of animals and appropriate rotation of the optics in order to simplify experimental procedures and minimize possible physiological changes of the vertical placement. Such developments can also facilitate the straightforward integration with another modality like X-ray CT.

Overall we have shown the capacity of capturing complete mouse surfaces and implementing them in 360° -projection non-contact free-space FMT acquisition schemes. The surface capture approach yields the diffuse-air boundary of each animal examined in three dimensions and it is necessary for computing appropriate forward models for FMT reconstructions. The accuracy of the surface capture achieved is well below the FMT resolution and it was experimentally confirmed that it is appropriate for FMT reconstructions. This approach therefore yields a robust method for implementing 360° -projection FMT systems.

4.3 Acquisition Optimization via Singular Value Analysis

Original tomographic systems for small animal imaging utilized only a small number of measurements and often employed matching fluids for simplifying methodological and theoretical requirements, yielding images of compromised performance [111, 141]. Recently, systems that operate without the need to bring fibers in contact with tissue or to use matching media have simplified experimental procedures and produce superior imaging performance [128, 131]. These new technologies now enable the implementation of complete projection 360° tomographic approaches using CCD cameras in non-contact detection mode and similarly non-contact illumination using appropriately oriented light beams [129]. Such implementations are common to most other tomographic imaging modalities (for example PET and SPECT) and in particular for X-ray CT, which also utilizes a two dimensional array of detectors for signal collection.

While 360° geometries using CCD cameras can maximize the information content available in the measurements, there has been little experience with such implementations for optical tomography applications through tissues. Cylindrical geometries have been implemented in the past for diffuse optical tomography applications [142–144] and their benefit over other geometrical implementations has also been demonstrated [145]. However these implementations considered sparse surface measurements, using a relatively small number of fibers placed symmetrically around the tissue boundary and in contact with the diffuse medium. Alternatively, slab geometry systems with direct CCD camera coupling have been considered, however such systems offered limited projection viewing [126, 127, 146]. Therefore limited knowledge has been available on the optimal implementation of experimental parameters for developing and utilizing the data obtained with a CCD camera based 360° tomographic imaging system, i.e. a complete projection system offering high spatial sampling of photon patterns propagating through tissue.

An important consideration in the design of 360° CCD camera based systems is the vast amount of data that can be collected. An FMT system developed in our laboratory using this technology [131, 140] typically collects $10^8 - 10^{10}$ measurements, when considering the size of a single CCD camera measurement (10^6) further multiplied by the number of possible projections (10–100) and light sources utilized (10–100). In addition, FMT requires a theoretical model (the forward model) that predicts photon propagation from a given source position through a diffusive medium to a given detector position. In most common implementations today this involves an approximation of the radiative transfer equation and yields a linear system $m = Wn$, where a weight matrix W couples the fluorochrome distribution n to the measurements m . This system is then solved for n by inverting the weight matrix W . The size of the weight matrix W is determined by the product of the number of measurements utilized and the number of voxels employed to discretize the fluorochrome

distribution n in the volume of interest. For example, more than 2^{32} matrix elements need to be computed and stored even when using moderate sampling parameters, for example by using 7×7 sources, 20×20 detectors, a $20 \times 20 \times 20$ discretization grid and 36 projections. It follows that such inversion problems can yield very high memory and computational requirements, which today's computers cannot satisfy. This is particularly true when high spatial resolution and better image fidelity is pursued as this involves increasing the number of sources and detectors as well as the discretization step of the reconstruction grid. Therefore, optimization of experimental parameters which maximizes the information content of the acquired measurements while minimizing the associated memory storage requirements and computational expense, is an important step towards achieving practical computation schemes. Besides the computational considerations, this optimization is equally important for minimizing acquisition times and suggesting optimal designs for hardware development.

In this section we address several open questions as to the optimal design and operation of new potent FMT systems employing complete projection (360°) illumination and detection in constant wave (CW) mode, i.e. using illumination of constant intensity. We employ the Singular Value Analysis (SVA) [147] as a tool for analytically assessing optimal experimental parameters. The SVA analysis has been employed in optimizing optode arrangement and the field of view in parallel plate geometries [148], for comparing parallel plate transmission and remission geometries [147] and for optimizing the placement of fibers for a hybrid magnetic resonance imaging / near infrared imaging device for small animal brain studies [149]. SVA generically evaluates the relative performance of different parameter sets (for example the spatial sampling of sources and detectors, or the field of view employed), and can be used to draw generic conclusions on optimal parameter sets. In this section, we employed SVA to study the 360° geometry in two assumed systems; the first considering a parallel plate system that can freely rotate for implementing 360° projection capacity and the second implementing a free-space system also using 360° non-contact rotation as explained in methods. The difference between these two systems is that the first describes an approach where a mouse is rotated within a slab geometry containing a matching fluid, whereas the second system reflects an implementation where a mouse is rotated in the absence of matching fluid (free-space) or equally, where the optical system is rotated around a mouse. SVA analysis was confirmed with experimental data from two corresponding experimental setups. We were particularly interested in identifying the optimal number of projections that should be employed for small animal imaging and whether a fan beam versus a scan beam illumination would be more appropriate for imaging purposes. In addition, we optimized the spatial sampling and the field of view for the sources, detectors and mesh points employed. In the following we present the methods used in our analysis, the theoretical and experimental results obtained and discuss the major findings and the limitations of this study.

These results have also been published in [150].

4.3.1 Methods

4.3.1.1 Forward model generation

The forward model used to predict photon propagation in a diffuse body was based on the normalized Born approximation to the diffusion equation (see section 4.1.1 and [123]). The normalized Born average intensity

$$U^{\text{nB}}(r_s, r_d) = \frac{U_{\text{fluo}}(r_s, r_d)}{U_0(r_s, r_d)}$$

is the ratio of the average intensities $U_{\text{fluo}}(r_s, r_d)$ at emission wavelength λ_2 and $U_0(r_s, r_d)$ at excitation wavelength λ_1 , each measured at detector position r_d for a source at position r_s . The normalized Born approximation then equates

$$U^{\text{nB}}(r_s, r_d) = \frac{S_0}{U(r_s, r_d, k^{\lambda_1})} \int_V U(r_s, r, k^{\lambda_1}) G(r_d - r, k^{\lambda_2}) \frac{n(r)}{D^{\lambda_2}} d^3r, \quad (4.8)$$

where $U(r_s, r, k^{\lambda_1})$ denotes the analytically calculated average photon intensity at excitation wavelength λ_1 induced at position r by a source at position r_s in a medium with wave number k^{λ_1} . $G(r_d - r, k^{\lambda_2})$ is the Greens function which solves the diffusion equation for photon propagation from position r to the detector position r_d at emission wavelength λ_2 . D^{λ_2} is the diffusion coefficient of the medium at emission wavelength λ_2 and $n(r)$ is the fluorochrome concentration at position r multiplied by fluorescent yield. The factor S_0 is a unit-less, experimentally determined factor that calibrates the equation for various system gain and attenuation factors, while V denotes the volume of investigation. Discretizing that volume V into N voxels r_1, \dots, r_N allows reformulation of equation (4.8) into a linear equation for the source-detector pair r_{s_i}, r_{d_i} ($i = 1, \dots, M$):

$$U^{\text{nB}}(r_{s_i}, r_{d_i}) = \left(W_{i1} \ \cdots \ W_{iN} \right) \begin{pmatrix} n(r_1) \\ \vdots \\ n(r_N) \end{pmatrix}$$

where

$$W_{ij} = \frac{S_0 U(r_{s_i}, r_j, k^{\lambda_1}) G(r_{d_i} - r_j, k^{\lambda_2})}{U(r_{s_i}, r_{d_i}, k^{\lambda_2}) D^{\lambda_2}}.$$

The resulting linear system for all M source-detector pairs is thus

$$\begin{pmatrix} U^{\text{nB}}(r_{s_1}, r_{d_1}) \\ \vdots \\ U^{\text{nB}}(r_{s_M}, r_{d_M}) \end{pmatrix} = \begin{pmatrix} W_{11} & \cdots & W_{1N} \\ \vdots & \ddots & \vdots \\ W_{M1} & \cdots & W_{MN} \end{pmatrix} \begin{pmatrix} n(r_1) \\ \vdots \\ n(r_N) \end{pmatrix}$$

or in short

$$m = Wn, \quad (4.9)$$

the standard algebraic formulation with m being the measurements, W the weight matrix and n the fluorochrome distribution.

4.3.1.2 Singular-value decomposition and noise threshold

To study generic characteristics of the weight matrix, the singular value decomposition $W = USV^t$ was considered, where U , V are orthonormal matrices ($U^{-1} = U^t$, $V^{-1} = V^t$) and S is a diagonal matrix consisting of the singular values of W [151]. Using this decomposition equation (4.9) can be rewritten as

$$U^t m = SV^t n,$$

thus the columns of U can be thought of as the detection-space modes of W , and the columns of V as the image-space modes of W . In this sense, the singular values of W specify the degree to which a given image-space mode is coupled to the corresponding detection-space mode, or in other words, how effectively a given image-space mode is detected by the experimental setup.

To obtain experimentally relevant conclusions, it is useful to determine a noise threshold in the singular-value domain that determines which singular values are important in the reconstruction outcome. We followed the method described by [148], where the noise threshold is determined as the cut-off point of a regularization process that yields optimal reconstruction results in control experimental reconstructions based on phantom measurements. We employed the same threshold value of 10^{-4} reported in [148] since similar experimental components and devices were employed here. The low sensitivity of the SVA to this cut-off value was confirmed by repeating the analysis described in the following using a range of threshold values.

4.3.1.3 Singular values above threshold

To observe general trends as a function of the various parameters studied, we focused on determining the number of useful singular values above the noise threshold (SVAT) for each of the parameters studied. To calculate the SVAT number, a weight matrix is computed for each of the different parameters studied and then decomposed by SVA to yield the SVAT. This number is used throughout the study and represents a measure of the useful information contained in the data under different implementation schemes.

4.3.1.4 Experimental setup

We examined two different complete projection implementations. In the first implementation we considered a parallel plate geometry that offers 360° rotation. This system corresponds to a parallel plate system, which contains a matching fluid, similar to the ones developed by [126, 127], with the exception that here the object is rotated within the chamber. In the second implementation, we studied the performance of a true cylindrical geometry where 360° illumination–detection can be achieved in free–space mode, i.e. in the absence of matching fluids. Both these systems have been implemented in our laboratory and provided experimental measurements. We note that in contrast to cylindrical geometries that use fiber–based point measurements around the boundary, herein we consider high spatial sampling of photon fields as can be offered by non–contact detection using CCD cameras.

Parallel–plate rotational geometry. This geometry implicates immersion of a subject in a parallel–plate (slab) chamber that contains a fluid that matches the average optical properties of the imaging sample. The sample is rotated inside the slab so that 360° projections can be achieved. This is not a preferred experimental geometry, especially for 360° implementations, but simplifies experimental requirements since simple theoretical models developed for photon propagation in diffusive slabs [152] can be employed. In addition, relaxed requirements for the dynamic range of the detection system are required in the slab geometry. To study the rotating parallel–plate geometry, we modeled the weight matrices after an existing FMT system previously reported [126] employing a single horizontal row of sources, a two-dimensional grid of detectors and a three-dimensional mesh as shown in Figure 4.12. The dimensions selected for the slab width (2cm) are settings commonly used for in–vivo imaging in our laboratory and represent average dimensions for mouse torso or head imaging in the rotating geometry.

We optimized parameters for five basic questions associated with the design and operation of the system and subsequent inversion performance as follows:

A1. Optimal number of projections. The number of projections (evenly distributed over the full circle) was varied while keeping the other parameters constant. This was done twice, first for a single centered source with 10×10 detectors and a $10 \times 10 \times 10$ mesh, and second for a single centered source with 16×16 detectors and a $16 \times 16 \times 16$ mesh.

A2. Optimal arrangement of sources (fan beam versus scan beam geometry). The number of sources was varied from one to seven, distributing them on a vertically centered horizontal line with a constant spacing of 0.33cm . The detector and mesh density

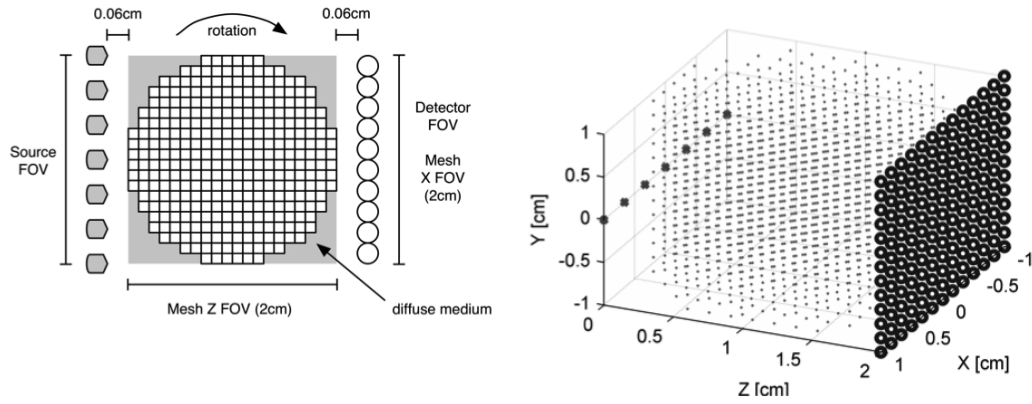


Figure 4.12: Diagram of the parallel-plate FMT setup used in the singular-value analysis (top view and three-dimensional side view). In a three-dimensional slab geometry, we study up to seven sources in a horizontal line (centered vertically, default FOV 2cm), a square matrix of detectors (default FOV 2cm for both x - and y -directions) and a rotating mesh grid of dimensions $2\text{cm} \times 2\text{cm} \times 2\text{cm}$ embedded in a diffuse medium.

were kept constant at 14×14 and $14 \times 14 \times 14$ respectively. This step was examined for 1, 5, 9 and 18 projections.

A3. Optimal detector spatial sampling. The density of the detectors was varied while keeping the number of projections (18) and sources (one centered source) constant. This was studied for $10 \times 10 \times 10$ and $20 \times 20 \times 20$ mesh density.

A4. Optimal mesh resolution. The density of the mesh was varied while the number of projections (18) and sources (one centered source) were kept fixed. This experiment was repeated for 10×10 and 20×20 detectors.

A5. Optimal detector field-of-view. The field-of-view (FOV) of the detectors (i.e. the area sampled by the detectors) was varied while keeping the FOV of the sources (i.e. the area illuminated by the sources) and all the other parameters constant at 18 projections, 14×14 detectors density and $14 \times 14 \times 14$ mesh density. This was repeated four times for varying the source FOV from 1cm to 4cm for seven equidistantly spaced sources.

Cylindrical rotational geometry. The cylindrical rotational geometry differs from the planar geometry considered above in that less diffusion is present in the data since no matching fluid is present. Therefore, a modified set of optimal parameters can be expected. To study the cylindrical geometry setup, we modeled the weight matrices after a cylindrical FMT system with a diameter of again 2cm , see Figure 4.13. Due to the larger amount of data that can be collected in the fluid-free setup and because of the larger viewing

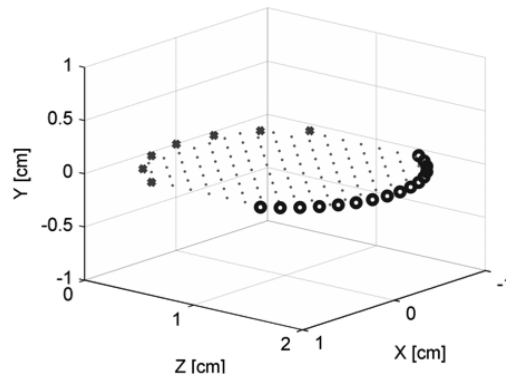


Figure 4.13: Diagram of the cylindrical FMT setup used in the SVA. Shown here are seven sources (crosses) equidistantly arranged at a FOV of 120° , an array of detectors (circles) equidistantly arranged at a FOV of 120° and a mesh grid of 2cm diameter. Several other configurations were studied.

angles that are available, we restricted this analysis to assuming that all measurements and fluorescence activity are contained within the same horizontal surface. The problem considers three-dimensional modeling of photon propagation (i.e. three-dimensional Green's functions solutions are assumed) but that the fluorochrome distribution is contained within a two-dimensional plane in order to achieve computationally manageable problems. This simplification is expected to generally preserve the trends observed in studies B1 to B4 due to the symmetric nature of the imaging problem along the y -axis, although some differences could be expected for truly three-dimensional arrangements.

Here we optimized parameters for the following four basic design decisions:

B1. Optimal number of projections. The number of evenly distributed projections was varied while keeping other parameters constant. The experiment was repeated twice; for a single source, 16 detectors arrayed in a 150° arc and 145 mesh points, and for a single source with 31 detectors arrayed in a 150° arc and 601 mesh points.

B2. Optimal number of sources (fan beam vs. scan beam geometry). The optimal number of sources distributed over an arc of 120° was studied, while the other parameters remained constant at 31 detectors arrayed in a 150° arc and 601 mesh points. This study was repeated for 1, 5, 9 and 15 projections.

B3. Optimal detector density. We studied a range of detector densities ranging from 20° to 5° spacing on a 150° arc and a 90° arc respectively. The remaining parameters were kept constant at a single source, 15 projections and 601 mesh points.

B4. Optimal arrangement of sources and detectors. Finally, the optimal arrangement of sources and detectors was studied. To achieve this, the number of sources was kept constant, while their FOV varied from a 30° arc to a 120° arc. The same was done for the detector arrangement, the arc ranging from 60° to 180° . The remaining parameters were fixed at 15 projections and 601 mesh points.

We did not include our results on choosing the mesh resolution for the cylindrical rotational geometry, as they exhibited the same trends as observed in study A4, where we optimized mesh resolution for the parallel-plate 360° geometry.

4.3.1.5 Experimental measurements

To confirm the findings of the singular value analysis, we further obtained experimental data from two phantoms, one in the parallel-plate rotational geometry and one in the free-space 360° geometry.

The first phantom consisted of three parallel tubes of 3.6mm diameter arranged in a triangular shape with a separation of 2.5mm , 2.5mm and 7.0mm on the far side, see Figure 4.14a. The tubes were filled with a 500nM solution of Cy5.5 fluorescent dye (Amersham Bioscience, Piscataway NJ, USA) and placed in a 2cm deep imaging chamber filled with an intralipid and ink matching fluid with absorption coefficient $\mu_a = 10\text{cm}^{-1}$ and reduced scattering coefficient of $\mu'_s = 1.16\text{cm}^{-1}$. The phantom was rotated in the chamber using a motorized rotation stage (stepper motor PR50PP, Newport Corp., Irvine CA, USA). Reconstructions were performed on key findings of the SVA analysis, i.e. those of study A2. Data inversion was performed using a randomized Algebraic Reconstruction Technique (ART, see section 3.3.1) employing 50 iterations. Measurements with less than 20 counts/s (16-bit camera, maximum 65,536 counts) in both the fluorescent or intrinsic channel were not considered for the inversion procedure.

The second phantom was a solid resin block, machined to an octagonal shape with optical properties those of the mid-torso of small animals, i.e. $\mu_a = 0.58\text{cm}^{-1}$ and $\mu'_s = 10\text{cm}^{-1}$. The radius of the phantom was 1.8cm and it contained two drilled tubes (0.19cm diameter, 3mm separation) that were filled with Cy5.5 fluorescent dye at a concentration of 250nM . Reconstructions were done to confirm the findings of study B2, the maximum number of sources employed however was limited to three for experimental simplicity. The necessary boundary conditions for modeling the non-contact acquisitions were incorporated into the normalized Born ratios using the Kirchhoff approximation as described in [138, 153]. The data was inverted using 50 iterations of randomized ART. Measurements below 20 counts/s in either the fluorescent and intrinsic channels were discarded.

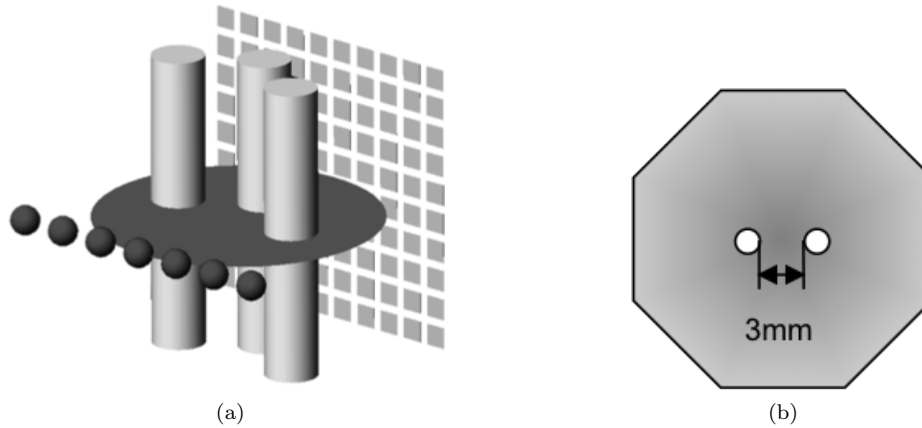


Figure 4.14: (a) Schematic of the three tube phantom placed in the imaging chamber. Fluorochrome concentration in each tube was $500nM$ of Cy5.5. (b) Schematic of the two tube phantom used for the non-contact experiment. Fluorochrome concentration in each tube was $250nM$ of Cy5.5.

4.3.2 Results

4.3.2.1 Singular-value analysis, slab geometry

The SVA focused on determining the number of useful singular values above the noise threshold (SVAT) assuming a threshold of 10^{-4} in the singular-value spectrum for each of the experimental setups in the parallel-plate geometry. An example of the singular-value spectra associated with the weight matrices for Study A1 is shown in Figure 4.15a, plotted on a logarithmic scale. The noise threshold of 10^{-4} is plotted as a horizontal dashed line and it has been calculated for the system employed based on experimentally determined noise characteristics as discussed in [148]. The analyses shown were repeated with thresholds ranging from 10^{-2} to 10^{-6} , corresponding to system with different noise levels than the one employed herein. This study demonstrated that the general trends in imaging performance observed were independent of the singular-value cutoff chosen, especially for thresholds within the 10^{-3} to 10^{-6} range, even though the absolute number of useful singular values changed with different thresholds.

Study A1: Figure 4.15b depicts the effect of multiple projections on the SVAT. As described in section 4.3.1.3, this data was generated by first calculating the SVA of different weight matrices, each constructed for a different number of projections and then plotting the SVAT as a function of the number of projections used. There is an initial step increase of the number of useful singular values up to 12 projections for the 10×10 detectors, $10 \times 10 \times 10$ mesh configuration and up to 18 projections for the 16×16 detectors, $16 \times 16 \times 16$ mesh configuration. Further increasing the mesh sampling yielded small improvements with increasing number of projections. An increasing number of SVAT corresponds to an increasing

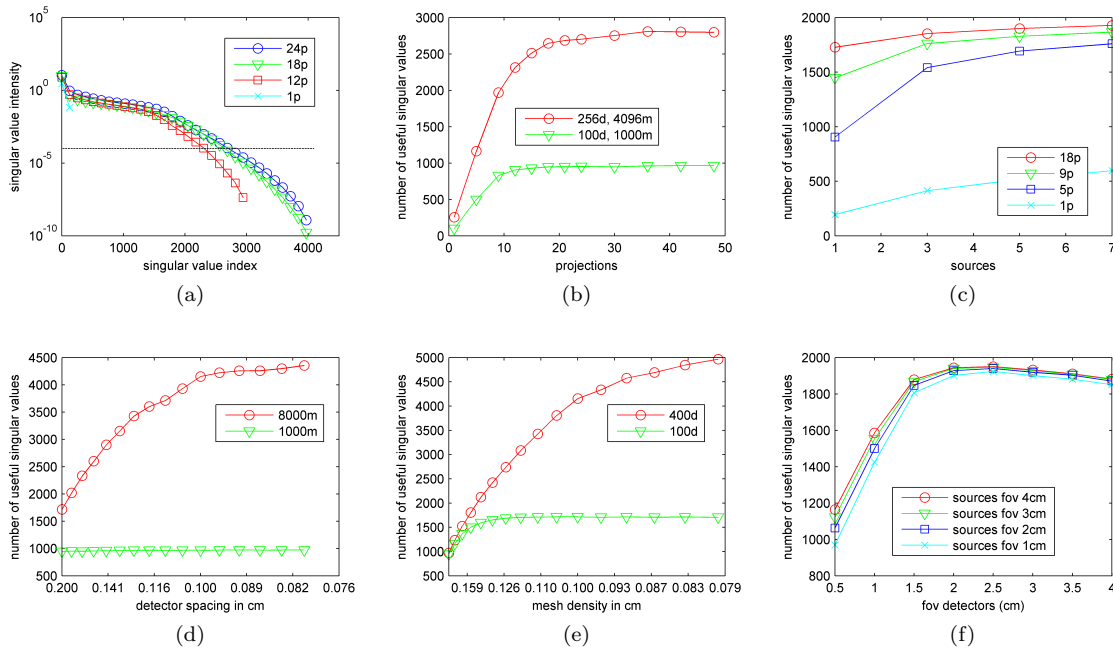


Figure 4.15: (a) Singular values (log scale) as a function of the number of projections used (evenly distributed over the full circle) for slab geometry. Singular–value spectra for weight matrices representing setups with one centered source, 16×16 detectors, a $16 \times 16 \times 16$ mesh and 1 projection (crosses), 12 projections (squares), 18 projections (triangles) and 24 projections (circles). The intersections of each spectrum with the empirically determined noise threshold (10^{-4}) yielded the number of non–noise, or useful, singular values for that experimental setup. (b) SVA of the effects of number of projections used (evenly distributed over the full circle) for slab geometry. Plot shows number of useful singular values (SVAT), extracted as shown in (a), versus number of projections for setups with one centered source, 10×10 detectors with a $10 \times 10 \times 10$ mesh (triangles) and one centered source, $16 \times 16 \times 16$ mesh (circles). (c) SVA of the effects of number of sources (arrayed on horizontal line) for slab geometry. Plot for setups with 14×14 detectors, a $14 \times 14 \times 14$ mesh and 1 projection (crosses), 5 projections (squares), 9 projections (triangles) and 18 projections (circles). (d) SVA of the effects of detector density for slab geometry. Plot for setups with one centered source, 18 projections and a $10 \times 10 \times 10$ mesh (triangles) and a $20 \times 20 \times 20$ mesh (circles) respectively. (e) SVA of the effects of mesh density for slab geometry. Plot for setups with one centered source, 18 projections and 10×10 detectors (triangles) and 20×20 detectors (circles) respectively. (f) SVA of the effects of detector FOV for slab geometry. Plot for setups with 18 projections, 14×14 detectors, a $14 \times 14 \times 14$ mesh and 7 sources (arrayed on a vertical line) with FOV 1cm (crosses), 2cm (squares), 3cm (triangles) and 4cm (circles).

number of image-space modes available for reconstruction, indicative of improving imaging performance. However, a further increase in the number of projections does not yield a corresponding gain in the SVAT, but it linearly increases the data size and computational burden as a function of projections. Therefore this result indicates that the range of 12–18 projections is optimal for CW 360° reconstructions. For this reason we chose 18 projections as the baseline for the following optimization studies.

Study A2. Figure 4.15c summarizes results from the study that examined the SVAT as a function of the number of sources in the slab geometry, for different numbers of projections. Adding more sources in a scan configuration generally increases the number of useful singular values. The relative gain observed however as a function of the number of sources employed is stronger when only five projections are used, but becomes less important as the number of projections increases to 9 or 18. Generally, a very low SVAT number is found for single projection systems. It is further observed that the addition of projections yields higher SVAT gain than the addition of more sources. This confirms the advantage of full-projection tomography over non-rotating slab FMT systems. It further indicates that a small number of sources in a scan beam configuration (i.e. three to five sources) is preferred over a purely fan beam configuration, i.e. a single source per rotation.

Study A3. The effects of detector density on SVAT are shown in Figure 4.15d. The detector density was varied from 10×10 to 25×25 , over a $2 \times 2 \text{ cm}^2$ FOV, which corresponded to spatial sampling of 2 mm to 0.8 mm . Two meshes were considered at $10 \times 10 \times 10$ and $20 \times 20 \times 20$ voxels. The analysis demonstrated that increasing the detector density yields little to no improvement for the $10 \times 10 \times 10$ configuration. The curve for the $20 \times 20 \times 20$ configuration, however, demonstrated a marked improvement with increasing detector density. Less improvement is seen, however, for sampling densities higher than one detector per millimeter. We note that this observation is linked to the selection of a moderately spaced grid of 1 mm^3 . In a previous study on the parallel-plate geometry without rotation, improvements were observed for finer detector sampling when a correspondingly finer discretization mesh was used [148].

Study A4. In Figure 4.15e we summarize the results of study A4, which studied the effects of increasing the mesh density from $10 \times 10 \times 10$ up to $25 \times 25 \times 25$, corresponding to spatial sampling of 0.2 cm to 0.08 cm , once each for a 10×10 and a 20×20 detector matrix. As in Study A3, increasing the mesh density increases the SVAT, which flattens out after the mesh sampling becomes smaller than the detector spacing.

Study A5. Finally, Figure 4.15f represents the optimization of FOV scanned by detectors and sources assuming 18 projections. 14×14 detectors were employed over a 0.5cm^2 to 4cm^2 FOV. This resulted in 0.036cm to 0.29cm spatial sampling. Correspondingly, the source FOV also varied from 1cm to 4cm using seven equidistantly spaced sources (i.e. 0.14cm to 0.57cm spatial sampling). The maximum SVAT was observed for a detector FOV of 2cm to 2.5cm . In this case, the source FOV was of lesser importance since results are weighted towards detector characteristics due their larger number compared to the number of sources employed. These findings suggest that keeping the source and detector FOV similar to the mesh dimensions yields the best SVAT number.

4.3.2.2 Experimental reconstructions, slab geometry

Figure 4.16 depicts the experimental verification of the most important finding of the SVA study with regard to improvements obtained as a function of the projections and the number of sources employed. The reconstructions employed a detector matrix and a mesh grid of 0.1cm resolution each. Confirming the results of the SVA analysis, the number of projections yields higher imaging performance gains as opposed to adding more sources. However, having more than one source seems equally advisable, similarly to the predictions seen in Figure 4.15c. Imaging performance here is significantly underperforming when only one projection is used. However, configurations developed for imaging in the slab geometry typically employ finer source sampling and elongated fields of view to partly compensate for the lack of complete projections and yield improved imaging performance compared to the one projection results obtained herein.

4.3.2.3 Singular-value analysis, cylindrical geometry

Study B1. Figure 4.17a represents the optimization of the number of projections for the free-space approach, yielding similar observations to the ones of Figure 4.15b. When 16 detectors are arranged over a 150° arc (10° step), the SVAT shows an asymptotic saturation for more than 12 projections. Conversely at 31 detectors (5° step), the SVAT saturates above ~ 18 projections. Interestingly, some oscillations in the SVAT are observed in this case. The “dips” of the oscillation are observed at 12, 18, 24, 36 and 48 projections, which represent symmetries in the inversion problem that yield data correlations and lower the SVAT values. For example, at 36 projections, all source–detector pairs for each projection at angle x are mirrored by one source–detector pair of the 15 subsequent projections starting from $x + 110^\circ$. This behavior does not occur in the parallel-plate geometry (see Study A1), as the sources and detectors are not arranged in a circular fashion and thus this exact symmetry of rotational step and source/detector step is not observable.

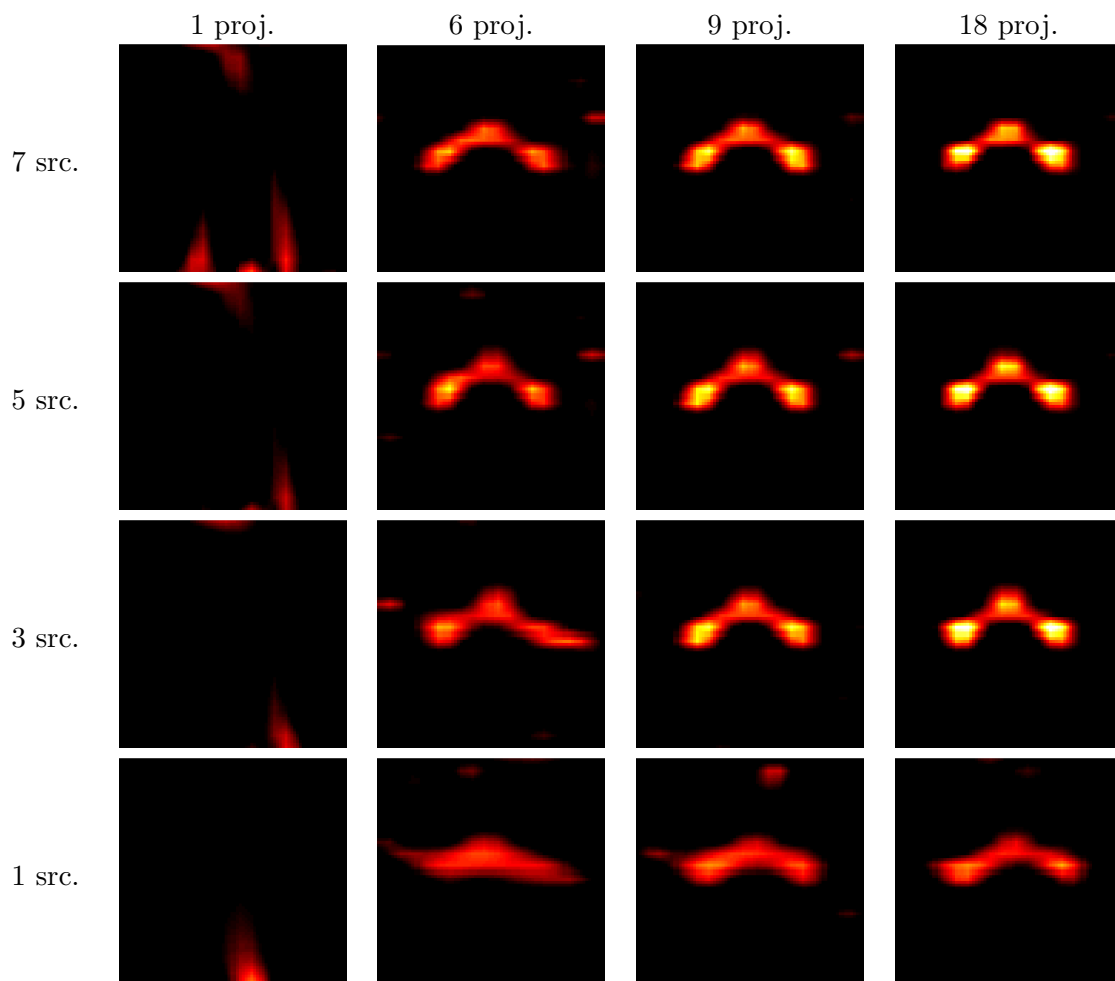


Figure 4.16: Reconstruction of three tubes using 1–18 projections, 1–7 sources. For each reconstruction, we used a 20×20 detector grid and a $20 \times 20 \times 20$ mesh, the inversion employed a randomized ART algorithm with 50 iterations.

Study B2. Figure 4.17b depicts the SVAT as a function of the number of sources and projections employed. Similar to the results of Study A2, significant gains are observed when increasing the number of projections compared to increasing the number of sources. In addition, the use of more than one source is shown to give a significantly higher SVAT value compared to a single source.

Study B3. The effects of detector density on the SVAT are shown in Figure 4.17c. Herein the singular values are plotted as a function of detector spacing in degrees for two configurations with a detector arc of 90° and 150° respectively. The configuration with the wider detector arc (and thus higher number of detectors) yields higher SVAT numbers throughout, as further elaborated in study B4 below. In both configurations, increasing the detector resolution yields virtually a linear dependence to the SVAT number. Although some saturation

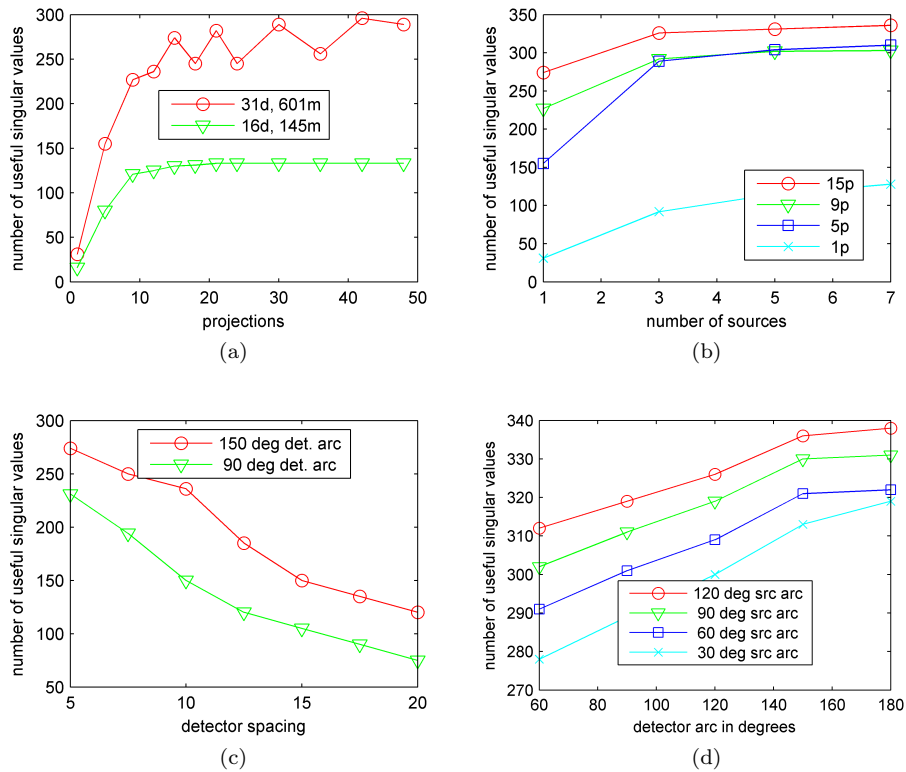


Figure 4.17: (a) SVA of the effects of number of projections used (evenly distributed over the full circle) for cylindrical geometry. Plot shows the number of useful singular values, extracted as shown in Figure 4.15a, versus number of projections for setups with one centered source, 16 detectors arrayed on a 150° arc and 145 mesh points (triangles) and one centered source, 31 detectors on a 150° arc and 601 mesh points (circles). (b) SVA of the effects of number of sources (arrayed on a 120° arc) for the cylindrical geometry. Plot for setups with 31 detectors on a 150° arc, 601 mesh points and 1 projection (crosses), 5 projections (squares), 9 projections (triangles) and 15 projections (circles). (c) SVA of the effects of detector density for the cylindrical geometry. Plot for setups with one centered source, 15 projections, 601 mesh points and the detectors arrayed on a 90° arc (triangles) and a 150° arc (circles) respectively. (d) SVA of the effects of source and detector arc for cylindrical geometry. Plot for setups with 15 projections, 31 detectors, 601 mesh points and 7 sources arrayed on a 30° arc (crosses), 60° arc (squares), 90° arc (triangles) and 120° arc (circles).

should be expected in finer degree sampling, this was not observed for arc sampling up to 5° (i.e. $\sim 0.9\text{mm}$ detector to detector distance).

Study B4. Finally, Figure 4.17d shows the SVAT obtained as a function of source and detector FOV. As already suggested in study B3, widening the detector arc from 60° to 150° shows a large increase in the SVAT number, which follows a linear increase as a function of the arc, except for the last step from 150° to 180° , where some saturation is observed. This is the reason that several of the tests were performed assuming a 150° detector arc as a baseline. Regarding the source arc, moving from a 30° arc up to a 120° arc increases

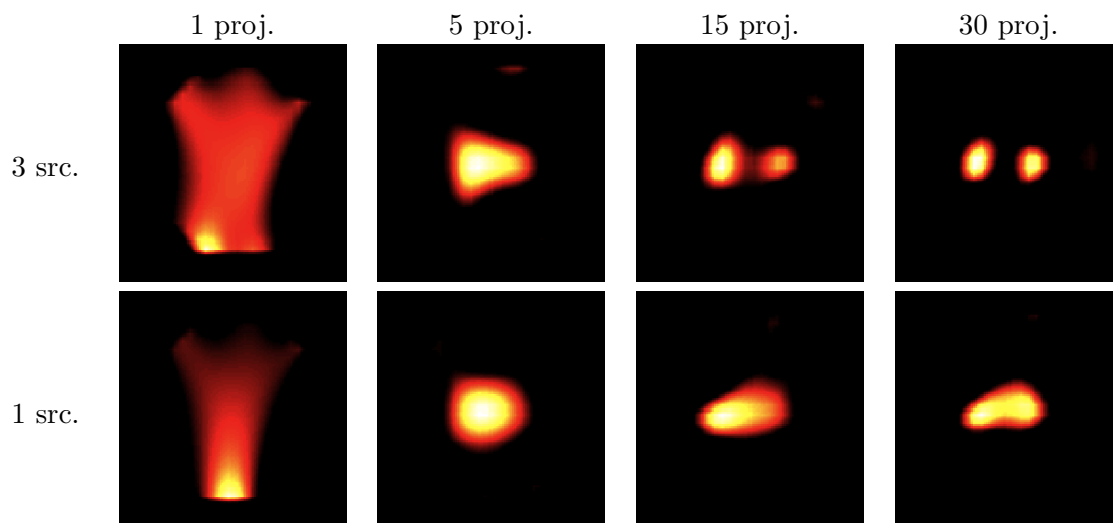


Figure 4.18: Reconstruction of two tubes using 1–30 projections, 1–3 non–contact sources. For each reconstruction, we used a 7×30 detector grid and a mesh of 0.07mm resolution, the inversion employed a randomized ART algorithm with 50 iterations.

the expected imaging performance noticeably with each step, which led us to use the 120° source arc for studies involving multiple sources (study B2).

4.3.2.4 Experimental reconstructions, cylindrical geometry

Figure 4.18 summarizes the results obtained for the phantom measurements as a function of number of projections and number of non–contact sources employed. The reconstructions were performed using 7×30 non–contact detectors and a mesh grid of 0.07cm resolution, the source arc had to be limited to $\sim 20^\circ$ because of experimental limitations. As in the results of study B2, increasing the number of projections yields significantly better imaging performance while adding more sources produces a smaller, but still very noticeable effect. Again, as in Figure 4.17b, it is confirmed that using more than one source is advised.

4.3.3 Discussion

As Fluorescence Molecular Tomography is evolving towards the new generation of non–contact, free–space imaging systems, it is important to optimize several of the design, data acquisition and reconstruction parameters to gain an understanding of the necessary experimental parameters that yield optimal imaging performance while maintaining efficient computational problems. In this section, we studied several of the most relevant parameters and studied the general importance of various experimental considerations.

For measurements using the matching fluid, it was found that 18 symmetrically arranged projections are a reasonable upper limit. This limit indicates data redundancy when exceeded. This is because of the correlation expected between adjacent measurements and projections due to the diffusive nature of photon propagation in the associated projections. Furthermore, the optimal spatial sampling was found to be 0.1cm for mesh and detector densities when considering the perturbative analytical method used and current computational limits. Reducing the density leads to noticeable worsening of imaging performance, whereas increasing the density yields currently unmanageable computational problem sizes without achieving significant image improvements. Figure 4.15d and 4.15e further suggest that similar sampling of mesh and detector (or source) densities yields optimal imaging performance. Similar conclusions can also be derived from Figure 4.15f.

Due to the added symmetries in data collection in the absence of matching fluids, 15 projections yielded a balanced choice for the free-space cylindrical geometry. Figure 4.17b indicated that a small number of in-plane sources (three to five) suffice to yield optimal illumination and the optimal spread was found to be over a 120° arc. Correspondingly, as seen in Figure 4.17c, optimal detector placement is best over a 150° arc where even at fine 5° detector spacings ($\sim 0.9\text{mm}$ distance between detectors) significant information gain was obtained.

Generally, both the two geometrical approaches considered — one at free-space imaging and one when using matching fluids — yielded similar trends. However, the free-space geometry offers more flexibility in the arrangement of sources and detectors, and an increasing SVAT for increasing arc measurements, as shown in Figure 4.17d. This implies not only more user-friendly systems than slab geometries but better imaging performance as well. It is therefore the preferred implementation geometry for new generation FMT systems.

Singular-value analysis reveals bulk characteristics that can lead to generic optimal parameters. Specific problems may require more accurate optimization that goes beyond the capacity of the current analysis. In addition, while this optimization was performed for the CW domain, different illumination-detection domains will possibly yield different optimal parameters. This is particularly true for systems utilizing early photons in complete projection tomography, as the photon propagation characteristics and corresponding correlation and redundancy in adjacent data is markedly different from the ones studied herein [129, 154].

Overall, we have shown that 360° projection collection schemes offer significant ability to improve the information available for image reconstruction and offer to yield systems of superior imaging capacity than current state of the art implementations. Importantly, they also outline a computational bottleneck in improving FMT performance for small animal imaging. Using the findings of this SVA analysis, optimal image parameters have therefore

been found that optimize imaging performance within our current computational ability. This also allows us to predict that improved imaging performance is to be expected in the future with improvements in computational efficiency of the diffuse optical tomography problem.

4.4 Ex-vivo and In-vivo Studies

For small animal imaging, it has been shown that high spatial sampling (i.e. $< 0.5mm$) of the photon fields propagating through an animal offers image improvements over coarser sampling [148] and leads to submillimeter tomographic resolution [126]. To achieve such high spatial sampling, it is imperative to utilize CCD cameras that offer high-density arrays of parallel detectors. Implementations of fluorescence tomography based on CCD camera measurements were developed for small animal imaging, but in the slab geometry [126–128, 155]. These systems have demonstrated the ability to resolve protease and receptor up-regulation, chemotherapeutic responses, or fluorochrome accumulation in-vivo [127, 156, 157], but with compromised resolution along the axis perpendicular to the detector plane due to the limited projection angles employed.

In analogy to X-ray CT, measurements obtained over 360° illumination and detection geometries are fundamental for achieving optimal three-dimensional performance compared with parallel-plate (slab) geometries. Photon measurements in the 360° geometry have been so far performed with fiber-based systems, typically by bringing fibers into physical contact with tissues or through the use of matching fluids (see for example Figure 4.3). In this section we consider the combination of 360° projection geometries with direct CCD-camera-based detection for the development of a new generation of FMT systems that combine the advantages of high spatial photon sampling with those offered by complete projection measurements, as already presented in section 4.2. This approach can enable (i) experimental simplicity, since no matching fluids are utilized and no fibers are brought into contact with tissue, and (ii) high-quality data sets, due to the high spatial sampling of photon fields allowed at any projection. Ultimately, this approach could fully capitalize on the potential of diffuse fluorescence tomography methods and seamlessly integrate with other imaging modalities such as X-ray CT.

The results of this section were also presented at [158, 159] and published in [140].

4.4.1 Methods

The system shown in Figure 4.19 was developed, where the animal imaged is placed on a rotation stage so that it intersects a laser beam being scanned on its surface. The scanner

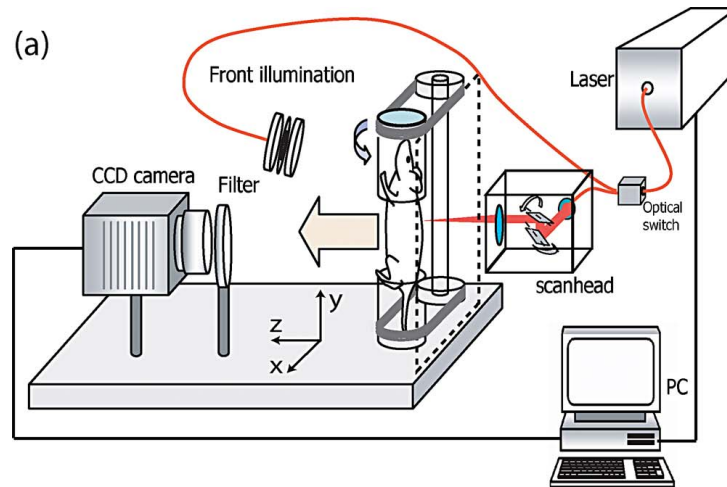


Figure 4.19: Schematic of the experimental setup utilizing non-contact illumination and detection. A photo-luminescent plate, indicated by the dotted line, can be inserted as shown to facilitate surface capturing.

employed a 748nm diode laser (B & W Tek, Newark, Delaware) coupled to a system of two galvanometer-controlled mirrors and a tele-centric scan lens (Nutfield Technology Inc., Windham, New Hampshire), which focused and scanned the laser beam onto the back surface of the animal imaged. The beam diameter at the focus plane was $300\mu\text{m}$, and the positional accuracy of the beam at the focus plane was better than $50\mu\text{m}$. The beam focus was maintained over 4mm of depth of field, as appropriate for irregular mouse shapes and some surface curvature present within the scanned field of view pursued here (i.e. 6mm horizontally across the mouse). The total power delivered to the object was approximately 20mW . A Princeton Instruments Inc. (Trenton, New Jersey) VersArray CCD camera with a 1024^2 pixel CCD array cooled to -70°C was placed on the opposite side of the animal to collect photon fields propagating through the animal in transillumination mode. Two three-cavity bandpass interference filters (Andover Corp., Salem, New Hampshire) were sequentially employed in front of the camera to capture photons at the excitation ($750 \pm 10\text{nm}$) and emission ($800 \pm 20\text{nm}$) wavelengths. Additional laser diodes and filters at different spectral bands have been added to this system but were not employed herein.

The custom-made animal chamber, shown in Figure 4.20, consisted of two rotating cylindrical chambers that housed the animal's extremities. Both chambers were rotated by a common shaft to achieve synchronous movement and avoid the application of torque on the animal. Rotation is facilitated by a stepper motor driven rotation stage (Model PR50PP, Newport Corp., Irvine, California) that can rotate the mouse with a resolution of 0.01° ($< 0.1^\circ$ absolute accuracy). The use of a vertical chamber is not a preferred implementation, but was directed by experimental hardware simplicity. Yet the vertical placement combined with the independent movement of the top and the bottom chambers and slow rotation at speeds of $< 5^\circ/\text{s}$ ensures that no skew or internal organ movement occurred during

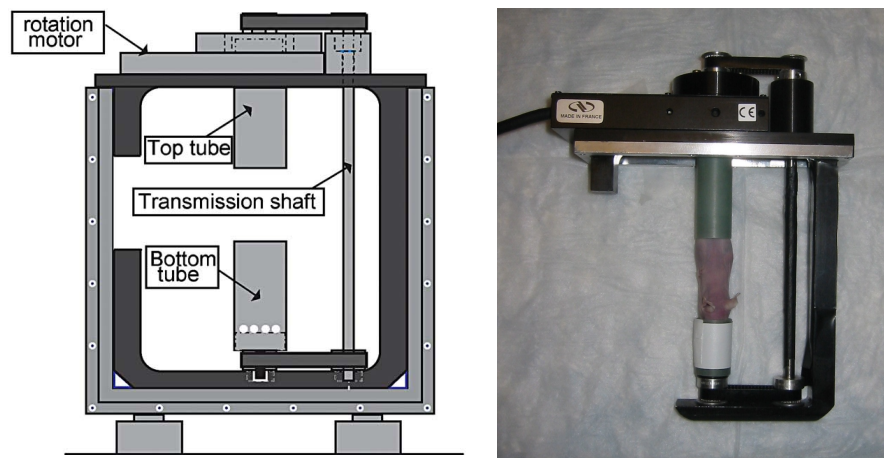


Figure 4.20: Schematic drawing and photograph (with inserted euthanized nude mouse) of the rotational device implementing 360° projection capacity.

experiments, which was important for facilitating these proof-of-concept experiments.

Diffuse fluorescence tomography is based on the use of physical models of photon propagation in tissues (see section 4.1.1). In this case, knowledge of the animal surface is required to separate photon propagation in air and tissue and accurately model photon propagation in the diffusive medium. For surface acquisitions, a $10\text{cm} \times 10\text{cm}$ photo-luminescent plate was placed between the animal and the laser source, with the laser beam switched off. This allowed visualization of the contours of the animal, as shown in Figure 4.21(a) for various representative projections. The axis of rotation was calculated along with the three-dimensional surface reconstruction using volume carving with 72 projections and the Visual Hull approximation to the real object [132]. Details on the surface extraction procedure are described in section 4.2 and [131]. A typical example of a three-dimensional surface reconstructed is shown in Figure 4.21(b). The accuracy of this method, experimentally measured on phantoms, was found to be of the order of $50\mu\text{m}$ at an 11cm field of view.

4.4.2 Experiments and Results

4.4.2.1 Ex-vivo

To demonstrate the ability of the method to three-dimensionally resolve fluorescent distributions, we implanted two plastic semi-translucent tubes filled with fluorescent dye in the torso of a euthanized nude mouse. Both tubes were 9mm long and 0.75mm in diameter. Tube 1 (T1, see Figure 4.22) was placed subcutaneously outside the ribcage on the right ventral side, and tube 2 (T2) was inserted in the esophagus parallel to T1. The tubes

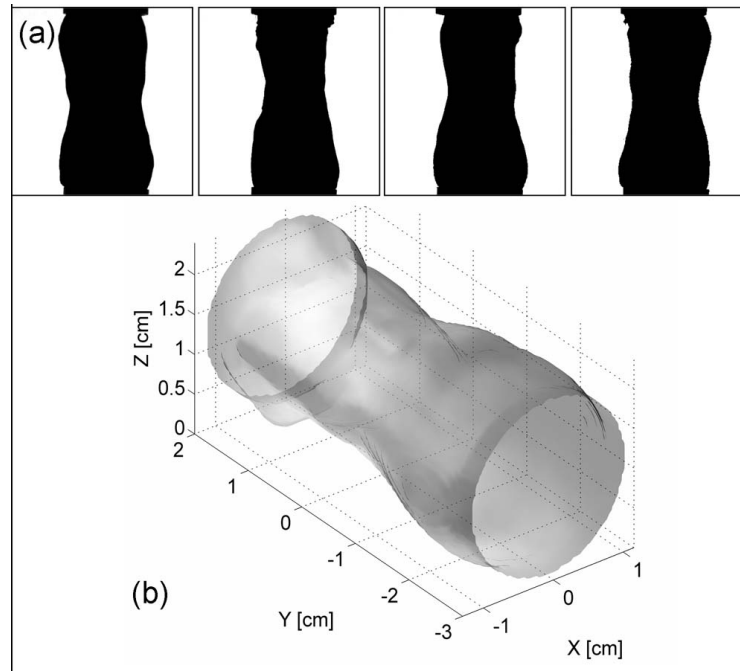


Figure 4.21: (a) Contours from various projections of a mouse against the photo-luminescent plate, (b) reconstructed three-dimensional surface.

contained 13 and $64 \times 10^{-12} \text{mol}$, respectively, of Alexa Fluor 750 (Invitrogen Corp., Carlsbad, California; absorption maximum 749nm , emission maximum 775nm), with a ratio of concentration $T2/T1 = 5$.

360° was performed utilizing 36 projections every 10° . For each projection the laser beam was scanned at an equidistant rectangular 12×3 pattern over a $14.5 \text{mm} \times 3.3 \text{mm}$ field of view. Thus for each projection 36 images were collected at each of the emission and excitation wavelengths. On each image we assumed a sampling of 11×12 virtual detectors over a $1.1 \text{cm} \times 1.3 \text{cm}$ field of view; each detector using herein a 4×4 CCD camera pixel binning. The complete measurement lasted 30min .

For image reconstruction, the volume of interest, measuring $2.4 \text{cm} \times 1.8 \text{cm} \times 2.3 \text{cm}$, was discretized to $21 \times 16 \times 22$ mesh points. This mesh is virtually rotated with the mouse around the axis of rotation. Using the calculated mouse surface, the mesh voxels can then be separated into the ones residing within or outside the mouse volume, the latter assumed as having no value after reconstruction. The sources and detectors were projected along the z axis (see Figure 4.19) to the surface of the mouse and the intersection points are calculated to find the geometrical coordinates of the virtual sources and detectors for the FMT problem.

The fluorescence measurements that are collected are divided by spatially corresponding measurements at the excitation wavelength and an analytical model based on a normalized

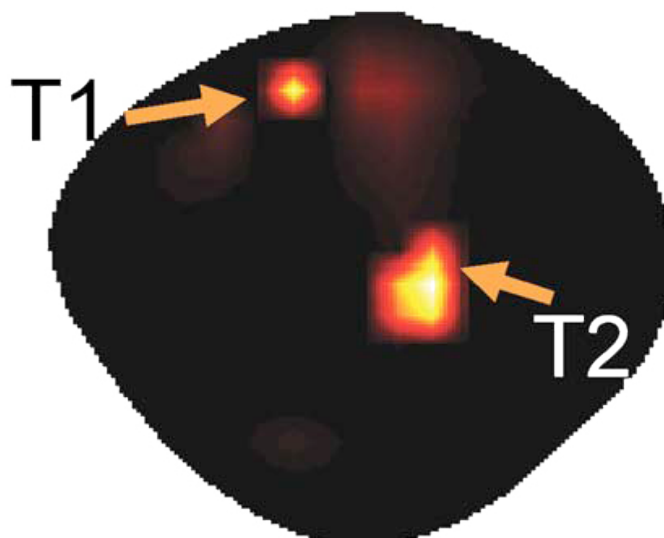


Figure 4.22: (a) Reconstructed FMT slice obtained from a euthanized nude mouse implanted with two fluorescent tubes, (b) corresponding X-ray CT slice, and (c) three-dimensional rendering of the tubes inside the animal surface. Arrows indicate the positions of the tubes.

Born solution of the diffusion equation [123] was employed to calculate the sensitivity functions of each voxel to each source–detector pair. Modeling of the boundary effects was based on the Kirchhoff approximation [128]. When written for the entire data set collected, this procedure results in a system of linear equations that is inverted for the unknown fluorescence concentrations in each voxel using the algebraic reconstruction technique (see section 3.3.1) after 50 iterations.

Following FMT imaging, X-ray micro CT imaging was performed on a X-SPECT system (Gamma Medica, Northridge, California) to anatomically confirm the location of the tubes. Figure 4.22 summarized the results most pertinent to the study. Figure 4.22(a) shows a reconstructed axial FMT slice passing through the tubes level. Figure 4.22(b) demonstrates a corresponding X-ray CT, where the tubes are indicated by arrows. Finally, figure 4.22(c) shows a three-dimensional rendering of the surface reconstruction and the underlying FMT rendering. We note that since the FMT and X-ray CT have been acquired on different systems, some shape and co-registration inaccuracies are present, but generally a good correspondence is observed between the results of the two modalities. Although the size of T2 is larger than that of T1, due to the noted drop in resolution as a function of depth [160], the sum of the reconstructed values in the T2 area is 3.9 times higher than the sum of the dye in the T1 area. This ratio of the reconstructed values is close to the original concentration ratio of $T2/T1 = 5$, which demonstrates the capability of the method for quantitative measurements. Such performance can be improved with spatially dependent

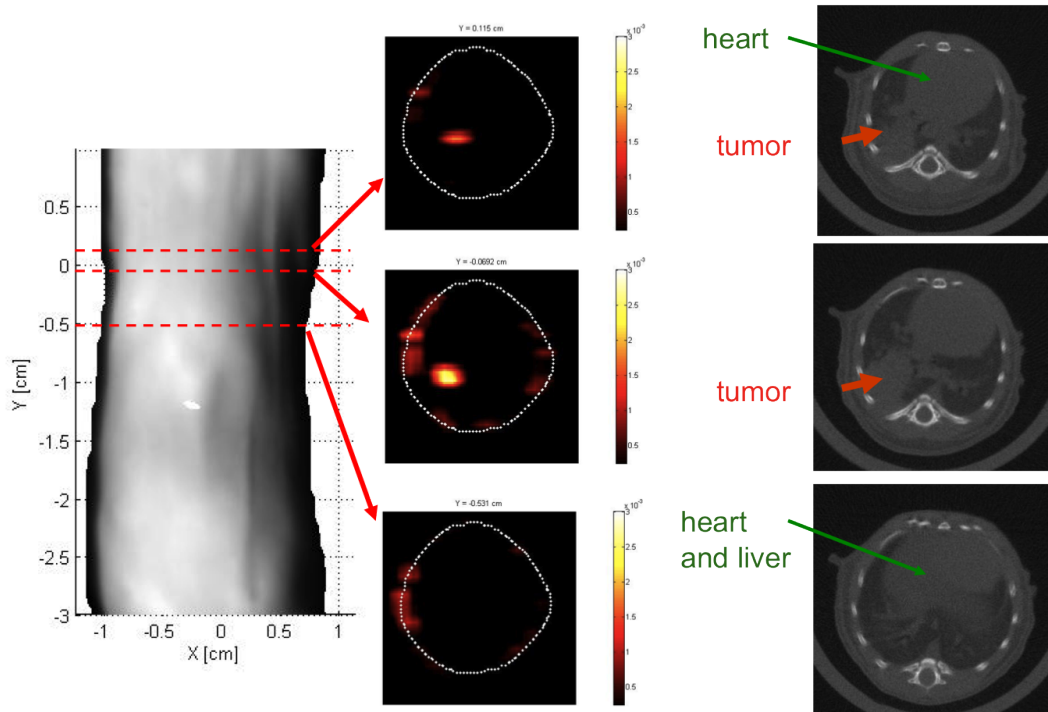


Figure 4.23: FMT and CT of a nude mouse with implanted lung tumor. *Left*: reconstructed mouse surface marked with FMT slice locations, *middle*: FMT slices at different heights, *right*: corresponding CT slices, tumor marked with red arrows.

regularization [160].

4.4.2.2 In-vivo

The same setup was used to perform in-vivo imaging of lung tumors in nude mice. 1×10^6 Lewis Lung Carcinoma (LLC) cells were administered intercostally into the right lung parenchyma of a nude mouse. Eight days after implantation, 2 nmol of Angiosense 750 (VisEn Medical, Bedford, Massachusetts) were injected via the tail vein. The mouse was imaged 36 hours later using 36 projections every 10° . For each projection the laser beam was scanned in a 7×3 pattern, while each image was sampled using 11×12 virtual detectors. The volume of interest was discretized into $24 \times 14 \times 22$ voxels using a 1 mm mesh resolution. The FMT reconstruction was generated using the same procedure as in the previous section. Following FMT, X-ray micro CT imaging was performed as well to confirm the FMT findings. Figure 4.23 shows the reconstructed mouse surface on the left as well as indicating the slice positions of the FMT reconstruction shown in the middle. The corresponding CT slices are shown on the right, the tumor is marked with red arrows. Again, some registration inaccuracies are present, but overall there is a good correspondence for the tumor in both modalities.

4.4.3 Discussion

We have demonstrated that free-space 360° tomography through entire animals is possible in the near infrared, both ex-vivo and in-vivo. This approach offers data that probes the animal volume more symmetrically than possible in slab geometry systems and offers high spatial sampling of photon fields as well as significant experimental simplicity compared with 360° fiber-based systems. This implementation can be further improved by the use of multiple cameras or systems of mirrors that allow concurrent viewing and sampling of photon fields over a wider angle of animal circumference per projection. However, even in the current implementation, imaging performance is limited by computational efficiency. Nevertheless, free-space 360° schemes as shown herein can offer data sets of maximum information content compared to other geometries or data-collection schemes and have the potential to bring out the best possible imaging performance for FMT as well as yield the next generation of small animal imaging systems.

4.5 Recent Developments

The results presented in this chapter were developed in the timeframe between 2005 and 2007. All the instrumentation and experimentation was performed at the Laboratory for Bio-optics and Molecular Imaging of Prof. Vasilis Ntziachristos at the CMIR, Massachusetts General Hospital, Harvard University in Boston, USA (Prof. Ntziachristos has moved to Technische Universität München in 2007). The software development and experimental evaluations were performed both at CMIR and from 2006 on at the chair I-16 of Prof. Nassir Navab at the Technische Universität München. Since that time, many developments have taken place.

While optical tomography is still a relatively young discipline, several groups are working in this field. As an example, parallel developments of a non-contact free-space FMT system very similar to the one presented in section 4.2 took place at FORTH in Heraklion Crete, Greece, see for example [161, 162]. The main differences here were in surface extraction (a filtered back-projection approach was used instead of volume carving) as well as in the design of the rotation stage.

Meanwhile, commercial implementations of the FMT imaging modality are also available for example by VisEn Medical (Bedford, Massachusetts). Their currently available products (FMT 1500 and FMT 2500 LX, as of October 2010) utilize free-space modeling without matching fluids by acquiring the mouse surface using photogrammetry, but do not employ full 360° projection tomography as presented in this chapter.

Advances have also been made on the theoretical side. Noise characteristics in the acquired data used by the normalized Born ratio have been largely ignored for the works in this chapter. It was shown in [163] that this noise can be incorporated into a stochastic model used in the forward problem, which is then inverted within a maximum likelihood framework based on fixed point iteration. Finite element modeling allows inclusion of prior-knowledge about the tissue being imaged. In the method presented in this chapter a major simplification was made in assuming that the tissue being imaged is homogeneous. This is not true in reality, but to overcome this deficiency the prior knowledge about tissue heterogeneity has to be acquired by a different imaging modality. One solution was presented in [164], where photo-acoustic imaging generated optical absorption maps which are included in the FMT forward problem via a finite element approach. Another solution is to use micro X-ray CT data (XCT) for anatomical priors. A hybrid system integrating XCT with FMT was recently developed [29], including the prior information using a finite element method and regularized LSQR inversion. The difficulty here is the automatic segmentation of the XCT [165] as well as modeling the optical parameters correctly from the segmented XCT data [166]. This hybrid FMT-XCT approach enabled for example the imaging of an Alzheimer mouse model [167] and lung inflammation [168]. To avoid biasing the solution by the prior information, data specific spatially varying regularization was introduced in [169].

Developments have of course also taken place in the development of fluorescent tracers. Intravascular probes have been shown to determine the vascular volume fraction [113], while combined MRI and fluorescent probes like CLIO-Cy5.5 allowed imaging of the myocardial macrophage infiltration [114]. In [170], biocompatible upconverting nanoparticles were employed to enable autofluorescence-free transillumination images of mice. The system presented in section 4.2 was used to image brain tumors in murine mouse models using a novel fluorescent protein [171] as well as an Alzheimer mouse model [167, 169]. Multispectral sources enable simultaneous visualization of several tracers, as demonstrated with the dual-wavelength approach to investigate breast cancer progression in [172].

A different approach to optical tomography is using time-resolved detection. Here, the laser source is synchronized with the detection cameras with an accuracy in the picoseconds range, allowing for example to detect the so-called *early* photons, that is the photons that transversed the imaged object largely without any scattering effects. This allows to use simple analytic inversion approaches as showcased in [129], but of course series expansion methods perform at least comparably if not better [173]. Early photon tomography has also successfully imaged protease activity in mice with lung cancer [174]. A favorable comparison of early photons with quasi-continuous-wave was performed in [175]

While FMT is a macroscopic imaging modality, mesoscopic optical imaging is also possible (mesoscopic is in between microscopic and macroscopic). The main difficulty here is that

the diffusion approximation of the FMT forward problem is not valid, as imaging is performed within a few lengths of the transport mean free path l_{tr} . One solution is to use Monte Carlo simulations based on the radiative transport equation (RTE, equation 4.1) to enable mesoscopic epifluorescence tomography [176]. Another solution is to employ the Fermi simplification to the Fokker–Planck solution of the RTE to enable in–vivo mesoscopic fluorescence tomography (MFT) as demonstrated in [177, 178]. In the case where mesoscopic ex–vivo samples can be cleared (made transparent), tomographic reconstruction of transmission images at several projections is called Optical Projection Tomography (OPT). Here, absorption can be reconstructed like in X–ray CT using analytical methods, for example with filtered back–projection (see section 2.3) implemented using CUDA for high throughput [179]. Fluorescent probes can be imaged simultaneously using Born–normalized fluorescence [180], demonstrated for example on an infarcted mouse hearts [181, 182].

Yet another different approach to optical imaging is a hybrid approach called photo–acoustic or optoacoustic imaging. Here ultrasound waves are generated by short laser pulses (due to transient thermoelastic expansion of light–absorbing structures), and then recorded by ultrasonic detectors placed around the sample, taking advantage of the high resolution of ultrasound which is unaffected by light diffusion. One of the systems performing multispectral optoacoustic tomography (MSOT) using finite element solvers was presented in [183–186], a review of MSOT can be found in [187]. Several improvements have been made since, like visualizing polarization contrast [188] or mesoscopic scale imaging using selective–plane illumination [189]. New algorithms have been developed to extract both absorption coefficient and photon density using sparse decompositions [190] or to iteratively correct for light attenuation [191]. Finally, physical models have been developed to also use the series expansion framework for example using LSQR for inversion [104], enabling video rate tomography of mouse kidney perfusion [192] and real–time visualization of cardiovascular dynamics in mice [193].

A very recent review of current optical imaging modalities across different photon penetration scales, including those mentioned in this chapter, is available in [194]. It confirms again the usefulness of series expansion techniques for any tomographic optical imaging modality.

Chapter 5

Application: Freehand SPECT

This chapter presents another application of the series expansion method explored in chapter 3 — Freehand SPECT. The SPECT functional imaging modality was already briefly introduced in section 1.3.2. The physical requirements of SPECT or SPECT/CT scanners necessitate specifically designed rooms with controlled temperatures and vibrations to house the bulky devices. Along with relatively long scanning times, this naturally limited the use of SPECT to pre-operative diagnostics and treatment planning. Unless one is willing to build an operating room around such a device (a costly and impractical undertaking), intra-operative use of SPECT requires a new approach. Freehand SPECT is such a new approach, employing tracked gamma detectors on a mobile system with low scanning times to enable localized, intra-operative 3D SPECT reconstructions. This chapter introduces the Freehand SPECT imaging modality and presents phantom studies as well as pre- and intra-operative patient studies to characterize its performance.

5.1 Freehand SPECT — A New Approach to Intra-operative 3D Nuclear Imaging

The improvements in PET/CT and SPECT/CT and their integration into the clinical routine have enabled the localization of small tumors and lymph nodes in several oncologic applications [195, 196]. The clinical impact of such precise localization has however been limited as the surgical excision of such structures is often impossible. The reason for this is twofold. On the one hand, the structures to be excised are small and there is no reliable method capable of localizing them precisely in the operating room (OR), that can be integrated easily into the surgical workflow. On the other hand, due to deformation of soft tissue during surgery the use of the pre-operative images as it is done in conventional navigated surgery is extremely hard and error prone [197].

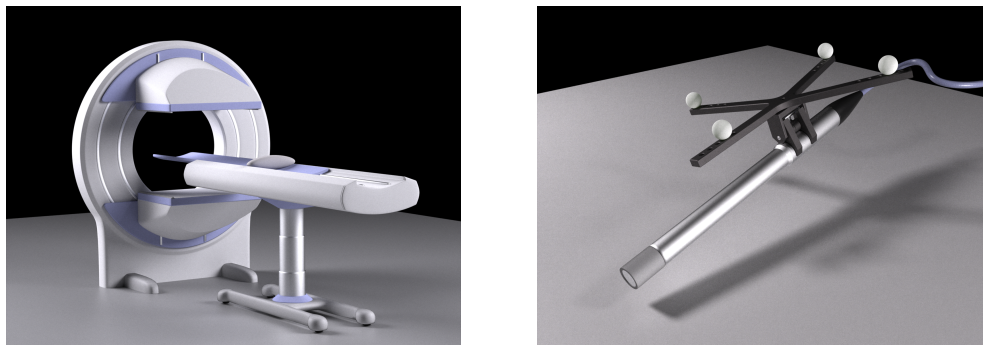


Figure 5.1: Schematic representations of a SPECT device (left) and a gamma probe (one-dimensional gamma detector) with a mounted tracking target (right). *Images courtesy of Alexandru Dului.*

The development of solutions for this specific problem is in perfect congruence with the strong trend in medicine towards quality assurance and patient tailored treatment. In order to exploit the advantages of state-of-the-art imaging technology, the use of intra-operative imaging has been proposed in neurosurgery and orthopedic surgery (for example [198] and [199] respectively). There, intra-operative 3D US, intra-operative MRI and X-ray C-arm based 3D imagers are transferring the precise diagnostics of US, MRI and CT into the OR with increasing spatial and temporal resolution and in full 3D. This is however not the case in nuclear imaging. Although the first 2D imagers have been made available commercially and there are increasingly reports of different applications (e.g. in laparoscopic sentinel lymph node biopsies, SLNBs, in prostate cancer [200], in SLNBs for difficult-to-find SLNs [201] or in radio-guided occult lesion localizations in breast cancer [202]), intra-operative nuclear imaging is only in its initial stages and has not made it into the clinical routine yet.

Intra-operative localization of labelled tumors, lymph nodes and metastases requires 3D imaging. The availability of depth information can play an important role in clinical procedures like sentinel lymph node biopsies in the breast, pelvis or neck, where improper localization may result in considerable morbidity and failure of the surgical procedure [203].

In this chapter, we present the technical background for our novel approach for intra-operative, 3D nuclear imaging called Freehand SPECT. In Freehand SPECT conventional hand-held 1D gamma probes (as used in state-of-the-art radio-guided surgery) are tracked with spatial positioning systems (as the ones used in navigated neurosurgery). Novel algorithms are employed to generate tomographic imaging data from sparse, limited-angle and irregularly sampled data acquired during a two to five minute ad-hoc freehand scan.

In typical full-body imaging modalities like SPECT, several detectors are mounted inside a moving gantry in a fixed, optimized geometry with full angular coverage (see Figure 5.1). In Freehand SPECT, only one detector (a hand-held 1D gamma probe, see Figure 5.1) is moved manually in a “freehand” scan over the localized object of interest (see Figure 5.2),

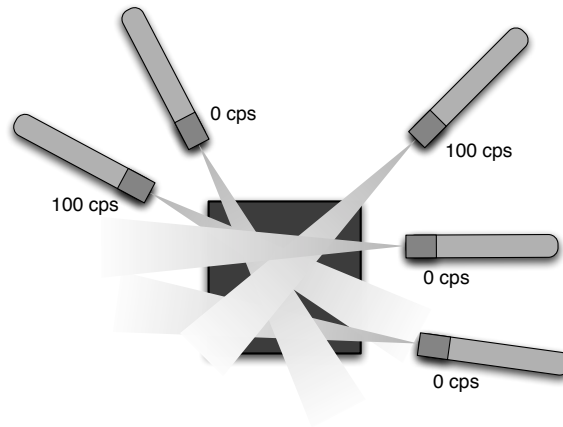


Figure 5.2: Illustration of freehand scan with 1D gamma detector (also called gamma probe).

resulting in a sparse, non-uniform and non-symmetric ad-hoc geometry with limited angular coverage. With a duration of two to five minutes, the freehand scan is also shorter than a typical SPECT scan, which can last between 15 to 60 minutes. Thus, while conventional SPECT systems record on the order of billions of gamma rays, Freehand SPECT records only on the order of a few hundred thousand events.

However, as an intra-operative imaging modality, it is sufficient for Freehand SPECT to only image a limited region of interest, and not the full body. Due to the localized nature of the scan, the detector is also typically closer to the actual sources of activity and thus has better sensitivity compared to the gantry-mounted detectors in conventional SPECT. To be useful in a clinical setting, Freehand SPECT has to provide an accuracy and resolution of around 5mm to 10mm , which is comparable to the SPECT resolution manufacturers quote for their modern full-body SPECT/CT scanners.

Since the hand-held gamma probe is already present in the OR for typical radio-guided surgeries, the additional overhead of a Freehand SPECT system, notably the tracking system and a computing workstation with a touchscreen for visualization and interaction, is minimal and cost-effective. Furthermore, thanks to the short scanning times of two to five minutes and fast reconstructions in around one minute, it only requires small changes in the workflow of a procedure and can be integrated smoothly.

5.2 Materials and Methods

5.2.1 Hardware Setup

The Freehand SPECT system used in this work was a prototype of the *CSS300* cart system (SurgicEye, Germany) attached to a *Gamma-Probe System* gamma detector (Crystal

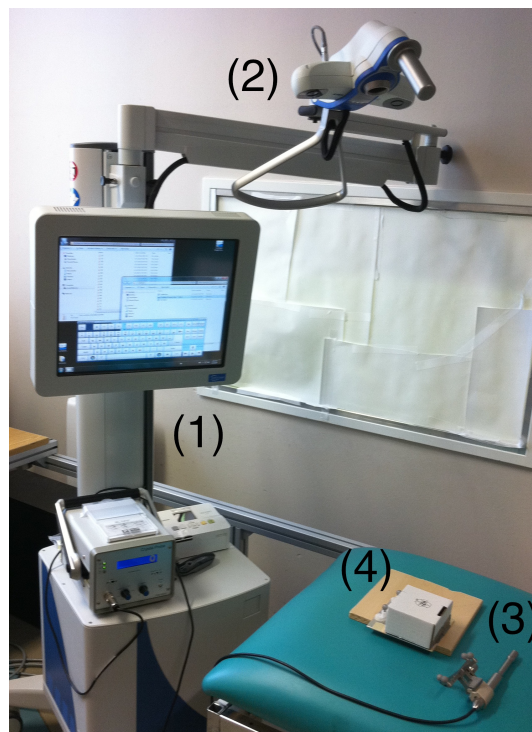


Figure 5.3: The Freehand SPECT hardware setup: (1) CSS300 cart system, (2) Tracking system, (3) Gamma detector, (4) Phantom.

Photonics, Germany). Spatial positioning was facilitated by an integrated *Polaris Vicra* infrared optical tracking system (Northern Digital, Canada) and reflective markers attached to the gamma detector, see Figure 5.3. A regular PC (Intel i7 920, 2.66GHz, 6GB RAM) integrated into the cart acquired and synchronized the data and provided augmented reality feedback during the scans as well as online reconstructions. The final reconstructions for the evaluation studies were performed on another PC (Intel i7 920, 3.33GHz, 12GB RAM) using custom software in C++.

5.2.2 Reconstruction Pipeline

Reconstructions for Freehand SPECT are performed using the series expansion method, see chapter 3 for an overview. For each measurement session, a reconstruction pipeline is executed to obtain the reconstructed image, the steps are illustrated in Figure 5.4 and described in more detail in the following.

First, a rectangular volume of interest $Y \subset \mathbb{R}^3$ is selected by pointing a tracked instrument to defined landmarks. This volume is discretized into n isotropic voxels $X = \{x_i : i = 1, \dots, n\} \subset Y$. Here, each $x_i \in \mathbb{R}^3$ denotes the center of the corresponding voxel, $i = 1, \dots, n$.

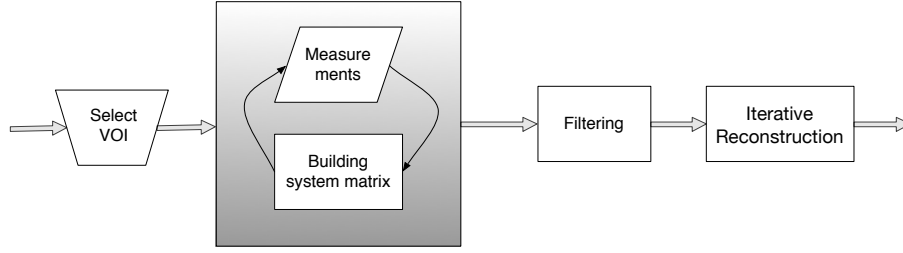


Figure 5.4: The reconstruction pipeline for Freehand SPECT.

The input are m measurements $M = \{(b_j, p_j, o_j) : b_j \in \mathbb{R}, o_j, p_j \in \mathbb{R}^3, j = 1, \dots, m\}$, where b_j denotes the count rate measured by the one-dimensional gamma detector and p_j, o_j denote the synchronized position and orientation of the gamma detector as determined by the tracking system. The gamma detector used in this work is rotationally symmetric in the z -axis (see Figure 5.3), so the tracking data is effectively only five-dimensional.

A system matrix $A = (a_{ji}) \in \mathbb{R}^{m \times n}$ is built successively, where each row corresponds to one measurement $(b_j, o_j, p_j) \in M$ and each column corresponds to one voxel $x_i \in X$. The entries of the system matrix A are computed using a custom physical model of the detection process, $a_{ji} = \text{model}(p_j, o_j, x_i)$ for $i = 1, \dots, n$ and $j = 1, \dots, m$. The model employed here is defined as follows:

$$\text{model}(p_j, o_j, x_i) = \begin{cases} \frac{\cos(a)}{2} \left(1 - \left(\frac{r_{\text{det}}^2}{\|p_j - x_i\|_2^2} \right)^{-\frac{1}{2}} \right) c_{\text{att}} & a \leq a_{\text{max}} \\ 0 & a > a_{\text{max}}, \end{cases} \quad (5.1)$$

where a denotes the angle between $-o_j$ and $p_j - x_i$, a_{max} denotes the maximum angle of the field of view of the collimator of the gamma detector, r_{det} is the radius of the detector element inside the gamma probe and c_{att} is the attenuation factor of the medium, modeled as a constant [204].

The model parameters were set according to the specifications of the employed gamma probe (Crystal Photonics, Germany), $a_{\text{max}} = 60^\circ$ and $r_{\text{det}} = 3\text{mm}$ (shielding 3.15mm) with the constant attenuation coefficient set as $c_{\text{att}} = 1$ to model air.

Let $x : X \rightarrow \mathbb{R}$ denote the unknown activity to be reconstructed and $b = (b_j) \in \mathbb{R}^m$ the vector of measured activities, then the resulting linear system can be written as

$$Ax = b. \quad (5.2)$$

This system is then filtered and run through an iterative reconstruction algorithm.

Filtering is performed in two steps. First, all rows j of the system (5.2) where $\sum_{i=1}^n a_{ji} \leq t_r$ are discarded as well as all columns i with $\sum_{j=1}^m a_{ji} \leq t_c$ with $t_r, t_c \geq 0$. This ensures that

there are no zero rows or columns in A . Since the acquisition is performed freehand, both situations frequently occur: zero rows correspond to measurements (b_j, p_j, o_j) that did not “touch” the region of interest X according to $\text{model}(p_j, o_j, x_i)$ for all $i = 1, \dots, n$, whereas zero columns correspond to voxels x_i that have not been scanned at all, i.e. typically voxels outside the object of interest. Furthermore, choosing $t_r, t_c > 0$ allows to discard measurements or voxels with very low relevance or confidence [205]. The second filtering step removes all voxels x_i that intersect with the detector during the scan, meaning those voxels are not located inside the object of interest but in the air, and can thus be discarded for reconstruction. This filtering is performed by geometric intersection of the region of interest X with the detector at (p_j, o_j) modeled as a cylinder ($j = 1, \dots, m$).

Let I_f denote the set of indices of voxels x_i that are not filtered out, and J_f the indices of the measurements b_j that are not filtered out. The filtered versions of A , x and b , where only the columns I_f and rows J_f are kept will be called A , x and b again for notational simplicity, along with their respective sizes n, m . The approximate solution x of the filtered system equation (5.2) is calculated using one of two iterative schemes described in the following. The resulting (unfiltered) reconstruction x is then set as

$$x = (x_i)_{i=1, \dots, n} = \begin{cases} x_i & i \in I_f \\ 0 & i \notin I_f. \end{cases} \quad (5.3)$$

One of the iterative schemes is the the standard maximum likelihood expectation maximization (MLEM, see section 3.4), which is very popular in emission tomography and used in variants in modern SPECT devices (for example with ordered subsets, OSEM). The MLEM iteration step for Freehand SPECT is defined as

$$\begin{aligned} x^0 &= (1, \dots, 1)^t \\ x_i^{k+1} &= \frac{x_i^k}{\sum_{p=1}^m a_{pi}} \sum_{j=1}^m \frac{b_j}{\sum_{l=1}^n a_{jl} x_l^k} a_{ji} \quad \forall i = 1, \dots, n, \end{aligned} \quad (5.4)$$

where $k = 1, \dots, \hat{k}$, and \hat{k} denotes the fixed number of iterations.

The other scheme is the Algebraic Reconstruction Technique (ART, see section 3.3.1), employed as a variant using randomized projection access order and a relaxation factor $\lambda > 0$,

$$\begin{aligned}
 x^0 &= (0, \dots, 0)^t & (5.5) \\
 \text{for } k &= 1, \dots, \hat{k} \\
 \hat{x}^0 &= x^{k-1} \\
 \text{for } l &= 1, \dots, m \\
 &\text{select } j \in \{1, \dots, m\} \text{ randomly} \\
 \hat{x}^l &= \hat{x}^{l-1} + \lambda \frac{b_j - \langle \hat{x}^{l-1}, a_j \rangle}{\|a_j\|_2^2} \\
 x^k &= \hat{x}^m
 \end{aligned}$$

where \hat{k} denotes the number of iterations and a_j denotes the j -th row of A . \hat{x}^l is forced to be positive in each iteration, any negative entry is set to 0. The probability for choosing projection j is set to be proportional to $\|a_j\|_2^2$. The strategy of choosing the projection access order in ART is decisive for reconstruction performance, see for example [70]. The selected randomization scheme is one of the potential strategies which can guarantee exponential convergence in certain cases [73], but not in general [74]. Lacking a fixed acquisition geometry, this seems to be one of the best available projection access schemes. Finally, the relaxation parameter λ also plays a crucial role especially for inconsistent systems as in our case, where a variable scheme with $\lambda \rightarrow 0$ as $\hat{k} \rightarrow \infty$ has been shown to be optimal [69]. For simplicity we settled on a constant $\lambda = 0.1$, a common choice justified for example in [206].

As each acquisition has a random geometry due to manual scanning of the detector, the system matrix A cannot be pre-computed as is common for conventional SPECT and other modalities with a fixed detector geometry in an imaging gantry. Thus the system matrix is computed on the fly during the acquisition process, inversion is performed only at the end. To ensure timely reconstructions the entire reconstruction pipeline was implemented as a library in C++ (NanuLib, see section 5.6 for more details), using the Eigen linear algebra library [207] for automatic vectorization and OpenMP for parallelization.

5.2.3 Acquisition Guidance

As each acquisition is performed freehand by the operator, it is entirely up to the operator to ensure that the volume of interest is adequately covered in terms of positions and angles by moving the detector around. While a good coverage as in tomographic modalities utilizing an imaging gantry can never be achieved, certain steps can be taken to ensure enough coverage for satisfying reconstruction quality. In this work we employed a two-step approach:

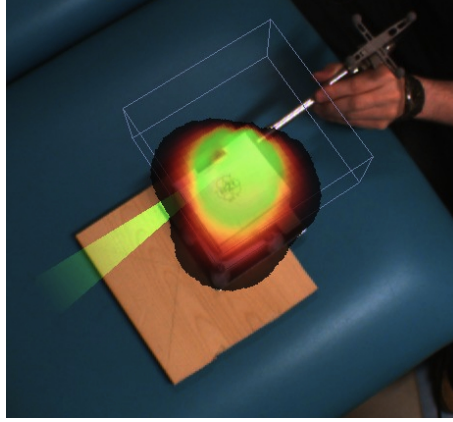


Figure 5.5: Screenshot of the augmented reality view during an acquisition. Note the rendered quality indicator volume overlaid over the picture.

1. Definition of a scanning scheme before the acquisition.
2. Online guidance display during the acquisition.

Generally the geometry of the object to be scanned is known in advance, as well as a guess as to a broad region where the activity is supposed to be. With that knowledge a scanning scheme is defined as a first step before the acquisition, one that is both practically realizable as well as ensuring the best coverage.

The second step is an on-screen, online guidance of the operator while he is performing the measurements. In an augmented reality view, the scene is shown with an overlay of the volume of interest and a visualization of how much attention each of the voxels $x_i \in X$ in the volume has already received by the measurements. To that effect, the column of the current system matrix A (which is built up row by row during the measurements) corresponding to x_i is summed up,

$$q_i = \sum_{j=1}^m a_{ji}, \quad (5.6)$$

and the resulting quality indicators q_i , $i = 1, \dots, n$, are rendered onto the augmented reality view screen, see Figure 5.5. As the later reconstruction process is using the same system matrix entries as a coupling factor of the voxel activity to the measurements, we found this to be an excellent indication of the current scan coverage, see section 5.4 or [208].

Other potential strategies. Other strategies of acquisition guidance have been studied over the course of this work as well. The two approaches outlined in the following seem promising, but so far we have not been able to provide a feasible implementation, mainly due to computational limitations.

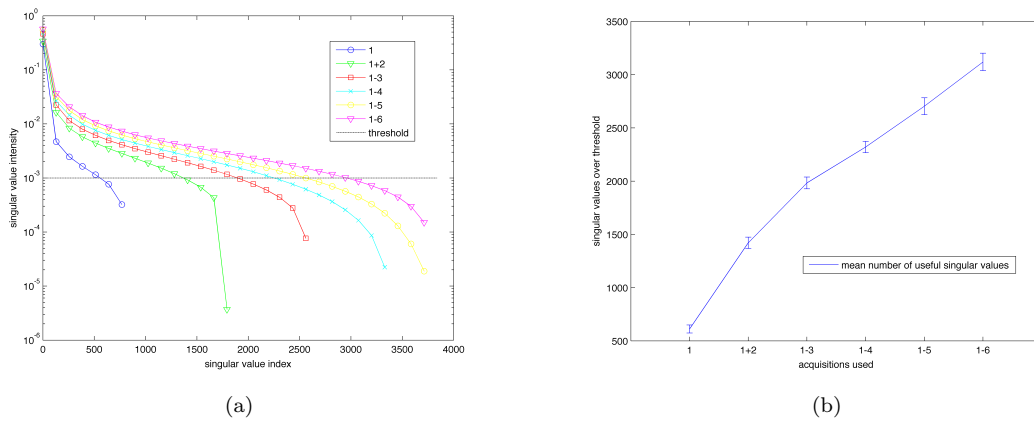


Figure 5.6: Singular value analysis performed in a phantom experiment with Freehand SPECT. Six general angular directions were scanned subsequently (labelled 1 to 6), (a) shows the singular value spectrum of the system matrix A computed using data from direction 1, 1 and 2 and so on up to 1–6. (b) shows the singular values above threshold (SVAT) as a function of the directions scanned, averaged over six scans.

The first strategy picks up the idea of section 4.3 and attempts to analyze the current acquisition geometry via singular value analysis of the current system matrix on-the-fly. The general validity of this approach for the Freehand SPECT imaging modality has been demonstrated in [209] in a phantom study. Let $A = USV^t$ be the singular value decomposition of A . As in other discrete ill-posed problems, the singular value spectrum $S = (\sigma_i)$ of the system matrix A evinces the typical shape, see Figure 5.6a. Consider the system equation $Ax = b$ using the SVD as

$$V^t x = S \cdot U^t b,$$

then the singular values S specify how the detection-space modes of A are coupled to the image-space modes of A . Selecting a noise threshold t_σ and counting the singular values above the threshold $\sigma_i > t_\sigma$ gives a measure of useful information contained in the current acquisition geometry. In the phantom study of [209] adding measurements from additional general angular directions showed clear improvement in the number of singular values above the threshold (SVAT), see Figure 5.6b.

The strategy for acquisition guidance is to analyze the current system matrix A during the acquisition procedure using SVD, and then to simulate adding a set of projections from different potential angles, calculating the SVAT for each set using an incremental SVD update. The set of projections with the highest SVAT would then be displayed in an augmented reality view as guidance where to scan next.

Unfortunately computing the SVD of big matrices like A , even incrementally, is quite computationally intensive, even when using massively parallel computing like CUDA on the

GPU [210, 211]. Thus this guidance strategy had to be abandoned at that time. We believe however that this strategy may become viable within a year for several reasons. The second version of our reconstruction library (see section 5.6) will allow a multi-resolution voxel grid, so the singular value analysis can be performed on a coarser grid than the actual reconstruction. Furthermore, the lookup-table forward model (see section 5.6) will allow much faster simulation of additional projection angle sets when computing the incremental SVDs. Last but not least, tremendous advances have been made (as usual) in the last two years in terms of available computing power, with current desktop processors providing up to 12 logical cores (for example the Intel i7 980X) along with graphics cards now providing up to 512 computing cores capable of double precision floating point operations (for example NVidia Geforce GTX580), that can be leveraged simultaneously and seamlessly using the new OpenCL heterogeneous computing standard [212].

The second strategy idea for acquisition guidance is to provide a live, real-time reconstruction during the acquisition process. The operator thus would be able to directly see the reconstruction develop and decide himself which areas need more attention for scanning until a satisfactory result is achieved. This however also poses the danger of introducing operator-based bias into the reconstructions, so to assure comparable reconstruction quality levels this approach will most likely have to be combined with other guidance measures or some quality indicator.

Again though, we have not been able to provide an actual working implementation of this approach yet due to computational limits. We have been working on two implementations of this approach so far. The first employs massively parallel computing on the GPU using CUDA, implemented by Alexandru Dului [211, 213]. The entire reconstruction pipeline has been moved onto the graphics processor to minimize costly bus transfers, however this comes at the cost of not being able to store the entire system matrix $A = (a_{ji})$ in local GPU memory. Thus when inverting the system $Ax = b$, all values a_{ji} had to be computed on-the-fly. Realistic parameters of 64^3 voxel discretization and ~ 3000 simulated measurements using 20 iterations of MLEM for inversion yielded computation times of 17s on a NVidia GTX260, while reducing the discretization to a 32^3 grid the process only took 2s as shown in [211].

The second implementation attempts to leverage the vectorization units and parallel processing units on modern multi-core CPUs like the Intel Core i7 series, see section 5.6 for more details on the reconstruction library called NanuLib. Reconstructions with parameters typical for SLN mapping procedures in breast cancer (see section 5.5) that used to take several minutes to reconstruct, now reliably reconstruct in under one minute with the current version of the NanuLib. This version of the NanuLib can also be found in the commercially available *declipseSPECT* cart system from SurgicEye (Munich, Germany).

A combination of both implementations using the OpenCL heterogeneous computing standard [212], improvements in the second version of the reconstruction library (see section 5.6) along with the above-mentioned performance increases in desktop computing hardware is expected to yield near real-time reconstruction capabilities in the coming year.

5.3 Phantom Studies

In a series of controlled phantom experiments the accuracy and the performance characteristics of Freehand SPECT as an imaging modality were studied and evaluated. The results of these studies are presented in this section, they have also been submitted as part of an article to the IEEE Transactions on Medical Imaging journal on September 17th, 2010, the paper is currently under review (as of October 2010).

5.3.1 Phantom Design

A common base was used for the phantoms studied in this section. A rectangular metal plate with several drilled holes served as a base for two *Micro Hollow Spheres (9.86)* (van Gahlen, Netherlands), which could be screwed into the plate in several different configurations. The spheres have an outer diameter of 9.86mm and a volume of $250\mu\text{l}$, which can be filled with a radioactive solution via the bottom. The centers of the spheres are located at a height of 24mm above the plate. There is no attenuating medium around the spheres. Additionally a target with three infrared reflective balls (SurgicEye, Germany) was mounted on the plate in the top left corner to facilitate optical tracking. Finally, a cardboard box was attached to the plate to cover the spheres in order to avoid bias in the scan, and to provide a guide for performing the proposed scanning scheme in Figure 5.7.

We tested three diagonal configurations of the spheres, C1 to C3, see table 5.1. Figure 5.8a shows a picture of phantom configuration C3 with the cardboard box open, and Figure 5.8b shows a CT of phantom configuration C1 acquired using a *Biograph 64* system (Siemens Healthcare, Germany).

Let B1 denote the sphere to the right hand side and B2 the one on the left hand side, see Figure 5.7 or 5.9b for an illustration.

For *Series 1* of the experiments, both spheres were filled with a solution of Tc-99m-pertechnetat with a measured activity of 100kBq in both B1 and B2. 10 scans were performed for each phantom configuration C1 to C3.

Table 5.1: Phantom configurations with distances between centers of spheres B1 and B2 and separation at center height of B1 and B2.

| Phantom | distance of sphere centers | sphere separation |
|---------|----------------------------|-------------------|
| C1 | 14.6mm | 3.7mm |
| C2 | 19.2mm | 9.4mm |
| C3 | 22.6mm | 12.8mm |

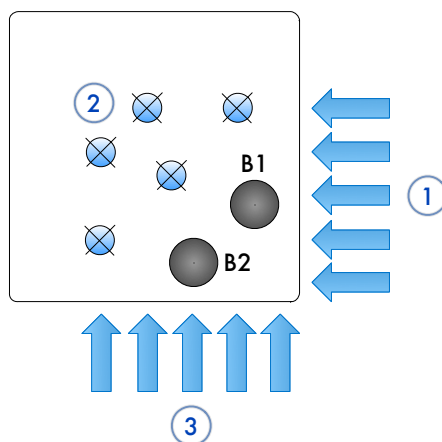


Figure 5.7: Top view of scanning scheme for the phantom (rectangle with two radioactive balls, B1 and B2), measurement positions from directions 1 (from right), 2 (orthogonally into the phantom) and 3 (from bottom).

For *Series 2* of the experiments, both spheres were again filled with a solution of Tc-99m-pertechnetat, however the measured activity in B1 was $100kBq$ and the activity in B2 was $990kBq$. 10 scans were performed for each phantom configuration C1 to C3.

5.3.2 Scanning Scheme

The scanning scheme was defined in advance. As the activity was known to be towards the lower right corner of a rectangular box, it was chosen accordingly. To keep the scans realistic, we selected only three planes of scan directions (similar to what is possible for example in breast scans), two from the sides and one from the top of the phantom, see Figure 5.7 for an illustration. Each plane is set to receive a certain number of measurements (dependent on the target scan duration), and the operator is asked to adhere to that scheme. The scheme however is not enforced.

5.3.3 Acquisition and Reconstruction

The region of interest Y was discretized as a $60 \times 60 \times 60$ volume with an isotropic voxel size of $1.25mm$, containing the entire cardboard box enclosing the phantom. Each phantom

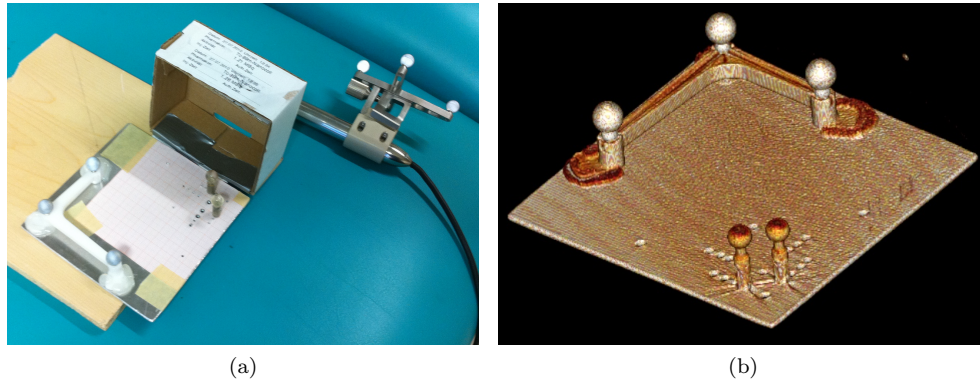


Figure 5.8: (a) photo of phantom configuration C3 with open cardboard cover. (b) rendering of CT of phantom configuration C1.

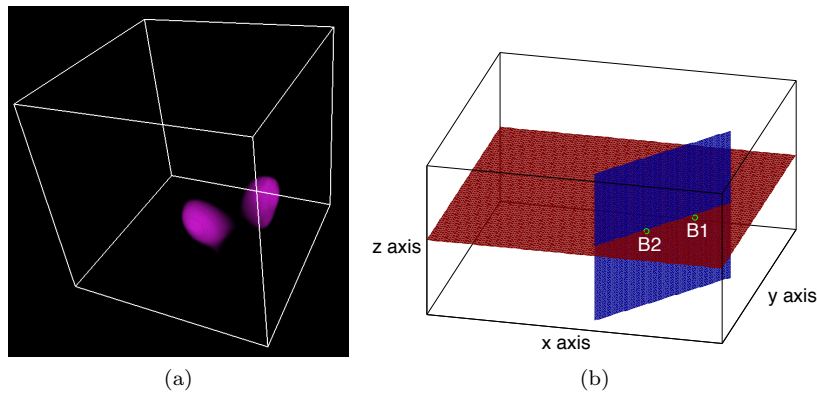


Figure 5.9: (a) 3D rendering of sample Freehand SPECT reconstruction for phantom C1. (b) Slice locations in Freehand SPECT volume: in red the horizontal slice S from Figure 5.10 used for the evaluations, in blue the slice T along the z axis from Figure 5.11.

configuration in both series was scanned 10 times by the same operator with the scan scheme outlined in Figure 5.7, where the three planes to be scanned were supposed to be scanned using approximately 1000 measurements each. The scan duration ranged from $2.35min$ to $2.44min$ (average $2.37min$) and each acquisition contained 3005 to 3097 measurements (average 3028) with a sampling rate of $20Hz$.

The acquisition was guided by the real-time visualization of q_i for each voxel $x_i \in X$, see equation (5.6) and Figure 5.5. For all acquisitions the mean quality of each scan $Q = \frac{1}{n} \sum_{i=1}^n q_i$ ranged from 5.94 to 6.63 (average 6.29). No decay correction was applied, as the scans were performed close enough in time.

The average size of the system matrix A was $4.99GB$, with the filtering stage removing 30.3% of that data on average. In detail, the first filtering step with $t_r = t_c = 0.0001$ removed on average 1.50 rows and 56.13 columns of A , while the second filtering step removed 65307 voxels in Y on average, modeling the gamma detector as a cylinder of $15mm$ diameter according to its physical dimensions. For MLEM, the number of iterations used was $\hat{k} = 20$,

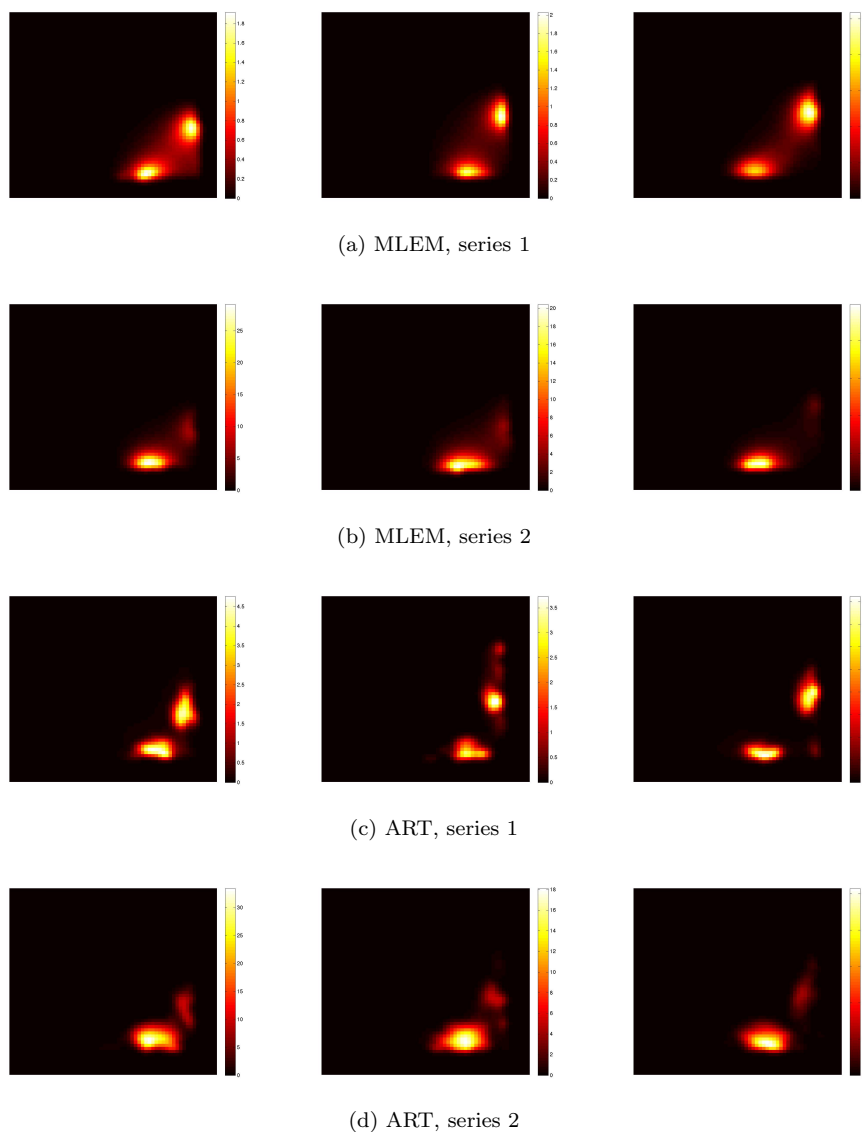


Figure 5.10: Image slice S of the Freehand SPECT reconstruction (red slice in Figure 5.9b) of example data sets using MLEM and ART, configurations from left to right: C1, C2 and C3. *Series 1*: B1 and B2 both containing a 100kBq Tc-99m solution. *Series 2*: B1 containing a 100kBq and B2 a 990kBq solution of Tc-99m.

for ART we set $\hat{k} = 20$. The mean time consumed to perform the entire reconstruction pipeline using MLEM was 46.66 seconds and 78.95 seconds for ART on a 3.36GHz Intel Core i7-920 with 12GB RAM.

The resulting reconstruction x was then passed through a standard 3D Gaussian filter with $\sigma = 1.25mm$. An example reconstruction is shown as a 3D rendering in Figure 5.9a. Example image slices S of the 3D reconstruction from one of the data sets each for phantom C1 to C3 for both series 1 and 2 are shown in Figure 5.10 using MLEM and ART, the corresponding image slice T is shown in Figure 5.11. The image slice locations of S and T are illustrated in Figure 5.9b.

5.3.4 Evaluation

First, the CT volumes of the phantom configurations C1 to C3 were registered to the Freehand SPECT coordinate system using point-based registration of the tracking target mounted on the phantom plate (see Figs. 5.8a and 5.8b). The metal mounting posts of the reflective spheres were automatically segmented in the CT and registered to the known, fixed geometry of the tracking target. Finally, the known transformations from the tracking target calibration and the volume of interest definition were applied to compute the final transformation from CT coordinates to Freehand SPECT coordinates.

All of the following evaluations were applied to the same 2D slice S of the reconstructed Freehand SPECT volume, as the centers of both spheres B1 and B2 were at the same height (see the red slice in Figure 5.9b). The location of slice S was selected via the CT by segmenting using fixed thresholds and region growing, and then calculating the centroids of B1 and B2.

In the Freehand SPECT slice S , the spheres B1 and B2 were segmented by thresholding. For 7 and 6 data sets of phantom C1 and C2 in series 2 using MLEM the two spheres were not segmentable, respectively, as B2 with ten times the activity of B1 overshadowed B1 with no drop in reconstructed intensity in between. All other data sets could be segmented properly. The centroids of B1 and B2 were calculated on the segmented slice S , and region growing determined the area of B1 and B2 in pixels as well as the minimum, maximum and mean intensity values of the pixels in those areas. The maximum intensity ratios of B2 and B1 were calculated from these values. Profiles c_S were plotted through the centroids of B1 and B2 of slice S in that order, and the relative drop in intensity values between B1 and B2 was calculated as $\frac{mp(c_S) - v(c_S)}{mp(c_S)}$, where $v(c_S)$ is the valley intensity between B1 and B2 for profile c_S and $mp(c_S)$ is the minimum of the peak intensities of B1 and B2 for profile c_S . Furthermore the profile c_S was fitted using a sum of two Gaussians with means μ_1, μ_2 and standard deviations σ_1, σ_2 . The distance $d(B1, B2)$ was then calculated as $d(B1, B2) = |\mu_1 - \mu_2|$ and the full width at half maximum (FWHM) of B1 and B2 as $FWHM(Bi) = 2\sqrt{2 \ln 2} \sigma_i$. To sum the reconstructed events in slice S at the real locations of B1 and B2, all pixels in a 9.86mm disc centered around the registered CT positions of B1 and B2 were summed up.

Finally, another slice T of the reconstructed 3D Freehand SPECT volume was extracted orthogonal to slice S through the centroids of B1 and B2, see the blue slice in Figure 5.9b. All the evaluations were performed using Matlab.

| intensity drop | C1 average | C2 average | C3 average |
|----------------|------------------|------------------|------------------|
| series 1 MLEM | 44.1% \pm 9.9 | 32.3% \pm 12.6 | 78.3% \pm 4.7 |
| series 2 MLEM | 5.8% \pm 1.0 | 7.3% \pm 9.7 | 12.9% \pm 5.1 |
| series 1 ART | 92.1% \pm 6.1 | 78.8% \pm 22.4 | 95.3% \pm 4.8 |
| series 2 ART | 45.1% \pm 22.4 | 51.6% \pm 26.5 | 83.8% \pm 18.3 |

Table 5.2: Relative drop in intensities between B1 and B2, measured from Freehand SPECT slice S (averaged over 10 data sets for each configuration in series 1 for both MLEM and ART as well as series 2 for ART, over 3, 4, 10 data sets for C1, C2, C3 in series 2 for MLEM).

5.3.5 Results

Freehand SPECT reconstructions were performed both with MLEM and ART for all 60 data sets, with 10 data sets each for phantom C1, C2 and C3 in series 1 (100kBq of Tc-99m solution in both B1 and B2) as well as in series 2 (100kBq of Tc-99m solution in B1 and 990kBq in B2). A 3D rendering of the reconstruction using MLEM of an example data set of phantom C1, series 1 is shown in Figure 5.9a. The reconstructed image slices S and T as illustrated in Figure 5.9b are shown for phantoms C1, C2 and C3 in both series using MLEM and ART in Figure 5.10 and 5.11 respectively. MLEM is producing more visually pleasing reconstructions, while ART reconstructs the spheres more sharply, however also showing more artifacts, especially in slice T .

Example profiles c_S plotted through the centroids of B1 and B2 of slice S are shown in Figure 5.12 for all the phantoms and series for both MLEM and ART. Again ART evinces a more clear separation of B1 and B2, especially for series 2, which is also confirmed by the average relative drop in intensities between B1 and B2 as listed in Table 5.2. Configuration C3 with the widest separation of the spheres (12.8mm) is showing a higher relative intensity drop than the two close configurations C1 and C2 with only 3.7mm and 9.4mm separation, respectively. In series 2 using MLEM, the peak in the profile c_S corresponding to B1 is barely noticeable especially for phantom C1 and C2, showing an average relative drop in intensity of only 5.8% and 7.3%, respectively. To note, phantom C1 and C2 in series 2 using MLEM are also the phantoms where only 3 and 4 out of the 10 data sets each allowed segmentation of B1 and B2, respectively, as in the remaining 7 and 6 data sets there was no peak for B1 in the profiles c_S , respectively. ART with its tendency to more sharply delineate the spheres produced segmentable reconstructions for all data sets.

The absolute localization error of B1 and B2 in slice S compared to CT is shown in Figure 5.13 for MLEM and in Figure 5.14 for ART. MLEM and ART both yielded similar results, with more variation for ART. In x axis direction, the error ranged between 0.76mm to 3.21mm on average for both spheres B1 and B2. In y axis direction, B1 in series 1 showed

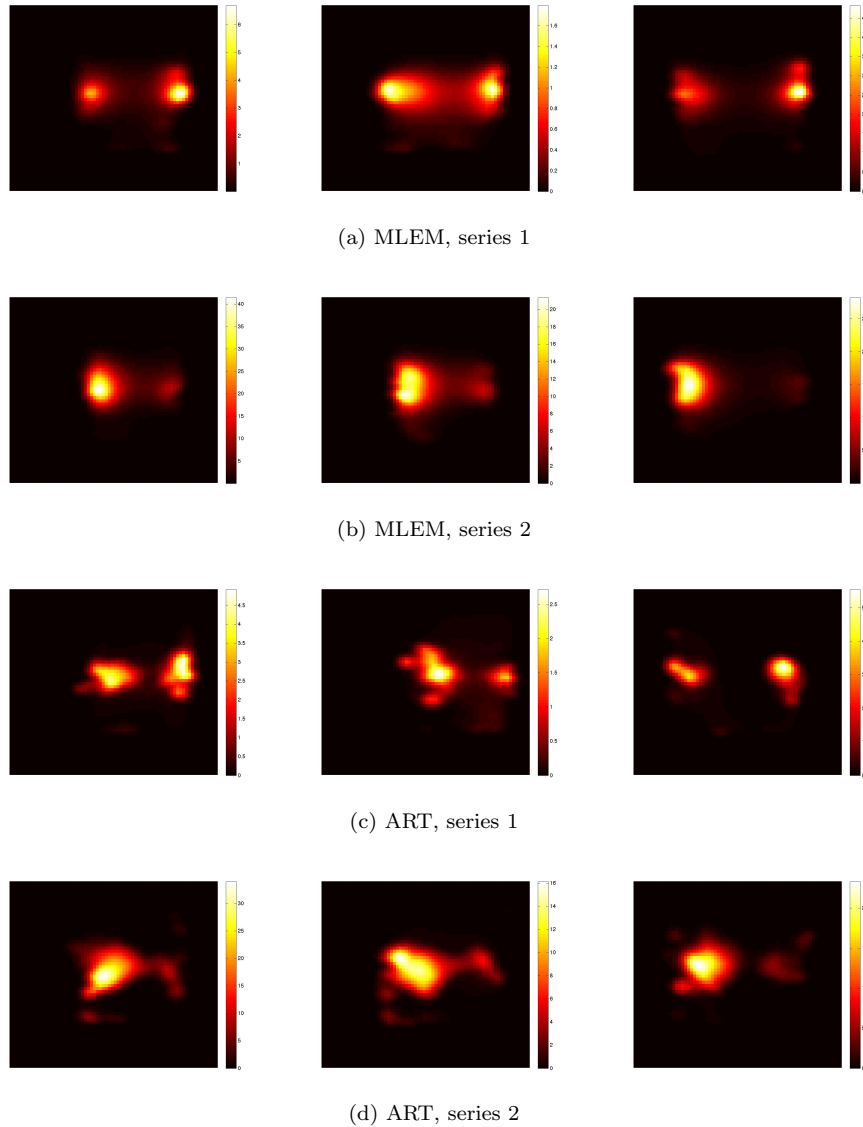


Figure 5.11: Image slice T of Freehand SPECT reconstruction (blue slice in Figure 5.9b) of example data sets using MLEM and ART, configurations from left to right: C1, C2 and C3. *Series 1*: B1 and B2 both containing a 100kBq Tc-99m solution. *Series 2*: B1 containing a 100kBq and B2 a 990kBq solution of Tc-99m.

errors between 1.49mm to 2.44mm on average, while in series 2 the sphere B1 (with one tenth of the activity of B2) was less accurately positioned with an error of 2.65mm to 5.36mm on average. However, for B2 the y axis localization error was consistently high, ranging from 5.30mm to 6.52mm on average for series 1 and from 3.91mm to 4.64mm on average for series 2. This indicates a systematic error. Indeed it turned out that for the second scanning plane (see Figure 5.7) the tracking data was less accurate than usual, as the gamma detector and its tracking target were almost perpendicular to the tracking cameras, an unfavorable situation where tracking was even lost completely a few times (during which no data was recorded). It is also notable that the absolute localization errors are all consistently off in the same

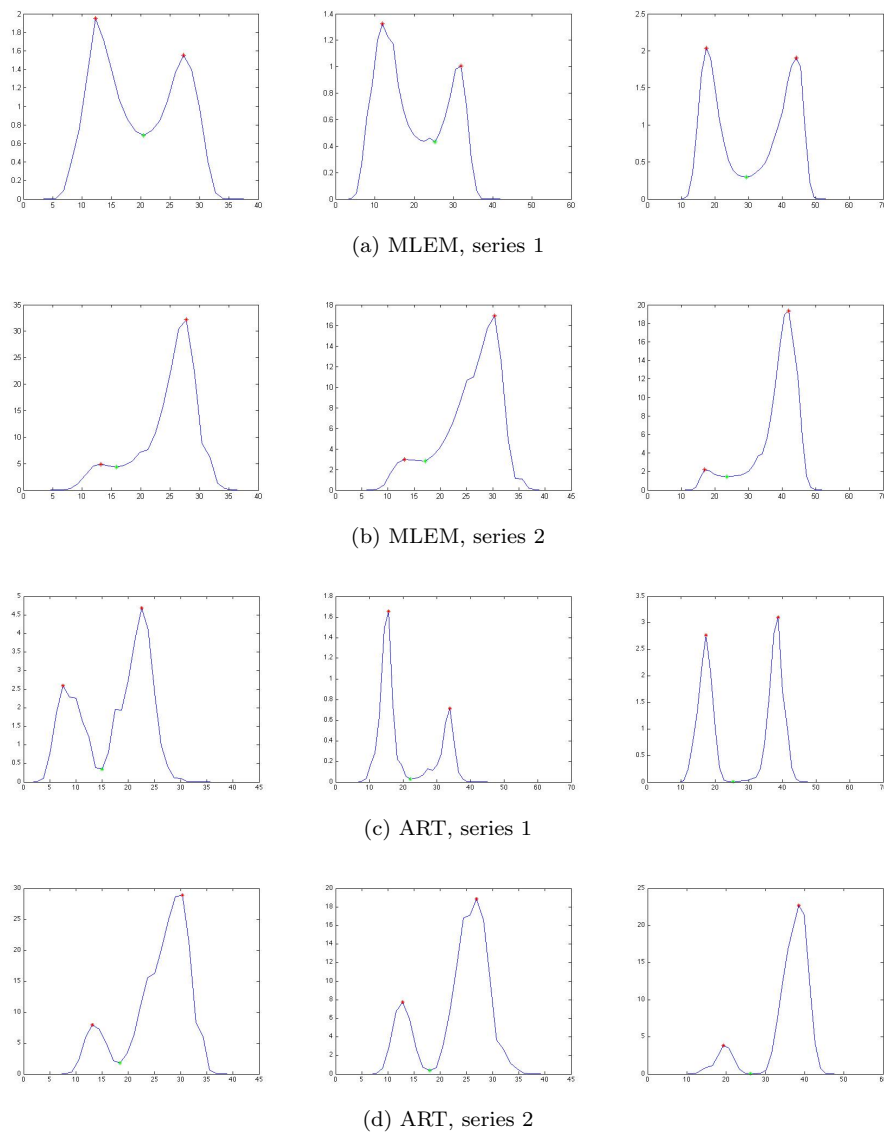


Figure 5.12: Profiles through the centroids of B1 and B2 of the Freehand SPECT image slice S of example data sets using MLEM and ART. *Series 1*: B1 and B2 both containing a 100kBq Tc-99m solution. *Series 2*: B1 containing a 100kBq and B2 a 990kBq solution of Tc-99m.

direction compared to CT, again indicating a systematic error in the tracking information and thus in the detector positions used for the reconstruction.

In terms of relative positioning, the distance between B1 and B2 in slice S compared to CT is listed in Table 5.3. For series 1, MLEM showed average errors between $1.88mm$ and $3.21mm$, while ART fared slightly worse with average errors between $1.99mm$ and $4.76mm$. For series 2 MLEM and ART returned similar results with average errors between $-0.54mm$ and $1.99mm$. In all cases B1 and B2 were placed too far apart compared to CT, except for phantom C2 in series 2.

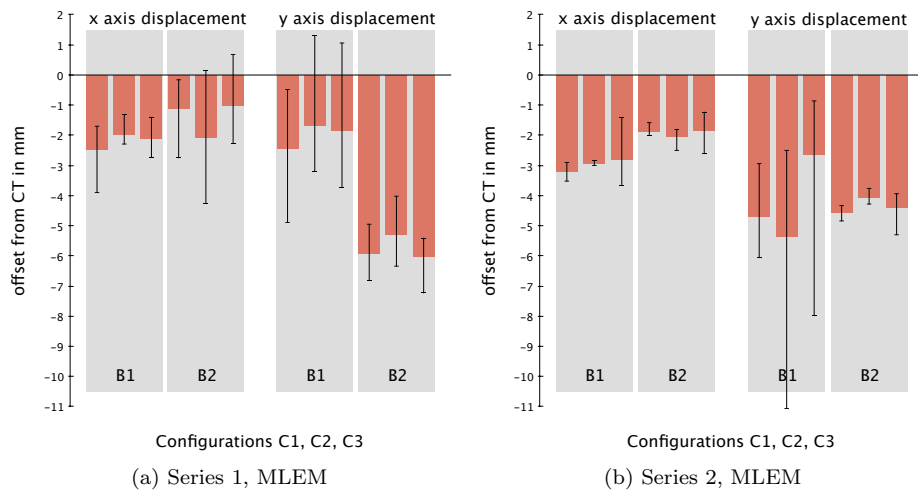


Figure 5.13: MLEM: Difference in the positions of B1 and B2 between CT and Freehand SPECT slice S using MLEM in x axis and y axis (averaged over 10 data sets for each configuration in series 1, over 3, 4, 10 data sets for C1,C2,C3 in series 2).

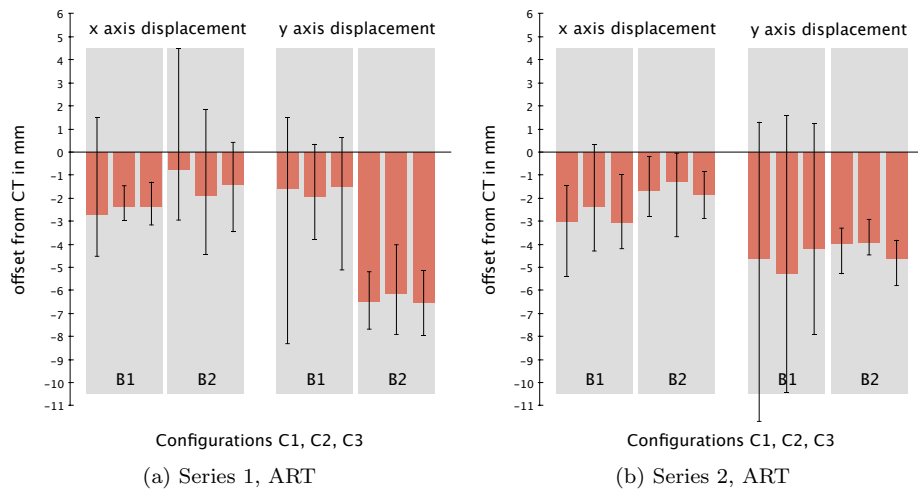


Figure 5.14: ART: Difference in the positions of B1 and B2 between CT and Freehand SPECT slice S using ART in x axis and y axis (averaged over 10 data sets for each configuration in both series).

The FWHM of B1 and B2 is shown in Figure 5.15 for both MLEM and ART. In series 1 and MLEM, B2 showed 1.06 to 1.58 times the FWHM of B1 on average, while for ART the ratio was closer to 1, ranging from 0.94 to 1.14 on average. In series 2 with B2 containing ten times the activity of B1, the ratios ranged from 1.73 to 2.78 on average for MLEM and from 1.49 to 1.72 for ART.

Table 5.4 shows the reconstructed intensity in slice S summed up over the discs of B1 and B2 located at the reference positions obtained from CT. In series 1 with both B1 and B2 containing the same activity, the activity reconstructed at the location of B1 was about 2 to 3 times higher than at B2 using MLEM, with ART this increased to roughly 4 to 6 times.

| dist($B1, B2$) (in mm) | from fhSPECT (average) | from CT | difference (average) |
|--------------------------------|---------------------------|---------|-------------------------|
| C1 series 1 MLEM | 17.26 ± 3.65 | 14.70 | 2.56 |
| C2 series 1 MLEM | 21.09 ± 3.36 | 19.21 | 1.88 |
| C3 series 1 MLEM | 25.82 ± 2.13 | 22.61 | 3.21 |
| C1 series 2 MLEM | 15.51 ± 1.26 | 14.70 | 0.81 |
| C2 series 2 MLEM | 18.67 ± 2.90 | 19.21 | -0.54 |
| C3 series 2 MLEM | 24.60 ± 1.75 | 22.61 | 1.99 |
| C1 series 1 ART | 19.46 ± 5.79 | 14.70 | 4.76 |
| C2 series 1 ART | 23.24 ± 2.60 | 19.21 | 4.03 |
| C3 series 1 ART | 26.27 ± 1.88 | 22.61 | 3.66 |
| C1 series 2 ART | 15.39 ± 1.88 | 14.70 | 0.69 |
| C2 series 2 ART | 18.85 ± 2.47 | 19.21 | -0.36 |
| C3 series 2 ART | 23.90 ± 2.22 | 22.61 | 1.29 |

Table 5.3: Distances of the centers of B1 and B2 in mm , measured from Freehand SPECT slice S and from CT (averaged over 10 data sets for each configuration in series 1 for MLEM and ART and series 2 for ART, over 3, 4, 10 data sets for C1,C2,C3 in series 2 and MLEM).

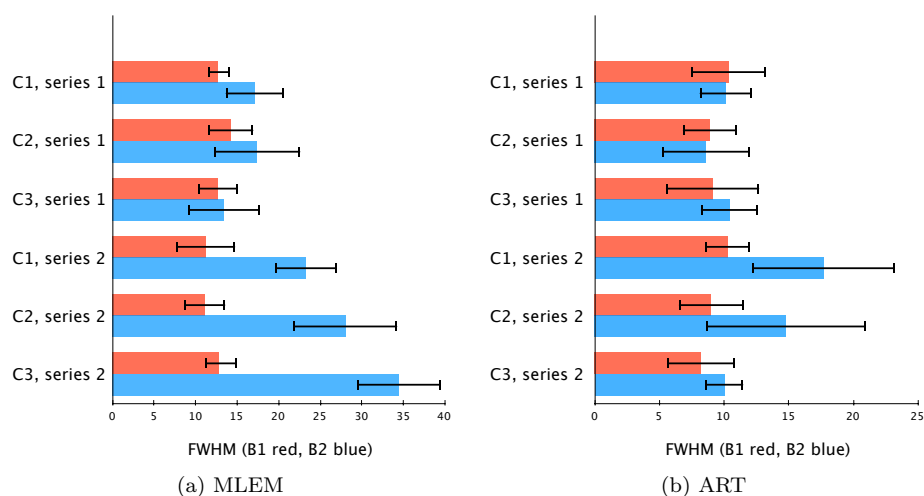


Figure 5.15: FWHM of B1 and B2 in Freehand SPECT slice S (averaged over 10 data sets for each configuration and both series for MLEM and ART).

| | intensity in area of B1 | intensity in area of B2 | max. intensity ratio B2/B1 | real activity ratio B2/B1 |
|------------------|----------------------------|----------------------------|-------------------------------|------------------------------|
| C1 series 1 MLEM | 56.07 ± 12.04 | 28.84 ± 5.08 | 78.71% | 100% |
| C2 series 1 MLEM | 68.67 ± 8.22 | 22.89 ± 2.53 | 39.35% | 100% |
| C3 series 1 MLEM | 59.88 ± 8.12 | 19.38 ± 2.96 | 86.39% | 100% |
| C1 series 2 MLEM | 82.27 ± 14.03 | 319.52 ± 28.93 | 469.52% | 1000% |
| C2 series 2 MLEM | 47.38 ± 6.43 | 241.21 ± 22.90 | 819.78% | 1000% |
| C3 series 2 MLEM | 41.35 ± 10.20 | 227.15 ± 37.46 | 1163.79% | 1000% |
| C1 series 1 ART | 67.51 ± 28.63 | 15.63 ± 8.49 | 72.78% | 100% |
| C2 series 1 ART | 85.27 ± 17.63 | 15.20 ± 5.70 | 52.17% | 100% |
| C3 series 1 ART | 71.14 ± 13.77 | 16.92 ± 8.91 | 117.35% | 100% |
| C1 series 2 ART | 128.65 ± 37.81 | 439.06 ± 80.78 | 335.45% | 1000% |
| C2 series 2 ART | 74.29 ± 21.49 | 335.88 ± 54.58 | 383.52% | 1000% |
| C3 series 2 ART | 71.40 ± 22.85 | 292.20 ± 69.14 | 399.01% | 1000% |

Table 5.4: Amount of reconstructed intensity in Freehand SPECT slice S contained in the area of B1 and B2 at the real positions as indicated by CT as well as maximum intensity ratio of B2 to B1 compared to real activities (averaged over 10 data sets for each configuration in both series, maximum intensities only over 3, 4, 10 data sets for C1,C2,C3 in series 2 using MLEM).

This relates to the absolute positioning errors observed in Figs. 5.13 and 5.14. Between phantoms C1, C2 and C3 in series 1, the reconstructed activity at both B1 and B2 is very consistent, with ART yielding slightly higher values for B1 and slightly lower values for B2. In series 2 with B2 containing ten times the activity of B1, the reconstructed activity at the reference position of B2 is about 5 times that of B1 for MLEM and about 4 times in the case of ART. Again ART is showing higher absolute values than MLEM.

The relative quantification using the maximum intensity ratios of the segmented spheres B2 and B1 in slice S is also listed in Table 5.4. In series 1 the configuration C3 with the farthest sphere separation, relative quantification with 86.39% for MLEM and 117.35% for ART was close to reality (100%), while in the closer configurations C1 and C2 the sphere B1 showed a higher maximum intensity than B2. Averaged over the entire series 1, relative quantification was off by 25%. For series 2, ART showed B2 having a 3 to 4 times higher maximum activity than B1, while in reality it was 10 times. MLEM fared better here, placing B2 at about 8 times the maximum intensity of B1 on average.

5.3.6 Discussion

The key factor in reconstructed image quality for Freehand SPECT is of course the quality of the acquired freehand data. Lacking a fixed detector geometry on an imaging gantry

with full angular coverage, the proposed online acquisition guidance has to ensure a sufficient coverage for image reconstruction. The quality of the reconstructed images would be improved by prolonging the scanning duration to acquire more measurements, providing better detection statistics along with potentially better angular coverage. However, the intra-operative workflow is already tight, and longer scanning times are difficult to fit in.

Other relevant factors include the accuracy of the spatial positioning system, which can degrade during a scan due to unfavorable viewing angles of the tracking system to the tracking target. This is seemingly the main cause for a systematic error observed in the absolute positions in Freehand SPECT compared to CT. As with all navigated solutions using optical tracking, unfavorable angles or occlusions hindering tracking performance can also occur in the operating room. Compensating for this issue is thus an ongoing topic of research.

Furthermore, the inversion method used to compute the reconstruction proved to be influential. In this work we evaluated the popular choice for emission tomography, MLEM, against a variant of randomized ART, which is commonly used in several tomographic imaging modalities. Qualitatively, MLEM produces more visually pleasing reconstructions, while ART is more prone to produce annoying artifacts and has higher computational demands. Quantitative performance was roughly similar in most areas, however ART reconstructs object more sharply, which proved to be highly beneficial in the close configurations C1 and C2 in series 2. Here MLEM was able to resolve the two spheres only in a part of the data sets. Nevertheless, MLEM has been the inversion method of choice for all of our patient experiments to date due to the qualitatively better reconstructions.

In a series of 60 controlled phantom experiments, we have studied the limitations and performance characteristics of Freehand SPECT. The setting of these experiments was kept realistic and clinically relevant with a scan duration of less than $2.5min$ while only covering three orthogonal planes around the object of interest, which is about the maximum one can expect while scanning some local body part intra-operatively. Our phantom experiments validated the claim of achieving an accuracy and resolution of $5mm$ to $10mm$, which is necessary for clinical usefulness. Even two radioactive spheres separated only by $3.7mm$ could be resolved.

5.4 Pre-operative Patient Studies in Sentinel Lymph Node Mapping

The sentinel lymph node (SLN) concept is now part of standard routine care in patients with invasive breast cancer [214]. A combination of pre-operative lymphatic mapping using

radio-colloids and blue dye labeling during surgery has been demonstrated to be a practicable approach for accurate localization of SLNs. This procedure has been shown to reduce morbidity and is now an integral part of European and American guidelines for patient management in early-stage breast cancer [214, 215].

Although most sentinel nodes can be identified during surgery with a hand-held gamma probe, SLN localization may be impracticable in certain cases. The overall success rate of the procedure exhibits a considerable range, resulting in an average false negative rate of 7% [216]; as a consequence, undetected nodal spread and inadequate adjuvant treatment may account for a significant number of breast cancer-related deaths.

Recently, hybrid SPECT/CT scanners have been suggested to increase the success rate of SLN identification. Husarik and Steinert highlighted the added value of SPECT/CT in breast cancer patients [217]. In 41 consecutive patients, findings from planar scintigrams and SPECT/CT were identical in only seven patients (17%). SPECT/CT indicated the correct anatomic localization in 29 patients (70%), according to the American Joint Committee on Cancer staging system (levels III). In six patients, additional SLNs were detected. Similar findings have been described previously by Lerman et al. [218]. In a pilot study by van der Ploeg et al., SPECT/CT was superior to SPECT for SLN detection, leading to a change in management in 5% of patients [219]. SPECT/CT has been shown to be especially useful in overweight patients [220]. The major disadvantage of hybrid imaging is that the intra-operative positioning of the patient prevents a direct correlation of pre-operative images and the operative situs. Consequently, there is an increasing need to be able to transfer the results of preoperative imaging technologies into the operating room (OR).

Intra-operative gamma imaging has been suggested for image-guided biopsy of SLNs. Several groups have introduced gamma camera systems permitting 2D scintigraphy in the OR [221–225]. These devices allow generation of images of a resolution up to 5mm, with acquisition times of approximately 30s. One of the major limitations of this approach is the requirement to hold the camera still during the acquisition in order to generate valid images. Furthermore, flexibility is an issue as the weight of the device is relatively high, at approx. 1.2kg for high- and 800g for low-resolution devices. Moreover, the limitation of missing anatomic information is still not solved. Finally, the effects of “shadowing” (SLNs masked by a nearby injection site) and “shine-through” (lymph nodes mistakenly considered as SLNs owing to sources above or below) and the cost compared with gamma probes have prevented the successful entrance of this technology into clinical practice.

In this section we evaluate the feasibility of Freehand SPECT for 3D nuclear imaging and present first pre-operative results regarding the detection and localization of SLNs in 85 breast cancer patients. The first 50 patients formed a pilot study to determine imaging parameters, the remaining 35 patients formed a validation study. As the acquisition protocol

strongly affects the performance of Freehand SPECT, the goal of this investigation was also to define thresholds and quality criteria that allow determination of an appropriate Freehand SPECT image quality.

The results of this section have been published in [208].

5.4.1 Methods

Inclusion and exclusion criteria. Inclusion and exclusion criteria were the same as used for routine SLN biopsy in breast cancer patients, as described in the guidelines for SLN diagnosis of the “Deutsche Gesellschaft für Senologie” [226]. Criteria therein are essentially equivalent to those of the American Society of Clinical Oncology [214]. Among these, the key inclusion criteria were the initial diagnosis of invasive breast cancer or advanced ductal carcinoma in situ (size $> 50mm$, confirmed by core needle biopsy), the lack of prior anticancer treatment, and age over 18 years. Key exclusion criteria were pre-operatively confirmed multi-centric tumor growth, clinically suspicious axillary lymph nodes, and pregnancy [226].

Clinical and histopathological characteristics of patients. A total of 85 consecutive patients (age 29–88 years, mean 59.5 years) undergoing conventional SLN biopsy were additionally scanned using Freehand SPECT and SPECT/CT, which served as reference. Six patients were not included during the final evaluation, due to missing information for a proper comparison (three during the pilot study and three during the validation study). According to the pre-operative clinical staging procedures, 71 out of 76 patients (93%) had a core needle biopsy confirming cT1 or cT2 invasive-ductal or invasive-lobular breast cancer (size 4–44mm) and no clinical suspicion of axillary lymph node involvement. Five patients had a locally advanced ductal carcinoma in situ (size 50–140mm). No metastatic disease was evident at the time of surgery. 58 patients (78%) received breast-conserving surgery; in 18 patients (24%) radical or subcutaneous mastectomy was performed owing to an unfavorable ratio of tumor and normal breast tissue. A single patient underwent a primary standard axillary dissection, due to the intra-operative presence of suspicious axillary lymph nodes. In 15 patients (20%), the SLN showed tumor cells in the frozen section and a standard axillary dissection of lymph nodes (levels I and II) was performed. Five patients had a tumor-free SLN in the histological frozen section but micro-metastases were described in the final pathology report following secondary axillary dissection (levels I and II).

Lymphatic mapping of sentinel lymph nodes. For lymphatic mapping, patients received a ^{99m}Tc -Nanocoll injection of approximately 0.2ml, distributed equally in four spots,

either periareolar (76 cases) or peritumoral (9 cases). The amount of radioactivity ranged from 35 to 87MBq (mean 57.9 ± 5.5 MBq). All but one patient underwent a 2-day protocol, which is the standard procedure at our institution. The injected activity was in the range of 10–20MBq for the 1-day protocol and 50–90MBq for the 2-day protocol. In all patients, dynamic planar lymphoscintigraphy representing the standard imaging protocol for lymphatic mapping at TUM was performed. Delayed planar images were used only in case of a negative early scan. For intra-operative identification of sentinel nodes, planar scintigraphy was used as reference method.

SPECT/CT. The SPECT/CT protocol consisted of 45 projections (180° using two opposing heads) of 7s each using a Symbia T6 hybrid scanner and LEHR collimators (Siemens Healthcare, Germany). For image reconstruction, an OSEM reconstruction algorithm with 16 subsets, 8 iterations, collimator blur, and attenuation and scatter correction (Flash3D software, Siemens Healthcare, Germany) was used. Post-processing was performed using an 8.4mm Gaussian filter; attenuation correction was performed using CT data. The reconstruction volume included the injection site and the axilla and neck region. The reconstruction voxel size was 4.7mm in each direction. For CT scanning, a low-dose procedure was used with a 3mm slice thickness (20–40mA tube current, 130keV tube voltage, shallow breathing, and expected absorbed dose of 0.2–0.4mSv, depending on patient size). In all patients, SPECT/CT was performed within 15min after planar scintigraphy. The level assignment (levels I–III) of SLNs was determined using the SPECT/CT images according to the current guidelines [214].

Freehand SPECT. For the Freehand SPECT acquisition (performed shortly before or after SPECT/CT), a gamma probe system (NodeSeeker, IntraMedical Imaging, USA) and an infrared optical tracking system (Polaris Vicra, Northern Digital, Canada) were combined in one system. Furthermore, a data processing unit was included in order to: (a) acquire the readouts of the probe and the position synchronously, (b) process the readings into a 3D image, and (c) display it for visualization. Infrared markers were attached to the gamma probe in order to acquire its position. To reference a common coordinate system, a configuration of optical markers (“patient target”) was used to determine the position of the patient, see Figure 5.16. The hardware was designed and adapted to be completely mobile so as to be suitable for application in the OR. The gamma probe was calibrated to include the 140keV peak of ^{99m}Tc with an energy window of 50keV. The collimator opening of the probe was measured using a point source and yielded approximately 50° .

The Freehand SPECT acquisition consisted of three steps. Initially, a volume of interest (VOI) was defined interactively by putting the tip of the tracked gamma probe over predefined anatomical landmarks; from the position of the landmarks a rectangular VOI was fixed



Figure 5.16: Freehand SPECT system in intra-operative setting consisting of (1) infrared tracking system, (2) touch screen monitor for display and interaction, (3) a hand-held gamma probe with mounted tracking target and (4) a patient tracking target to determine the position of the patient in a common coordinate system.

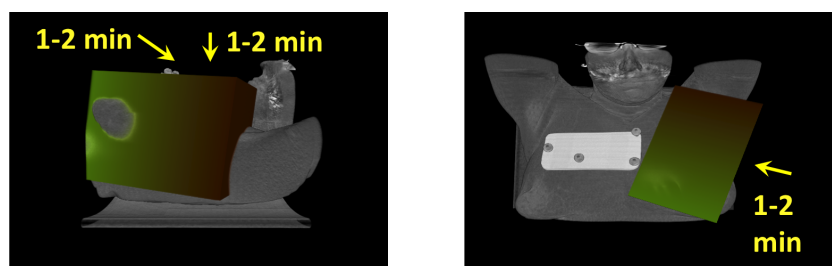


Figure 5.17: Scan protocol used for the Freehand SPECT acquisition. The arrows indicate the general direction of the probe during the scan, the rectangular volume on top of the patient is the volume of interest.

relative to the patient tracking target. Subsequently, the region of interest (axillary region) was scanned by moving the gamma probe. Finally, visualization of reconstructed images was performed. Reconstruction was performed as detailed in section 5.2.2 using MLEM. The output was generally filtered with a 6mm 3D Gaussian filter and visualized. In the event of node localization in close proximity to the injection site, the filter was set down to 4mm to determine whether there was a clear separation between node and injection site. Additional voxels were added in the required direction a posteriori if the volume of reconstruction did not cover the complete VOI as indicated by SPECT/CT imaging.

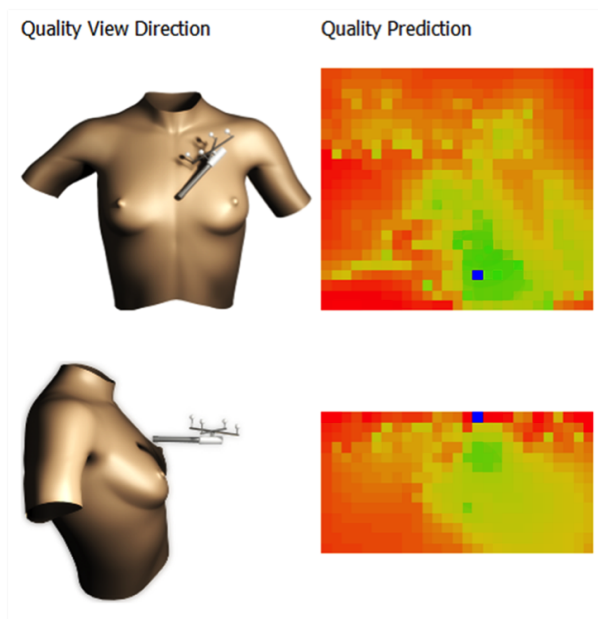


Figure 5.18: Acquisition guidance system used for 35 patient validation study. The accumulated information density in the VOI is displayed, as seen in the dorsal and medial direction. The denser the information, the greener the color. Red areas indicate very low information density. The blue dot shows the current position of the gamma probe relative to the VOI. Dark green was chosen to be the threshold for a good scan as defined during the 50 patient pilot study.

The scanning protocol consisted of a scan of the injection site and was divided into 1–2min acquisitions in the medial direction, 1–2min pointing in the dorsal direction, and 1–2min in a craniodorsal direction (see Figure 5.17). The scanning protocol was validated by several phantom acquisitions. For the first 50 patients (pilot study), no feedback on the quality of the acquisition was given during the scan. For the second group of 35 patients (validation study), the information density accumulated in each single voxel of the VOI was displayed during the acquisition (see Figure 5.18). The scan was only stopped when the complete volume reached a sufficient information density and thus a sufficient quality. Quantitative thresholds on this quality measure were derived from the data of the pilot study with 50 patients.

Comparison of Freehand SPECT and SPECT/CT. In order to compare SPECT/CT and Freehand SPECT images in an identical coordinate system, a tracking target was attached to the patient. The target consisted of a fixed configuration of optical markers (1cm diameter) that could be easily identified on CT images, enabling a point-based registration of the coordinate system of the optical positioning system and CT. SPECT images were co-registered with CT images according to the information in the DICOM tag. The Freehand SPECT images were generated in the coordinate system of the optical markers

of the patient target. The registration error of the target was calculated to be 0.6–3.1mm (average 1.1mm).

Data analysis. Each anonymized SPECT/CT image was reviewed by two expert nuclear medicine physicians in random order. The number of detected SLNs or lymph node conglomerates and their position were documented. Lymph node conglomerates were considered as a single entity. This information was used to calculate the uptake in each node/conglomerate using attenuation-corrected SPECT data. The uptake was expressed as percentage of total activity in the reconstruction area and calculated from the counts inside the manually segmented lymph node and the total counts in the attenuation-corrected SPECT image. The complete injection site and the drainage area of the breast were included in all SPECT images in order to obtain the true relative uptake. The segmentation was done directly in the 3D images to avoid errors resulting from projections. Subsequently, two nuclear medicine physicians evaluated Freehand SPECT images in random order and in a combined visualization together with the video stream of the procedure or CT data in order to correlate functional data with anatomy (see Figure 5.19). The number of lymph nodes and lymph node conglomerates was recorded together with their respective anatomic position.

Statistical evaluation. The results of the blinded analyses of SPECT/CT and Freehand SPECT were considered together with the uptake calculated from attenuation-corrected SPECT. In addition, for the first 50 patients, the quality of the scan was assessed using the positions and orientations measured and the position of the lymph nodes as segmented manually by the physicians.

For each position and orientation of the gamma probe during a scan, the expected count rate (expressed in cps/kBq) was calculated as if a point source of $1kBq$ was located in the position of the segmented SLN, according to a model based on the geometric information (see Figure 5.20). This count rate was averaged over all measurements which included the lymph node in the corresponding scan. This value was used as information density and consequently quality value Q of the scan for the lymph node. A small value of Q means that the scan did not fully cover the position of the SLN, such that the average information acquired coming from its position was very low. A high value of Q means that the position of the SLN was inside the field of view of the probe in several of the measurements, leading to accumulation of a higher amount of information.

Accuracy was calculated using SPECT/CT findings as reference. It was calculated for the overall patient group, as well as for each scan quality level and also with respect to the relative and absolute tracer uptake in the SLNs. In order to give a measure for the available

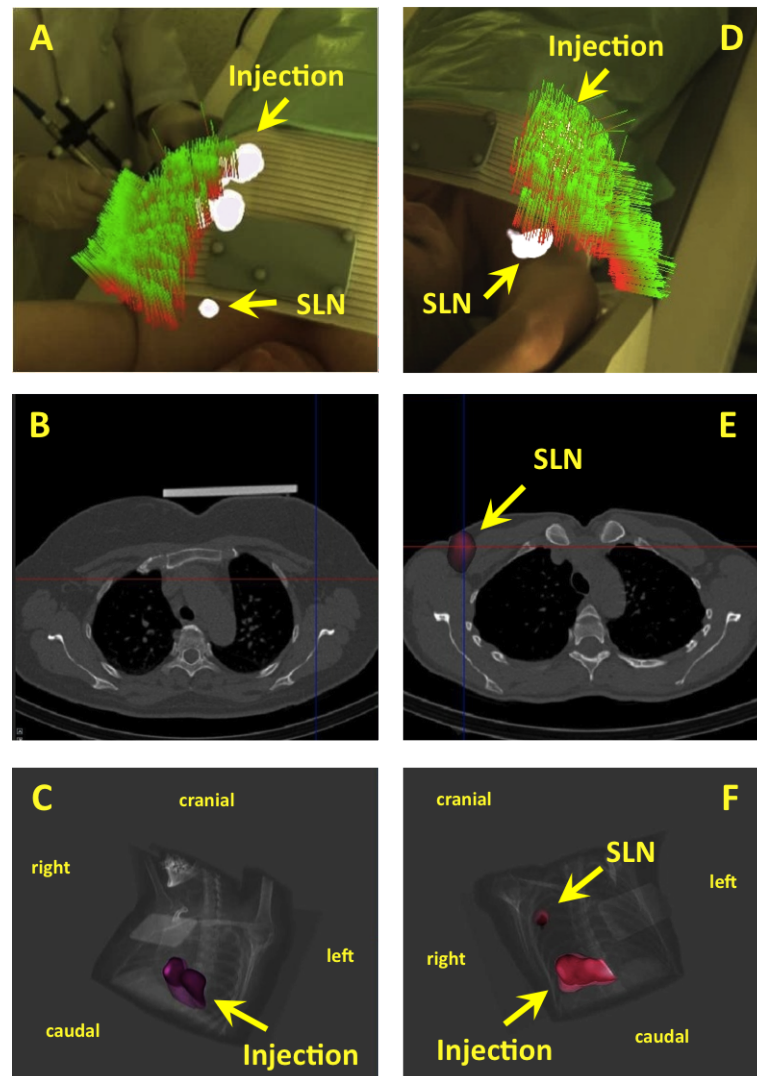


Figure 5.19: Examples of a poor quality scan (A–C) and a good quality scan (D–F). The lines shown in A and D represent the positions and orientations of the gamma probe during the scan. In A and D, the injection site and the SLNs as seen in the SPECT image are also shown, co-registered in the correct position. In B and E, the Freehand SPECT images are co-registered with CT data derived from SPECT/CT data. In C and F, co-registered visualization is rendered from an arbitrary point of view. One SLN can be seen in 3D fused visualization for the good scan (F) together with the injection site. In the poor quality scan, only the injection site is visible (C). The poor scan clearly misses the SLN (A), while several readings cover the SLN in the case of the good scan (D).

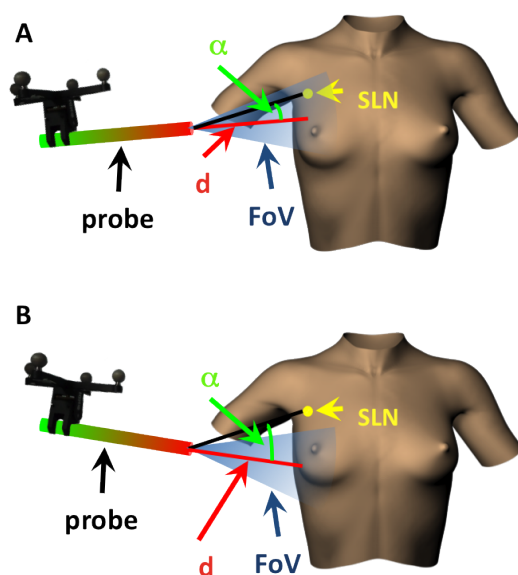


Figure 5.20: Mock-up of the methodology used to calculate the quality of a scan. In A the tracked gamma probe (tip red, back green) receives information from the radioactivity in its field of view (FOV). Using the position of the SLN segmented manually by the physician and the position and orientation of the gamma probe, the distance d and the angle α can be calculated. Subsequently, these values are used to calculate the expected count rate measured by the probe assuming $1kBq$ at the position of the SLN. For calculation, the solid angle and the parameters of the gamma probe were used. In B, a measurement is shown where the probe does not include the SLN in its FOV. Accordingly, there is no contribution with respect to the quality of the scan.

information for the reconstruction, the mean number of readings per voxel was calculated from the quotient of the total amount of readings and the total amount of voxels.

5.4.2 Results

Findings of SPECT/CT. A total of 125 SLNs were detected on SPECT/CT (83 and 42 in each part of the examination, respectively). At least one SLN was detected in 96.2% of the patients (76/79); see details in Table 5.5.

The average relative uptake in the SLNs was $0.86 \pm 1.3\%$ (range 0.003–14.1%) of the total radioactivity administered at attenuation-corrected SPECT. The absolute uptake presented a similar distribution, being in the range of 1.3–7882.3kBq (mean $499.5 \pm 741.0kBq$). No radioactivity beyond the injection site and lymphatic draining region could be detected in all of the patients. Out of 125 SLNs, 64 nodes were located in level I, 15 in level II and 4 in level III, respectively (pilot study). In the validation study, 34, 5 and 3 SLNs were located in levels I, II and III, respectively. SPECT/CT images were acquired approximately $78 \pm 37min$ (pilot study) or $66 \pm 15min$ (validation study) after injection of the radiopharmaceutical.

| | Pilot study ($n = 50$) | | Validation study ($n = 35$) | |
|-----------------------|--------------------------|---------|-------------------------------|---------|
| | SPECT/CT | fhSPECT | SPECT/CT | fhSPECT |
| Patient dropouts | 3 | 3 | 3 | 3 |
| Patients without SLNs | 3 | 27 | 0 | 4 |
| Patients with 1 SLN | 23 | 17 | 23 | 20 |
| Patients with 2 SLNs | 12 | 2 | 8 | 7 |
| Patients with 3 SLNs | 4 | 1 | 1 | 1 |
| Patients with 4 SLNs | 3 | 0 | 0 | 0 |
| Patients with 5 SLNs | 0 | 0 | 0 | 0 |
| Patients with 6 SLNs | 2 | 0 | 0 | 0 |
| SLNs in level I | 64 | 21 | 34 | 29 |
| SLNs in level II | 15 | 2 | 5 | 3 |
| SLNs in level III | 4 | 1 | 3 | 3 |

Table 5.5: Detection of SLNs in the pilot and validation studies.

The dynamic imaging protocol started approximately 7.8 or 7.7min (range 1–32min or 2–29min) after injection and was completed 29.6 or 26.3min (range 15–57min or 15–59min) after injection, respectively.

Acquisition parameters for Freehand SPECT. The mean VOI defined for reconstructing Freehand SPECT images had 27349 voxels (range 15200–65664) with a standardized voxel size of $5 \times 5 \times 5mm^3$ for most patients. In 22 patients, the voxel size had to be increased to $6 \times 6 \times 6mm^3$ owing to the large VOI needed to cover the injection site and axilla. The dimensions of the volume were on average $39 \times 26 \times 27$ voxels in the longitudinal, medial, and transverse axis, respectively. The scan duration was documented to be $4.3 \pm 1.2min$ on average (range 0.9–11.5min) and the mean number of data acquired during the scan was 3004 ± 701 (range 542–7078). The average number of readings per voxel was calculated to be 0.126 (i.e. 126 readings per 1000 voxels), ranging from 0.024 to 0.408 readings/voxel, with a standard deviation of 0.038 readings/voxel. The time interval for the overall procedure (including patient positioning, volume definition, scanning, and visualization) ranged from 3 to 12min (mean 6.5min). This time frame was considered acceptable with respect to an application in the OR.

The requirement of acquiring data in such a way that the complete VOI had a minimum quality resulted in an increased scanning time. While for the first patient group (pilot study) the mean time interval was 3.5min (range 0.9–7.4min), in the validation study, scan time ranged from 1.9 to 11.5min with an average of 5.5min. This also entailed a higher amount of readings per voxel of 0.187 versus 0.126 for the first patient group, respectively.

On average, Freehand SPECT images were acquired $72 \pm 40min$ after injection in the pilot study and $62 \pm 26min$ in the validation study. Freehand SPECT images were acquired within $14.4min$ (range 2–26min) or $15min$ (range 4–29min) prior to or after SPECT/CT acquisition (before SPECT/CT, 21% and 35% of Freehand SPECT acquisitions, respectively).

Definition of quality thresholds. For evaluation of the scan quality (pilot study), the quality of the acquisition based on each detected node was calculated. The average was $1.37 \pm 1.12cps/kBq$, ranging from 0.31 to $8.25cps/kBq$. Taking only those measurements into account yielding Q values higher than $2cps/kBq$, an accuracy that was similar to that of conventional SLN mapping was achieved (“good quality” group). The lower threshold was selected to divide the low-quality range equally. Thus, the quality of scan Q was ranked in three levels: good ($Q > 2cps/kBq$), intermediate ($1cps/kBq < Q < 2cps/kBq$), or poor ($Q < 1cps/kBq$). According to this quality assessment, 9 nodes in the pilot study were scanned with a quality that fulfilled the criteria of a good scan. In 35 nodes the scans were rated as intermediate and in 39 as poor quality.

Mapping performance of Freehand SPECT. *Pilot study:* In the subgroup of SLNs with a good scan quality, Freehand SPECT detected 77.8% of the SLNs (7/9), while for intermediate and poor quality scans, 34.3% (12/35) and 12.8% (5/39) of the nodes were detected, respectively. No false positive findings were reported, making sensitivity and accuracy equal in the pilot study. Accordingly, the positive predictive value was 100%. Both relative and absolute uptake (see Figure 5.21) affected the accuracy of Freehand SPECT. In general, the results showed that the higher the uptake, the lower the required quality of scan needed to map the SLN. For example, three of the five nodes which were scanned with a poor quality but were correctly mapped had an absolute uptake above $600kBq$ corresponding to 1% of relative uptake. On the other hand, with a good quality of scan, Freehand SPECT was able to map two nodes with an uptake of below $50kBq$ corresponding to 0.1% of relative uptake. Freehand SPECT mapped successfully 21/64 level I nodes, 2/15 level II nodes and 1/4 level III nodes.

Validation study: In a total of 35 patients, three patients dropped out of the study. In the remaining 32 patients, Freehand SPECT detected 83.3% of the nodes (35/42). There were seven false negative findings in five patients and two false positive findings in two patients. Thus the accuracy was 80%, the sensitivity 83%, and the positive predictive value 95%. As expected, the accuracy for the validation study was in the range of the 77.8% obtained for the good quality scans of the pilot study. The influence of the uptake was also consistent with the results in this group of patients (see Figure 5.22). Here, the seven nodes missed by Freehand SPECT had a small relative uptake (mean 0.19%, range 0.07–0.49%), as well

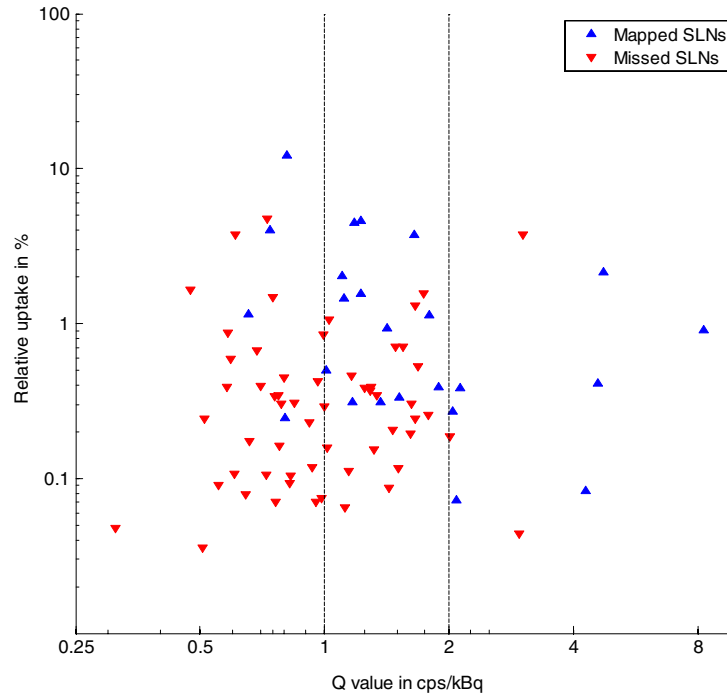


Figure 5.21: Scatter plot of the results for the first patient group (pilot study). Nodes mapped with Freehand SPECT (blue) and nodes missed (red) are placed according to respective quality of scan (x -axis) and relative or absolute uptake (y -axis). Two vertical lines separating good, intermediate and poor scan qualities are also shown ($Q = 1\text{cps/kBq}$ and $Q = 2\text{cps/kBq}$). Both axes are logarithmic and nodes with a quality of scan equal to zero are not displayed. The higher the uptake, the lower is the required quality of scan in order to map a node correctly.

as absolute uptake (mean 107kBq , range $38\text{--}285\text{kBq}$). For the correctly mapped SLNs, the mean uptake was 0.9% or 522kBq , respectively. There were, however, cases where nodes with uptake as low as 0.003% and 1.33kBq were correctly mapped. Regarding the level assignment, Freehand SPECT managed to map $29/34$ level I nodes, $3/5$ level II nodes and $3/3$ level III nodes.

5.4.3 Discussion

Lymphatic mapping and SLN biopsy have become the standard of care for patients with invasive breast cancer [214]. Meta-analyses of results published in recent years have however shown a considerable spread in the overall success rate of the procedure [216]. This results in an average false negative rate of 7% and thus in suboptimal post-operative treatment planning that may give rise to undetected nodal spread and eventually death. There is a growing interest in improving the procedure, as well as in providing enhanced tools for optimal detection, localization, and resection of SLNs.

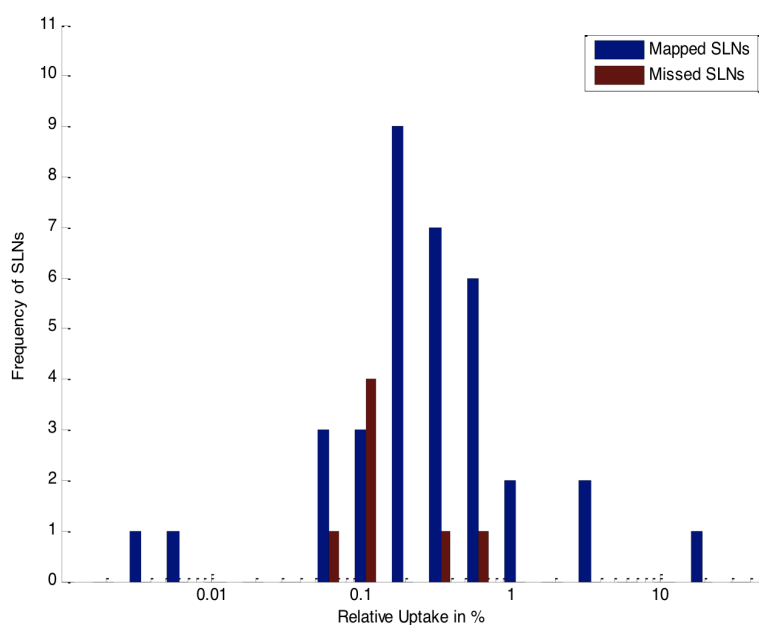


Figure 5.22: Histograms of nodal uptake in the validation study. Nodes that were not mapped are indicated in red and successfully mapped nodes in blue. Although the average uptake in missed nodes is lower than in detected nodes, there is a significant overlap. This demonstrates that uptake and scan quality do not sufficiently explain the ability to detect the SLN.

This is the first study to evaluate the feasibility of the novel technology Freehand SPECT for the detection and localization of SLNs in breast cancer. The aim of the study was twofold and consequently two consecutive patient groups were investigated. First, in a pilot study, the feasibility of Freehand SPECT was tested and thresholds on a selected quality criterion were set in order to guarantee a good image quality. Second, the employed thresholds were evaluated in a validation study in a second group of patients to guide the acquisition and permit evaluation of the effect of these thresholds on the overall performance of Freehand SPECT.

The navigated system described here aims to improve the intra-operative detection rate of SLNs. In principle, by enabling image-guided resection of SLNs, a standardization of the procedure can be achieved that will allow high detection rates even in less experienced institutions, and thus minimize the spread in overall success rate between less experienced and experienced physicians; this would represent a significant step towards quality assurance in SLN biopsy.

A sensitivity of 83.3% and a positive predictive value of 95% with respect to the gold standard (SPECT/CT) as reported in the validation study are at least within one standard deviation of the average values of gamma probe-based intra-operative detection [216]. Thus,

given a sufficient quality of scan, the accuracy of SLN detection may approach levels of clinical applicability.

Freehand SPECT may aid the process of surgical resection of the SLN in various fashions. First, due to its freehand nature and the flexible, mobile hardware required, it can be integrated into the OR without considerably changing the standardized workflow. In practical terms, the instrumentation already present in the OR is extended by a positioning system and the processing means in order to generate images. In a future application of SLN biopsy, the system will enable the generation of 3D images with the patient already lying on the OR table. As a consequence, in situ planning of the biopsy will be possible. Second, the possibility of generating images in the OR could be used again after the end of the procedure, but before closing the wounds, in order to confirm biopsy of all labeled structures. This opportunity in combination with the potential to reduce the risk of damaging vulnerable structures such as nerves and blood vessels in the axilla aids in improving the safety at the level of surgery, as well as at the level of overall treatment. In this preliminary study, the lymphatic mapping procedure in breast cancer was selected as an initial indication. The motivation for this was the relative simplicity of the procedure, the minimal modifications required in the current clinical workflow, and also the fact that this technique is a standard of care in most industrialized countries.

Of particular interest is the availability of 3D information to identify deep lying nodes. In particular, level II and III nodes in the axilla may be difficult to detect and to extract in a minimal invasive way. The performance of Freehand SPECT in this regard, with 75% detected level II and III nodes in the validation study, is promising. An even larger impact is expected from the use for localizing deep lying nodes in the abdomen or the pelvis which seems useful in prostate, colorectal or cervix carcinoma [200].

Other possible applications of this modality include procedures that are already based on SPECT isotopes like lymphatic mapping and SLN biopsy in melanoma or prostate cancer, but also other radio-guided procedures such as localization of neuroendocrine tumors and related metastases using ^{111}In -octreotide [227, 228]. Of particular relevance are ROLL techniques (radio-guided occult lesion localization) [229] in which impalpable tumors seen at mammography or MRI are labeled using stereotactic MRI-guided needle placement and the deposition of a highly concentrated dose of $^{99\text{m}}\text{Tc}$ -MAA. This hot spot is then used in the OR for localization and precise resection of the lesion. Here, the availability of Freehand SPECT would allow an image-guided procedure.

Several technical aspects, however, remain to be addressed. Despite the considerable improvements shown by using an online feedback during the acquisition, Freehand SPECT still yields false negative and false positive findings. Accordingly, further research should

be directed at optimizing methods to classify good and bad acquisitions and thus provide better feedback on the quality of the scan.

The proximity to the injection site apparently played an important role in the false negative findings of the validation study. In particular, in three patients with peritumoral injection, the injection site extended to the position of the SLN in the Freehand SPECT images. Unfortunately, neither changing the thresholds nor altering the defined filter range made it possible to separate the SLN from the injection site. In the results presented here, the iteration number was fixed. There might be the option of gaining resolution by using a larger iteration number. Furthermore, periareolar injection and fixation of the breast towards a medial direction during the SLNB are options to be explored.

Further issues to be considered are automatic quality control and improved quality criteria, denser scan of the axillary and subclavicular regions, and optimization of reconstruction parameters, such as number of iterations, post-processing filter, etc. Another important issue is the relative uptake of the radiopharmaceutical within the SLN. Scans with only intermediate or even poor quality yielded good results if SLNs presented high uptake. Quantification in attenuation-corrected SPECT has not generally been validated, but our results are in accordance with uptake values reported in the literature. Although absolute uptake behaved very similar to the relative uptake, one issue to be addressed in future is to test if Freehand SPECT performs better using a 1-day protocol. The influence of timing regarding diffusion of the radio-tracer was considered to be minimal, as the average difference between SPECT/CT and Freehand SPECT acquisitions was in the range of $15min$ and approximately $1h$ after injection.

In summary, there are still ways to improve the Freehand SPECT technology. Nevertheless, the results obtained adding only the guided acquisition in the version used during the validation study demonstrate its great potential.

5.5 First Intra-operative Patient Studies

After the promising results of the pre-operative study, a series of intra-operative studies of SLNB in breast cancer and in melanoma was started by Thomas Wendler at the Women's Hospital at Technische Universität München to evaluate the feasibility of Freehand SPECT in the operating room. Preliminary results have been presented in [230, 231].

Figures 5.23 and 5.24 present two example patients from that series, illustrating how intra-operative Freehand SPECT reconstructions can support the surgeon during the procedure. Figure 5.23a shows the intra-operative Freehand SPECT reconstruction pre-excision in an augmented reality view, while Figure 5.23b shows the pre-operative 2D scintigraphy for

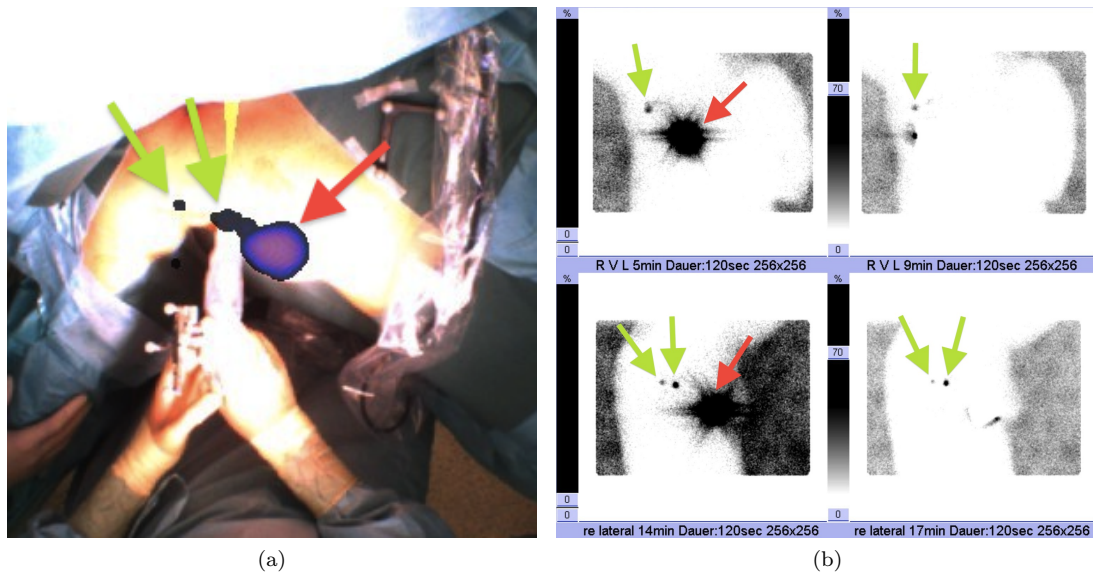


Figure 5.23: (a) Intra-operative Freehand SPECT reconstruction during SLNB of a patient with a tumor in the right breast rendered in an augmented reality view, red arrow marking injection site, green arrow the active nodes in the axilla (b) Pre-operative scintigraphy of same patient with a homogeneous cobalt flood phantom as background, *top row*: anterior-posterior images, *bottom row*: lateral images; in the two images on the right the injection site was covered with a lead plate.

comparison. The tumor was located in the right breast, and the huge radioactivity injection site is visible along with two active nodes in the axilla, both in the scintigraphy and in the intra-operative Freehand SPECT.

Another example patient from that series is shown in Figure 5.24: the left image is showing the Freehand SPECT reconstruction in an augmented reality view pre-excision, the right image post-excision. The tumor was located in the right breast, and the big radioactivity injection site is visible along with two active nodes in the axilla pre-excision and no nodes post-excision.

As presented in [230], 29 breast cancer patients were scanned intra-operatively until September 2010. Freehand SPECT was able to detect SLNs with 91% sensitivity, compared to a sensitivity of 72% when just using the regular gamma probe. In fact, Freehand SPECT led to seven additionally resected SLNs due to the post-excision scan, increasing the patients' prognosis.

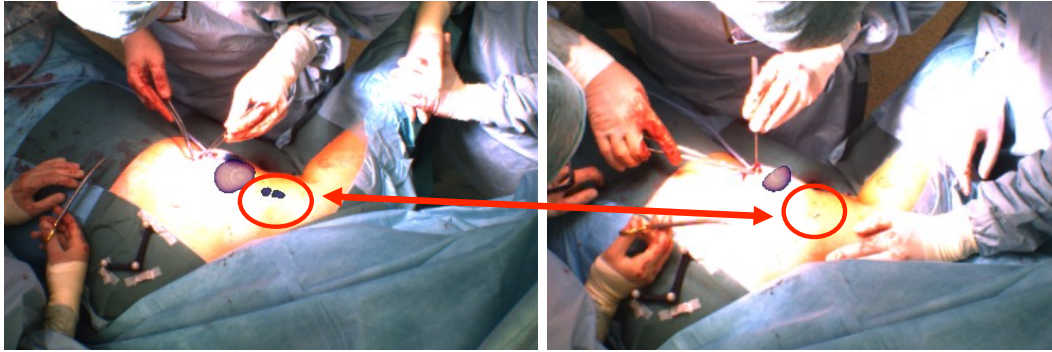


Figure 5.24: Intra-operative Freehand SPECT reconstruction during SLNB of a patient with a tumor in the right breast in an augmented reality view. *Left*: pre-excision, *Right*: post-excision. The red circles indicates two active nodes in the axilla that were resected during the procedure.

5.6 NanuLib: the Engine of Freehand SPECT

Since its inception in 2007 [232], Freehand SPECT has undergone a lot of developments in terms of software as well as in hardware. In 2009, the freehand reconstruction stand-alone software library called *NanuLib* was created to implement the reconstruction pipeline outlined in section 5.2.2. It was employed for all the reconstructions shown in this chapter. It has also been integrated into the commercially available “declipseSPECT” cart system by SurgicEye (Munich, Germany).

In the following two sections the *NanuLib* is described in more detail. The first section describes the design and implementation of the current, first version of the *NanuLib*. The second section gives an overview of the newly designed second version, started in mid 2010 and currently nearing completion.

5.6.1 Design and Implementation: first version

The *NanuLib* is a fully templated, header-only library written in portable C++, making use of the Eigen linear algebra library [207] for automatic vectorization and OpenMP for parallelization. A schematic drawing illustrating the major parts of the library is shown in Figure 5.25.

The interface to the user is provided by the class *TomographicSystem*. Besides setting the necessary parameters, the main interaction occurs via the two methods *pushbackMeasurement()* pushing a new *Measurement* into the system, and *getReconstruction()* to receive a *ReconVolume* containing the current reconstruction. Another method is *getColumnSums()* to return the current q_i values from equation (5.6) for online acquisition guidance.

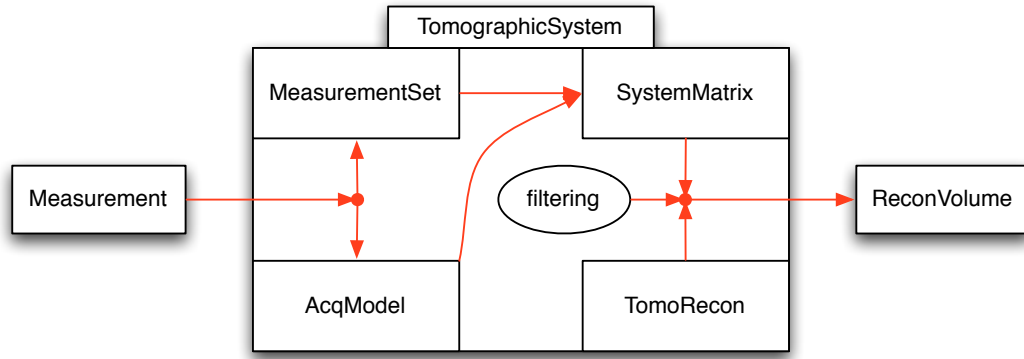


Figure 5.25: Schematic drawing of NanuLib components (first version).

Internally, the class *MeasurementSet* is storing all the recorded measurements. Employing the selected forward model encoded in *AcqModel*, each new *Measurement* pushed into *TomographicSystem* causes the calculation of a new row of the system matrix A to be pushed into the class *SystemMatrix*. When a reconstruction is requested, using the filtering methods outlined in section 5.2.2 a separate copy of the filtered system matrix A is created in contiguous memory. The selected inversion procedure from class *TomoRecon* is then applied to this filtered A , using the b vector from *MeasurementSet* to produce a reconstruction, which is stored in the class *ReconVolume*.

Several different variations of the forward model from equation (5.1) are implemented in *AcqModel*. For inversion, SVD-based solvers, ART with a constant relaxation factor, randomization and non-negativity constraints, MLEM as well as LSQR are implemented (for algorithm details see chapter 3). *SystemMatrix* is extensible to use different filtering algorithms.

The major weakness of this design is the need to create a filtered copy of the system matrix. This almost doubles the memory requirements of the reconstruction process, and with system matrices typically the size of a few gigabytes, the time taken for the copying itself is non-trivial as well. However, not creating a filtered copy would require calculating the system matrix twice, once for acquisition guidance and filtering, once for inversion, which in terms of computation time is the bigger trade-off in most cases. Another approach would be to filter rows before they get stored in *SystemMatrix* and mask out filtered columns only after the reconstruction is complete. However this introduces inaccuracies in the reconstruction for non-zero columns as activity gets distributed among voxels which should not have any, and creates issues with some of the inversion methods that cannot deal with zero columns.

This version of the NanuLib has been in use in several iterations over the last year, it was employed for all the reconstructions shown in this chapter. It is also used in the current

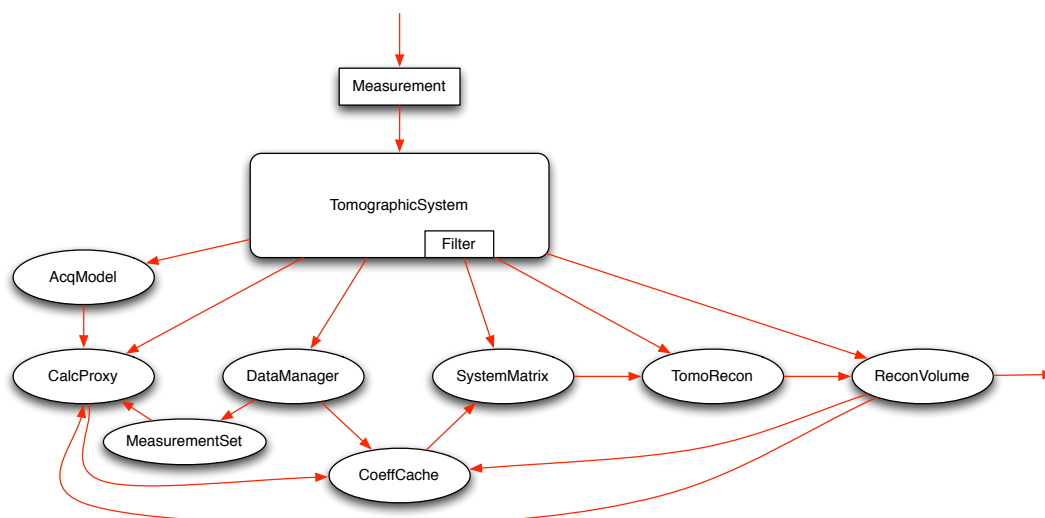


Figure 5.26: Schematic drawing of NanuLib components (second version).

version of the commercially available “declipseSPECT” (formerly called CSS300) cart system by SurgicEye (Munich, Germany).

5.6.2 Advancing the Design: second version

With the experience gained from the first version of the NanuLib, a second more powerful version was designed mid 2010, it is currently close to completion. The main new features are the support of a dynamic *ReconVolume* (for example using multi-resolution), support of sparse and on-the-fly *SystemMatrix* as well as the support of caching schemes obviating the necessity of creating a filtered copy of the system matrix. The new design also enables the creation of a specialized version having the reconstruction pipeline fully implemented on the GPU using for example CUDA or OpenCL, with maximum code reuse of the CPU version. A schematic drawing of the new design of the library is shown in Figure 5.26.

The public interface is almost identical to the first version, however the inlined templates are now limited to only the performance-critical parts of the library, making instantiation and extensions of *TomographicSystem* more user-friendly.

The major change, which enables the new features, is that *SystemMatrix* no longer acts as data storage, but instead just provides proxies to access parts of the system matrix, either as a dense or sparse matrix, or as on-the-fly computed coefficients. Instead, the class *DataManager* is managing all the incoming data, while *CoeffCache* provides a caching interface to system matrix coefficients. It provides an option to use a filtered copy of the system matrix, just like in the first library version, but it also allows avoiding that copy, necessitating calculating the system matrix coefficients twice in the worst case. Caching algorithms are employed to minimize the performance impact. This is particular interesting

for the look-up table forward model variant of *AcqModel*, where instead of having to calculate the forward model for a system matrix coefficient, a pre-calculated value is stored in a look-up table, typically generated by extensive reference measurements with the specific gamma probe on a positioning table. *CalcProxy* provides the inlined, templated functor to ensure maximum performance in all calculations.

ReconVolume now also supports dynamic volumes of interest (VOI). One variant for example represents the VOI as an octree (a tree where each internal node has 8 child nodes), enabling different detail levels in different regions of the volume. Thanks to *CoeffCache* changes in the representation cause minimal changes in the already computed system matrix coefficients. A suitable application for this would be automatic selection of the VOI: starting with the maximum tracking volume, each incoming *Measurement* would cause the field-of-view of the probe to be rendered in more detail, while leaving the rest of the VOI as is. Another application would be iterative refinement of the reconstruction: first a reconstruction is calculated at the default resolution level of the octree, and would then be iteratively refined in only the regions where activity was reconstructed, the previous reconstruction serving as an initial value for the subsequent inversion. Last but not least, with sufficiently reduced levels of the octree this should enable live real-time reconstructions during the acquisition process.

We hope this design will be flexible enough to support another year of research in freehand reconstructions.

5.7 Conclusion and Outlook

In summary, in this chapter we have introduced Freehand SPECT, a new approach for intra-operative 3D nuclear imaging. We presented the technical background and the novel fast algorithms developed for tomographic imaging from sparse, limited-angle and irregularly sampled data acquired using ad-hoc random detector geometries. We also presented a pre-operative evaluation of Freehand SPECT for lymphatic mapping in breast cancer patients along with first intra-operative patient reconstructions. The small and mobile Freehand SPECT system fits easily into the operating room, while the low scanning time and the fast computations do not hinder the workflow in clinical routine, thus enabling a practical and efficient solution for intra-operative 3D nuclear imaging.

The Freehand SPECT idea was first developed by my colleague Thomas Wendler, a lot of the work presented in this chapter has been his contribution, especially the connection to the medical side of things. When Thomas Wendler together with my colleague Jörg Traub founded the company SurgicEye, new possibilities opened up. Suddenly a whole team was

working on providing a usable, polished device for Freehand SPECT, allowing us at the research side of things to concentrate on the relevant parts. The cooperation with the company has been very fruitful for us both and I hope it will continue to do so.

Freehand SPECT has a lot of exciting possibilities for future development. For developments in the medical application area, the reader is referred to [230]. On the technical side, one uncomfortable necessity so far has been the need to manually select the volume of interest (VOI) before a scan. An automatic way to determine the VOI from the measurements would be very comfortable. In fact, the recent version of “declipseSPECT” implements such a method, starting with a huge volume encompassing the entire trackable area, and subsequently reducing it to the area that is actually scanned. However, without anatomical knowledge this can be risky in terms of reconstruction quality. In SLN mapping procedures for example, the injection site at the breast is not necessarily scanned in particular, but rather the axillary area containing the SLNs. Since the injection site has very high activity compared to any SLN, the gamma detector will likely pick up some readings from it in its field of view, but if the injection site is not included in the VOI due to not being explicitly scanned, artifacts will occur as the inversion procedure tries to place the measured activity somewhere. A constantly changing VOI also plays havoc with many of the acquisition guidance approaches.

A multi-resolution approach as outlined in section 5.6 however could cover the entire tracking volume automatically with no need to choose a separate VOI at little computational cost. Meanwhile, the savings in empty, low-resolution areas can be turned into a resolution advantage in the more active areas of hotspots like SLNs, doing away with the need to select a specific resolution of the VOI in advance as well. Live, real-time reconstructions would also be easier to implement using the multi-resolution approach.

Connected to this is also the development of more sophisticated online guidance schemes of the acquisition procedure. An option currently being discussed is the inclusion of miniaturized robot arms (for example mounted on the patient bed) performing the scan, allowing for better and more regular coverage, guided in real-time by the software. While this might detract from the simplicity of the hardware, it might prove beneficial enough to be worth the drawback.

On the more theoretical side, better forward models of the physical detection process inside the gamma probe are currently under development, potentially increasing reconstruction quality. New models are also being developed for portable gamma cameras, which provide a 2D detector grid instead of the 1D detector of the gamma probe. While portable gamma cameras are still quite heavy and too unwieldy for freehand scans, hardware miniaturization

is proceeding at a steady pace. Once they reach practical dimensions, the wealth of information acquired in a scan would multiply, either enabling shorter scanning times or higher reconstruction accuracy.

In a similar vein, the development of an inversion method even better suited to the limited-angle, sparsely sampled data inverse problem is an interesting topic. Models of the error propagation in the tracking data could be adapted to the reconstruction process, for example by weighting data known to be less accurate accordingly in the inversion method.

Another topic that came up in the clinical studies of Freehand SPECT is the ability to update the reconstruction during the procedure. For example in the SLN procedure, right now there are two scans pre- and post-excision, with the Freehand SPECT image remaining static during the excision process. During the operation, tissue is being cut away and deformed, invalidating the pre-excision Freehand SPECT reconstruction, so once the actual SLN is found and excised, the Freehand SPECT image overlay may no longer be accurate. A gamma camera watching the scene during the procedure would allow for updates of the Freehand SPECT reconstruction. Another option is the combination with another imaging modality like multi-spectral optical cameras [233], so procedure guidance switches to live, optical images once the Freehand SPECT reconstruction is no longer valid. Due to the limited depth penetration of optical imaging, the Freehand SPECT is still needed for pre-excision planning and post-excision validation.

Last but not least, the freehand concept of image reconstruction seems also adaptable to other imaging modalities. One example is the navigated beta-probe surface imaging shown in [234], another example currently being pursued is Freehand PET, an extension of Freehand SPECT to high-energy gamma probes. A more ambitious project called EndoTOF-PET (EU FP7) starting 2011 is trying to detect γ -coincidences from β^+ -tracers with a tracked, endoscopic PET probe combined with an external plate detector, utilizing picosecond time-of-flight data as well.

Chapter 6

Conclusion

This work presented an overview of tomographic imaging in chapter 1. Solution approaches to inverse tomographic problems were explored, analytical methods (chapter 2) as well as series expansion methods (chapter 3). Series expansion methods have established themselves as the method of choice in many imaging modalities, thus it is only consequent that the two novel imaging modalities presented in this work, Fluorescence Molecular Tomography (chapter 4) and Freehand SPECT (chapter 5) are employing series expansion methods.

Fluorescence Molecular Tomography (FMT) allows visualization of molecular processes in vivo using non-ionizing radiation. This work presents a full-projection free-space FMT approach along with a thorough analysis of the system design for the new acquisition geometries. The system was evaluated on phantoms as well as on mice, both ex vivo and in vivo.

Freehand SPECT is a novel imaging modality transferring 3D functional imaging capabilities to the operating theater. Thanks to tracked, hand-held gamma detectors, localized SPECT reconstructions are possible using sparse ad-hoc acquisition geometries. Experiments and evaluations were performed on phantoms to characterize the performance of Freehand SPECT, and pre- as well as intra-operative patient experiments demonstrated the feasibility of this new approach to imaging.

While I am no longer actively working on optical tomography, valuable experience was gained during the time spent working on FMT. Freehand SPECT is now my current research focus, providing an exciting, relatively unexplored field of tomographic reconstruction using sparse, ad-hoc acquisition geometries. Now that the concept has been proven both on phantoms and on patients, there will be ample opportunities in the future to improve the Freehand imaging technique both in terms of practical, intra-operative usability as well as imaging quality. Exciting times are ahead!

Appendix A

List of Publications

Over the course of this work several publications were created. Here is a list, current as of October 2010.

A.1 Journal Publications

- T. Wendler, K. Herrmann, A. Schnelzer, **T. Lasser**, J. Traub, O. Kutter, A. Ehlerding, K. Scheidhauer, T. Schuster, M. Kiechle, M. Schwaiger, N. Navab, S.I. Ziegler, A.K. Buck. First demonstration of 3-D lymphatic mapping in breast cancer using freehand SPECT. *European Journal of Nuclear Medicine and Molecular Imaging*, 37(8):1452–1461, 2010.
- **T. Lasser**, A. Soubret, J. Ripoll, and V. Ntziachristos. Surface reconstruction for free-space 360 fluorescence molecular tomography and the effects of animal motion. *IEEE Transactions on Medical Imaging*, 27:188–194, 2008.
- **T. Lasser** and V. Ntziachristos. Optimization of 360 projection fluorescence molecular tomography. *Medical Image Analysis*, 11(4):389–399, 2007.
- N. Deliolanis, **T. Lasser**, D. Hyde, A. Soubret, J. Ripoll, and V. Ntziachristos. Free-space fluorescence molecular tomography utilizing 360 geometry projections. *Optics Letters*, 32(4):382–384, 2007.

A.1.1 Submitted Journal Publications

- **T. Lasser**, T. Wendler, S.I. Ziegler and N. Navab. Freehand SPECT: a new approach for intra-operative 3D nuclear imaging. Submitted to *IEEE Transactions on Medical Imaging*, in September 2010.

A.2 Conference publications, full papers

- A. Safi, V. Castaneda, **T. Lasser** and N. Navab. Skin Lesion Classification with Optical Spectroscopy. In *Intl. Workshop MIAR*, Beijing, China, September 2010.
- A. Hartl, T. Wendler, **T. Lasser**, S.I. Ziegler and N. Navab. Confident radioactivity surface reconstruction for control of resection borders. In *International Workshop AMI-ARCS 2008*, New York, USA, October 2008.
- T. Wendler, M. Feuerstein, J. Traub, **T. Lasser**, J. Vogel, F. Daghighian, S.I. Ziegler, and N. Navab. Real-time fusion of ultrasound and gamma probe for navigated localization of liver metastases. In *International Conference on Medical Image Computing and Computer-Assisted Intervention, MICCAI 2007*, volume 4792 of LNCS, pages 252260, Brisbane, Australia, October 2007.
- T. Wendler, A. Hartl, **T. Lasser**, J. Traub, F. Daghighian, S.I. Ziegler, and N. Navab. Towards intra-operative 3d nuclear imaging: reconstruction of 3d radioactive distributions using tracked gamma probes. In *International Conference on Medical Image Computing and Computer-Assisted Intervention, MICCAI 2007*, volume 4792 of LNCS, pages 909917, Brisbane, Australia, October 2007.

A.3 Conference publications, short papers

- **T. Lasser**, S.I. Ziegler and N. Navab. Freehand SPECT in low uptake situations. In *SPIE Medical Imaging*, Orlando, USA, February 2011.
- A. Safi, V. Castaneda, **T. Lasser**, D.C. Mateus and N. Navab. Manifold Learning for Dimensionality Reduction and Clustering of Skin Spectroscopy Data. In *SPIE Medical Imaging*, Orlando, USA, February, 2011.
- A. Dului, **T. Lasser**, T. Wendler, A. Safi, S.I. Ziegler, and N. Navab. Navigated tracking of skin lesion progression with optical spectroscopy. In *Proc. SPIE Medical Imaging 7624:76243P*, San Diego, USA, February 2010.
- **T. Lasser**, T. Wendler, S.I. Ziegler, and N. Navab. Towards reproducibility of free-hand 3d tomographic nuclear imaging. In *IEEE Medical Imaging Conference 2008*, Dresden, Germany, October 2008.
- T. Wendler, **T. Lasser**, S.I. Ziegler, and N. Navab. Towards confident 3d tomographic reconstruction for asymmetric, sparse detector geometries. In *IEEE Medical Imaging Conference 2008*, Dresden, Germany, October 2008.

- T. Wendler, I. Faure de Pebeyre, **T. Lasser**, and N. Navab. Integrated surface acquisition for hand-held probes. In *OSA BIOMED topical meeting 2008*, St. Petersburg, USA, March 2008.
- D. Hyde, A. Soubret, J. Dunham, **T. Lasser**, E. Miller, D. Brooks and V. Ntziachristos. Analysis of reconstructions in full view fluorescence molecular tomography. In *Proc. SPIE, Medical Imaging 6498:649803*, January 2007.
- **T. Lasser**, N. Deliolanis, A. Soubret, J. Ripoll, and V. Ntziachristos. 360 free space Fluorescence Molecular Tomography using silhouette surface reconstruction. In *Proc. SPIE, OSA Biomedical Optics 6629:662936*, Munich, Germany, June 2007.
- N. Deliolanis, **T. Lasser**, M. Niedre, A. Soubret, and V. Ntziachristos. In-vivo Lung Cancer Imaging in Mice using 360 Free-space Fluorescence Molecular Tomography. In *IEEE International Conference of the Engineering in Medicine and Biology Society*, September 2006.
- **T. Lasser** and V. Ntziachristos. Surface Reconstruction from Contours for Non-contact Fluorescence Molecular Tomography. In *OSA Biomedical Optics Topical Meeting 2006*, Fort Lauderdale, USA, March 2006.

A.4 Conference contributions, abstracts

- A.K. Buck, A. Schnelzer, T. Wendler, **T. Lasser**, J. Traub, O. Kutter, T. Schuster, A. Ehlerding, K. Scheidhauer, M. Kiechle, N. Navab, S.I. Ziegler, and M. Schwaiger. First demonstration of 3D lymphatic mapping in breast cancer using freehand SPECT. In *DGN Nuklearmedizin 2010*, Leipzig, Germany, April 2010.
- A. Ehlerding, A. Schnelzer, T. Wendler, K. Herrmann, **T. Lasser**, K. Scheidhauer, O. Kutter, T. Schuster, M. Schwaiger, A.K. Buck, S.I. Ziegler, N. Navab, S. Paepke and M. Kiechle. Vorstellung der Pilotstudie zur 3D-Darstellung des Wächterlymphknotens bei Brustkrebspatientinnen mittels Freehand-SPECT. In *Annual Meeting of DGS*, Hamburg, Germany, July 2010.
- K. Herrmann, A. Schnelzer, T. Wendler, M. Hoyer, D. Weisgerber, **T. Lasser**, S. Paepke, M. Martignoni, M. Kiechle, N. Navab, S.I. Ziegler, and M. Schwaiger. Evaluation of feasibility of freehand SPECT in the operating room. In *DGN Nuklearmedizin 2010*, Leipzig, Germany, April 2010.
- K. Herrmann, T. Wendler, A. Schnelzer, **T. Lasser**, J. Traub, O. Kutter, A. Ehlerding, K. Scheidhauer, T. Schuster, M. Kiechle, M. Schwaiger, N. Navab, S.I. Ziegler and A.K.

- Buck. First demonstration of 3D lymphatic mapping using freehand SPECT. In *Intl. Conf. SNB*, Copenhagen, Denmark, May 2010.
- X. Feng, K. Szajkowska, **T. Lasser**, S.I. Ziegler, N. Navab and T. Wendler. 2D/3D registration of freehand SPECT and planar scintigraphy for clinical evaluation of 3D thyroid scintigraphy. In *World Congress on Medical Physics and Biomedical Engineering 2009*, Munich, Germany, September 2009.
 - K. Herrmann, T. Wendler, M. Chen, A. Bartel, **T. Lasser**, K. Scheidhauer, J. Traub, T. Schuster, S.I. Ziegler, M. Schwaiger, A.K. Buck, and N. Navab. Freehand SPECT: first in-vivo use for lymphatic mapping and comparison to conventional imaging. In *DGN Nuklearmedizin 2009*, Leipzig, Germany, April 2009.
 - **T. Lasser**, A. Dului, T. Wendler, S.I. Ziegler, and N. Navab. Interactive reconstruction for freehand SPECT: An approach to acquisition guidance? In *EANM Annual Congress 2009*, Barcelona, Spain, October 2009.
 - C. Oezguer, J. Bieniarz, **T. Lasser**, S.I. Ziegler, N. Navab, and T. Wendler. Phenomenological models for intraoperative positron emission surface imaging using hand-held probes. In *World Congress on Medical Physics and Biomedical Engineering 2009*, Munich, Germany, September 2009.
 - J. Traub, K. Herrmann, **T. Lasser**, N. Navab, S.I. Ziegler, A.K. Buck and T. Wendler. Freehand SPECT/Ultrasound fusion for hybrid image-guided resection. In *RSNA 95th Scientific Assembly and Annual Meeting 2009*, Chicago, USA, December 2009.
 - J. Traub, K. Herrmann, T. Wendler, **T. Lasser**, M. Schwaiger, N. Navab, S.I. Ziegler and A.K. Buck. First clinical results of freehand SPECT and planar scintigraphy for clinical evaluation of 3D thyroid scintigraphy. In *Molekular Bildgebung (MOBI)*, Berlin, Germany, June 2009.
 - T. Wendler, X. Feng, K. Herrmann, **T. Lasser**, J. Traub, S.I. Ziegler, N. Navab, and A.K. Buck. 2D/3D registration of freehand SPECT and planar scintigraphy for clinical evaluation of 3d thyroid scintigraphy. In *EANM Annual Congress 2009*, Barcelona, Spain, October 2009.
 - T. Wendler, X. Feng, **T. Lasser**, K. Herrmann, J. Traub, K. Scheidhauer, S.I. Ziegler, D. Lenhart, J. Grahneis, M. Schwaiger, N. Navab, and A.K. Buck. Freehand SPECT for 3d thyroid scintigraphy: first patient report. In *DGN Nuklearmedizin 2009*, Leipzig, Germany, April 2009.
 - T. Wendler, K. Herrmann, **T. Lasser**, J. Traub, M. Schwaiger, N. Navab, S.I. Ziegler, and A.K. Buck. First experience with freehand SPECT for lymphatic mapping in

- melanoma in upper body. In *EANM Annual Congress 2009*, Barcelona, Spain, October 2009.
- T. Wendler, K. Herrmann, **T. Lasser**, J. Traub, M. Schwaiger, S.I. Ziegler, N. Navab, and A.K. Buck. Freehand SPECT: first in-vivo evaluation and comparison to conventional lymphatic mapping. In *SNM Annual Meeting 2009*, Toronto, Canada, June 2009.
 - T. Wendler, K. Herrmann, A. Schnelzer, **T. Lasser**, J. Traub, O. Kutter, T. Schuster, M. Kiechle, M. Schwaiger, N. Navab, S.I. Ziegler, and A.K. Buck. Clinical introduction of freehand SPECT for image-guided sentinel lymph node biopsy. In *EANM Annual Congress 2009*, Barcelona, Spain, October 2009.
 - T. Wendler, **T. Lasser**, J. Traub, S.I. Ziegler, and N. Navab. Freehand SPECT / ultrasound fusion for hybrid image-guided resection. In *EANM Annual Congress 2009*, Barcelona, Spain, October 2009.
 - A. Hartl, T. Wendler, J. Traub, **T. Lasser**, S.I. Ziegler, and N. Navab. Confident radioactivity surface reconstruction for control of resection borders. In *SNM Annual Meeting 2008*, Houston, USA, June 2008.
 - **T. Lasser**, A. Dului, T. Wendler, J. Becker, S.I. Ziegler, and N. Navab. Computer-assisted spectral quantification of disease progression in CTCL. In *World Molecular Imaging Congress 2008*, Nice, France, September 2008.
 - **T. Lasser**, A. Dului, T. Wendler, S.I. Ziegler, and N. Navab. Navigated tracking of skin lesion progression with optical spectroscopy. In *SNM Annual Meeting 2008*, Houston, USA, June 2008.
 - **T. Lasser**, T. Wendler, J. Traub, S.I. Ziegler, and N. Navab. Definition of optimal collimator geometries for 3d tomographic thyroid scintigraphy using navigated gamma probes. In *EANM Annual Congress 2008*, Munich, Germany, October 2008.
 - T. Wendler, A. Hartl, **T. Lasser**, J. Traub, S.I. Ziegler, and N. Navab. 3d intra-operative nuclear imaging for SLNB in neck. In *SNM Annual Meeting 2008*, Houston, USA, June 2008.
 - T. Wendler, A. Hartl, **T. Lasser**, J. Traub, S.I. Ziegler, and N. Navab. Tracking-based statistical correction for radio-guided cancer surgery. In *World Molecular Imaging Congress 2008*, Nice, France, September 2008.
 - T. Wendler, **T. Lasser**, A.K. Buck, C. Oezguer, M. Schwaiger, S.I. Ziegler, and N. Navab. First in vivo use of a fused gamma ultrasound system. In *RSNA 94th Scientific Assembly and Annual Meeting 2008*, Chicago, USA, December 2008.

-
- T. Wendler, J. Traub, **T. Lasser**, M. Feuerstein, S.I. Ziegler, and N. Navab. Combined ultrasound and gamma probe imaging for examination of thyroid nodules. In *SNM Annual Meeting 2008*, Houston, USA, June 2008.
 - T. Wendler, **T. Lasser**, A.K. Buck, J. Traub, M. Schwaiger, S.I. Ziegler, and N. Navab. First case report of 3d tomographic thyroid scintigraphy with tracked gamma probes. In *EANM Annual Congress 2008*, Munich, Germany, October 2008.
 - T. Wendler, J. Traub, A. Hartl, **T. Lasser**, M. Burian, A.K. Buck, F. Daghighian, M. Schwaiger, S.I. Ziegler, and N. Navab. Adding navigation to radio-guided surgery: new possibilities, new problems, new solutions. In Joachim Hornegger et. al, editor, *Proceedings of RBC Biomed 2007*, pages 96100, Erlangen, Germany, July 2007.

Bibliography

- [1] M. Rivera-Ruiz, C. Cajavilca, and J. Varon, “Einthoven’s string galvanometer: the first electrocardiograph.” *Tex Heart Inst J*, vol. 35, no. 2, pp. 174–178, 2008.
- [2] W. Einthoven, *Nobel Lectures, Physiology or Medicine 1922–1941*. Elsevier Publishing Company, 1965.
- [3] H. Rockwell and S. Rockwell, “Hardness–Tester,” US Patent 1294171, 1919.
- [4] A. Carangeot, “Un goniomètre ou mesure-angle,” *Nouvelles de la République des lettres et des arts*, vol. 14, 1782.
- [5] W. C. Röntgen, “Ueber eine neue Art von Strahlen. (Vorläufige Mittheilung).” *Aus den Sitzungsberichten der Würzburger Physik.–medic. Gesellschaft*, 1895.
- [6] ———, *Nobel Lectures, Physics 1901–1921*. Elsevier Publishing Company, 1967.
- [7] A. Vallebona, “Nouvelle méthode roentgenstratigraphique,” *Radiol. Clin. (Basel)*, 1947.
- [8] G. Hounsfield, “Computerised transverse axial scanning (tomography): Part 1. Description of system,” *Br. J. Radiol.*, vol. 46, pp. 1016–1022, 1973.
- [9] A. M. Cormack, “Representation of a function by its line integrals, with some radiological applications,” *J. Appl. Phys.*, vol. 34, pp. 2722–2727, 1963.
- [10] ———, “Representation of a function by its line integrals, with some radiological applications. II,” *J. Appl. Phys.*, vol. 35, pp. 2908–2913, 1964.
- [11] G. Hounsfield, *Nobel lectures, Physiology or Medicine 1971–1980*. World Scientific Publishing Co., 1992.
- [12] T. Beyer and J. Czernin, “Is conflict of interest in our best interest?” *Eur. J. Nucl. Med. Mol. Imaging*, vol. 37, no. 6, pp. 1063–8, Jun 2010.
- [13] J. Hadamard, “Sur les problèmes aux dérivées partielles et leur signification physique,” *Princeton University Bulletin*, pp. 49–52, 1902.

-
- [14] R. Weissleder and V. Ntziachristos, “Shedding light onto live molecular targets,” *Nature Medicine*, vol. 9, no. 1, pp. 123–128, Jan 2003.
- [15] G. Watts, “John Wild,” *British Medical Journal*, vol. 339, p. 4428, 2009.
- [16] P. Lauterbur, “Image formation by induced local interactions: Examples employing nuclear magnetic resonance,” *Nature*, vol. 242, pp. 190–191, 1973.
- [17] M. Xu and L. V. Wang, “Photoacoustic imaging in biomedicine,” *Review of Scientific Instruments*, vol. 77, p. 041101, 2006.
- [18] M. Ter-Pogossian, M. Phelps, E. Hoffmann, and N. Mullani, “A positron–emission transaxial tomograph for nuclear imaging (PET),” *Radiology*, vol. 114, no. 1, pp. 89–98, 1975.
- [19] D. Kuhl and R. Edwards, “Image separation radioisotope scanning,” *Radiology*, vol. 80, no. 4, pp. 653–661, 1963.
- [20] G. de Hevesy, *Nobel Lectures, Chemistry 1942–1962*. Elsevier Publishing Company, 1964.
- [21] M. Rudin and R. Weissleder, “Molecular imaging in drug discovery and development,” *Nature reviews Drug discovery*, vol. 2, no. 2, pp. 123–31, Feb 2003.
- [22] G. T. Herman, *Fundamentals of Computerized Tomography*. Springer-Verlag London, 2009.
- [23] F. Natterer, *The Mathematics of Computerized Tomography*. SIAM, 2001.
- [24] F. Natterer and F. Wübbeling, *Mathematical Methods in Image Reconstruction*. SIAM, 2001.
- [25] M. N. Wernick and J. N. Aarsvold, “Emission tomography: the fundamentals of PET and SPECT,” p. 576, Jan 2004.
- [26] F. Natterer, “Inversion of the attenuated radon transform,” *Inverse problems*, vol. 17, p. 113, 2001.
- [27] D. Finch, “The attenuated X-ray transform: recent developments,” *Inside out: inverse problems and applications*, pp. 47–66, 2003.
- [28] M. Blume, A. Martinez-Möller, A. Keil, N. Navab, and M. Rafecas, “Joint reconstruction of image and motion in gated positron emission tomography,” *IEEE Transactions on Medical Imaging*, p. doi:10.1109/TMI.2010.2053212, 2010.

- [29] R. B. Schulz, A. Ale, A. Sarantopoulos, M. Freyer, E. Soehngen, M. Zientkowska, and V. Ntziachristos, "Hybrid system for simultaneous fluorescence and x-ray computed tomography," *IEEE Transactions on Medical Imaging*, vol. 29, no. 2, pp. 465–73, Feb 2010.
- [30] F. Natterer, "Numerical methods in tomography," *Acta Numerica*, vol. 8, pp. 107–141, 1999.
- [31] J. Radon, "Über die Bestimmung von Funktionen durch ihre Integralwerte längs gewisser Mannigfaltigkeiten," *Berichte über die Verhandlungen der Sächsischen Akademie der Wissenschaften zu Leipzig. Mathematisch-Physische Klasse*, vol. 69, pp. 262–277, 1917.
- [32] —, "On the determination of functions from their integral values along certain manifolds," *IEEE Transactions on Medical Imaging*, vol. 5, no. 4, pp. 170–176, 1986.
- [33] L. Shepp and B. Logan, "The Fourier reconstruction of a head section," *IEEE Transactions on Nuclear Science*, vol. 21, pp. 21–43, 1974.
- [34] F. Natterer, "Fourier reconstruction in tomography," *Numerische Mathematik*, vol. 47, no. 3, pp. 343–353, 1985.
- [35] H. Stark, J. Woods, I. Paul, and R. Hingorani, "An investigation of computerized tomography by direct Fourier inversion and optimum interpolation," *IEEE Transactions on Biomedical Engineering*, no. 7, pp. 496–505, 1981.
- [36] D. Gottlieb, B. Gustafsson, and P. Forssen, "On the direct Fourier method for computer tomography," *Medical Imaging, IEEE Transactions on*, vol. 19, no. 3, pp. 223–232, 2002.
- [37] J. Walden, "Analysis of the direct Fourier method for computer tomography," *IEEE Transactions on Medical Imaging*, vol. 19, no. 3, pp. 211–222, 2002.
- [38] H. Stark, J. Woods, I. Paul, and R. Hingorani, "Direct Fourier reconstruction in computer tomography," *Acoustics, Speech and Signal Processing, IEEE Transactions on*, vol. 29, no. 2, pp. 237–245, 2003.
- [39] G. Ramachandran and A. Lakshminarayanan, "Three-dimensional reconstruction from radiographs and electron micrographs: Application of convolutions instead of Fourier transforms," *Proc. Natl. Acad. Sci. U.S.A.*, vol. 68, pp. 2236–2240, 1971.
- [40] P. Kinahan and J. Rogers, "Analytic 3D image reconstruction using all detected events," *IEEE Transactions on Nuclear Science*, vol. 36, no. 1, pp. 964–968, 1989.

- [41] L. Feldkamp, L. Davis, and J. Kress, "Practical cone-beam algorithm," *J. Opt. Soc. Am. A*, vol. 6, pp. 612–619, 1984.
- [42] S. Matej, G. T. Herman, T. K. Narayan, S. S. Furuie, R. M. Lewitt, and P. E. Kinahan, "Evaluation of task-oriented performance of several fully 3D PET reconstruction algorithms," *Physics in Medicine and Biology*, vol. 39, no. 3, pp. 355–67, Mar 1994.
- [43] M. Daube-Witherspoon, S. Matej, J. Karp, and R. Lewitt, "Application of the row action maximum likelihood algorithm with spherical basis functions to clinical . . .," *Nuclear Science*, vol. 48, no. 1, pp. 24–30, Jan 2001.
- [44] J. R. Bilbao-Castro, R. Marabini, C. O. S. Sorzano, I. García, J. M. Carazo, and J. J. Fernández, "Exploiting desktop supercomputing for three-dimensional electron microscopy reconstructions using ART with blobs," *Journal of Structural Biology*, vol. 165, no. 1, pp. 19–26, Jan 2009.
- [45] S. Matej and R. Lewitt, "Efficient 3D grids for image reconstruction using spherically-symmetric volume elements," *IEEE Transactions on Nuclear Science*, vol. 42, no. 4, pp. 1361–1370, 1995.
- [46] S. Matej and R. M. Lewitt, "Practical considerations for 3-D image reconstruction using spherically symmetric volume elements," *IEEE Transactions on Medical Imaging*, vol. 15, no. 1, pp. 68–78, Jan 1996.
- [47] P. C. Hansen, *Rank-Deficient and Discrete Ill-Posed Problems*. SIAM, 1998.
- [48] A. Björck, *Numerical methods for least square problems*. SIAM, 1996.
- [49] R. J. Hanson, "A numerical method for solving Fredholm integral equations of the first kind using singular values," *SIAM J. Numer. Anal.*, vol. 8, pp. 616–622, 1971.
- [50] J. M. Varah, "On the numerical solution of ill-conditioned linear systems with applications to ill-posed problems," *SIAM J. Numer. Anal.*, vol. 10, pp. 257–267, 1973.
- [51] G. W. Stewart, "Rank degeneracy," *SIAM J. Sci. Stat. Comput.*, vol. 5, pp. 403–413, 1984.
- [52] D. L. Phillips, "A technique for the numerical solution of certain integral equations of the first kind," *J. Assoc. Comput. Mach.*, vol. 9, pp. 84–97, 1962.
- [53] A. N. Tikhonov, "Solution of incorrectly formulated problems and the regularization method," *Soviet Math. Dokl.*, vol. 4, pp. 1035–1038, 1963.
- [54] P. C. Hansen, "The truncated SVD as a method for regularization," *BIT*, vol. 27, pp. 534–553, 1987.

- [55] G. H. Golub, M. T. Heath, and G. Wahba, "Generalized cross-validation as a method for choosing a good ridge parameter," *Technometrics*, vol. 21, pp. 215–223, 1979.
- [56] G. Wahba, "Practical approximate solutions to linear operator equations when the data are noisy," *SIAM J. Numer. Anal.*, vol. 14, pp. 651–667, 1977.
- [57] K. Miller, "Least squares methods for ill-posed problems with a prescribed bound," *SIAM J. Math. Anal.*, vol. 1, pp. 52–74, 1970.
- [58] C. L. Lawson and R. J. Hanson, *Solving Least Square Problems*. Englewood Cliffs, NJ: Prentice-Hall, 1974.
- [59] H. Bauschke and J. Borwein, "On projection algorithms for solving convex feasibility problems," *SIAM Review*, vol. 38, no. 3, pp. 367–426, 1996.
- [60] Y. Saad and H. van der Vorst, "Iterative solution of linear systems in the 20th century," *J Comput Appl Math*, vol. 123, no. 1-2, pp. 1–33, Jan 2000.
- [61] C. L. Byrne, *Applied Iterative Methods*. A. K. Peters, Ltd., 2007.
- [62] C. Byrne, "A unified treatment of some iterative algorithms in signal processing and image reconstruction," *Inverse Problems*, vol. 20, no. 1, pp. 103–120, 2004.
- [63] S. Kaczmarz, "Angenäherte Auflösung von Systemen linearer Gleichungen," *Bulletin International de l'Academie Polonaise des Sciences et des Lettres, series A*, vol. 35, pp. 355–357, 1937.
- [64] R. Gordon, R. Bender, and G. Herman, "Algebraic reconstruction techniques (ART) for threedimensional electron microscopy and x-ray photography," *Journal of Theoretical Biology*, vol. 29, pp. 471–481, 1970.
- [65] Y. Censor, "Row-action methods for huge and sparse systems and their applications," *SIAM review*, vol. 23, no. 4, pp. 444–466, 1981.
- [66] K. Tanabe, "Projection method for solving a singular system of linear equations and its applications," *Numer. Math.*, vol. 17, pp. 203–214, 1971.
- [67] G. T. Herman, A. Lent, and P. H. Lutz, "Relaxation methods for image reconstruction," *Commun. Assoc. Comput. Mach.*, vol. 21, pp. 152–158, 1978.
- [68] P. Eggermont, G. Herman, and A. Lent, "Iterative algorithms for large partitioned linear systems, with applications to image reconstruction," *Linear Algebra Appl.*, vol. 40, pp. 37–67, 1981.
- [69] Y. Censor, P. Eggermont, and D. Gordon, "Strong underrelaxation in Kaczmarz method for inconsistent systems," *Numer Math*, vol. 41, no. 1, pp. 83–92, Jan 1983.

- [70] G. T. Herman and L. B. Meyer, "Algebraic reconstruction techniques can be made computationally efficient [positron emission tomography application]," *IEEE Transactions on Medical Imaging*, vol. 12, no. 3, pp. 600–9, Jan 1993.
- [71] K. Mueller, R. Yagel, and J. Cornhill, "The weighted–distance scheme: a globally optimizing projection ordering method for ART," *IEEE Transactions on Medical Imaging*, vol. 16, no. 2, pp. 223–230, 1997.
- [72] X. Intes, V. Ntziachristos, J. Culver, A. Yodh, and B. Chance, "Projection access order in algebraic reconstruction technique for diffuse optical tomography," *Phys. Med. Biol.*, vol. 47, pp. N1–N10, 2002.
- [73] T. Strohmer and R. Vershynin, "A randomized solver for linear systems with exponential convergence," in *Approximation, Randomization, and Combinatorial Optimization. Algorithms and Techniques*, ser. Lecture Notes in Computer Science. Springer Berlin / Heidelberg, 2006, vol. 4110, pp. 499–507.
- [74] Y. Censor, G. Herman, and M. Jiang, "A note on the behavior of the randomized Kaczmarz algorithm of Strohmer and Vershynin," *Journal of Fourier Analysis and Applications*, vol. 15, no. 4, pp. 431–436, 2009.
- [75] Y. Censor and S. Zenios, *Parallel Optimization*. New York, USA: Oxford University Press, 1997.
- [76] C. Byrne, *Signal Processing: A Mathematical Approach*. Wellesley, MA: AK Peters, 2005.
- [77] R. Leahy and C. Byrne, "Recent developments in iterative image reconstruction for PET and SPECT," *IEEE Transactions on Medical Imaging*, vol. 19, no. 4, pp. 257–60, Apr 2000.
- [78] K. Sezan and H. Stark, *Image Recovery: Theory and application*. Academic Press, 1987, ch. Applications of convex projection theory to image recovery in tomography and related areas, pp. 415–462.
- [79] Y. Censor and T. Elfving, "A multiprojection algorithm using Bregman projections in a product space," *Numer. Algorithms*, vol. 8, pp. 221–239, 1994.
- [80] C. L. Byrne, "Iterative oblique projection onto convex sets and the split feasibility problem," *Inverse Problems*, vol. 18, pp. 441–453, 2002.
- [81] W. Mann, "Mean value methods in iteration," *Proc. Amer. Math. Soc.*, vol. 4, pp. 506–510, 1953.

- [82] L. Landweber, “An iterative formula for fredholm integral equations of the first kind,” *American Journal of Mathematics*, vol. 73, no. 3, pp. 615–624, 1951.
- [83] A. Anderson and A. Kak, “Simultaneous algebraic reconstruction technique (SART): a superior implementation of the ART algorithm,” *Ultrason. Imaging*, vol. 6, pp. 81–94, 1984.
- [84] G. Cimmino, “Caclolo approssimato per soluzioni die sistemi di equazioni lineari,” *La Ricerca Scientifica XVI, Series II, Anno IX*, vol. 1, pp. 326–333, 1938.
- [85] P. Gilbert, “Iterative methods for three–dimensional reconstruction from projections,” *Journal of Theoretical Biology*, vol. 36, pp. 105–117, 1972.
- [86] A. van der Sluis and H. A. van der Vorst, “SIRT and CG–type methods for the iterative solution of sparse linear least squares problems,” *Linear Algebra and its Applications*, vol. 130, pp. 257–302, 1990.
- [87] Y. Censor, D. Gordon, and R. Gordon, “Component averaging: An efficient iterative parallel algorithm for large and sparse unstructured problems,” *Parallel Computing*, vol. 27, no. 6, pp. 777–808, 2001.
- [88] —, “BICAV: a block-iterative parallel algorithm for sparse systems with pixel-related weighting,” *IEEE Transactions on Medical Imaging*, vol. 20, no. 10, pp. 1050–60, Oct 2001.
- [89] M. Chan, G. Herman, and E. Levitan, “Bayesian image reconstruction using a high-order interacting MRF model,” *Image Analysis and Processing*, pp. 608–614, 1995.
- [90] L. Shepp and Y. Vardi, “Maximum likelihood reconstruction for emission tomography,” *IEEE Transactions on Medical Imaging*, vol. MI-1, no. 2, pp. 113–122, Mar 1982.
- [91] A. Dempster, N. Laird, and D. Rubin, “Maximum likelihood from incomplete data via the EM algorithm,” *J. Roy. Statist. Soc. B*, vol. 39, pp. 1–38, 1977.
- [92] Y. Vardi, L. Shepp, and L. Kaufman, “A statistical model for positron emission tomography,” *J. Amer. Stat. Assoc.*, vol. 80, pp. 8–20, 1985.
- [93] L. Bregman, “The relaxation method of finding the common point of convex sets and its application to the solution of problems in convex programming,” *USSR Comput. Math. Math. Phys.*, vol. 7, pp. 200–217, 1967.
- [94] H. Bauschke and J. Borwein, “Legendre functions and the method of random Bregman projections,” *J. Convex Anal.*, vol. 4, pp. 27–67, 1997.

- [95] S. Kullback and R. Leibler, "On information and sufficiency," *Ann. Math. Stat.*, vol. 22, pp. 79–86, 1951.
- [96] C. Byrne, "Iterative image reconstruction algorithms based on cross-entropy minimization," *IEEE Transactions on Image Processing*, vol. IP-2, pp. 96–103, 1993.
- [97] S. Holte, P. Schmidlin, A. Linden, G. Rosenqvist, and L. Eriksson, "Iterative image reconstruction for positron emission tomography: a study of convergence and quantitation problems," *IEEE Transactions on Nuclear Science*, vol. 37, pp. 629–635, 1990.
- [98] H. Hudson, B. Hutton, and R. Larkin, "Accelerated EM reconstruction using ordered subsets," *J. Nucl. Med.*, vol. 33, p. 960, 1992.
- [99] H. M. Hudson and R. S. Larkin, "Accelerated image reconstruction using ordered subsets of projection data," *IEEE Transactions on Medical Imaging*, vol. 13, no. 4, pp. 601–9, Jan 1994.
- [100] J. Browne and A. D. Pierro, "A row-action alternative to the EM algorithm for maximizing likelihood in emission tomography," *IEEE Transactions on Medical Imaging*, vol. 15, no. 5, pp. 687–699, 1996.
- [101] C. Byrne, "Block-iterative methods for image reconstruction from projections," *IEEE Transactions on Image Processing*, vol. 5, pp. 792–794, 1996.
- [102] —, "Accelerating the EMLL algorithm and related iterative algorithms by rescaled block-iterative (RBI) methods," *IEEE Transactions on Image Processing*, vol. 7, pp. 100–109, 1998.
- [103] C. Paige and M. Saunders, "LSQR: An algorithm for sparse linear equations and sparse least squares," *ACM Transactions on Mathematical Software (TOMS)*, vol. 8, no. 1, pp. 43–71, 1982.
- [104] A. Rosenthal, D. Razansky, and V. Ntziachristos, "Fast semi-analytical model-based acoustic inversion for quantitative optoacoustic tomography," *IEEE Transactions on Medical Imaging*, vol. 29, no. 6, pp. 1275–85, Jun 2010.
- [105] S. Achilefu, "Lighting up tumors with receptor-specific optical molecular probes," *Technology in Cancer Research & Treatment*, vol. 3, pp. 393–409, 2004.
- [106] D. J. Bornhop, C. H. Contag, K. Licha, and C. J. Murphy, "Advance in contract agents, reporters and detection," *Journal of Biomedical Optics*, vol. 6, pp. 106–110, 2001.
- [107] C. H. Tung, "Developing fluorescence probes for in vivo molecular imaging," *Abstract of Papers of the American Chemical Society*, vol. 227, p. U146, 2004.

- [108] V. Ntziachristos, J. Ripoll, and R. Weissleder, "Would near-infrared fluorescence signals propagate through large human organs for clinical studies?" *Optics Letters*, vol. 27, no. 5, pp. 333–335, 2002.
- [109] C. Bremer, V. Ntziachristos, U. Mahmood, C. H. Tung, and R. Weissleder, "Fortschritte in der optischen Bildgebung," *Der Radiologe*, vol. 41, no. 2, pp. 131–137, 2001.
- [110] A. Hielscher, "Optical tomographic imaging of small animals," *Current Opinion in Biotechnology*, vol. 16, no. 1, pp. 79–88, 2005.
- [111] M. Gurfinkel, S. Ke, X. Wen, C. Li, and E. Sevick-Muraca, "Near-infrared fluorescence optical imaging and tomography," *Dis. Markers*, vol. 19, pp. 107–121, 2003.
- [112] V. Ntziachristos, J. Ripoll, L. Wang, and R. Weissleder, "Looking and listening to light: the evolution of whole-body photonic imaging," *Nat. Biotechnol.*, vol. 23, pp. 313–320, 2005.
- [113] X. Montet, J.-L. Figueiredo, H. Alencar, V. Ntziachristos, U. Mahmood, and R. Weissleder, "Tomographic fluorescence imaging of tumor vascular volume in mice," *Radiology*, vol. 242, no. 3, pp. 751–8, Mar 2007.
- [114] D. E. Sosnovik, M. Nahrendorf, N. Deliolanis, M. Novikov, E. Aikawa, L. Josephson, A. Rosenzweig, R. Weissleder, and V. Ntziachristos, "Fluorescence tomography and magnetic resonance imaging of myocardial macrophage infiltration in infarcted myocardium in vivo," *Circulation*, vol. 115, no. 11, pp. 1384–91, Mar 2007.
- [115] J. Haller, D. Hyde, N. Deliolanis, R. de Kleine, M. Niedre, and V. Ntziachristos, "Visualization of pulmonary inflammation using noninvasive fluorescence molecular imaging," *J. Appl. Physiol.*, vol. 104, no. 3, pp. 795–802, Mar 2008.
- [116] D. Boas, D. Brooks, E. Miller, C. Dimarzio, and et al., "Imaging the body with diffuse optical tomography," *Signal Processing Magazine*, Jan 2001.
- [117] K. M. Case and P. F. Zweifel, *Linear Transport Theory*. Addison Wesley MA, 1967.
- [118] A. Ishimaru, *Wave Propagation and Scattering in Random Media*. NY Academic, 1978, vol. 1.
- [119] J. Ripoll, *Light Diffusion in Turbid Media with Biomedical Application*. PhD thesis, Universidad Autonoma of Madrid, 2000.
- [120] J. Ripoll, V. Ntziachristos, R. Carminati, and M. Nieto-Vesperinas, "Kirchhoff approximation for diffusive waves," *Physical Review E*, vol. 64, 2001.

- [121] J. Ripoll, R. B. Schultz, and V. Ntziachristos, “Free-space propagation of diffuse light: Theory and experiments,” *Physical Review Letters*, vol. 91, no. 10, 2003.
- [122] M. A. O’Leary, D. A. Boas, X. D. Li, B. Chance, and A. G. Yodh, “Fluorescence lifetime imaging in turbid media,” *Optics Letters*, vol. 21, no. 2, pp. 158–160, 1996.
- [123] V. Ntziachristos and R. Weissleder, “Experimental three-dimensional fluorescence reconstruction of diffuse media by use of a normalized Born approximation,” *Optics Letters*, vol. 26, no. 12, pp. 893–895, 2001.
- [124] M. A. O’Leary, D. A. Boas, B. Chance, and A. G. Yodh, “Experimental images of heterogeneous turbid media by frequency-domain diffusing-photon tomography,” *Optics Letters*, vol. 20, no. 5, pp. 426–428, 1995.
- [125] A. Godavarty, M. Eppstein, C. Zhang, S. Theru, A. Thompson, M. Gurfinkel, and E. Sevick-Muraca, “Fluorescence-enhanced optical imaging in large tissue volumes using a gain modulated ICCD camera,” *Phys. Med. Biol.*, vol. 48, pp. 1701–1720, 2003.
- [126] E. Graves, J. Ripoll, R. Weissleder, and V. Ntziachristos, “A sub-millimeter resolution fluorescence molecular imaging system for small animal imaging,” *Medical Physics*, vol. 30, pp. 901–911, 2003.
- [127] S. Patwardhan, S. Bloch, S. Achilefu, and J. Culver, “Time-dependent whole-body fluorescence tomography of probe bio-distributions in mice,” *Optics Express*, vol. 13, pp. 2564–2577, 2005.
- [128] R. Schultz, J. Ripoll, and V. Ntziachristos, “Fluorescence tomography of tissues with non-contact measurements,” *IEEE Transactions on Medical Imaging*, vol. 23, pp. 492–500, 2004.
- [129] G. Turner, G. Zacharakis, A. Soubret, J. Ripoll, and V. Ntziachristos, “Complete-angle projection diffuse optical tomography by use of early photons,” *Optics Letters*, vol. 30, pp. 409–411, 2005.
- [130] H. Meyer, A. Garofalakis, G. Zacharakis, E. Economou, C. Mamalaki, S. Papamath-eakis, V. Ntziachristos, and J. Ripoll, “A multi-projection non-contact tomography setup for imaging arbitrary geometries,” in *Proc. SPIE Optical Technologies Biophys. Medicine VI*, vol. 5771, 2005, pp. 244–251.
- [131] T. Lasser, A. Soubret, J. Ripoll, and V. Ntziachristos, “Surface reconstruction for free-space 360° fluorescence molecular tomography and the effects of animal motion,” *IEEE Transactions on Medical Imaging*, vol. 27, no. 2, pp. 188–194, 2008.

- [132] M. Potmesil, "Generating octree models of 3-D objects from their silhouettes in a sequence of images," in *Comput. Vis. Graph. Image Process.*, vol. 40, no. 1, 1987, pp. 1–29.
- [133] A. Laurentini, "The visual hull: A new tool for contour-based image understanding," in *Proc. 7th Scand. Conf. Image Anal.*, 1991, pp. 993–1002.
- [134] —, "The visual hull concept for silhouette-based image understanding," *IEEE Trans. Pattern Anal. Mach. Intell.*, vol. 16, no. 2, pp. 150–162, 1994.
- [135] —, "How far 3-D shapes can be understood from 2-D silhouettes," *IEEE Trans. Pattern Anal. Mach. Intell.*, vol. 17, no. 2, pp. 188–195, 1995.
- [136] Y. Katz, "Pattern recognition of meteorological satellite cloud photography," in *Proc. 3rd Symp. Remote Sensing Environ.*, 1965, pp. 173–214.
- [137] W. Lorensen and H. Cline, "Marching cubes: A high resolution 3-D surface construction algorithm," *Comput. Graph.*, vol. 21, pp. 163–169, 1987.
- [138] J. Ripoll and V. Ntziachristos, "Imaging scattering media from a distance: theory and applications of noncontact optical tomography," *Mod. Phys. Lett. B*, vol. 18, pp. 1403–1431, 2004.
- [139] A. Klose, V. Ntziachristos, and A. Hielscher, "The inverse source problem based on the radiative transfer equation in optical molecular imaging," *J. Comput. Phys.*, vol. 202, pp. 323–345, 2005.
- [140] N. Deliolanis, T. Lasser, D. Hyde, A. Soubret, J. Ripoll, and V. Ntziachristos, "Free-space fluorescence molecular tomography utilizing 360 degrees geometry projections," *Optics Letters*, vol. 32, no. 4, pp. 382–4, Feb 2007.
- [141] V. Ntziachristos, C. Bremer, E. Graves, J. Ripoll, and R. Weissleder, "In vivo tomographic imaging of near-infrared fluorescent probes," *Mol. Imaging*, vol. 1, pp. 82–88, 2002.
- [142] B. Pogue, S. Poplack, T. McBride, W. Wells, K. Osterman, U. Osterberg, and K. Paulsen, "Quantitative hemoglobin tomography with diffuse near-infrared spectroscopy: pilot results in the breast," *Radiology*, vol. 218, pp. 261–266, 2001.
- [143] S. Colak, M. van der Mark, G. Hooft, J. Hoogenraad, E. van der Linden, and F. Kuijpers, "Clinical optical tomography and NIR spectroscopy for breast cancer detection," *IEEE J. Select. Top. Quantum Electron.*, vol. 5, pp. 1143–1158, 1999.
- [144] C. Schmitz, M. Locker, J. Lasker, A. Hielscher, and R. Barbour, "Instrumentation for fast functional optical tomography," *Rev. Sci. Instrum.*, vol. 73, pp. 429–439, 2002.

- [145] B. Pogue, T. McBride, U. Osterberg, and K. Paulsen, “Comparison of imaging geometries for diffuse optical tomography of tissue,” *Optics Express*, vol. 4, pp. 270–286, 1999.
- [146] J. Culver, R. Choe, M. Holboke, L. Zubkov, T. Durduran, A. Slemp, V. Ntziachristos, B. Chance, and A. Yodh, “Three-dimensional diffuse optical tomography in the parallel plane transmission geometry: evaluation of a hybrid frequency domain/continuous wave clinical system for breast imaging,” *Medical Physics*, vol. 30, pp. 235–247, 2003.
- [147] J. Culver, V. Ntziachristos, M. Holboke, and A. Yodh, “Optimization of optode arrangements for diffuse optical tomography: a singular value analysis,” *Optics Letters*, vol. 26, pp. 701–703, 2001.
- [148] E. Graves, J. Culver, J. Ripoll, R. Weissleder, and V. Ntziachristos, “Singular value analysis and optimization of experimental parameters in fluorescence molecular tomography,” *J. Opt. Soc. Am. A*, vol. 21, pp. 231–241, 2004.
- [149] H. Xu, H. Dehghani, and B. Pogue, “Near-infrared imaging in the small animal brain: optimization of fiber positions,” *J. Biomed. Opt.*, vol. 8, pp. 102–110, 2003.
- [150] T. Lasser and V. Ntziachristos, “Optimization of 360 degrees projection fluorescence molecular tomography,” *Medical Image Analysis*, vol. 11, no. 4, pp. 389–99, Aug 2007.
- [151] W. Press, B. Flannery, S. Teukolsky, and W. Vetterling, “Singular Value Decomposition,” in *Numerical Recipes in FORTRAN: The Art of Scientific Computing*. Cambridge: Cambridge University Press, 1992.
- [152] T. Farrell, M. Patterson, and B. Wilson, “A diffusion theory model of spatially resolved, steady-state diffuse reflectance for the non-invasive determination of tissue optical properties in vivo,” *Medical Physics*, vol. 19, pp. 879–888, 1992.
- [153] J. Ripoll, M. Nieto-Vesperinas, R. Weissleder, and V. Ntziachristos, “Fast analytical approximation for arbitrary geometries in diffuse optical tomography,” *Optics Letters*, vol. 27, pp. 527–529, 2002.
- [154] R. Alfano, S. Demos, P. Galland, S. Gayen, Y. Guo, P. Ho, X. Liang, F. Liu, L. Wang, Q. Wang, and W. Wang, “Time-resolved and nonlinear optical imaging for medical applications.” *Ann. N. Y. Acad. Sci.*, vol. 838, pp. 14–28, 1998.
- [155] C. D’Andrea, L. Spinelli, D. Comelli, G. Valentini, and R. Cubeddu, “Localization and quantification of fluorescent inclusions embedded in a turbid medium,” *Phys. Med. Biol.*, vol. 50, no. 10, p. 2313, 2005.

- [156] V. Ntziachristos, C.-H. Tung, C. Bremer, and R. Weissleder, "Fluorescence molecular tomography resolves protease activity in vivo," *Nature Medicine*, vol. 8, pp. 757–761, 2002.
- [157] V. Ntziachristos, E. A. Schellenberger, J. Ripoll, D. Yessayan, E. Graves, A. Bogdanov, L. Josephson, and R. Weissleder, "Visualization of antitumor treatment by means of fluorescence molecular tomography with an annexin V–Cy5.5 conjugate," *Proc. Natl. Acad. Sci. U.S.A.*, vol. 101, no. 33, pp. 12 294–12 299, 2004.
- [158] N. Deliolanis, T. Lasser, M. Niedre, A. Soubret, and V. Ntziachristos, "In-vivo lung cancer imaging in mice using 360 degrees free-space fluorescence molecular tomography," in *Proc. Ann. Intl. Conf. IEEE Engineering in Medicine and Biology Society*, vol. 1, Jan 2006, pp. 2370–2372.
- [159] T. Lasser, N. Deliolanis, A. Soubret, J. Ripoll, and V. Ntziachristos, "360° free space fluorescence molecular tomography using silhouette surface reconstruction," in *Proc. of SPIE*, Munich, Germany, June 2007.
- [160] B. W. Pogue, T. O. McBride, J. Prewitt, U. L. Österberg, and K. D. Paulsen, "Spatially variant regularization improves diffuse optical tomography," *Applied Optics*, vol. 38, no. 13, pp. 2950–2961, 1999.
- [161] H. Meyer, A. Garofalakis, G. Zacharakis, S. Psycharakis, C. Mamalaki, D. Kioussis, E. N. Economou, V. Ntziachristos, and J. Ripoll, "Noncontact optical imaging in mice with full angular coverage and automatic surface extraction," *Applied Optics*, vol. 46, no. 17, pp. 3617–27, Jun 2007.
- [162] A. Garofalakis, G. Zacharakis, H. Meyer, E. N. Economou, C. Mamalaki, J. Papatheakis, D. Kioussis, V. Ntziachristos, and J. Ripoll, "Three-dimensional in vivo imaging of green fluorescent protein-expressing T cells in mice with noncontact fluorescence molecular tomography," *Mol. Imaging*, vol. 6, no. 2, pp. 96–107, Jan 2007.
- [163] D. Hyde, E. Miller, D. H. Brooks, and V. Ntziachristos, "A statistical approach to inverting the born ratio," *IEEE Transactions on Medical Imaging*, vol. 26, no. 7, pp. 893–905, Jul 2007.
- [164] D. Razansky and V. Ntziachristos, "Hybrid photoacoustic fluorescence molecular tomography using finite-element-based inversion," *Medical Physics*, vol. 34, no. 11, p. 4293, 2007.
- [165] M. Freyer, A. Ale, R. B. Schulz, M. Zientkowska, V. Ntziachristos, and K.-H. Engelmeier, "Fast automatic segmentation of anatomical structures in XCT images to improve FMT reconstruction," *Journal of Biomedical Optics*, vol. 15, no. 3, p. 036006, 2010.

- [166] D. Hyde, R. Schulz, D. Brooks, E. Miller, and V. Ntziachristos, "Performance dependence of hybrid x-ray computed tomography/fluorescence molecular tomography on the optical forward problem," *Journal of the Optical Society of America A, Optics, image science, and vision*, vol. 26, no. 4, pp. 919–23, Apr 2009.
- [167] D. Hyde, R. de Kleine, S. A. Maclaurin, E. Miller, D. H. Brooks, T. Krucker, and V. Ntziachristos, "Hybrid FMT-CT imaging of amyloid-beta plaques in a murine Alzheimer's disease model," *NeuroImage*, vol. 44, no. 4, pp. 1304–11, Feb 2009.
- [168] A. Ale, R. B. Schulz, A. Sarantopoulos, and V. Ntziachristos, "Imaging performance of a hybrid x-ray computed tomography–fluorescence molecular tomography system using priors," *Medical Physics*, vol. 37, p. 1976, 2010.
- [169] D. Hyde, E. L. Miller, D. H. Brooks, and V. Ntziachristos, "Data specific spatially varying regularization for multimodal fluorescence molecular tomography," *IEEE Transactions on Medical Imaging*, vol. 29, no. 2, pp. 365–74, Feb 2010.
- [170] C. Vinegoni, D. Razansky, S. A. Hilderbrand, F. Shao, V. Ntziachristos, and R. Weissleder, "Transillumination fluorescence imaging in mice using biocompatible upconverting nanoparticles," *Optics Letters*, vol. 34, no. 17, pp. 2566–8, Sep 2009.
- [171] N. C. Deliolanis, J. Dunham, T. Wurdinger, J.-L. Figueiredo, B. A. Tannous, T. Bakhos, and V. Ntziachristos, "In-vivo imaging of murine tumors using complete-angle projection fluorescence molecular tomography," *Journal of Biomedical Optics*, vol. 14, no. 3, p. 030509, Jan 2009.
- [172] J. Baeten, J. Haller, H. Shih, and V. Ntziachristos, "In vivo investigation of breast cancer progression by use of an internal control," *Neoplasia*, vol. 11, no. 3, pp. 220–227, 2009.
- [173] G. M. Turner, A. Soubret, and V. Ntziachristos, "Inversion with early photons," *Medical Physics*, vol. 34, no. 4, p. 1405, 2007.
- [174] M. J. Niedre, R. H. de Kleine, E. Aikawa, D. G. Kirsch, R. Weissleder, and V. Ntziachristos, "Early photon tomography allows fluorescence detection of lung carcinomas and disease progression in mice in vivo," *Proc. Natl. Acad. Sci. U.S.A.*, vol. 105, no. 49, pp. 19 126–19 131, 2008.
- [175] M. Niedre and V. Ntziachristos, "Comparison of fluorescence tomographic imaging in mice with early-arriving and quasi-continuous-wave photons," *Optics Letters*, vol. 35, no. 3, pp. 369–71, Feb 2010.
- [176] S. Björn, V. Ntziachristos, and R. Schulz, "Mesoscopic epifluorescence tomography: reconstruction of superficial and deep fluorescence in highly-scattering media," *Optics Express*, vol. 18, no. 8, pp. 8422–9, Apr 2010.

- [177] C. Vinegoni, C. Pitsouli, D. Razansky, N. Perrimon, and V. Ntziachristos, “In vivo imaging of drosophila melanogaster pupae with mesoscopic fluorescence tomography,” *Nature Methods*, vol. 5, no. 1, pp. 45–7, Jan 2008.
- [178] C. Vinegoni, D. Razansky, C. Pitsouli, N. Perrimon, V. Ntziachristos, and R. Weissleder, “Mesoscopic fluorescence tomography for in-vivo imaging of developing drosophila,” *J. Vis. Exp.*, no. 30, Jan 2009.
- [179] C. Vinegoni, L. Fexon, P. F. Feruglio, M. Pivovarov, J. Figueiredo, M. Nahrendorf, A. Pozzo, A. Sbarbati, and R. Weissleder, “High throughput transmission optical projection tomography using low cost graphics processing unit,” *Optics Express*, vol. 17, no. 25, pp. 22 320–22 332, 2009.
- [180] C. Vinegoni, P. F. Feruglio, V. Cortez-Retamozo, D. Razansky, B. D. Medoff, V. Ntziachristos, A. Sbarbati, M. Pittet, and R. Weissleder, “Imaging of molecular probe activity with born-normalized fluorescence optical projection tomography,” *Optics Letters*, vol. 35, no. 7, pp. 1088–90, Apr 2010.
- [181] C. Vinegoni, D. Razansky, J.-L. Figueiredo, M. Nahrendorf, V. Ntziachristos, and R. Weissleder, “Normalized born ratio for fluorescence optical projection tomography,” *Optics Letters*, vol. 34, no. 3, pp. 319–21, Feb 2009.
- [182] C. Vinegoni, D. Razansky, J. Figueiredo, L. Fexon, M. Pivovarov, M. Nahrendorf, V. Ntziachristos, and R. Weissleder, “Born normalization for fluorescence optical projection tomography for whole heart imaging,” *J. Vis. Exp.*, vol. 28, p. 1389, 2009.
- [183] D. Razansky, C. Vinegoni, and V. Ntziachristos, “Multispectral photoacoustic imaging of fluorochromes in small animals,” *Optics Letters*, vol. 32, no. 19, pp. 2891–3, Oct 2007.
- [184] D. Razansky, M. Distel, C. Vinegoni, R. Ma, N. Perrimon, R. Köster, and V. Ntziachristos, “Multispectral opto-acoustic tomography of deep-seated fluorescent proteins in vivo,” *Nature Photonics*, vol. 3, no. 7, pp. 412–417, 2009.
- [185] R. Ma, A. Taruttis, V. Ntziachristos, and D. Razansky, “Multispectral optoacoustic tomography (MSOT) scanner for whole-body small animal imaging,” *Optics Express*, vol. 17, no. 24, pp. 21 414–26, Nov 2009.
- [186] D. Razansky, J. Baeten, and V. Ntziachristos, “Sensitivity of molecular target detection by multispectral optoacoustic tomography (MSOT),” *Medical Physics*, vol. 36, p. 939, 2009.
- [187] V. Ntziachristos and D. Razansky, “Molecular Imaging by Means of Multispectral Optoacoustic Tomography (MSOT),” *Chem. Rev.*, vol. 110, no. 5, pp. 2783–2794, 2010.

- [188] D. Razansky, C. Vinegoni, and V. Ntziachristos, "Polarization-sensitive optoacoustic tomography of optically diffuse tissues," *Optics Letters*, vol. 33, no. 20, pp. 2308–10, Oct 2008.
- [189] —, "Imaging of mesoscopic-scale organisms using selective-plane optoacoustic tomography," *Physics in Medicine and Biology*, vol. 54, no. 9, pp. 2769–77, May 2009.
- [190] A. Rosenthal, D. Razansky, and V. Ntziachristos, "Quantitative optoacoustic signal extraction using sparse signal representation," *IEEE Transactions on Medical Imaging*, vol. 28, no. 12, pp. 1997–2006, Dec 2009.
- [191] T. Jetzfellner, D. Razansky, A. Rosenthal, R. Schulz, K.-H. Englmeier, and V. Ntziachristos, "Performance of iterative optoacoustic tomography with experimental data," *Applied Physics Letters*, vol. 95, no. 1, p. 013703, 2009.
- [192] A. Buehler, E. Herzog, D. Razansky, and V. Ntziachristos, "Video rate optoacoustic tomography of mouse kidney perfusion," *Optics Letters*, vol. 35, no. 14, pp. 2475–7, Jul 2010.
- [193] A. Taruttis, E. Herzog, D. Razansky, and V. Ntziachristos, "Real-time imaging of cardiovascular dynamics and circulating gold nanorods with multispectral optoacoustic tomography," *Optics Express*, vol. 18, no. 19, pp. 19 592–602, Sep 2010.
- [194] V. Ntziachristos, "Going deeper than microscopy: the optical imaging frontier in biology," *Nature Methods*, vol. 7, no. 8, pp. 603–14, Aug 2010.
- [195] A. K. Buck, S. Nekolla, S. Ziegler, A. Beer, B. J. Krause, K. Herrmann, K. Scheidhauer, H.-J. Wester, E. J. Rummeny, M. Schwaiger, and A. Drzezga, "SPECT/CT," *J. Nucl. Med.*, vol. 49, no. 8, pp. 1305–1319, Aug 2008.
- [196] J. Czernin, M. R. Benz, and M. S. Allen-Auerbach, "PET/CT imaging: The incremental value of assessing the glucose metabolic phenotype and the structure of cancers in a single examination," *Eur J Radiol*, vol. 73, no. 3, pp. 470–480, Mar 2010.
- [197] M. Baumhauer, M. Feuerstein, H.-P. Meinzer, and J. Rassweiler, "Navigation in endoscopic soft tissue surgery: perspectives and limitations." *J. Endourol.*, vol. 22, no. 4, pp. 751–766, Apr 2008.
- [198] N. Foroglou, A. Zamani, and P. Black, "Intra-operative MRI (iop-MR) for brain tumour surgery," *Br. J. Neurosurg.*, vol. 23, no. 1, pp. 14–22, Feb 2009.
- [199] M. Fujii and T. Wakabayashi, "Image-guided neurosurgery using intraoperative MRI," *Brain Nerve*, vol. 61, no. 7, pp. 823–834, Jul 2009.

- [200] L. Vermeeren, R. A. Valdes Olmos, W. Meinhardt, A. Bex, H. G. van der Poel, W. V. Vogel, F. Sivo, C. A. Hoefnagel, and S. Horenblas, "Intraoperative radioguidance with a portable gamma camera: a novel technique for laparoscopic sentinel node localisation in urological malignancies." *Eur. J. Nucl. Med. Mol. Imaging*, vol. 36, no. 7, pp. 1029–1036, Jul 2009.
- [201] S. Vidal-Sicart, P. Paredes, G. Zanón, J. Pahisa, S. Martinez-Román, X. Caparrós, A. Vilalta, R. Rull, and F. Pons, "Added value of intraoperative real-time imaging in searches for difficult-to-locate sentinel nodes." *J. Nucl. Med.*, vol. 51, no. 8, pp. 1219–1225, Aug 2010.
- [202] P. Paredes, S. Vidal-Sicart, G. Zanón, N. Roé, S. Rubí, S. Lafuente, J. Pavía, and F. Pons, "Radioguided occult lesion localisation in breast cancer using an intraoperative portable gamma camera: first results." *Eur. J. Nucl. Med. Mol. Imaging*, vol. 35, no. 2, pp. 230–235, Feb 2008.
- [203] R. A. Valdes Olmos, S. Vidal-Sicart, and O. E. Nieweg, "Technological innovation in the sentinel node procedure: towards 3-D intraoperative imaging." *Eur. J. Nucl. Med. Mol. Imaging*, vol. 37, no. 8, pp. 1449–1451, Aug 2010.
- [204] A. Hartl, S. I. Ziegler, and N. Navab, "Models of Detection Physics for Nuclear Probes in Freehand SPECT Reconstruction," presented at IEEE Medical Imaging Conference, Knoxville, USA, October 2010.
- [205] T. Wendler, T. Lasser, S. I. Ziegler, and N. Navab, "Towards Confident 3D Tomographic Reconstruction for Asymmetric, Sparse Detector Geometries," presented at IEEE Medical Imaging Conference, Dresden, Germany, October 2008.
- [206] D. Ros, C. Falcón, I. Juvells, and J. Pavía, "The influence of a relaxation parameter on SPECT iterative reconstruction algorithms," *Physics in Medicine and Biology*, vol. 41, no. 5, p. 925, 1996.
- [207] G. Guennebaud, B. Jacob *et al.* (2010) The Eigen C++ template library for linear Algebra. [Online]. Available: <http://eigen.tuxfamily.org>
- [208] T. Wendler, K. Herrmann, A. Schnelzer, T. Lasser, J. Traub, O. Kutter, A. Ehlerding, K. Scheidhauer, T. Schuster, M. Kiechle, M. Schwaiger, N. Navab, S. I. Ziegler, and A. K. Buck, "First demonstration of 3-D lymphatic mapping in breast cancer using freehand SPECT," *Eur. J. Nucl. Med. Mol. Imaging*, vol. 37, no. 8, pp. 1452–1461, Mar 2010.
- [209] T. Lasser, T. Wendler, S. I. Ziegler, and N. Navab, "Towards Reproducibility of Freehand 3D Tomographic Nuclear Imaging," in *Proc. IEEE Medical Imaging Conference*, Dresden, Germany, October 2008.

- [210] Compute Unified Device Architecture. [Online]. Available: http://www.nvidia.com/object/cuda_home_new.html
- [211] A. Dului, "Interactive Tomographic Reconstruction for Freehand SPECT using the GPU," Master's thesis, Technische Universität München, 2009.
- [212] OpenCL - The open standard for parallel programming of heterogeneous systems. [Online]. Available: <http://www.khronos.org/opencl/>
- [213] T. Lasser, A. Dului, T. Wendler, S. I. Ziegler, and N. Navab, "Interactive Reconstruction for Freehand SPECT: An Approach to Acquisition Guidance?" in *Proc. Annual Congress EANM*, Barcelona, Spain, October 2009.
- [214] G. Lyman, A. Guiliano, M. Somerfield, A. Benson, D. Bodurka, and H. B. et al., "American society of clinical oncology guideline recommendations for sentinel lymph node biopsy in early-stage breast cancer," *J. Clin. Oncol.*, vol. 23, pp. 7703–7720, 2005.
- [215] G. Cserni, I. Amendoeira, N. Apostolikas, J. Bellocq, S. Bianchi, and G. B. et al., "Pathological work-up of sentinel lymph nodes in breast cancer. Review of current data to be considered for the formulation of guidelines," *Eur. J. Cancer*, vol. 39, pp. 1654–1667, 2003.
- [216] T. Kim, A. Guiliano, and G. Lyman, "Lymphatic mapping and sentinel lymph node biopsy in early-stage breast carcinoma: a metaanalysis," *Cancer*, vol. 106, pp. 4–16, 2006.
- [217] D. Husarik and H. Steinert, "Single-photon emission computed tomography/computed tomography for sentinel node mapping in breast cancer," *Semin. Nucl. Med.*, vol. 37, pp. 29–33, 2007.
- [218] H. Lerman, U. Metser, G. Lievshitz, F. Sperber, S. Schneebaum, and E. Even-Sapir, "Lymphoscintigraphic sentinel node identification in patients with breast cancer: the role of SPECT-CT," *Eur. J. Nucl. Med. Mol. Imaging*, vol. 33, pp. 329–337, 2006.
- [219] I. van der Ploeg, R. V. Olmos, O. Nieweg, E. Rutgers, B. Kroon, and C. Hoefnagel, "The additional value of SPECT/CT in lymphatic mapping in breast cancer and melanoma," *J. Nucl. Med.*, vol. 48, pp. 1756–1760, 2007.
- [220] H. Lerman, G. Lievshitz, O. Zak, U. Metser, S. Schneebaum, and E. Even-Sapir, "Improved sentinel node identification by SPECT/CT in overweight patients with breast cancer," *J. Nucl. Med.*, vol. 48, pp. 201–206, 2007.

- [221] A. Abe, N. Takahashi, J. Lee, T. Oka, K. Shizukuishi, and T. K. et al., “Performance evaluation of a hand-held, semiconductor (CdZnTe)-based gamma camera,” *Eur. J. Nucl. Med. Mol. Imaging*, vol. 30, pp. 805–811, 2003.
- [222] E. Barranger, K. Kerrou, S. Pitre, M. Duval, Y. Charon, and S. Uzan, “Place of a hand-held gamma camera (POCI) in the breast cancer sentinel node biopsy,” *Breast*, vol. 16, pp. 443–444, 2007.
- [223] C. Mathelin, S. Salvador, D. Huss, and J. Guyonnet, “Precise localization of sentinel lymph nodes and estimation of their depth using a prototype intraoperative mini gamma-camera in patients with breast cancer,” *J. Nucl. Med.*, vol. 48, pp. 623–629, 2007.
- [224] F. Sánchez, J. Benlloch, B. Escat, N. Pavón, E. Porrás, and D. K.-H. et al., “Design and tests of a portable mini gamma camera,” *Medical Physics*, vol. 31, pp. 1384–1397, 2004.
- [225] O. Schillaci, G. D’Errico, R. Scafè, A. Soluri, N. Burgio, and A. Santagata, “Sentinel node detection with imaging probe,” *Tumori*, vol. 88, pp. S32–35, 2002.
- [226] T. Kühn, A. Bembenek, T. Decker, D. Munz, M. Sautter-Bihl, and M. U. et al., “A concept for the clinical implementation of sentinel lymph node biopsy in patients with breast carcinoma with special regard to quality assurance,” *Cancer*, vol. 103, pp. 451–461, 2005.
- [227] M. D. Jong, R. Valkema, F. Jamar, L. Kvols, D. Kwekkeboom, and W. B. et al., “Somatostatin receptor-targeted radionuclide therapy of tumors: preclinical and clinical findings,” *Semin. Nucl. Med.*, vol. 32, pp. 133–140, 2002.
- [228] D. Kwekkeboom and E. Krenning, “Somatostatin receptor imaging,” *Semin. Nucl. Med.*, vol. 32, pp. 84–91, 2002.
- [229] R. Nadeem, L. Chagla, O. Harris, S. Desmond, R. Thind, and A. F. et al., “Tumour localisation with a metal coil before the administration of neo-adjuvant chemotherapy,” *Breast*, vol. 14, pp. 403–407, 2005.
- [230] T. Wendler, “3D intraoperative functional imaging with navigated probes,” Ph.D. dissertation, Technische Universität München, 2010.
- [231] N. Navab, T. Wendler, K. Herrmann, A. Ehlerding, J. Säckl, M. E. Martignoni, A. Schnelzer, S. I. Ziegler, and A. K. Buck, “Freehand SPECT in the operating room: first feasibility study on 21 patients,” presented at Intl. Conf. Soc. Medical Innovation and Technology (SMIT), 2010.

- [232] T. Wendler, A. Hartl, T. Lasser, J. Traub, F. Daghighian, S. I. Ziegler, and N. Navab, "Towards intra-operative 3D nuclear imaging: reconstruction of 3D radioactive distributions using tracked gamma probes," in *Proc. Intl. Conf. on Medical Image Computing and Computer-Assisted Intervention (MICCAI)*, vol. 10, no. Pt 2, Brisbane, Australia, October 2007, pp. 909–17.
- [233] L. M. A. Crane, G. Themelis, R. G. Pleijhuis, N. J. Harlaar, A. Sarantopoulos, H. J. G. Arts, A. G. J. van der Zee, N. Vasilis, and G. M. van Dam, "Intraoperative multispectral fluorescence imaging for the detection of the sentinel lymph node in cervical cancer: A novel concept," *Molecular Imaging and Biology*, Sep 2010.
- [234] D. Shakir, J. Bieniarz, T. Wendler, N. Navab, and S. Ziegler, "A first study on biological feasibility of intraoperative control of tumor resection borders with navigated beta-probe surface imaging," in *Proc. Annual Meeting SNM*, 2010.